ABSTRACT

Title of Dissertation: ALL-OPTICAL
QUANTUM DIAMOND MAGNETIC SENSING

Xiechen Zheng
Doctor of Philosophy, 2026

Dissertation Directed by: Professor Ronald L. Walsworth
Department of Electrical and Computer Engineering

Nitrogen-vacancy (NV) centers in diamonds have emerged as a versatile solid-state spin defect platform for magnetic sensing under wide-ranging conditions. The negatively charged nitrogen-vacancy (NV^-) center combines robust optical excitation and readout via spin-state-dependent photoluminescence (PL) with long spin coherence times at room temperature. This combination makes NV^- an attractive platform for highly sensitive magnetometry across a broad range of applications in the physical and life sciences. Conventional NV^- magnetic sensing protocols, such as optically detected magnetic resonance (ODMR), rely on microwave irradiation to coherently manipulate the NV^- spin states. Microwave irradiation, however, introduces additional experimental complexity and may perturb the sample under study.

This work pursues all-optical (AO), microwave-free magnetic sensing using NV^- ensembles in diamond. At low magnetic fields ($< 2\,\mathrm{mT}$) under continuous-wave (CW) NV^- optical readout, we demonstrate AO-PL contrast features arising from resonant NV-

NV dipolar interactions, known as NV-NV cross-relaxation, between NV^- centers of different crystallographic orientations. We further resolve sub-structure within these contrast features arising from NV^- hyperfine interaction with the nitrogen nuclear spin. To improve measurement robustness, we introduce a pulsed AO sequence that uses two PL readouts within an optical pulse to suppress common-mode noise, achieving up to $10\times$ improvement in the low-frequency noise floor over conventional CW AO magnetometry near zero field. Beyond the low-field regime, we show that AO-PL changes induced by magnetic fields misaligned from the NV^- symmetry axis may be able to support AO magnetic sensing in demanding electromagnetic environments such as inside a nuclear fusion reactor, where efficient microwave delivery is impractical. Using the pulsed-sensing technique, we can detect AO-PL changes reliably in a complex optical environment, where optical intensity noise is substantial. Given the robustness of the diamond host and NV^- properties, AO magnetometry may be suited to harsh environments involving extreme temperature, pressure, radiation, or chemically corrosive conditions. Finally, we develop a simple benchtop NV^- system capable of CW-ODMR magnetometry for educational use in a quantum hardware laboratory course. This work informs NV-diamond sample optimization for effective AO operation across diverse applications and extends the operation range of NV^- quantum sensing beyond controlled laboratory settings.

All-Optical Quantum Diamond Magnetic Sensing

by

Xiechen Zheng

Dissertation submitted to the Faculty of the Graduate School of the
University of Maryland, College Park in partial fulfillment
of the requirements for the degree of
Doctor of Philosophy
2026

Advisory Committee:
Professor Ronald L. Walsworth, Chair/Advisor
Professor Giuliano Scarcelli, Dean's Representative
Professor Cheng Gong
Professor Julius Goldhar
Professor Saikat Guha

© Copyright by
Xiechen Zheng
2026

Preface

I was interested in studying *quantum* technology when I started graduate school. With my bachelor's degree in Electrical Engineering, I wanted to work on hands-on projects that put quantum effects to practical use. What followed was over a year of chasing one deceptively simple question: what does quantum actually offer? Quantum computing had always been the headline act, promising exponential speedup and the ability to outrun classical computers for solving complex problems, *if* enough stable qubits could ever be built. But I was not drawn to this *if*. Building foundational pieces on the hope that they would one day contribute to a working system, one that itself might not even be engineering-feasible within a decade, was not a path I wanted to spend the next several years chasing.

While I was still figuring out what to actually work on, I sat in on a seminar about using diamonds for quantum sensing, specifically, monitoring activity in integrated circuits. I remembered telling my friend Nate afterward that the whole idea sounded fun, but hard. I think it was the first time I had heard the phrase "quantum sensing", and unlike quantum computing, it felt real. Not long after, I reached out to my now-PI, Ronald L. Walsworth, and started working in the lab in fall 2020.

Looking back, curiosity, persistence, intuition, and luck are the four words that summarize my PhD journey, which centered on NV-diamond experiments for magnetic field sensing.

Without curiosity, I would not have investigated an unexpected signal that appeared on the oscilloscope under an uncontrolled experimental condition, a signal that eventually became the foundation of most of my dissertation on all-optical (AO) NV photoluminescence (PL) response at low magnetic fields.

Without persistence, I would not have looked twice on the one "spike" that kept showing up on an otherwise linear curve, a spike that led to much more complicated signals, nor would I have spent months refining experiments to resolve a very weak AO signal until our theory and results agreed. Persistence is also what produced the pulsed AO sequence to suppress common-mode noise, a solution that only emerged after the simpler cw approach kept losing to optical intensity noise in our setups.

Without intuition, I would not have hypothesized that the "mysterious" sub-features we observed were due to hyperfine interactions with nuclear spins, or that lower laser power is needed to resolve crucial narrow linewidth AO signals from NVs in a thin layer of the diamond at the cost of low PL collection. Both hypotheses turned out to be correct.

Without (bad) luck, I would not have shifted my focus to lead my own low-field AO project after receiving a piece of faulty equipment critical to my main project at that time, and I would have missed a fruitful journey working with many wonderful colleagues along the way. Luck cut both ways, though. Without (good) luck, I would not have successfully measured the expected AO signals at all, since some optical tables are more magnetic than the one I decided to build the setup on and could easily have perturbed my measurements instead.

Curiosity, persistence, intuition, and luck got the experiments done. What they were done *for* is a question I kept returning to as the PhD went on.

As I progressed through PhD, I started wondering: what applications outside of scientific research could truly benefit from the improved sensitivity that quantum sensing offers? This is a question I am still actively exploring. This dissertation focuses on NV AO protocols for quantum sensing, which trade some sensitivity for simplicity by removing the microwave components required by conventional magnetometry protocols. That trade-off can make AO sensing a harder sell in scientific publications, where higher sensitivity is often treated as the measure of innovation. But through the National Science Foundation's I-Corps customer discovery program, I learned that industry tends to care less about a sensor's absolute sensitivity, and more about whether it can operate reliably under real-world conditions, provided it is sensitive enough to begin with.

The message I want to leave with readers is that quantum sensing for practical applications isn't just about being highly sensitive. What matters more is the ability to be deployed in the targeted environment and get the job done. This brings me back to where this preface started. I wanted to put quantum effects to practical use; my reluctance to build foundational pieces on the hope that they would one day contribute to a working system still holds true. But now, at the end of my PhD journey, AO sensing feels like a different kind of piece, one whose simplicity and robustness, inherited in part from diamond's own resilience as a host material, give it a real chance of becoming part of a working system, rather than a promise deferred to some uncertain future. Quantum sensing as a field is just beginning its transition out of fundamental research, and I believe AO magnetic sensing with diamonds can help it land in the space of practical applications sooner rather than later.

Dedication

To my family, and especially my parents. Oceans and years apart, you have been my beacon.

Acknowledgments

Prof. Ronald Walsworth, my research advisor, often reminds us that a Ph.D. journey is like a marathon. It has been a long journey, one I could not have completed on my own. It has been a journey carried by the support of many others, and I am sincerely grateful for everyone's presence along the way.

I owe a debt of gratitude to my family more than to anyone else: my father, Shangwei Zheng; my mother, Zheyan Zhu; my cousins, Feifei Zheng and Xuanle Zheng; and my grandparents, Liangying Zhu, Bingfen Zhang, Fuguo Zheng and Yuyan Xu. Despite not being able to visit home for eight years throughout graduate school, it is the support and compassion of my family that has put my mind in peace, knowing that they will always have my back and help me worry less.

I would like to thank Ron for his guidance. Six years ago, affected by the pandemic, I was hesitant about which research direction suited me best, and even whether I wanted to continue in the graduate program at all. Ron welcomed me warmly into the group regardless. His input and feedback over the years have tremendously helped me grow as a scientist, to think and communicate scientifically, and to avoid being tunnel-visioned in my research direction. Ron has also provided many opportunities and encouraged me to step outside the lab and connect with people outside our field. These experiences helped shape me toward an engineering role I would like to pursue further: the quantum sensing science we explore in the lab is exciting, but what does the world outside academia

actually need from this technology?

I have been fortunate to have mentors in Connor Hart, Matthew Turner, and Kevin Olsson, whose patience positively shaped my learning experience, especially since almost everything about NV quantum sensing was new to me. Matthew Turner's deep knowledge of experiment techniques has profoundly inspired me, helping me grow from barely knowing optical alignment to being proud of my rapid-prototyping skills and my rigor in running experiments. As I matured as a Ph.D. student, I was grateful for the opportunity to mentor Jeyson Támara-Isaza and Kristine Ung in turn. Ron once asked me:

> "Looking back through your Ph.D, what is your most memorable experience?"

I think of Jeyson immediately: our many hours-long discussions brainstorming new experiment ideas, our time spent constructing the initial low-field AO system, our excitement when we acquired the two-dimensional NV-PL response for the first time and confirmed the existence of NV-NV cross-relaxation features, our confusion working through the physics, and our frustration when simulation and experiment refused to agree. Having mostly built my experiments alone before then, I cherish the days we spent together, every one filled with excitement and unknowns, always another idea to explore or refine. It was hard to say goodbye when you left the group, but I am proud to see you pursue your next scientific chapter. Kristine, our time together comes to mind for a different reason: when I was among the first to move into our new lab space in the IDEA Factory, the quiet of an empty lab was discouraging, until you filled the room with your joy and laughter, turning what would otherwise have been a dull move-in process into something enjoyable. Your

time with me has also taught me how to be a better mentor, and I am happy to see you grow as a scientist through your own achievements.

I am grateful for my "AO-QDM" research team: Matthew, Connor, Jeyson, Kristine, Paul Petruzzi, John Blanchard, Johannes Cremer, Michael Crescimanno, and Zechuan Yin. Much of the work in this dissertation is the result of the fruitful discussions with this team: I learned many optical fiber handling techniques from Paul, admired John's great instinct for applying different numerical methods to our experimental data, absorbed Johannes' philosophy of adopting quick, sometimes "inelegant," ways to make things work, and learned to stay alert to confirmation bias, guided by Mike's rigorous approach to data interpretation. As a physics professor, Mike brought a welcome outside perspective; I was honored to learn that he found my research topic genuinely interesting, and he has brought tremendous energy into the team ever since. I can still remember chatting with him in the lab, energized by his curiosity as we worked through which new measurements might help validate the numerical model he had developed. I am proud that we, as a team, published a manuscript together, though this would not have been possible without everyone's extensive edit suggestions. More recently, I have had the pleasure of working alongside Corey Hawkins, who has generously shared the experimental setup from his ongoing NV-NMR project whenever I needed to run quick high-field measurements for my AO work; he brings impressive focus and has been consistently helpful in diagnosing problems along the way.

I am also thankful to Prof. Julius Goldhar, whose unwavering passion for science continues to inspire me even after his recent retirement, for the opportunity to collaborate with him on the quantum hardware laboratory course he developed. His time and

encouragement helped turn my NV quantum sensing demo unit into the benchtop education module now used in the course, with further improvements realized by Gavishta Liyanage. It is a small but lasting mark I am glad to leave on this university, a place I've called home for so long.

I have the fortune to be part of the Walsworth group, where the bonds we share extend well beyond the routine research. I cherish the time spent playing sports and going on hiking adventures with Saipriya Satyajit, Mason Camp, Jiashen Tang, Zechuan, Corey, Kristine, Andrew Beling, Richard Escalante, and Katrijn Everaert; the laughter shared at parties with JJ Oon, Emma Huckestein, Smriti Bhalerao, Camille McDonnell, Atli Davidsson, and Niko Reed; and I feel lucky to have witnessed Jeyson's beautiful proposal to his now-wife, Juliana. I wish you two the best.

Next, I wish to thank the many friends I have met at different stages of life.

To my high school friends Yunzhong Gao, Xinsen Lu, and Peiyi Shen, our friendship has migrated from China to the United States. I treasure the moments we spend reminiscing over old times while sharing a meal in DC or New York City, and I congratulate you all on your career success. And to Yang Zhou, Xian Cui, and Yufeng Shi, though we remain oceans apart, our joy, our life updates, and even our gossip still find a way to cross the distance between us, a reminder that friendship does not need geography to survive.

To my undergraduate colleagues Ran Chen and Peng Chen, your kindness and help made navigating adult life, just as I was starting the Ph.D. program, far less daunting, and I admire the happy family lives you are leading now.

To my graduate school companion Nathaniel Ferlic, I remember the countless times

we scratched our heads together working through problem sets in nonlinear optics or electromagnetism, along with many post-seminar discussions. Those shared struggles helped me feel less intimidated by difficult course material, and I'm grateful you were there working through them with me. And to Yan Li, Xinyan Xiang, and Mira Swartzlander, thank you for the conversations about your fields of study and the jokes we shared about graduate school life. I wish you all the best for the rest of your Ph.D. journeys.

To Israel Kinfu, Scott Shen, and Peter Tan, I treasure the time we spent together tweaking and testing our designs for the UMD 125-mile E-bike Challenge during my first year of graduate school. Although we did not win, the excitement of tackling that challenge with you has stayed with me through the remainder of my Ph.D.

Gaming has always been one of my main ways to unwind after a long day of work, and I have been fortunate to meet many wonderful people through it: Keith Fung, Beth Reinhard, Jason Reinhard, Abdulla Kayyali, Matt Abate, Cristi Clark, Zach Clark, Caitlin Williams, Ken Paredes, Kyle Lengsfeld, and Agam Chopra, from the "Lavender Town" server, whose friendship has transcended virtual boundaries and grown into real life, tremendously helping me integrate into the culture here. And to Lydia K., Kiera L., Shanna P., Jacob J., Brandon R., and Justin L., from "The Living Room" server, thank you all for the laughter that broke the silence of so many nights.

To Chris Tan and Jeremy Kiggundu, I will keep learning from your creativity in photography, and you will always be the photographers I trust.

To Tâm Thu Doan and Jackie Gao, I am honored to have tried your baking, and I will always hold myself to the same standard you set for the ingredients and love that go into it.

But gratitude isn't only for the good times. Life is not all sunshine and rainbows, and every marathon has its harder miles.

There were times when I felt stuck in the mud, lost, and drained of the motivation to push forward, and I am forever grateful for everyone who was there for me. Andy Leong, Sai, JJ, Katrijn, Richard, Ella Ainslie, Cristi, Beth, Tâm, Abdulla, Matt, and Jason Gitlin, thank you for patiently listening to me and comforting me when I was struggling.

Keith, I cannot thank you enough. You have always been a great friend, and your presence has helped me grow in more ways that I can count. You invited me to countless hangouts that helped me become more accustomed to the social world here; your commentary during our gaming sessions has consistently been the highlight, lightening the mood every time; your climbing technique suggestions have helped me improve tremendously; you have lent your ear through my difficulties and offered a great deal of advice that helped me mature as a person; and you are always someone I can trust, whether the question is about fashion or cars. I have witnessed the changes you've gone through, and I am truly happy to see you discovering and being yourself. As sad as I am that you will be moving to New York City, and that we won't be able to hang out as often, I am excited for your next chapter in life.

Over the past year, climbing has been a meaningful part of my personal life. Tâm, Katrijn, Richard, Sai, Andy, and Jason, I value the many conversations we have had in the gym together; Katrijn and Richard, I relive our outdoor sessions at Great Falls, listening to helicopters skim across the Potomac River behind us before heading out for a beer; and Richard, I reminisce about my first ice climb and first mountain trad climb with you, discovering new unknowns while facing down my fears. I am also thankful to many others

I have met at the gym: Jin Seng Kan, Yunqing Jia, Ellie T., Ben T., Kaylee L., Jonah R., and Justin K. I cherish the friend circle that formed around this shared hobby, and every experience we've had together.

To Jessica Jiang, though we have since gone our separate ways, our time together helped shape who I am today. I wish you the best in your future.

Finally, I wish to thank my girlfriend, Mackenzie Willis. Although we have only been together for a short time, you have been a wonderful source of emotional support, especially toward the end of this journey as I have focused on writing this dissertation. Though many miles apart, your kindness, encouragement, and understanding always comfort me when I feel anxious or stressed, and I am grateful for your presence in my life. I look forward to the years ahead, and I hope we can close the distance between us soon.

A Ph.D. is like a marathon, and I am near its finish line. I am writing this acknowledgment while sitting beside a campfire, reflecting on the years behind me. Though I am camping alone tonight, the fire's warmth reminds me of everyone's presence, and that I was never truly alone. Looking back, I feel peaceful and accomplished, knowing that I have had a fulfilling run, a memory I will carry with me always.

Table of Contents

Preface ii

Dedication v

Acknowledgements vi

Table of Contents xiii

List of Tables xvii

List of Figures xviii

List of Abbreviations xxx

Chapter 1: Introduction 1
- 1.1 Nitrogen-Vacancy Centers in Diamond . . . 2
  - 1.1.1 Optical Spin Polarization and Readout . . . 6
  - 1.1.2 NV^- Rate Equations for PL Emission . . . 6
- 1.2 NV^- Magnetic Sensing . . . 10
  - 1.2.1 Microwave-based Static or Broadband Magnetometry . . . 10
  - 1.2.2 All-Optical, Microwave-Free Magnetometry . . . 15
- 1.3 Organization of this Dissertation . . . 18

Chapter 2: All-Optical Photoluminescence Response of Nitrogen-Vacancy Ensembles in Diamond at Low Magnetic Fields 21
- 2.1 Principles of NV-NV Cross-Relaxation . . . 22
- 2.2 Experimental Details and Calibrations . . . 23
  - 2.2.1 Experimental Setup . . . 23
  - 2.2.2 Experimental Operation . . . 26
  - 2.2.3 Calibration of Applied Magnetic Fields . . . 27
  - 2.2.4 Dependence of Lock-in Output Amplitude on Magnetic Field Modulation Frequency . . . 29
  - 2.2.5 Calibration of Magnetic Field Amplitude Modulation Strength . . . 30
- 2.3 Experimental Results . . . 33
  - 2.3.1 NV-NV Cross-Relaxation Features for a Dense Ensemble . . . 33
  - 2.3.2 AO-PL Spectra with Different NV Concentrations . . . 35
  - 2.3.3 Hyperfine Interaction and NV-NV Cross-relaxation . . . 36

2.3.4 AO Sensitivity Characterization . . . 40
2.3.5 Dependence of AO-PL Contrast on Laser Power . . . 42
2.4 Numerical Simulation of AO-PL Response to Magnetic Field and Laser Power . . . 44
2.4.1 Numerical Simulation Model for AO-PL as a Function of Magnetic Field . . . 44
2.4.2 Hamiltonian Analysis of AO-PL Features . . . 50
2.4.3 Modeling AO-PL Contrast Changes from Optical Pumping and Resonant NV-NV Interaction . . . 55
2.5 Characterization of AO-PL Contrast Feature Lineshapes . . . 61
2.5.1 Polarization Lifetime (T_1) Measurements . . . 61
2.5.2 AO-PL Linewidth as a Function of Laser Power . . . 62
2.5.3 Contribution of Hyperfine Splitting to Separation of AO-PL Contrast Peaks . . . 64
2.5.4 AO-PL Line Shape Comparisons Between Near-Zero-field and Low-Field . . . 67
2.6 Outlook . . . 69

Chapter 3: Noise Suppression via Pulsed All-Optical Magnetometry with Nitrogen-Vacancy Ensembles 71
3.1 Experimental Details . . . 73
3.1.1 Experimental Setup . . . 73
3.1.2 Experimental Principle and Operation . . . 75
3.2 Experimental Results . . . 76
3.2.1 Normalization with Two AO-PL Measurements . . . 76
3.2.2 Pulsed AO-PL Contrast as a Function of Signal Readout Timing t_r 78
3.2.3 Pulsed AO-PL Contrast as a Function of Dark Time τ . . . 79
3.2.4 Comparison of Noise Suppression Performance Between Pulsed and CW AO Operation . . . 83
3.2.5 Pulsed AO-PL Contrast from Spin-State Mixing . . . 87
3.2.6 Comparison of Near-Zero-Field AO-PL Contrast Features Between ^{14}N and ^{15}N Samples . . . 88
3.2.7 Comparison of AO-PL Contrast Feature Linewidth Between CW and Pulsed Operation . . . 90
3.2.8 Pulsed AO-PL Fit Linewidth as a Function of Signal Readout Timing t_r . . . 91
3.3 Discussion . . . 92

Chapter 4: All-Optical Magnetometry at High Magnetic Fields 95
4.1 Motivation . . . 96
4.1.1 Magnetic Diagnostics for Fusion Plasmas . . . 96
4.1.2 Limitations of Current Sensors . . . 97
4.1.3 Motivation for AO NV Magnetometry . . . 99
4.2 NV Spin-Mixing Physics . . . 100
4.2.1 Numerical Simulation for Spin-Mixing . . . 102

4.3 Experimental Results . . . 105
4.3.1 AO-PL Changes with Intermediate Bias Magnetic Fields . . . 105
4.3.2 AO-PL Changes in Strong Bias Magnetic Fields . . . 108
4.4 Future Work . . . 114
4.4.1 Mechanical Improvements . . . 114
4.4.2 Pulsed AO magnetometry Protocol . . . 114
4.4.3 Measurement of Possible Radiation-induced Effects on AO Operation . . . 115

Chapter 5: NV-Diamond CW-ODMR Magnetometry for a Quantum Hardware Teaching Lab 116
5.1 Motivation . . . 117
5.2 Learning Objectives . . . 117
5.2.1 NV Physics . . . 117
5.2.2 Experiment Control . . . 118
5.3 Experiment Apparatus . . . 119
5.3.1 Optical Excitation and Collection . . . 120
5.3.2 NV-diamond Sample . . . 120
5.3.3 Microwave Excitation . . . 122
5.3.4 Bias Magnetic Field Control . . . 122
5.3.5 Optomechanical Components . . . 123
5.3.6 Data Acquisition . . . 124
5.4 Experiment Results . . . 124
5.5 Outlook . . . 127

Chapter 6: Outlook 129
6.1 Near-Zero-Field AO Wide-field Magnetic Imaging . . . 129
6.2 Near-Zero-Field Vector AO Magnetometry . . . 134
6.3 Open Questions . . . 135

Appendix A: Principles of Lock-in Detection 138
A.1 Basic Working Principle . . . 138
A.1.1 Phase-Sensitive Detection . . . 138
A.1.2 Dual-Phase Detection: Amplitude and Phase . . . 140
A.2 Bandwidth and Settling Time . . . 141
A.3 Application to Lock-in CW-ODMR and AO Magnetometry . . . 141
A.3.1 Small-Signal Derivation for Lock-in CW-ODMR . . . 142
A.3.2 Lock-in AO Measurements . . . 143
A.3.3 Hardware for Lock-in Detection . . . 145

Appendix B: Towards a Fiberized NV Magnetometer with Lock-in CW-ODMR 147
B.1 Optical System Design . . . 147
B.1.1 Large-Diameter Multimode Fiber with Discrete Lens Systems . . . 147
B.1.2 Large-Diameter Multimode Fiber with Direct Fiber-to-Diamond Contact . . . 150

B.1.3 Small-Diameter Fiber . . . 151
B.2 Demonstration of Fiberized NV Magnetometer Sensitivity . . . 152
B.2.1 Possible Effect of MW and Photodiode Cross-Talk . . . 154

Appendix C: Modeling Readout Optimization in a Pulsed AO Sequence 158
C.1 Seven-Level Rate-Equation Model . . . 158
C.2 Implementation . . . 159
C.3 Simulation Results . . . 161

Appendix D: Time-resolved NV-PL Decomposition Technique 164
D.1 Decomposition Formalism . . . 164
D.2 Decomposition on Simulated Data . . . 165
D.3 Decomposition on Experimental Data . . . 168
D.4 Future Steps . . . 171

Appendix E: Summary of Samples 173

Bibliography 174

List of Tables

1.1 Approximate NV^- decay rates and prefactors at room temperature [1]. Dashed lines (-) indicate prefactor values associated with the spin-conserving decay rate Γ. 8

2.1 Diamond samples used in this chapter. All samples are electronic-grade plates (a few mm on each side and about 0.5 mm thick), with a 10 μm-thick surface layer of enhanced nitrogen and NV concentration ([N] = 16 ppm, >99.995% ^{12}C) as reported by Element Six Ltd. 25

2.2 Relaxation rates between NV spin sublevels, both with (Γ and D) and without ($\Gamma|_{d=0}$ and $D|_{d=0}$) spin-state degeneracies, as used in the 4-level rate equation simulation model. Values with * are determined experimentally. Other values are inferred from measurements as described in Sec. 2.4.3. 60

E.1 Summary of diamond samples used in this dissertation. The indicated properties are listed as reported by the manufacturer, Element Six Ltd. The dominant nitrogen isotope is listed along with the reported total nitrogen concentration, when available, with relevant additional information provided in the main text. 173

List of Figures

1.1 (a) Model of NV centers in a unit cell aligned with four possible crystallographic axes [111], [$1\bar{1}\bar{1}$], [$\bar{1}1\bar{1}$], and [$\bar{1}\bar{1}1$]. (b) Energy level diagram for the negatively-charged NV center (NV^-). The ground $^3A_2$ spin triplet state has a zero-field splitting (ZFS) of approximately 2.87 GHz between the $|m_s = 0\rangle$ and $|m_s = \pm 1\rangle$ electronic states. Under optical illumination (near 532 nm, green arrows), NV^- is excited to the excited triplet state ^3E, from which it decays radiatively back to the ground state, emitting PL in the 650–800 nm range (red arrows) through a mostly spin-conserving process. NV^- in $|m_s = \pm 1\rangle$ can also decay through intersystem crossing (ISC) via the singlet states $^1A_1$ and ^1E, before returning to the $^3A_2$ ground state, which does not contribute to the 650-800 nm PL band. Expanded view: Electronic spin sublevels of $^3A_2$ ground state, where the $|m_s = 0\rangle$ state is split from the $|m_s = \pm 1\rangle$ states by the ZFS D. Under an applied magnetic field, the $|m_s = \pm 1\rangle$ sublevels further exhibit a Zeeman splitting and hyperfine splitting for ^{14}N (I = 1/2) and ^{15}N (I = 1). The hyperfine energy levels for ^{14}N are further shifted by quadrupolar interactions. . . . 3

1.2 5-level energy diagram for NV^- rate equations. 7

1.3 Simulated NV PL emission intensity as a function of applied laser duration for optical saturation parameter $s = 0.1$ (a) and $s = 1$ (b). The PL intensity reaches steady-state at a shorter time with higher s. The PL intensity when the initial spin population is in $|m_s = \pm 1\rangle$ (orange) is reduced comparing to when the initial spin population is in $|m_s = 0\rangle$ (blue). 9

1.4 Schematic timing and duration of laser pulses, MW pulses, and readout windows for common MW-based broadband NV magnetometry protocols: (a) CW-ODMR, (b) pulsed ODMR with a MW π pulse, and (c) Ramsey magnetometry with a variable free-precession interval τ between two MW $\pi/2$ pulses. 11

1.5 Example CW-ODMR spectrum with about 1.1 mT magnetic field applied to one of the NV orientations, creating the outermost pair of resonances. The inner pair of resonances corresponds to the overlapped transition frequencies of the remaining three NV orientations. Each resonance exhibits three distinct features, separated by ~ 2.16 MHz, which arise from the hyperfine coupling of the NV electronic spin to the ^{14}N nuclear spin ($I = 1$). 12

1.6 Experimentally measured AO NV-PL (a) and its derivative signal given by the in-phase output X of the lock-in amplifier (LIA) (b) as a function of the applied magnetic field, reported in Ref. [2]. 16
1.7 Simulated transition frequencies as a function of applied magnetic field along [111] crystallographic axis, from aligned NV (blue), non-aligned NVs (red), and P1 center (green). Multiple crossings occur near 50 mT, 60 mT, and 100 mT (dotted orange lines), coinciding with the PL reductions observed at these magnetic fields in Fig. 1.6. 17

2.1 Illustration of avoided crossing from two interacting near-resonant NV electronic spins at low magnetic fields (<2 mT). Resonant NV-NV dipolar interactions at the avoided crossing increase the NV depolarization rate and reduce total PL emission. 23
2.2 (a) AO-PL measurements utilize three sets of Helmholtz coils to control bias magnetic field magnitude and direction. NV centers in a single crystal diamond plate are optically excited by 532 nm laser light and emit PL ($\approx$ 637–800 nm), collected by a photodiode (not shown). A microwave antenna (not shown) enables comparison CW-ODMR measurements. Inset: dipolar interactions between different NV centers contribute to AO-PL contrast at low magnetic fields. (b) Illustration of applied magnetic fields and four NV orientations along unit vectors $\hat{n}_\lambda$, $\hat{n}_\phi$, $\hat{n}_\chi$ and $\hat{n}_\kappa$. The on-axis magnetic field $B_\parallel$ is along the [111] crystallographic axis. The off-axis magnetic field $B_\perp$ is along the [$\bar{1}$10] crystallographic axis. θ is the polar angle from $B_\parallel$. 24
2.3 (a) Schematic of unit vectors parallel to the four NV symmetry axes within a diamond sample, relative to the bias magnetic field Cartesian coordinates, with $\hat{z}$ vertical in the lab frame. (b) CW-ODMR spectra measured from sample S2-15N with 0.9 A, 1.8 A, and 2.7 A applied to the y-axis Helmholtz coil, with the diamond oriented such that the coil generates a magnetic field only along the [100] crystallographic orientation. Vertical offsets are applied to the spectra for better clarity. The results from x and z-axis coils behave similarly. (c) Lorentzian fit to measured CW-ODMR spectra yields magnetic field along y-axis as a function of current applied to the y-axis Helmholtz coil. Linear fit (solid line) produces a current-to-magnetic-field calibration constant $k_y = 0.4068 \pm 0.0009$ mT/A. 27
2.4 Experimental demodulated AO-PL LIA spectrum from NV-NV cross-relaxation for sample S3-14N around $B_\perp \approx 1.05$ mT and at fixed $B_\parallel = 1.24$ mT for modulation frequency f_m of 100 Hz (blue) and 500 Hz (orange). The upper trace is multiplied by 5 and shifted upwards for better clarity. A significant phase difference can be seen between the two traces, along with about 14 times lower peak amplitude for the higher modulation frequency. 30

2.5 (a) Demodulated CW-ODMR spectrum from sample S3-14N using frequency-modulated microwave signals. A linear fit is applied to the section indicated by the dash dotted orange line. (b) Zoom-in view of the linear fit applied at the zero-crossing point of the left resonance feature in the demodulated CW-ODMR spectrum, yielding slope of 0.591 ± 0.007 V/MHz. (c) FFT spectrum of time-averaged lock-in CW-ODMR measurements, with amplitude modulated $B_\perp$ applied with 0.1 V_{pp} at 100 Hz. Calibration measurements allow expression of the FFT spectrum in magnetic field units, with peak modulated field amplitude of $10.23 \pm 0.12\,\mu$T 31
2.6 (a) Experimentally determined AO-PL contrast as a function of applied magnetic fields using sample S1-14N with ≈ 3.8 ppm NV concentration. Large AO-PL contrast around zero applied field, as well as line features at specific θ values are observed. (b) Simulated AO-PL contrast using a fixed dipolar interaction strength. (c) Expanded view of the upper right quadrant in Fig. 2.6(b), with labels at specific line features indicating the cross-relaxation between NVs of orientations along (i) $\hat{n}_\phi$, $\hat{n}_\chi$ and $\hat{n}_\kappa$ at $\theta = 0°$; (ii) $\hat{n}_\kappa$ at $\theta = 22.2°$; (iii) $\hat{n}_\lambda$ and $\hat{n}_\chi$; $\hat{n}_\phi$ and $\hat{n}_\kappa$ at $\theta = 39.3°$; (iv) $\hat{n}_\lambda$ and $\hat{n}_\kappa$ at $\theta = 58.5°$; (v) $\hat{n}_\lambda$ and $\hat{n}_\phi$ at $\theta = 90°$. NV hyperfine interactions contribute to parallel line structures within AO-PL contrast features. 33
2.7 (a) (Top) Experimentally measured AO-PL contrast as a function of applied magnetic fields using sample S5-14N with ≈ 0.3 ppm [NV]. Weak NV-NV cross-relaxation features are observed in addition to the background contrast from magnetic-field-dependent spin mixing. (Bottom) Simulated AO-PL contrast using a fixed dipolar interaction strength from 0.3 ppm [NV]. Both spin mixing and NV-NV cross-relaxation AO-PL contrast features are seen. (b) (Top) Experimentally measured AO-PL contrast as a function of applied magnetic fields using sample S1-14N with ≈ 3.8 ppm [NV]. (Bottom) Simulated AO-PL contrast using a fixed dipolar interaction strength from 3.8 ppm [NV]. 35

2.8 (a) Experimentally measured AO-PL contrast as a function of $B_{\parallel}$ and $B_{\perp}$ using ^{14}N-enriched sample S1-14N (top) and ^{15}N-enriched sample S2-15N (bottom) with the same NV concentration (≈ 3.8 ppm). Horizontal dashed lines (orange for S1-14N and purple for S2-15N) indicate line-cut of data shown in Fig. 2.8(b) for $B_{\parallel}$ = 1.24 mT. (b) Experimentally measured AO-PL contrast for samples S1-14N and S2-15N (solid lines) and numerical simulations (dashed lines) at fixed $B_{\parallel} = 1.24$ mT. Vertical offsets are applied to the simulation results for visual clarity. In each measurement as $B_{\perp}$ approaches 0 mT, there are overlapping, unresolved AO-PL contrast peaks from the increased number of near-degenerate spin transitions for all NV orientations. At $B_{\perp} \approx 0.5$ mT, the limited SNR in experimental measurements hinders the identification of cross-relaxation features predicted by numerical simulations. At $B_{\perp} \approx 1.05$ mT, there are five (three) AO-PL contrast peaks with separation $\Delta B_{14N} \approx 0.09$ mT ($\Delta B_{15N} \approx 0.13$ mT) and amplitude ratio of 1:2:3:2:1 (1:2:1) in the top (bottom) data and simulations, respectively, consistent with the effect of NV hyperfine interactions in the two samples. 37

2.9 (a) Normalized AO-PL LIA measurements as a function of $B_{\perp}$ from ^{15}N-enriched sample S2-15N at fixed $B_{\parallel} = 1.24$ mT. Focus is on LIA features around 0.5 mT (purple) and 1 mT (orange). (b) AO-PL LIA signals with a smaller $B_{\perp}$ step size (≈ 0.002 mT) from shaded areas in (a). Two weak features are observed in the shoulder of the dispersive signal with central zero crossing at about 0.53 mT (left). Near 1 mT, three dispersive features are measured with splitting $\Delta B_{15N} \approx 0.13$ mT (right). For both (left) and (right), vertical dashed lines indicate near-degeneracy of hyperfine transitions. (c) Summary of measurements of microwave-based CW-ODMR NV spin transition frequencies as a function of $B_{\perp}$, including different NV orientations and hyperfine splitting, for the same sample (S2-15N) and at fixed $B_{\parallel} = 1.24$ mT. Between $B_{\perp} \approx 0.4$ mT and 0.65 mT (left), NVs along orientation $\hat{n}_{\kappa}$ experience near-zero total applied magnetic field, leading to multiple avoided crossings between the hyperfine-split $|m_s = +1 \leftrightarrow 0\rangle$ and $|m_s = -1 \leftrightarrow 0\rangle$ spin transitions. Between $B_{\perp} \approx 0.8$ mT and 1.3 mT (right), results are shown for all NV orientations, including only hyperfine-split $|m_s = +1 \leftrightarrow 0\rangle$ transitions for better clarity. (Consistent CW-ODMR results are found for $|m_s = -1 \leftrightarrow 0\rangle$ transitions.) Two groups of NV spin resonances are observed, each of which consists of two different NV orientations (along $\hat{n}_{\lambda}$ and $\hat{n}_{\chi}$; $\hat{n}_{\phi}$ and $\hat{n}_{\kappa}$). Within each spin resonance group, a single hyperfine resonance overlaps at both $B_{\perp} \approx 0.93$ mT and 1.19 mT; whereas two hyperfine resonances overlap at $B_{\perp} \approx 1.05$ mT. $B_{\perp}$ values for near-degenerate spin transition frequencies align well with those of zero crossings in the AO-PL LIA signals in (b), indicated by vertical dashed lines. 39

2.10 Demodulated AO-PL LIA spectrum for sample S2-15N around $B_\perp \approx 1.05$ mT with fixed $B_\parallel$ =1.24 mT. A linear fit is applied around the zero-crossing point to convert the LIA output voltage to the magnetic field strength along the [$\bar{1}$10] direction. The sensitivity for magnetically sensitive (insensitive) regions of the spectrum is calculated using the standard deviation σ from nine LIA output voltage measurements at $B_\perp \approx 1.05$ mT ($B_\perp \approx 1.35$ mT), respectively. 41
2.11 AO-PL contrast at $B_\parallel = 1.24$ mT and $B_\perp = 1.05$ mT as a function of laser power and intensity for samples S3-14N ([NV] $\approx$ 3.8 ppm) and S4-14N ([NV] $\approx$ 2 ppm). The laser intensity is calculated by approximating a Gaussian excitation laser beam profile of radius $\approx 30\,\mu m$. Markers indicate values determined from experimental measurements, with the standard deviation given by error bars; solid lines are from a rate-equation model with NV-concentration and spin-resonance-dependent relaxation rates between spin sublevels. For both samples, the contrast exhibits a maximum determined by the trade-off between optical pumping and spin relaxation. Sample S3-14N has higher overall AO-PL contrast, for all laser powers, because of its larger [NV] and hence stronger NV-NV dipolar interactions and cross-relaxation features. 43
2.12 Numerical simulation of low-field AO-PL contrast as a function of applied magnetic fields, from: (a) dipole-dipole electronic interactions only (i.e., no hyperfine); (b) full Hamiltonian including hyperfine interactions, with clusters of linear AO-PL contrast features labeled for the first quadrant; (c) only secular terms $H_A + H_B$; (d) only $H_C + H_D$; and (e) only $H_E + H_F$. 50
2.13 Decomposition of simulated AO-PL contrast as a function of applied magnetic fields, for specifically oriented interacting NV center pairs with contributions from the secular terms ($H_A + H_B$). Each panel contains 16 sub-figures, corresponding to decompositions for NV pairs aligned along one of the four possible crystallographic orientations. 51
2.14 Decomposition of simulated AO-PL contrast as a function of applied magnetic fields, for specifically oriented interacting NV center pairs with contributions from non-secular terms ($H_E + H_F$). Each panel contains 16 sub-figures, corresponding to decompositions for NV pairs aligned along one of the four possible crystallographic orientations. 52
2.15 (a) Simplified 4-level system used in the rate-equation model by integrating out the intersystem crossing singlet state manifold shown in Fig. 1.1(b). Relaxation rates are included between ground (Γ) and excited (D) spin sublevels. (b) Simulated AO-PL contrast as a function of $B_\perp$ at fixed $B_\parallel = 1.24$ mT using the 4-level population model provides comparable results to the density matrix method described in Sec. 2.4.1. 57

2.16 Measurement of sample S3-14N polarization lifetime (T_1) under different magnetic field configurations. (a) Experimental sequence used to measure T_1. (b) CW-ODMR measurement with spectrally well-separated spin resonances for all NV orientations ($B_\parallel \approx 2.4\,\text{mT}$ and $B_\perp \approx 1.1\,\text{mT}$). (c) Measured peak amplitude of leftmost ODMR resonance in (b) as a function of delay time τ shown in experimental sequence in (a). Fit of decay yields $T_1 = 5.46 \pm 0.05\,\text{ms}$. T_1 measurements and fits are repeated for all ODMR resonances in (b), giving averaged $\overline{T_1} = 5.51 \pm 0.15\,\text{ms}$. (d) CW-ODMR measurement with degenerate spin resonance for NV orientations $\hat{n}_\lambda$ and $\hat{n}_\chi$; $\hat{n}_\phi$ and $\hat{n}_\kappa$. (e) Measured peak amplitude of leftmost ODMR resonance in (d) as a function of τ; fit yields $T_1 = 4.72 \pm 0.04\,\text{ms}$. T_1 measurements and fits are repeated for all ODMR resonances (d), giving averaged $\overline{T_1} = 4.74 \pm 0.1\,\text{ms}$. 62

2.17 Experimentally measured AO-PL contrast as a function of $B_\perp$ and at fixed $B_\parallel = 1.24\,\text{mT}$ (dotted markers) with multi-Lorentzian fits (solid lines) for sample S3-14N at (a) 2 mW and (b) 50 mW laser excitation power. Fit values for the AO-PL contrast peak linewidth γ are shown. A linear shift of baseline due to magnetic-field-dependent spin mixing becomes more prominent at higher laser powers accompanied by a reduction of AO-PL contrast. 64

2.18 Extracted AO-PL contrast feature linewidths γ from fits to measurements around $B_\perp \approx 1\,\text{mT}$ using samples S3-14N (blue) and S4-14N (orange) as a function of laser power and intensity. The laser intensity is calculated by the same procedure described in Fig. 2.11. Each sample exhibits broader linewidth at higher laser power. Sample S3-14N has higher [NV] and significantly larger linewidth than sample S4-14N. 65

2.19 (a) Measured AO-PL contrast as a function of $B_\perp$ (dotted markers) with multi-Lorentzian fit (solid line) for sample S2-15N and fixed $B_\parallel = 1.24\,\text{mT}$. The extracted separation between AO-PL contrast peaks $\Delta B_{15N,\text{AO–PL}} = 0.1289 \pm 0.0002\,\text{mT}$. (b) Linear fit applied to CW-ODMR transition frequencies as a function of $B_\perp$ for NV orientations $\hat{n}_\chi$ and $\hat{n}_\kappa$, from measurements shown in Fig. 2.9(c, right) with fixed $B_\parallel = 1.24\,\text{mT}$. The linear slope $m = 23.568 \pm 0.034\,\text{MHz/mT}$ can be treated as the effective gyromagnetic ratio of the NV electronic spin for $B_\perp$ along $[\bar{1}10]$. 66

2.20 Measured AO-PL contrast as a function of $B_\perp$ (dotted markers) with multi-Lorentzian fits (solid lines) using samples (a, b) S4-14N and (c, d) S3-14N. Left: results near zero-field ($B_\parallel = 0.05\,\text{mT}$). Right: results near $B_\parallel = 1.24\,\text{mT}$ and $B_\perp = 1.05\,\text{mT}$. Both samples exhibit AO-PL contrast feature linewidths $\sim 2.5\times$ broader than values at low-field. Sample S4-14N has $\sim 2\times$ lower [NV] and also narrower AO-PL contrast feature linewidths than sample S3-14N. $B_\perp$ values for maximum AO-PL contrast in (a, c) are shifted from 0 due to the presence of a background field. . . . 68

2.21 Demodulated AO-PL LIA spectra for sample S3-14N around (a) near-zero-field with fixed $B_{\parallel} = 0.05\,\text{mT}$ and (b) $B_{\perp} \approx 1.06\,\text{mT}$ with fixed $B_{\parallel}$ =1.24 mT. Linear fits are applied around the zero-crossing point. The slope k from low-field measurements is larger than the near-zero-field slope by a factor of $\sim 3\times$. 69

3.1 Schematic of the experimental setup for near-zero-field pulsed AO magnetometry. 73

3.2 (a) Relaxometry pulse sequence for measuring the NV electronic spin lifetime T_1. (b) Example time-resolved PL intensity during optical illumination for resonant NV-NV cross-relaxation at near-zero magnetic field (blue) and for off-resonant conditions with an applied magnetic field (orange), respectively. The intensity of PL signals during NV-NV cross-relaxation is reduced. 75

3.3 (a) Relaxometry pulse sequence for measuring the NV electronic spin lifetime T_1. (b) Example time-resolved PL intensity during optical illumination for resonant NV-NV cross-relaxation at near-zero magnetic field (blue) and for off-resonant conditions with an applied magnetic field (orange), respectively. The intensity of PL signals during NV-NV cross-relaxation is reduced. 77

3.4 Pulsed AO-PL contrast of sample S3-14N measured for signal readout pulse values $t_r = 0.4\,\mu$s and $t_r = 1\,\mu$s, with dark time $\tau = 2\,$ms. $t_r < 1\,\mu$s yields weaker AO-PL contrast and worse SNR due to poor optical spin polarization after the optical pulse. 79

3.5 Normalized difference of transient PL intensity between from resonant NV-NV cross-relaxation at near-zero magnetic field and from off-resonant conditions with an applied magnetic field. A moving average filter with $1\,\mu$s window length is applied to both transient PL measurements before taking the difference. The maximum occurs near $t_r = 1\,\mu$s and is in agreement with the result in Fig. 3.3. 80

3.6 (a) Pulsed AO-PL contrast at $B_0 = 0.03\,$mT, 275 mW laser power, and $t_r = 1\,\mu$s, as a function of dark time τ for samples S3-14N ([NV] $\approx$ 3.8 ppm) and S4-14N ([NV] $\approx$ 2 ppm). Markers are the experimental contrast values $C(\tau)$, with measurement uncertainty indicated. Solid lines are from a bi-exponential fit to experimental $C(\tau)$ values. For both samples, the fit yields two characteristic timescales T_{cr} and T_{in} that can be associated with NV-NV cross-relaxation and intrinsic depolarization, respectively. (b) Pulsed AO-PL contrast at $B_0 = 0.03\,$mT and $t_r = 1\,\mu$s as a function of dark time τ for sample S3-14N ([NV] $\approx$ 3.8 ppm) at two laser powers, 57 mW and 275 mW. The two fit timescales are consistent within error bars. 81

3.7 (a) Experimentally-determined NV ground-state spin-polarization lifetime (T_1) of sample S3-14N as a function of dark time τ. Fits of pulsed AO-PL decay (not shown) yield $T_1 = 2.602 \pm 0.008$ ms with cross-relaxation magnetic field at $B_0 = 0.03$ mT, and $T_1 = 3.70 \pm 0.012$ ms with off-resonant magnetic field at $B_0 = 0.45$ mT. (b) Differences of T_1 results in Fig. 3.7(a) and a bi-exponential fit to the measured AO-PL contrast of sample S3-14N in Fig. 3.6(a) as a function of dark time τ, with good consistency found between the methods. 82
3.8 Normalized power-spectral-density (PSD) relative to a test signal (1 μT, 43 Hz) for CW and pulsed AO measurements of sample S3-14N. (a) No AM noise added to the AOM RF power. (b) Additional AM noise with 0.2% depth and 200 Hz bandwidth. 85
3.9 Measured near-zero-field AO-PL contrast of sample S3-14N using pulsed (blue) and CW (orange) methods as a function of B_0. Additional optical intensity noise is applied through AM with 1% depth and 200 Hz bandwidth from noise modulation of the AOM RF power. The pulsed method can still resolve clear AO-PL contrast features under substantial optical intensity noise. 86
3.10 Pulsed AO-PL contrast as a function of applied magnetic field magnitude and direction, for: (a) signal readout pulse value $t_r = 1\,\mu$s; (b) reference readout pulse value $t_r = 79\,\mu$s; and (c) after normalization, using sample S5-14N with $\approx$0.3 ppm [NV] (top) and sample S3-14N with $\approx$3.8 ppm [NV] (bottom). Implementing two PL readout normalization with sample S5-14N allows the characterization of pulsed AO-PL contrast from both spin-state mixing as a non-negligible background and weak NV-NV cross-relaxation as stripelike features. Unlike pulsed AO-PL contrast from NV-NV cross-relaxation, which is primarily observed in the signal readout measurement (a, bottom), a significant portion of pulsed AO-PL contrast from spin-state mixing appears in the reference readout measurement (b, top). Future studies will explore optimizing AO pulse sequences for specific operational conditions. 88
3.11 Measured near-zero-field AO-PL contrast of sample S3-14N (a) and S2-15N (b) as a function of B_0. The simpler hyperfine structure from ^{15}N leads to a cleaner contrast feature with three prominent peaks. The increased pulsed AO-PL contrast in (b) may result from the better spectral overlap near zero field. 89
3.12 Measured near-zero-field AO-PL contrast of sample S2-15N using pulsed (dotted blue) and CW (dotted orange) methods with multi-Lorentzian fits (solid lines) as a function of B_0. The sample exhibits a AO-PL contrast feature linewidth of 114.25 $\pm$ 1.89 μT (112.63 $\pm$ 2.23 μT) using pulsed (CW) protocols, respectively. No significant variation in this linewidth of AO-PL contrast features is observed between the two measurements. . . 92

3.13 Fit amplitude (a) and linewidth (b) from the central near-zero-field AO-PL contrast of sample S2-15N as a function of signal readout timing t_r. Markers are the fit values with uncertainty indicated. While the amplitude reduces as t_r increases (consistent with results from Fig. 3.2.2(b) using sample S3-14N), the fit linewidth values are roughly consistent within error bars. 93

4.1 Example of toroidal and poloidal magnetic field for tokamak plasma confinement [3]. In high-field tokamaks, the toroidal field is ∼20 T and the poloidal field is ∼5 T at magnetic sensor locations. 96
4.2 Example locations of diagnostic magnetic sensors in a tokamak [4]. The left panel shows top-down view of a tokamak vacuum vessel; red notations indicate four toroidal locations of sensor locations in this example. The right panel shows a side section view of a tokamak vacuum vessel; red and blue notations indicate poloidal sensor locations and the typical spatial sensor density needed for plasma control and turbulence measurements. 98
4.3 Under the presence of a non-negligible transverse field relative to the NV symmetry axis (a), the NV energy levels and associated transition rates between spin levels at zero field (b) are altered due to the spin-mixing effect (c) [5]. 101
4.4 Simulated normalized AO-PL intensity as a function of B_z from 0 mT to 150 mT. The spin-mixing effect leads to a prominent AO-PL intensity reduction between 0 and 40 mT. Two sharp AO-PL intensity drops are visible near 50 and 100 mT, due to the ESLAC and GSLAC processes, respectively. 104
4.5 (a) Simulated normalized AO-PL intensity from an NV ensemble as a function of axial field B_z from 0.15 to 15 T and transverse field $B_\perp$ from 0.15 to 5 T. (b) Derivative of the normalized AO-PL intensity with respect to $B_\perp$, showing nontrivial sensitivity to $B_\perp$ changes. (c) Derivative of the normalized AO-PL intensity with respect to B_z. In the high field regime, sensitivity to B_z changes is reduced by roughly a factor of 10 relative to $B_\perp$. Boxed purple areas indicate optimal NV alignment in order to be sensitive to $B_\perp$ at high fields inside a tokamak. 105
4.6 Schematic of the optical system to measure spin-mixing-induced AO-PL changes in a bulk NV-ensemble diamond. A permanent magnet provides a bias field of about 19 mT. Two coils placed near the NV-diamond provide B_z and $B_\perp$ modulations separately. An AOM and a balanced photodiode, together with a feedback system, mitigate long-timescale PL intensity drift due to local temperature changes at the NV-diamond. 106

4.7 An example AO-PL intensity measurement from the photodiode voltage over one modulation period. During this period, the fields produced by both coils are modulated to form four distinct readout windows. The AO-PL intensity with both coils turned off (0, 0) serves as the baseline measurement. Short-timescale drifts is mitigated by keeping the baseline measurements consistent across the $(B_\perp, B_z)$ scan during data post-processing. 108
4.8 (a) Experimentally determined normalized AO-PL intensity as a function of applied magnetic fields. (b) Simulated normalized AO-PL intensity using the model described in Sec. 4.2.1. The experimental AO-PL changes from an NV ensemble are about $10\times$ smaller than the numerically predicted results modeled from a single NV. 109
4.9 The electromagnet provides a bias field up to ~ 300 mT. Two rotational stages allow careful alignment of the NV orientations to the applied field. A single-mode fiber transmits a CW or pulsed laser beam to optically excite the NV-diamond, and a separate liquid light guide collects the NV PL. 110
4.10 Experimentally measured pulsed AO-PL intensity as a function of B_z from 0 to 240 mT, with sequence dark time $\tau = 3$ ms (blue) and $\tau = 1$ ms (orange). Inset shows the resolved AO-PL feature from the GSLAC process around 100 mT, measured with $\tau = 3$ ms. 111
4.11 (a) Illustration of the perturbation field produced by a coil that is perpendicular to the NV-diamond's [100] face (purple). The perturbation field for the measurement is 54.73° relative to the B_z bias field, instead of 90°. (b) Experimentally measured pulsed AO-PL intensity as a function of applied current to the perturbation coil under a bias field $B_z = 20$ mT (blue), $B_z = 120$ mT (orange), and $B_z = 300$ mT (green). Spin-mixing-induced AO-PL intensity change is visible at $B_z = 20$ mT, but is inconsistent at the higher fields $B_z = 120$ mT and $B_z = 300$ mT. 113
4.12 Simulated derivative of the normalized AO-PL intensity with respect to $B_\perp$ as a function of transverse field $B_\perp$ from 50 to 100 mT and axial field B_z from 100 to 300 mT. Around 0.01% of AO-PL contrast is predicted for every mT change of $B_\perp$ with a misalignment of the NV system inside the electromagnet producing a maximum bias field of 300 mT, as indicated by the purple box. 113

5.1 An overview of the NV CW-ODMR education module, with (a) computer and display for experiment control and data analysis; (b) oscilloscope for data collection; (c) RF signal generator; (d) optical system on a breadboard; and (e) power supply to drive electrical coils to produce magnetic fields with controllable magnitudes. 119

5.2 (a) Schematic of the experimental setup for the NV CW-ODMR education module. (b) Optical components include a 520 nm laser diode, optical mirrors, a dichroic beamsplitter, and a photodetector. (c) A f=25 mm plano-convex lens focuses the laser beam onto the NV-diamond mounted on a glass substrate. A home-made antenna is placed around the NV-diamond to provide a MW control field. 121
5.3 An monodie synthetic single crystal HPHT diamond (Element Six Monodie MD111) with red PL emission, imaged by a camera in the optical setup. . 122
5.4 A pair of transverse coils and an axial coil provide bias magnetic fields of controllable direction and magnitude for CW-ODMR measurements. . . 123
5.5 Experimentally measured (blue) and simulated (orange) CW-ODMR spectra as a function of MW frequency, for NV-diamond rotation angles of (a) $\theta = 0°$ and (b) $\theta = 30°$ and a bias field produced by the transverse coils. The experimental and simulated results are in good agreement for both cases. Hyperfine structures are visible in the leftmost resonance of (a). . . 126
5.6 Adapt from Ref. [6]. Measured MW-on (red) and MW-off (blue) PL spectra with both the NV^0 and NV^- zero-phonon lines (indicated by gray arrows) visible at 575 nm and 637 nm, respectively. 128

6.1 Illustrations of a Quantum Diamond Microscope (QDM) [7]. Example QDM setups using (a) a pair of permanent magnets and (b) Helmholtz coils to apply a bias magnetic field. A 532-nm excitation laser enters the NV-diamond at an angle to perform total internal reflection fluorescence (TIRF) microscopy, with the NV PL captured by a camera. 130
6.2 Experimentally determined near-zero-field AO-PL contrast as a function of applied magnetic fields B_x and B_y, measured using the Köhler illumination technique and a camera. (a) Averaged over the entire region of interest (ROI). (b) From a single pixel, showing worse SNR than (a) due to fewer collected photons. 133

A.1 Hardware wiring diagram to perform lock-in CW-ODMR and AO operations. 146

B.1 Zemax ray tracing simulation of C110TMD-A and C330TMD-A aspheric lens system. Left: Green light propagates from a multimode optical fiber to the diamond. Right: Red PL propagates from the diamond to the fiber. Green propagation forms about a 20 μm spot size and red propagation forms about a 200 μm spot size. 149
B.2 In-lab photo of an NV optical system using a GRIN lens. 150
B.3 Zemax simulation of the beam profile propagating through diamond [8]. Left: direct fiber and diamond contact. Right: through GRINTECH GT-LFRL-050-025-50-NC (670) lens to form a well-collimated beam entering/exiting diamond. 151
B.4 (a) CW-ODMR and (b) demodulated (lock-in) CW-ODMR spectra, both measured with a bias field of ≈ 3.8 mT. 153

B.5 Demonstrated fiberized NV sensitivity spectra, with a mean sensitivity ≈ 30 nT/$\sqrt{\text{Hz}}$ from 1 to 200 Hz. The peaks at 60 Hz and its harmonics can be associated with ambient magnetic noise, for example from the power line, and are not observed in the magnetically insensitive case. The noise floor for the magnetically insensitive case is obtained with the MW frequency tuned off resonance (2000 MHz). 155
B.6 CW-ODMR spectra measured with the fiber-coupled photodiode (blue) and the near-diamond photodiode (orange). The latter shows non-unity contrast between neighboring resonances across the 2800–2950 MHz range. 156
B.7 Fiberized NV sensitivity spectra measured with the near-diamond photodiode, with a mean sensitivity ≈ 30 nT/$\sqrt{\text{Hz}}$ from 1 to 200 Hz. Peaks at 120 Hz and 240 Hz appear in both the magnetically sensitive and insensitive cases, and may result from cross-talk between the MW drive and the photodiode. 157

C.1 Modified seven-level rate-equation model, with spin-sublevel relaxation added within the ground state (rate k_g) manifolds. Solid arrows: optical excitation (green, rate $\beta\Gamma$) and spin-conserving radiative decay (red, rate Γ). β is the optical saturation parameter. Dashed arrows: spin-selective intersystem crossing into the singlet manifold and singlet decay back to the ground state. 159
C.2 (a) Simulated time-resolved PL as a function of laser duration between cross-relaxation ($T_1 = 4.7$ ms, blue) and spectrally-separated ($T_1 = 5.5$ ms, orange) conditions, for $\beta = 0.1$ (top) and $\beta = 1$ (bottom). (b) Normalized difference of time-resolved PL between cross-relaxation and spectrally-separated conditions in (a). The yellow dashed line indicates the corresponding laser duration for the maximum PL difference. Stronger optical pumping leads to a larger PL difference, occuring at a shorter timescale. . 162

D.1 Simulated time-resolved PL basis traces (for initial population of 70% in $|0\rangle$ and $|1\rangle$) and an example $\pi/2$ trace (equal initial populations) used for decomposition validation. 166
D.2 (Top) Regression coefficient A for $|m_s = 0\rangle$ as a function of MW π-pulse duration. (Bottom) Regression coefficient A as a function of theoretical coefficient of spin distribution follows a linear response. 168
D.3 Experimental basis traces ($|0\rangle$ and $|1\rangle$). The early transient dynamics contains more information for decomposition. 169
D.4 Rabi curve obtained from "sig/ref" measurement (blue), compared against the regression coefficient (yellow) for $|0\rangle$ obtained from time-resolved PL data via the decomposition technique of Sec. D.1. 170

List of Abbreviations

AO	All-optical
AOM	Acoustic-optic Modulator
BFP	back focal plane
CVD	Chemical Vapor Deposition
CW	Continuous-wave
DAQ	Data Acquisition
DEMO	Demonstration Power Plant
ESLAC	Excited State Level Anti-crossing
FOV	Field of View
FPS	Frames Per Second
GRIN	Gradient-index
GSLAC	Ground State Level Anti-crossing
HTS	High-temperature Superconductor
ISC	Intersystem Crossing
ITER	International Thermonuclear Experimental Reactor
LIA	Lock-in Amplifier
LTS	Low Temperature Superconductor
MHD	Magnetohydrodynamics
MW	Microwave
NA	Numerical Aperture
NV	Nitrogen-vacancy
ODMR	Optically Detected Magnetic Resonance

PL	Photoluminescence
PSD	Power Spectral Density
P1	Substitutional Nitrogen
QDM	Quantum Diamond Microscope
RF	Radio Frequency
ROI	Region of Interest
SNR	Signal-to-noise Ratio
SQUID	Superconducting Quantum Interference Device
SWaP	Size, Weight, and Power
TIRF	Total Internal Reflection Fluorescence
ZFS	Zero-field Splitting
ZPL	Zero-phonon Line

Chapter 1: Introduction

Sensors are ubiquitous in modern life, embedded across countless systems and applications. They convert physical quantities — such as temperature, pressure and humidity — into measurable signals, providing essential data for a wide range of tasks. Classical electronic sensors are deeply integrated into everyday devices, with examples including: piezoelectric accelerometers that track daily steps via smartwatches and Hall effect magnetometers that detect the closure of a laptop lid, triggering its sleep mode. Despite their versatility, classical sensors face inherent limitations such as susceptibility to drift, reduced sensitivity under extreme conditions, and the need for regular calibration. Quantum sensors, by leveraging the principles of quantum mechanics, address these challenges by offering enhanced sensitivity, stability, and precision. Central to quantum sensing is the qubit, the fundamental unit of quantum information, which directly interacts with external fields. The precise shift of energy levels within qubits, even in response to the smallest perturbations, is governed by fundamental physical constants, enabling quantum sensors to achieve unparalleled precision and significantly reduce the need for calibration. While not entirely immune to drift, quantum sensing holds the potential for self-calibration, making it ideal for applications requiring long-term stability and reliability.

Magnetic sensing, or magnetometry, is one of the key measurement modalities enabled by quantum sensing to characterize magnetic fields. Many platforms, such as cold atoms, trapped ions, superconducting quantum interference devices (SQUIDs), and solid state defects, have emerged and been extensively researched for quantum magnetometry. While SQUIDs offer superior magnetic sensitivity, their operation is limited by extremely low temperature in order to maintain superconductivity. Solid state defects, in particular nitrogen-vacancy (NV) centers in diamond, offer crucial technological advantages, such as operation under ambient conditions while maintaining a good magnetic sensitivity, making them well suited for real-world applications.

1.1 Nitrogen-Vacancy Centers in Diamond

The NV center in diamond is a solid-state point defect center, consisting of a substitutional nitrogen atom and a vacancy on adjacent carbon lattice sites [9]. As a result, the defect's symmetry axis can be oriented along one of four possible crystallographic axes ([111], [$1\bar{1}\bar{1}$], [$\bar{1}1\bar{1}$], and [$\bar{1}\bar{1}1$]), as shown in Fig. 1.1(a). Among all three charge states of NV centers (NV^-, NV^0, NV^+), the negatively-charged NV center (NV^-) is commonly used for sensing.

The triplet ($S = 1$) ground state ($^3A_2$) Hamiltonian of NV^- center exhibits fine, hyperfine, and nuclear-quadrupole structures [10],

$$\hat{H}_{gs}/h = \hat{\mathbf{S}} \cdot \mathbf{D} \cdot \hat{\mathbf{S}} + \hat{\mathbf{S}} \cdot \mathbf{A} \cdot \hat{\mathbf{I}} + \hat{\mathbf{I}} \cdot \mathbf{Q} \cdot \hat{\mathbf{I}}, \tag{1.1}$$

where h is Planck's constant, $\hat{\mathbf{S}} = (\hat{S}_x, \hat{S}_y, \hat{S}_z)$ and $\hat{\mathbf{I}} = (\hat{I}_x, \hat{I}_y, \hat{I}_z)$ are the dimension-

less electronic spin-1 and nuclear spin operator of the intrinsic nitrogen atom, respectively. The first term describes the electron spin-spin (fine-structure) interaction through the tensor $\mathbf{D}$; the second describes the hyperfine coupling between the electronic spin and the host nitrogen nuclear spin through the tensor $\mathbf{A}$; and the third describes the nuclear electric-quadrupole interaction through the tensor $\mathbf{Q}$, which is nonzero only for the ^{14}N isotope with $I = 1$.

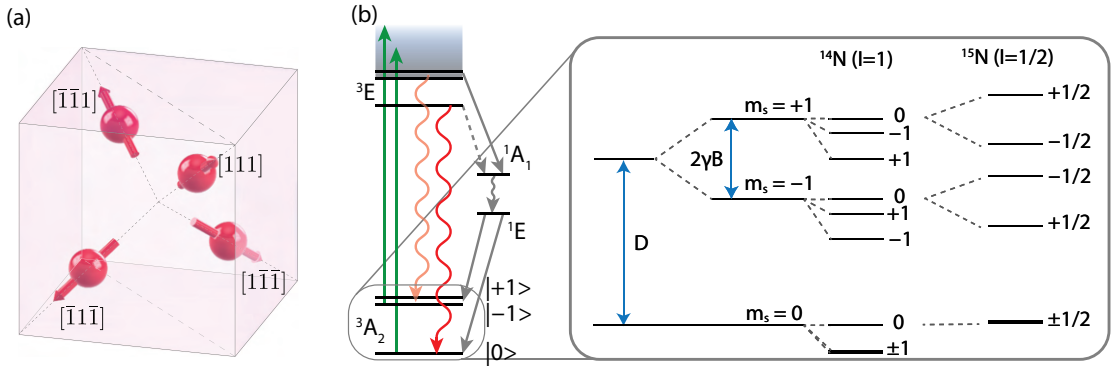


Figure 1.1: (a) Model of NV centers in a unit cell aligned with four possible crystallographic axes [111], [1$\bar{1}\bar{1}$], [$\bar{1}$1$\bar{1}$], and [$\bar{1}\bar{1}$1]. (b) Energy level diagram for the negatively-charged NV center (NV$^-$). The ground $^3A_2$ spin triplet state has a zero-field splitting (ZFS) of approximately 2.87 GHz between the $|m_s = 0\rangle$ and $|m_s = \pm 1\rangle$ electronic states. Under optical illumination (near 532 nm, green arrows), NV$^-$ is excited to the excited triplet state ^3E, from which it decays radiatively back to the ground state, emitting PL in the 650–800 nm range (red arrows) through a mostly spin-conserving process. NV$^-$ in $|m_s = \pm 1\rangle$ can also decay through intersystem crossing (ISC) via the singlet states $^1A_1$ and ^1E, before returning to the $^3A_2$ ground state, which does not contribute to the 650-800 nm PL band. Expanded view: Electronic spin sublevels of $^3A_2$ ground state, where the $|m_s = 0\rangle$ state is split from the $|m_s = \pm 1\rangle$ states by the ZFS D. Under an applied magnetic field, the $|m_s = \pm 1\rangle$ sublevels further exhibit a Zeeman splitting and hyperfine splitting for ^{14}N (I = 1/2) and ^{15}N (I = 1). The hyperfine energy levels for ^{14}N are further shifted by quadrupolar interactions.

As a result of NV C_{3v} symmetry, $\mathbf{D}$, $\mathbf{A}$, and $\mathbf{Q}$ are all diagonal when expressed in the NV coordinate frame with z along the NV symmetry axis, and Eq. (1.1) reduces to

$$\hat{H}_{gs}/h = D(T)\,\hat{S}_z^2 + A_\parallel \hat{S}_z \hat{I}_z + A_\perp \left(\hat{S}_x \hat{I}_x + \hat{S}_y \hat{I}_y\right) + P\,\hat{I}_z^2. \tag{1.2}$$

The zero-field splitting (ZFS) $D(T) \approx 2.87\,\text{GHz}$ separates the $|m_s = 0\rangle$ and $|m_s = \pm 1\rangle$ sublevels with a temperature dependence of $dD/dT \approx -74\,\text{kHz/K}$. The axial and transverse hyperfine constants, $A_\parallel$ and $A_\perp$, differ between the two stable nitrogen isotopes: for naturally abundant ^{14}N ($I = 1$), $A_\parallel \approx -2.14\,\text{MHz}$ and $A_\perp \approx -2.70\,\text{MHz}$, while for the less abundant but isotopically simpler ^{15}N ($I = 1/2$), $A_\parallel \approx 3.03\,\text{MHz}$ and $A_\perp \approx 3.65\,\text{MHz}$. The axial nuclear quadrupole constant $P \approx -5.0\,\text{MHz}$ applies only to ^{14}N.

An external magnetic field $\vec{B} = (B_x, B_y, B_z)$ couples to the NV electronic spin through the Zeeman interaction and lifts the spin degeneracy of the $|m_s = \pm 1\rangle$ sublevels,

$$\hat{H}_{\text{Zee}}/h = g_e \mu_B \left(B_x \hat{S}_x + B_y \hat{S}_y + B_z \hat{S}_z \right), \tag{1.3}$$

with electronic g-factor $g_e \approx 2.003$ and Bohr magneton $\mu_B = 9.274 \times 10^{-24}\,\text{J/T}$, corresponding to an NV electronic spin gyromagnetic ratio $\gamma_e/2\pi \approx 28.04\,\text{GHz/T}$. Because D is large compared to the achievable Zeeman splitting for laboratory-scale fields, the transverse components B_x, B_y contribute only at second order and are typically neglected when the bias field is applied along, or close to, the NV axis; only the axial projection B_z enters the leading-order transition frequencies derived below.

Local strain and electric fields $\vec{E} = (E_x, E_y, E_z)$ couple to the NV ground state

Hamiltonian with additional terms:

$$\hat{H}_{\text{strain}}/h = M_z\hat{S}_z^2 + M_x\left(\hat{S}_x^2 - \hat{S}_y^2\right) + M_y\left(\hat{S}_x\hat{S}_y + \hat{S}_y\hat{S}_x\right) + N_x\left(\hat{S}_x\hat{S}_z + \hat{S}_z\hat{S}_x\right) + N_y\left(\hat{S}_y\hat{S}_z + \hat{S}_z\hat{S}_y\right), \tag{1.4}$$

$$\hat{H}_{\text{elec}}/h = d_{\parallel}E_z\hat{S}_z^2 - d_{\perp}E_x\left(\hat{S}_x^2 - \hat{S}_y^2\right) + d_{\perp}E_y\left(\hat{S}_x\hat{S}_y + \hat{S}_y\hat{S}_x\right), \tag{1.5}$$

where M_x, M_y, M_z, N_x, N_y are strain-coupling coefficients set by the local stress tensor, and $d_{\parallel} \sim 10^2$ Hz/(V/m) and $d_{\perp} \approx 0.17$ Hz/(V/m) are the axial and transverse components of the NV ground-state electric dipole moment, respectively. The axial terms, $M_z\hat{S}_z^2$ and $d_{\parallel}E_z\hat{S}_z^2$, shift the ZFS D. The transverse terms are, for a bias field applied along the NV symmetry axis, suppressed relative to the axial terms and are therefore frequently neglected in magnetometry applications.

Considering only the dominant axial contributions from Eqs. (1.2)–(1.5) and neglecting the comparatively small hyperfine and quadrupole structure, the transition frequencies between $|0\rangle$ and $|\pm1\rangle$ ground-states (E_0 and $E_{\pm1}$, respectively) can be expressed as:

$$f_{\pm} = |E_{\pm1} - E_0| = D(T) + M_z + d_{\parallel}E_z \pm \frac{g_e\mu_B}{h}B_z. \tag{1.6}$$

Equation (1.6) indicates that temperature, strain, and axial electric field induce a common-mode shift to f_+ and f_- together through D, M_z, and $d_{\parallel}E_z$, while an axial magnetic field shifts these two transition frequencies in opposite directions through the Zeeman term.

1.1.1 Optical Spin Polarization and Readout

Optical excitation at wavelengths shorter than NV^-'s 637 nm zero-phonon line, commonly employed with 532 nm due to its commercial availability, excites the NV^- centers non-resonantly into the ^3E excited triplet state, from which it predominantly follows a spin-conserving radiative decay to the $^3A_2$ ground state, emitting broadband red photoluminescence (PL) in the range of 650-800 nm [Fig. 1.1(b)]. Alternatively, the NV^- centers in the excited state can decay through intersystem crossing (ISC) via the singlet states $^1A_1$ and ^1E, before returning to the $^3A_2$ ground state. This non-radiative pathway favors $|m_s = \pm 1\rangle$ spin sublevels and distributes the spin population to ground $|m_s = 0\rangle$ and $|m_s = \pm 1\rangle$ roughly equally [11]. These two pathways form the physical basis of optical spin polarization: continuous optical excitation preferentially initialize the NV^- electronic spin into the $|m_s = 0\rangle$ state.

Because optical excitation is generally spin-conserving, and $|m_s = \pm 1\rangle$ excited states are preferentially coupled to the ISC pathway that does not contribute to the 650-800 nm PL band, NV^- polarized in the ground $|m_s = 0\rangle$ (bright) state emit more photons than those in ground $|m_s = \pm 1\rangle$ (dark) states. This spin-state-dependent PL mechanism enables optical NV^- spin readout for NV quantum sensing even under ambient conditions.

1.1.2 NV^- Rate Equations for PL Emission

The time-resolved NV^--PL under optical excitation can be approximated through solving a system of rate equations. For simplicity, the energy level diagram depicted

in Fig. 1.1(b) can be reduced to a 5-level system by considering the $|m_s = \pm 1\rangle$ states are near-degenerate in both the ground and excited electronic states. Here in Fig. 1.2,

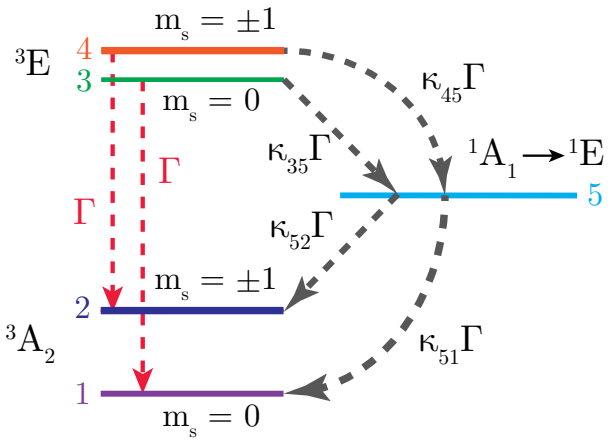


Figure 1.2: 5-level energy diagram for NV^- rate equations.

levels 1 and 2 represent the $|m_s = 0\rangle$ and $|m_s = \pm 1\rangle$ ground states ($^3A_2$), levels 3 and 4 represent the $|m_s = 0\rangle$ and $|m_s = \pm 1\rangle$ excited states (^3E), and level 5 represents the singlet state manifold ($^1A_1 \rightarrow {}^1E$). We choose the spin-conserving decay rate from the triplet excited states to the triplet ground states (from level 4 to 2 and from level 3 to 1) to be $\Gamma = 67\,\mu\text{s}^{-1}$. The decay rates through the singlet state manifold are expressed in terms of Γ with prefactors κ_{ij} from level i to level j, where $\kappa_{45} = 1$, $\kappa_{35} = 1/7$, $\kappa_{52} = 1/50$, and $\kappa_{51} = 1/25$. The various approximated rates are summarized in Table 1.1.

Table 1.1: Approximate NV^- decay rates and prefactors at room temperature [1]. Dashed lines (-) indicate prefactor values associated with the spin-conserving decay rate Γ.

Decay rates	**Values**	**Units**
Γ	67	μs^{-1}
κ_{45}	1	-
κ_{35}	$1/7$	-
κ_{52}	$1/50$	-
κ_{51}	$1/25$	-

We calculate the time-dependent NV^- electronic spin distribution across the 5 levels $n_{i=1:5}$ through solving the following system of first-order differential equations:

$$\begin{aligned}
n_1'(t)/\Gamma &= -sn_1(t) + n_3(t) + \kappa_{51}n_5(t) \\
n_2'(t)/\Gamma &= -sn_2(t) + n_4(t) + \kappa_{52}n_5(t) \\
n_3'(t)/\Gamma &= sn_1(t) - (1+\kappa_{35})n_3(t) \\
n_4'(t)/\Gamma &= sn_2(t) - (1+\kappa_{45})n_4(t) \\
n_5'(t)/\Gamma &= \kappa_{35}n_3(t) + \kappa_{45}n_4(t) - (\kappa_{51}+\kappa_{52})n_5(t).
\end{aligned} \tag{1.7}$$

Here, $s = I/I_{\text{sat}}$ is the optical saturation parameter with incident optical intensity I and I_{sat} determined by Γ and the NV^- absorption cross section at 532 nm [12]. The PL emission rate $R(t)$ can then be calculated using the spin population in level 3 $n_3(t)$ and level

4 $n_4(t)$ as

$$R(t) = \Gamma[n_3(t) + n_4(t)]. \tag{1.8}$$

Fig. 1.3 shows the calculated PL emission rate for a single NV with initial spin population all in level 1 ($|m_s = 0\rangle$, blue) or 2 ($|m_s = \pm 1\rangle$, orange) for two optical saturation parameters $s = 0.1$ and $s = 1$. Under stronger optical excitation, the NV reaches steady-state at a shorter time with a higher emission intensity. In addition, the PL emission intensity when the initial NV electronic spin population is all in $|m_s = \pm 1\rangle$ is reduced relative to the case when the spin population is all in $|m_s = 0\rangle$, due to the additional decay pathway through the singlet state manifold.

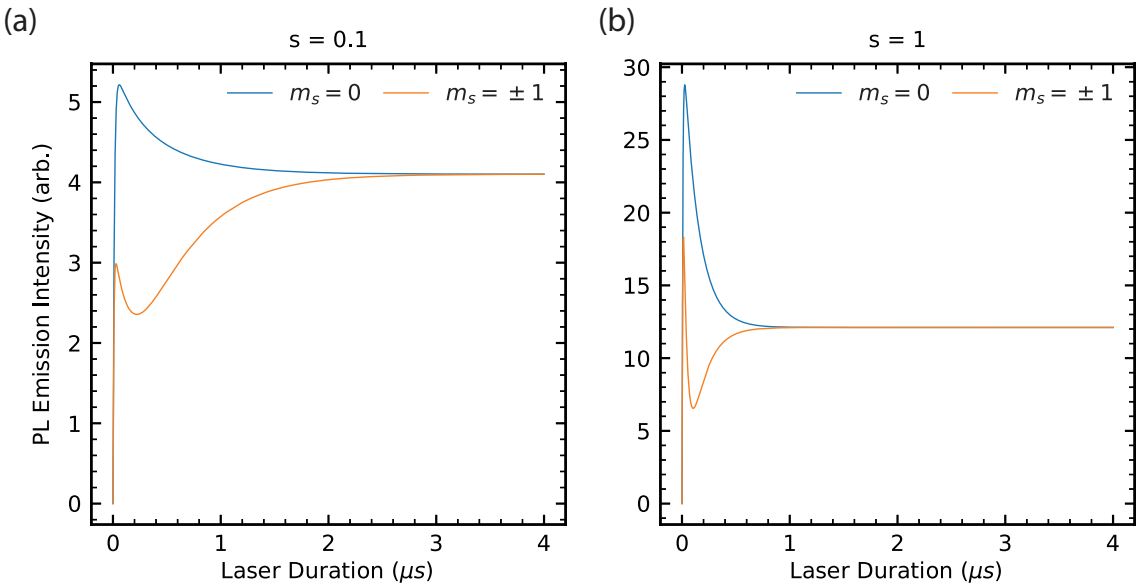


Figure 1.3: Simulated NV PL emission intensity as a function of applied laser duration for optical saturation parameter $s = 0.1$ (a) and $s = 1$ (b). The PL intensity reaches steady-state at a shorter time with higher s. The PL intensity when the initial spin population is in $|m_s = \pm 1\rangle$ (orange) is reduced comparing to when the initial spin population is in $|m_s = 0\rangle$ (blue).

1.2 NV^- Magnetic Sensing

1.2.1 Microwave-based Static or Broadband Magnetometry

Coherent control of the ground-state spin is achieved by driving microwave (MW) irradiation resonant with f_+ or f_- from Eq. 1.6, which become nondegenerate once $B_z \neq 0$. Combined with the optical initialization and spin-dependent fluorescence readout described in Sec. 1.1.1, this microwave control forms the basis of NV magnetometry: an external perturbation shifts the NV ground state spin resonances $f_\pm$, resulting in changes of the measured NV-PL intensities.

This section provides an overview of protocols conventionally used to measure static, slowly-varying, or broadband magnetic signals (roughly DC to 100 kHz): continuous-wave optically detected magnetic resonance (CW-ODMR), pulsed ODMR, and Ramsey-based magnetometry. Fig. 1.4 provides an overview of these three protocols with timing and duration of laser pulses, MW pulses, and readout windows. Sources of such magnetic signals include the remanent magnetization of geological grains [13], single-neuron action potentials [14], current flow in integrated circuits [15], and ambient geomagnetic field encountered in navigation applications.

More complex protocols, such as Hahn echo and dynamical decoupling sequences, to detect narrowband oscillating fields (1 kHz–20 MHz), and high-frequency fields in the gigahertz (GHz) range, are beyond the scope of this dissertation.

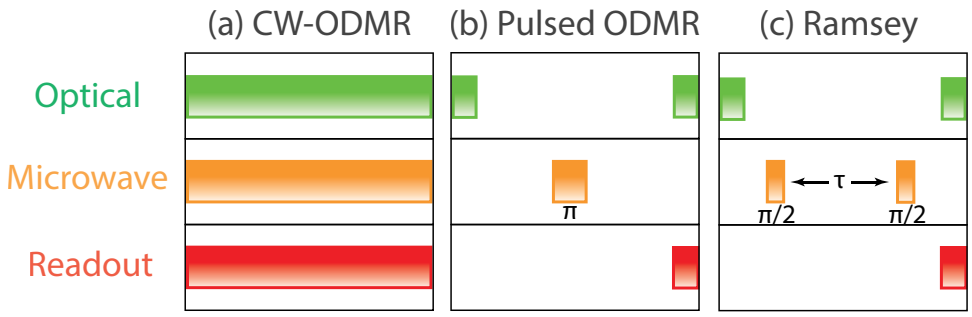


Figure 1.4: Schematic timing and duration of laser pulses, MW pulses, and readout windows for common MW-based broadband NV magnetometry protocols: (a) CW-ODMR, (b) pulsed ODMR with a MW π pulse, and (c) Ramsey magnetometry with a variable free-precession interval τ between two MW $\pi/2$ pulses.

1.2.1.1 Continuous-Wave (CW) and Pulsed ODMR

CW-ODMR is the most widely adopted NV magnetometry protocol with the benefit of its easy implementation. In a CW-ODMR protocol, the NV ensemble is optically illuminated continuously while a microwave field is applied simultaneously [Fig. 1.4(a)]. When the microwave frequency approaches either resonance f_+ or f_- from Eq. (1.6), population is driven from $|m_s = 0\rangle$ into the corresponding $|m_s = \pm 1\rangle$ sublevel, competing with the optical repolarization back into $|m_s = 0\rangle$; the resulting steady-state PL reduction produces a resonance feature in the ODMR spectrum, and the resonance center frequency directly connects the external magnetic field through Eq. (1.6). Fig. 1.5 shows an example of CW-ODMR spectrum as a function of MW frequency, with a bias magnetic field of 1.1 mT along one of the NV symmetry axis.

Magnetometry can be performed by sweeping the MW frequency to measure the shift of extracted resonance frequencies. Alternatively, one or a small number of fixed frequencies can be applied at the points of maximum slope on the ODMR lineshape, so that a magnetic-field-induced shift of the resonance produces a proportional change

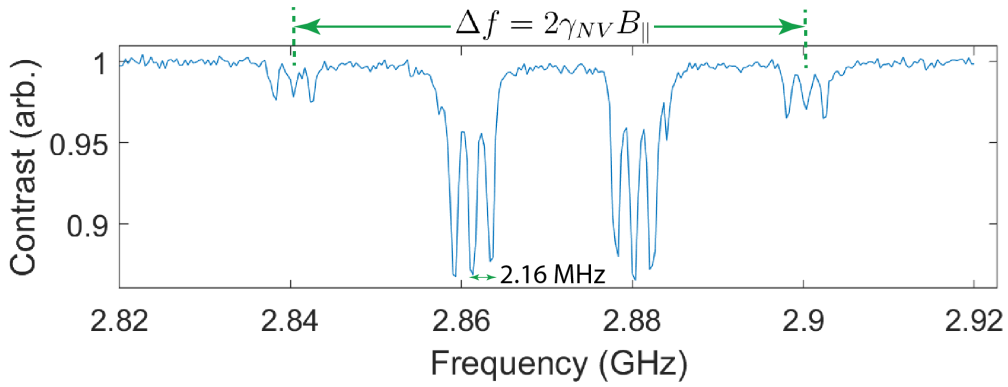


Figure 1.5: Example CW-ODMR spectrum with about 1.1 mT magnetic field applied to one of the NV orientations, creating the outermost pair of resonances. The inner pair of resonances corresponds to the overlapped transition frequencies of the remaining three NV orientations. Each resonance exhibits three distinct features, separated by $\sim$ 2.16 MHz, which arise from the hyperfine coupling of the NV electronic spin to the ^{14}N nuclear spin ($I = 1$).

in the detected fluorescence at fixed measurement bandwidth. In addition, driving multiple hyperfine-split resonance frequencies simultaneously can recover a good amount of ODMR contrast and help separate field-induced shifts from resonance broadening or thermal drift of $D(T)$ [14]. To suppress common-mode noise and improve signal-to-noise ratio (SNR) for sensitive measurements, lock-in ODMR with frequency-modulated MW is often employed in CW operation [16]. The principle of lock-in detection is discussed in Appendix A. Another option is to perform signal measurement (sig) with MW applied on-resonance, and reference measurement (ref) with MW applied away from resonance or with MW turned off, so that the normalized contrast is given by C = sig/ref. This method is particularly useful for the pulsed protocols where performing lock-in measurements are no longer viable.

While the CW-ODMR protocol is often favored for its technical simplicity, the magnetic sensitivity of CW-ODMR is fundamentally limited by the fact that the optical and MW fields are present simultaneously throughout the measurement. Continuous opti-

cal illumination competes with MW-driven spin population transfer, and continuous MW driving power-broadens the resonance linewidth beyond its intrinsic, dephasing-limited value; both effects reduce the achievable slope at resonance and therefore the sensitivity. Pulsed ODMR addresses this by separating the optical and MW fields in time: an initial optical pulse polarizes the ensemble into $|m_s = 0\rangle$, a MW π-pulse then transfers population toward $|m_s = \pm 1\rangle$ if applied near resonance, and a final optical pulse reads out the resulting spin population before repolarizing the ensemble for the next cycle [Fig. 1.4(b)]. Because the MW and optical fields are no longer applied simultaneously, the sensitivity is improved, through the steeper slope from narrower observed resonance, relative to CW-ODMR. The linewidth measured from pulsed ODMR protocol is set by two parameters: the intrinsic, dephasing-limited linewidth associated with ensemble inhomogeneous dephasing time (T_2^*), and broadening from the finite duration of the MW π-pulse itself [1]. Balancing π-pulse duration, which is determined by the MW power, against the dephasing time T_2^* to equalize these two contributions is a standard step in optimizing a pulsed ODMR measurement.

1.2.1.2 Ramsey Magnetometry

During CW and pulsed ODMR magnetometry, external magnetic fields are sensed from the change of NV spin population transfer during the applied MW duration. Ramsey-based magnetometry, however, detects magnetic field during the interval when both optical and MW fields are absent. A Ramsey sequence begins with an optical pulse that polarizes the NV ensemble into $|0\rangle$, followed by a resonant MW $\pi/2$-pulse that prepares

a coherent superposition of two ground-state sublevels, most commonly $|m_s = 0\rangle$ and $|m_s = +1\rangle$ (or $|m_s = -1\rangle$). During the subsequent free-precession interval τ, both optical and MW fields are switched off, and the superposition accumulates a relative phase

$$\phi = 2\pi \, |\Delta m| \, \gamma_e \, B_z \, \tau, \tag{1.9}$$

set by the projection of the local field B_z along the NV axis and the difference $|\Delta m| = 1$ between the two spin sublevels in superposition. A second MW $\pi/2$-pulse converts this accumulated phase into a population difference between the sensing sublevels, which is then read out optically exactly as in pulsed ODMR [Fig. 1.4(c)].

Sweeping free-precession time τ produces Ramsey fringes: an oscillatory signal whose envelope decays with the ensemble inhomogeneous dephasing time T_2^*, which can be described with the corresponding ODMR resonance Lorentzian linewidth Γ as $T_2^* = (\pi\Gamma)^{-1}$. For magnetometry, rather than mapping out the full fringe pattern, the free-precession interval is fixed near $\tau \approx T_2^*$, the point at which the fringe slope with respect to B_z is steepest, and the resulting DC magnetometry curve linearly converts small magnetic-field changes into a proportional change in PL contrast about that operating point. In addition, the phase of the final $\pi/2$-pulse (for example between x and $-x$) can be alternated during successive Ramsey sequences, so that the two resulting signals can be combined into a normalized contrast that rejects common-mode, low-frequency noise sources such as laser-intensity drift.

Because the optical and MW fields are absent during the sensing interval itself, Ramsey magnetometry avoids the power-broadening effect that limits both CW and pulsed

ODMR protocols and permits higher optical and MW irradiation intensities during initialization and readout, increasing the photon yield per measurement cycle. Its sensitivity is consequently limited only by the ensemble dephasing time T_2^* itself, together with photon shot noise in the readout.

1.2.2 All-Optical, Microwave-Free Magnetometry

Conventional NV magnetometry protocols, including CW-ODMR, pulsed ODMR, and Ramsey interferometry (see Sec. 1.2.1), rely on resonant MW fields to coherently drive NV electronic spin population between the $|m_s = 0\rangle$ and $|m_s = \pm 1\rangle$ ground-state sublevels, with the resulting spin population read out through spin-state-dependent PL. This use of MW fields can introduce a few experimental challenges, including: the electronics to generate radio frequency (RF) signals of desired frequencies, the incorporation of MW antenna(s), and the MW amplifier chain (to achieve efficient spin population manipulation), which can substantially increase the size, weight, power (SWaP) and design complexity. In addition, the MW irradiation may disturb sensitive samples of interest such as superconducting or biological specimens.

All-optical (AO), microwave-free magnetometry instead infers the magnetic field directly from magnetic-field-dependent changes in the NV PL intensity itself. The removal of MW drive can address the limitations posed by the conventional NV magnetometry protocols discussed above. AO magnetometry does not rely only on a single physical mechanism to give PL contrast that changes with magnetic field, but rather on any of several field-dependent processes at distinct regions of the applied bias field, as

shown in Fig. 1.6 [2].

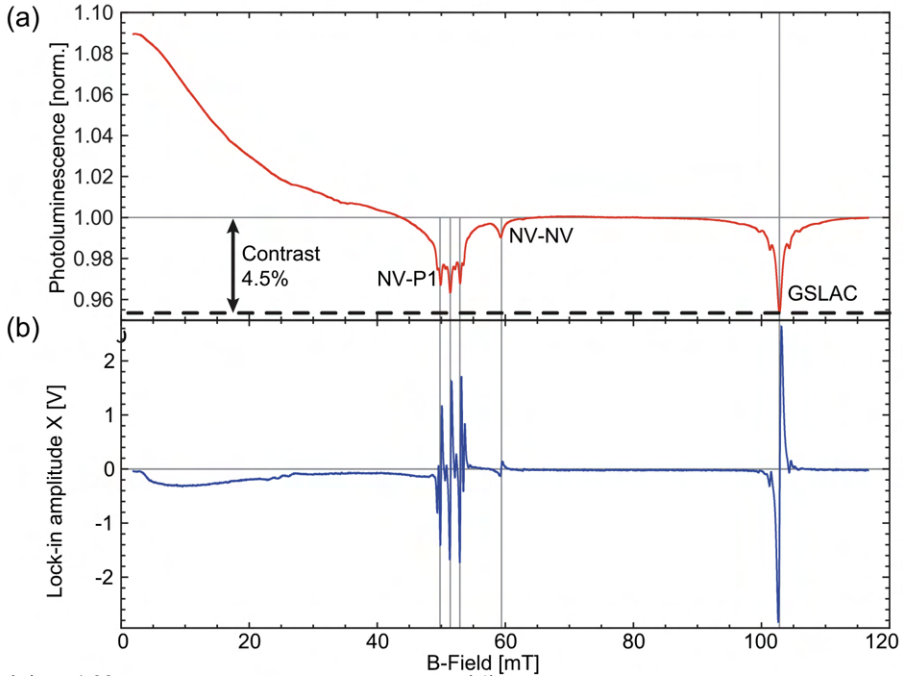


Figure 1.6: Experimentally measured AO NV-PL (a) and its derivative signal given by the in-phase output X of the lock-in amplifier (LIA) (b) as a function of the applied magnetic field, reported in Ref. [2].

A magnetic field not aligned with the NV symmetry axis mixes the nominally pure $|m_s = 0\rangle$ and $|m_s = \pm 1\rangle$ eigenstates. As a result, the optical transitions are no longer spin-conserving, reducing optical NV spin polarization and therefore PL emission intensity. At intermediate fields along one of the NV symmetry axes, on the order of 10 mT, this spin-mixing effect leads to a significant reduction in PL intensity from the other three non-aligned NV classes.

Near 50 mT, cross-relaxation between the NV electronic spin and the substitutional-nitrogen (P1) electronic spin bath occurs. This NV-P1 cross-relaxation process opens an additional field-dependent electronic spin depolarization channel that reduces PL intensity when the NV and P1 spin transition frequencies become degenerate [Fig. 1.7].

Around the same field near 50 mT, NV excited-state level anti-crossing (ESLAC) also occurs, which leads to the $|m_s = 0\rangle$ and $|m_s = -1\rangle$ electron spin states in the excited state overlap. This anti-crossing allows for efficient transfer of electron spin polarization to adjacent nuclear spins, thus reducing the PL intensity. The ESLAC process, however, occurs during an extremely short (tens of nanoseconds) window due to the short NV excited state lifetimes. While the AO ESLAC feature is observable in a single NV center [17], the corresponding AO signal in an NV ensemble around 50 mT is predominantly driven by NV–P1 cross-relaxation and has been utilized to perform eddy-current imaging [18].

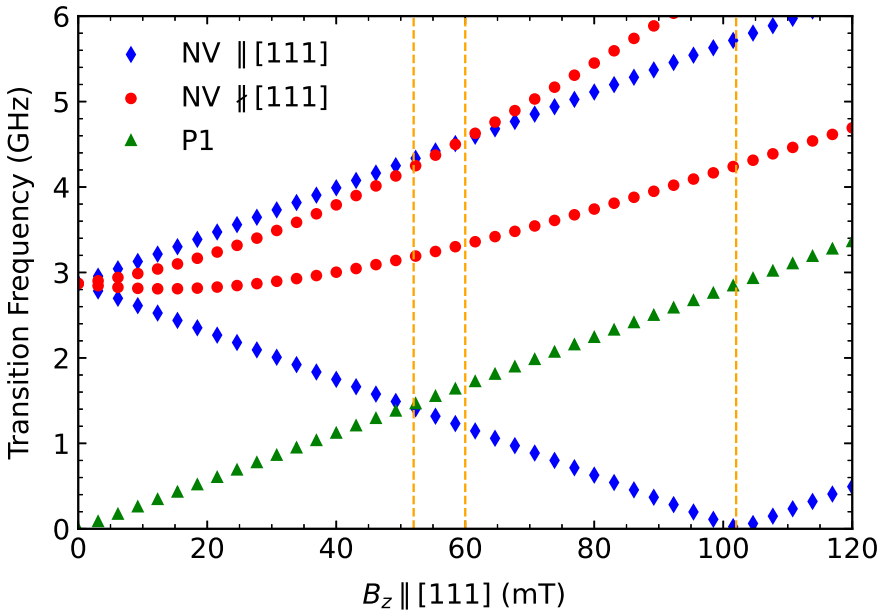


Figure 1.7: Simulated transition frequencies as a function of applied magnetic field along [111] crystallographic axis, from aligned NV (blue), non-aligned NVs (red), and P1 center (green). Multiple crossings occur near 50 mT, 60 mT, and 100 mT (dotted orange lines), coinciding with the PL reductions observed at these magnetic fields in Fig. 1.6.

A related but distinct effect occurs near 60 mT, where NV centers along different crystallographic orientations reach near-degenerate spin transitions and undergo NV-NV cross-relaxation directly, again reducing PL through enhanced depolarization.

At higher field approximately 102.4 mT, the NV ground-state spin sublevels approach a ground-state level anti-crossing (GSLAC), creating strong state mixing and hyperfine-mediated dynamic nuclear polarization. Similar to ESLAC but with longer ground state electronic spin lifetimes, GSLAC process leads to a pronounced field-dependent PL feature usable for AO magnetometry in an NV ensemble [2, 19].

While all three AO protocols of NV-P1 cross-relaxation ($\approx$ 50 mT), ESLAC ($\approx$ 50 mT), and GSLAC ($\approx$ 100 mT) can create prominent PL reductions for sensitive AO magnetometry, the employment of substantial applied fields ($>$ 50 mT) can increase system complexity due to its precise field alignment requirement and SWaP (size, weight, and power); and also induce undesired effects, such as perturbing magnetic materials of interest [20] or being unsuitable for magnetically shielded environments. These limitations can be avoided during AO measurements utilizing NV-NV cross-relaxation effect near zero magnetic fields from the near-degeneracy of various different NV classes, which will be discussed with more details in Chapter 2. In contrast, by exploiting the spin-mixing effect induced by non-negligible off-axis fields as seen near 10 mT, AO magnetometry may still be performed beyond the $\sim$ 100 mT bias field amplitude for GSLAC, which will be explained in more details in Chapter 4. Such AO operation may be suitable for environments where applying high-frequency ($\gtrsim$ 5 GHz) MW control fields can be challenging.

1.3 Organization of this Dissertation

This dissertation is organized to present AO magnetic sensing at various applied magnetic fields using NV centers in diamond, starting with continuous-wave detection of

AO-PL response at low magnetic fields; showcasing the pulsed AO sequence for noise suppression; measuring AO-PL changes under strong bias magnetic fields; and finally developing an NV magnetometry module for education purposes.

Chapter 2 describes the characterization of room-temperature AO-PL contrast features at low magnetic fields ($<$2 mT) using dense NV ensembles at ppm concentrations. Sec. 2.3.1 presents various AO-PL contrast features due to NV-NV cross-relaxation between different NV orientations. Sec. 2.3.3 then discusses the additional structures within each AO-PL contrast feature, arising from NV hyperfine interaction. Further substantiation of this physical picture is provided by consistency between the magnetic field values of measured AO-PL contrast peaks and those for near-degenerate NV spin and hyperfine transitions observed in CW-ODMR spectra. Sec. 2.3.5 describes the impact of laser power on measurement AO-PL contrast and identifies the interplay between NV electronic spin optical pumping rate and depolarization rate from NV-NV cross-relaxation. Sec. 2.4 details the results from two different numerical simulation, one using a two-NV model of dipolar interactions, and another using a modified four-level spin population model to provide reasonable agreement with various experimental measurements.

Chapter 3 introduces pulsed AO magnetometry, highlighting the benefits of using two AO PL measurements within an optical pulse to suppress common-mode noise, which offers improved magnetic sensitivity over continuous-wave based AO operation. Sec. 3.2.2 presents the characterization of pulsed AO-PL contrast as a function of readout timing with fixed dark time τ. Sec. 3.2.3 shows the investigation of pulsed AO-PL contrast as a function of dark time τ, with fixed readout timing found in Sec. 3.2.2. Sec 3.2.4 details the comparison of the noise suppression performance of pulsed AO to conven-

tional CW AO operation, achieving up to 10$\times$ improvement in the low-frequency noise floor.

Chapter 4 presents ongoing work on measuring AO-PL changes induced from an off-axis magnetic field, with a substantial bias field. The chapter begins by discussing the fundamental challenges associated with MW-based magnetic sensing inside a Tokamak nuclear fusion reactor. It further presents the simulation of AO-PL contrast as a function of on- (B_z) and off-axis ($B_\perp$) magnetic fields, indicating the optimal application of bias magnetic field to be sensitive to external off-axis fields $B_\perp$. It then demonstrates the experimentally measured AO-PL contrast as a function of on-axis magnetic field B_z up to 240 mT, with resolvable contrast features due to GSLAC, and presents preliminary results of AO-PL changes induced from an external coil, achieved using the pulsed AO sequence described in Chapter 3. The chapter concludes by outlining the future work needed to optimize the pulsed AO sequence in order to be optimally sensitive to external off-axis fields $B_\perp$.

Chapter 5 summarizes recent progress toward developing an NV system capable of CW-ODMR magnetometry for educational use in a quantum hardware laboratory course, offered by the department of Electrical and Computer Engineering. The chapter details the learning goal, design considerations to produce the setup used by undergraduate students to understand the basic operation of NV magnetometry.

Finally, Chapter 6 provides a brief outlook highlighting future research directions for the application of NV-based AO magnetic sensing.

Chapter 2: All-Optical Photoluminescence Response of Nitrogen-Vacancy Ensembles in Diamond at Low Magnetic Fields

This chapter is primarily based on the work reported in Ref. [21]. I have been fortunate to work with Jeyson Támara-Isaza, who leads the numerical simulation model for AO-PL as a function of magnetic field, and Michael Crescimanno, who develops the model for AO-PL contrast changes from optical pumping and resonant NV-NV interaction.

As discussed in Chapter 1, conventional AO magnetometry protocols employ substantial applied fields that can increase system complexity and SWaP (size, weight, and power); and also induce undesired effects, such as perturbing magnetic materials of interest [20] or being unsuitable for magnetically shielded environments. In this work, we investigate room-temperature AO PL at low magnetic fields ($<$2 mT) using diamonds with NV ensembles at ppm concentrations. Measured AO-PL contrast features as a function of applied magnetic field magnitude and direction are correlated with near-degenerate NV electronic spin and hyperfine transitions from different NV orientations within the diamond host.

Reasonable agreement is found between low-field AO-PL measurements and model-based simulations of the effects of resonant dipolar interactions between NV centers.

Maximum observed AO-PL contrast depends on both NV concentration and laser illumination intensity at 532 nm. These results imply different optimal conditions for low-field AO NV sensing compared to conventional ODMR techniques, suggesting new research and application opportunities using AO measurements with lower system complexity and SWaP.

2.1 Principles of NV-NV Cross-Relaxation

In an NV ensemble, NV-NV dipolar interactions increase the spin relaxation (depolarization) rate between the PL bright $|m_s = 0\rangle$ and dark $|m_s = \pm 1\rangle$ states [22].

The interaction Hamiltonian H_{int} between two NV centers with electronic spin operators $\vec{S}_{1,2}$, and dipolar interaction strength D_{dd} along a unit vector $\hat{n}_{12}$, is given by:

$$H_{\text{int}} = D_{\text{dd}}[3(\vec{S}_1 \cdot \hat{n}_{12})(\vec{S}_2 \cdot \hat{n}_{12}) - (\vec{S}_1 \cdot \vec{S}_2)]. \tag{2.1}$$

The ground state Hamiltonian for two interacting NVs is then $H = H_{gs1} + H_{gs2} + H_{\text{int}}$. The depolarization rate is further enhanced when different NV centers have equal transition frequencies between electronic spin states. For such degenerate spin transitions, resonant NV-NV dipolar interactions induce spin state mixing, i.e., NV-NV cross-relaxation [22, 23]. Consequently, a reduction in both the NV spin polarization lifetime (T_1) and PL intensity can be observed [Fig. 2.1] [24]. Each NV within an ensemble in a single crystal diamond sample is oriented along one of the four crystallographic axes, with typically an equal fraction (one fourth) of the NV ensemble along each axis. By adjusting the applied magnetic field direction and magnitude in the low-field regime (<2 mT), one can tune the

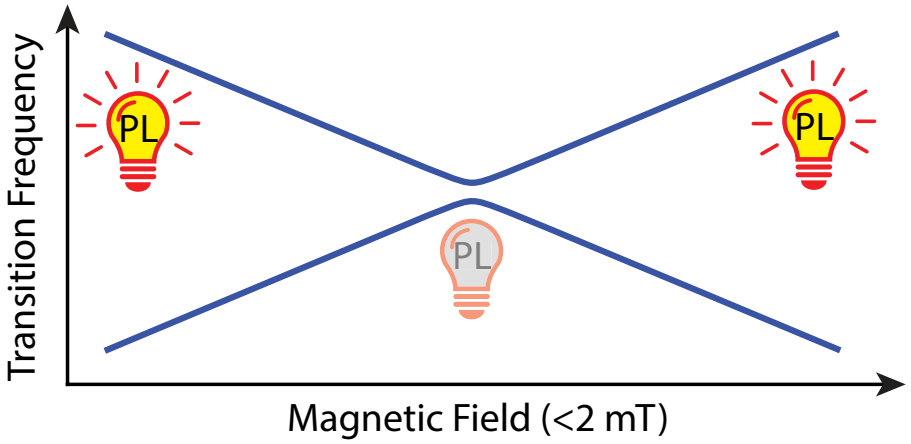


Figure 2.1: Illustration of avoided crossing from two interacting near-resonant NV electronic spins at low magnetic fields (<2 mT). Resonant NV-NV dipolar interactions at the avoided crossing increase the NV depolarization rate and reduce total PL emission.

spin transition frequencies of the four NV orientation classes and spectrally overlap their resonances. This magnetic field tuning enables careful measurement of low-field AO-PL signals, i.e., without applied microwaves.

2.2 Experimental Details and Calibrations

2.2.1 Experimental Setup

532 nm CW laser light (Lighthouse Photonics Sprout-H-10W) is focused into a diamond sample with a microscope objective (Olympus 20X/NA 0.45) to optically excite the NV centers, with a typical Gaussian excitation laser beam profile of radius $\approx 30\,\mu m$. Table 2.1 summarizes the characteristics of different CVD-grown NV-diamond samples employed in this work. We observe NV-NV cross-relaxation features in low-field AO-PL measurements for diamond samples with NV concentration $\gtrsim 0.3$ ppm, corresponding to an average distance between NVs $\lesssim 26$ nm. A half-wave plate (Thorlabs WPHSM05-

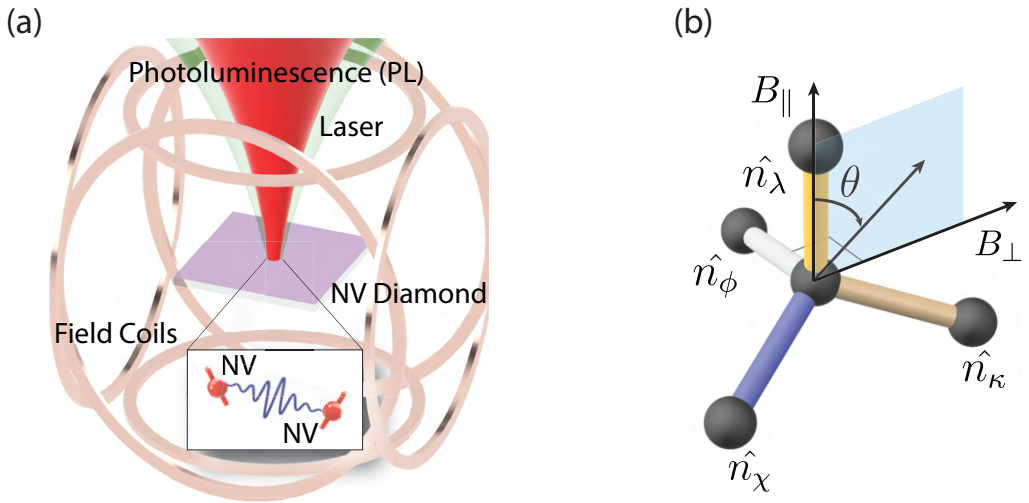


Figure 2.2: (a) AO-PL measurements utilize three sets of Helmholtz coils to control bias magnetic field magnitude and direction. NV centers in a single crystal diamond plate are optically excited by 532 nm laser light and emit PL ($\approx$ 637–800 nm), collected by a photodiode (not shown). A microwave antenna (not shown) enables comparison CW-ODMR measurements. Inset: dipolar interactions between different NV centers contribute to AO-PL contrast at low magnetic fields. (b) Illustration of applied magnetic fields and four NV orientations along unit vectors $\hat{n}_\lambda$, $\hat{n}_\phi$, $\hat{n}_\chi$ and $\hat{n}_\kappa$. The on-axis magnetic field $B_\parallel$ is along the [111] crystallographic axis. The off-axis magnetic field $B_\perp$ is along the [$\bar{1}$10] crystallographic axis. θ is the polar angle from $B_\parallel$.

532) is mounted before the microscope objective to control the optical polarization direction. NV-PL is collected through the same objective, directed with a dichroic mirror (Semrock FF552-DI02), filtered with a long-pass filter (Semrock BLP01-532R-25), and imaged onto an avalanche photodiode (Thorlabs APD410A) through a 50 mm lens (Thorlabs LA1131-B-ML). A polarizing beamsplitter (Thorlabs PBS12-532-HP) and a half-wave plate (Thorlabs WPHSM05-532) held within a rotation mount (Thorlabs CRM05) are used to control the laser power delivered to the diamond sample.

Table 2.1: Diamond samples used in this chapter. All samples are electronic-grade plates (a few mm on each side and about 0.5 mm thick), with a 10 μm-thick surface layer of enhanced nitrogen and NV concentration ([N] = 16 ppm, $>$99.995% ^{12}C) as reported by Element Six Ltd.

Sample #	**[NV] (ppm)**	**N Isotope**
S1-14N	≈ 3.8	^{14}N
S2-15N	≈ 3.8	^{15}N
S3-14N	≈ 3.8	^{14}N
S4-14N	≈ 2	^{14}N
S5-14N	≈ 0.3	^{14}N

A bias magnetic field of controllable magnitude and direction is provided by three-axis Helmholtz coils (Ferronato BH300-3-A) connected to a three-channel power supply (Rohde & Schwarz HMP4030). Relay boards are used to alter the magnetic field directions. The diamond plate under study is attached to a dielectric mirror (Thorlabs BB1-E02) to boost optical collection efficiency. The diamond-mirror system is then mounted on a piezoelectric rotational stage (Thorlabs ELL14) to align the longitudinal and transverse directions of the [111] NV-axis to the applied magnetic field. An additional coil connected to a microwave signal generator (SRS SG384) is used to perform CW-ODMR measurements.

The output of the photodiode used to collect NV PL is sent to a data-acquisition device (National Instruments USB-6363) for direct measurements, or to a LIA (SRS SR865)

for lock-in detection of AO PL. To apply small magnetic field amplitude modulation as part of lock-in AO-PL measurements, the output of a LIA local frequency generator is connected to the Helmholtz coils through a Class-D audio amplifier (Sure Electronics TDA7492).

2.2.2 Experimental Operation

Fig. 2.2(a) depicts the experimental setup used to study low-field AO-PL, including NV-NV cross-relaxation features. An NV diamond sample is exposed to a controllable magnetic field, with magnitude and direction determined by three sets of Helmholtz coils aligned along the diamond's [110], [$\bar{1}$10], and [001] crystallographic axes. The unit vectors parallel to the NV symmetry axes are $\hat{n}_\lambda$, $\hat{n}_\phi$, $\hat{n}_\chi$, and $\hat{n}_\kappa$ along [111], [$\bar{1}\bar{1}$1], [1$\bar{1}\bar{1}$], and [$\bar{1}$1$\bar{1}$], respectively. As illustrated in Fig. 2.2(b), the on-axis magnetic field $B_\parallel$ is defined as parallel to NVs along axis $\hat{n}_\lambda$; and the off-axis magnetic field $B_\perp$ is perpendicular to both axes $\hat{n}_\lambda$ and $\hat{n}_\phi$. Amplitude modulation of $B_\perp$ at a rate of 100 Hz is applied to perform LIA measurements and improve the SNR. The AO-PL contrast for each on/off-axis magnetic field value ($B_\parallel$, $B_\perp$) is determined by the normalized difference in intensities between a measured AO-PL signal I_{sig} and an AO-PL reference I_{ref}. I_{ref} is given by the maximum measured AO-PL from a given scan of ($B_\parallel$, $B_\perp$) values in which the NV orientation classes are spectrally separated. The AO-PL contrast is then calculated as $C = 1 - I_{\text{sig}}/I_{\text{ref}}$. Further details of the experimental calibration are given in the following sections.

2.2.3 Calibration of Applied Magnetic Fields

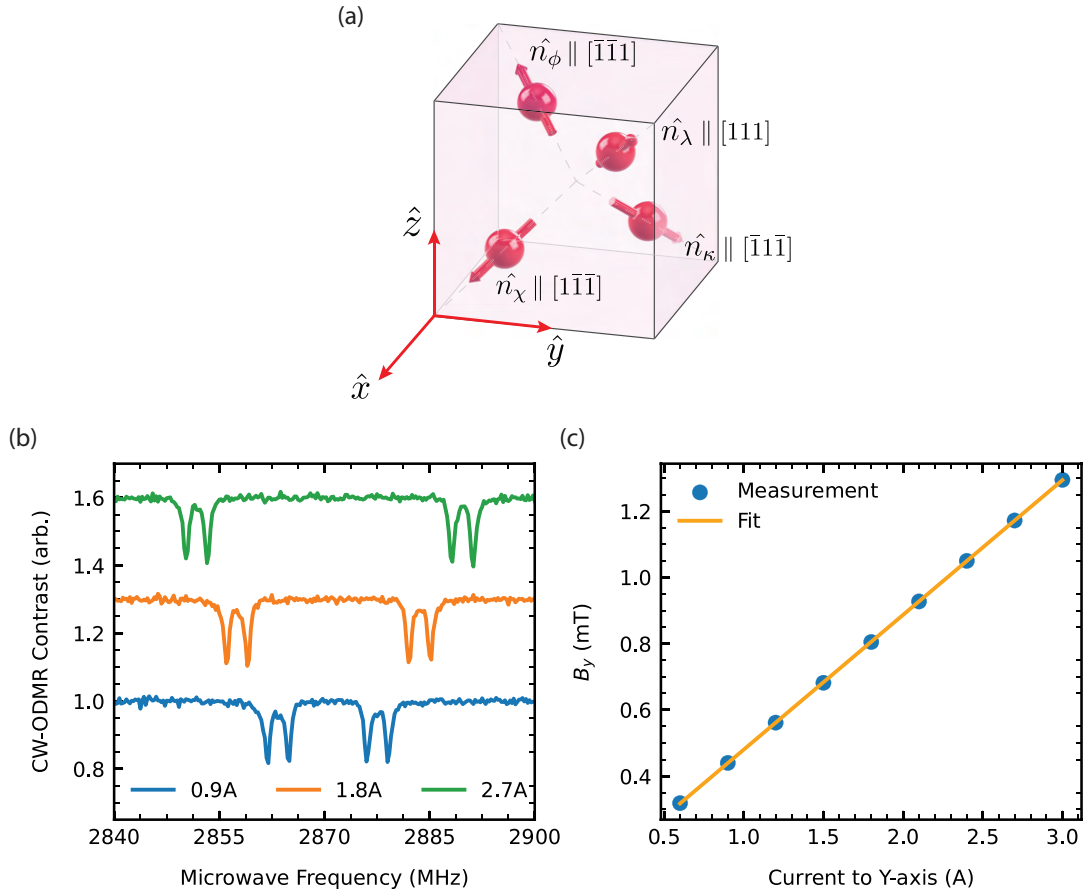


Figure 2.3: (a) Schematic of unit vectors parallel to the four NV symmetry axes within a diamond sample, relative to the bias magnetic field Cartesian coordinates, with $\hat{z}$ vertical in the lab frame. (b) CW-ODMR spectra measured from sample S2-15N with 0.9 A, 1.8 A, and 2.7 A applied to the y-axis Helmholtz coil, with the diamond oriented such that the coil generates a magnetic field only along the [100] crystallographic orientation. Vertical offsets are applied to the spectra for better clarity. The results from x and z-axis coils behave similarly. (c) Lorentzian fit to measured CW-ODMR spectra yields magnetic field along y-axis as a function of current applied to the y-axis Helmholtz coil. Linear fit (solid line) produces a current-to-magnetic-field calibration constant k_y = 0.4068 $\pm$ 0.0009 mT/A.

We calibrate magnetic fields generated by the three-axis Helmholtz coils by first rotating the diamond sample so that the magnetic field in $\hat{y}$ produced by one set of coils is along the diamond's [100] crystallographic orientation. As a result, the mag-

netic fields from coils along the x, y, and z axes individually project with equal magnitude onto all four NV orientations within a single-crystal diamond sample, illustrated in Fig. 2.3(a). We then perform CW-ODMR measurements by using a microwave coil connected to a microwave signal source to coherently manipulate the NV ground state electronic spin states. The central hyperfine resonance frequencies from both the $|m_s = +1\rangle$ to $|m_s = 0\rangle$ transition and $|m_s = -1\rangle$ to $|m_s = 0\rangle$ transition can be extracted through a multi-Lorentzian fit to CW-ODMR data, with good overlap of the CW-ODMR spectra from all four NV orientations. Next, we calculate the applied magnetic field amplitude $B = \Delta f/[2\gamma_e \cos(109.47°/2)]$, where Δf is the frequency difference between the $|m_s = \pm 1\rangle$ to $|m_s = 0\rangle$ transitions, γ_e is the gyromagnetic ratio of the NV electronic spin, and $\cos(109.47°/2)$ is the angle factor due to the applied magnetic field being aligned along the diamond's [100] orientation and not along the [111] symmetry axis. By repeating this procedure for the fields produced from each of the three Helmholtz coils, and performing linear fitting of the calculated magnetic fields to the corresponding applied currents, we obtain the current-to-magnetic-field calibration constants for each of the three directions. Fig. 2.3(b, c) show example measured CW-ODMR spectra for different applied currents to the y-axis Helmholtz coil, and a linear fit to extract the calibration constant in $\hat{y}$. Using this method, we obtain the current-to-magnetic-field calibration constants k_x = 0.406 $\pm$ 0.002 mT/A, k_y = 0.4068 $\pm$ 0.0009 mT/A, and k_z = 0.5119 $\pm$ 0.0008 mT/A for the three directions in the lab frame.

To apply magnetic fields with on-axis field $B_\parallel$ along [111] and off-axis field $B_\perp$ along [$\bar{1}$10] crystallographic axes, we rotate the diamond sample around the z axis by 45°. $B_\parallel$ is then described by a linear combination of B_y and B_z, with $B_z = B_y/\sqrt{2}$; and

$B_\perp$ is given by $B_x = I_x k_x$ in the lab frame. For example, setting $I_y = 2\,\text{A}$ for the y-axis coil yields $B_y = I_y k_y = 0.814\,\text{mT}$ and hence $B_z = B_y/\sqrt{2} = 0.575\,\text{mT}$, equivalent to applying $I_z = B_z/k_z = 1.12\,\text{A}$. In this example, $B_\parallel = \sqrt{B_y^2 + B_z^2} = 0.997\,\text{mT}$. The alignment of applied magnetic fields is further characterized by comparing the polar angles θ of different observed AO-PL cross-relaxation features with the expected values from symmetry considerations. Our findings indicate that the experimental alignment is consistent with theoretical expectations, with magnetic field misalignment limited to less than 1°.

2.2.4 Dependence of Lock-in Output Amplitude on Magnetic Field Modulation Frequency

We observe a dependence of the LIA output amplitude on the modulation frequency f_m as we amplitude modulate $B_\perp$. Fig. 2.4 presents an example measured demodulated AO-PL LIA spectrum around $B_\perp \approx 1.05\,\text{mT}$ and at fixed $B_\perp = 1.24\,\text{mT}$ for sample S3-14N. The phase from the LIA is set to 0° so that the amplitude measured with $f_m = 100\,\text{Hz}$ is maximized. Although higher f_m is desired to avoid low frequency noise and improve SNR ratio, we find the peak amplitude from the central demodulated spectral feature decreases by a factor of about 14 as f_m increases from 100 Hz to 500 Hz. In addition, there is a noticeable distortion (i.e., phase shift) of the dispersive line shapes at higher f_m. These observations are similar to the results reported in Ref. [25] where adiabatic exchange of NV electronic spin population across the avoided crossings at low f_m produces larger demodulated output amplitude. In order to resolve various AO-PL

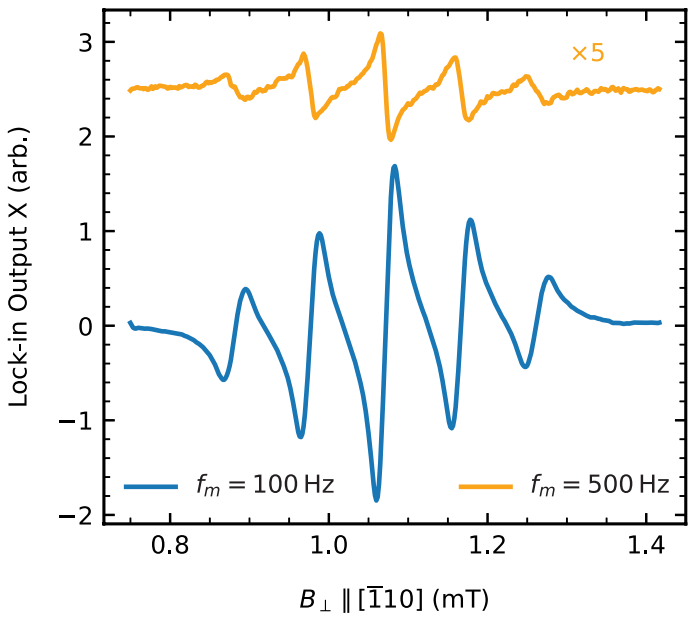


Figure 2.4: Experimental demodulated AO-PL LIA spectrum from NV-NV cross-relaxation for sample S3-14N around $B_\perp \approx 1.05$ mT and at fixed $B_\parallel = 1.24$ mT for modulation frequency f_m of 100 Hz (blue) and 500 Hz (orange). The upper trace is multiplied by 5 and shifted upwards for better clarity. A significant phase difference can be seen between the two traces, along with about 14 times lower peak amplitude for the higher modulation frequency.

line shapes from NV-NV cross-relaxation more clearly without compromising the SNR from low frequency noise, we perform all LIA measurements reported in this Chapter with $f_m = 100$ Hz. The larger demodulated peak amplitude at this modulation frequency helps to resolve the two shoulder signals from dipolar interactions between NVs along $\hat{n}_\kappa$ in Fig. 2.9(c, left).

2.2.5 Calibration of Magnetic Field Amplitude Modulation Strength

As described in the previous section, we perform AO-PL LIA measurements by amplitude modulating $B_\perp$ at a rate (modulation frequency f_m) of 100 Hz. The SRS LIA outputs a sine wave with $0.1 V_{pp}$, which is passed through an audio amplifier to drive cur-

rent through the x-axis Helmholtz coil and generate the modulated field. A 3.5 Ω resistor is connected in series to the Helmholtz coil to improve impedance matching and provide stronger modulation amplitude. To calibrate the $B_\perp$ modulation amplitude produced by the Helmholtz coil, we perform lock-in CW-ODMR measurements. We apply an unmodulated bias field in the $[\bar{1}10]$ direction so that the measurement can be optimally sensitive to $B_\perp$ modulation in the same direction. The microwave signal generator used for CW-ODMR outputs frequency modulated sine-wave signals with 1 MHz deviation and 10 kHz rate; this modulated microwave signal is then amplified and sent to a custom microwave loop antenna to coherently manipulate the NV spin states.

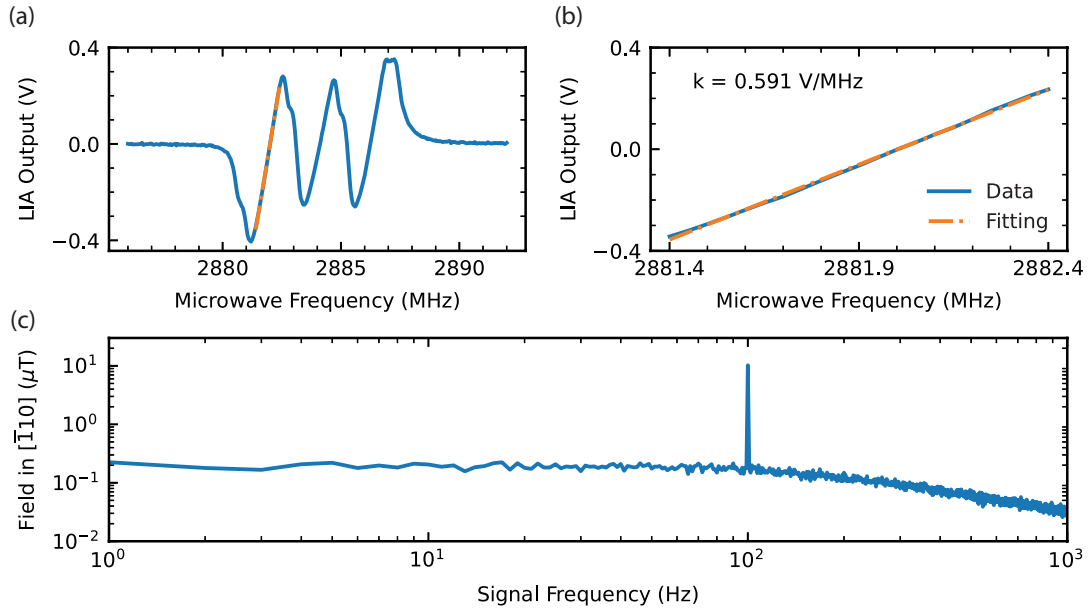


Figure 2.5: (a) Demodulated CW-ODMR spectrum from sample S3-14N using frequency-modulated microwave signals. A linear fit is applied to the section indicated by the dash dotted orange line. (b) Zoom-in view of the linear fit applied at the zero-crossing point of the left resonance feature in the demodulated CW-ODMR spectrum, yielding slope of 0.591 ± 0.007 V/MHz. (c) FFT spectrum of time-averaged lock-in CW-ODMR measurements, with amplitude modulated $B_\perp$ applied with 0.1 V_{pp} at 100 Hz. Calibration measurements allow expression of the FFT spectrum in magnetic field units, with peak modulated field amplitude of $10.23 \pm 0.12\,\mu$T .

Fig. 2.5(a) shows an example demodulated CW-ODMR spectrum from measure-

ments on sample S3-14N. A linear slope of 0.591 ± 0.007 V/MHz of LIA output to microwave frequency is obtained from a linear fit applied to the steepest part of the left NV hyperfine resonance [Fig. 2.5(b)]. Since the relevant NV spin transition frequencies are sensitive to the projection of magnetic fields along the symmetry axis in the [111] direction, and the bias field used in these lock-in CW-ODMR measurements is in the $[\bar{1}10]$ direction, the NV magnetic sensitivity to the modulated $B_\perp$ field is reduced by an angle factor of $\cos(109.47°/2) \approx 0.577$. The measured linear slope of LIA output as a function of microwave frequency can then be converted into a calibration constant of 9.56 ± 0.12 mV/μT using the NV electronic spin gyromagnetic ratio $\gamma_e = 28.024$ kHz/μT and the angle factor. This calibration process is similar to that described in Sec. 2.2.3 for application of bias magnetic fields with the Helmholtz coils.

To avoid the low-pass filter from the LIA affecting the measured signal with $f_m = 100$ Hz, we set the LIA 3 dB point at 1 kHz with a first order filter slope of 6 dB/octave. For typical LIA measurements, we acquire $n = 30$ consecutive 1 s time traces using a National Instruments USB-6363 data I/O device at a sampling rate of 100 kHz. The averaged time-domain signal is then transformed into a frequency-domain representation using Fast Fourier Transform (FFT) analysis. The amplitude of the FFT spectrum is converted to the magnetic field unit of μT using the calibration constant; and the standard deviation σ of the peak amplitudes at 100 Hz from $n = 30$ acquisitions characterizes the measurement uncertainty. Fig. 2.5(c) depicts an example measured spectrum of the modulated $B_\perp$ field, with peak amplitude of 10.23 ± 0.12 μT at 100 Hz determined using the above calibration procedure.

2.3 Experimental Results

2.3.1 NV-NV Cross-Relaxation Features for a Dense Ensemble

We experimentally determine the low-field AO-PL contrast as a function of $B_\parallel$ and $B_\perp$, starting with a 3.8 ppm NV concentration diamond enriched with ^{14}N (sample S1-14N) [Fig. 2.6(b)]. We vary both $B_\parallel$ and $B_\perp$ over a range of about 1.5 to -1.5 mT, with step size ≈ 0.02 mT. The resulting two-dimensional plot of experimental AO-PL contrast is in reasonable agreement with a numerical simulation based on the simple two-NV coupled Hamiltonian described by Eqs. (1.1, 2.1) with a fixed dipolar interaction strength [Fig. 2.6(b)] [26]. Differences between the experimental and simulated mag-

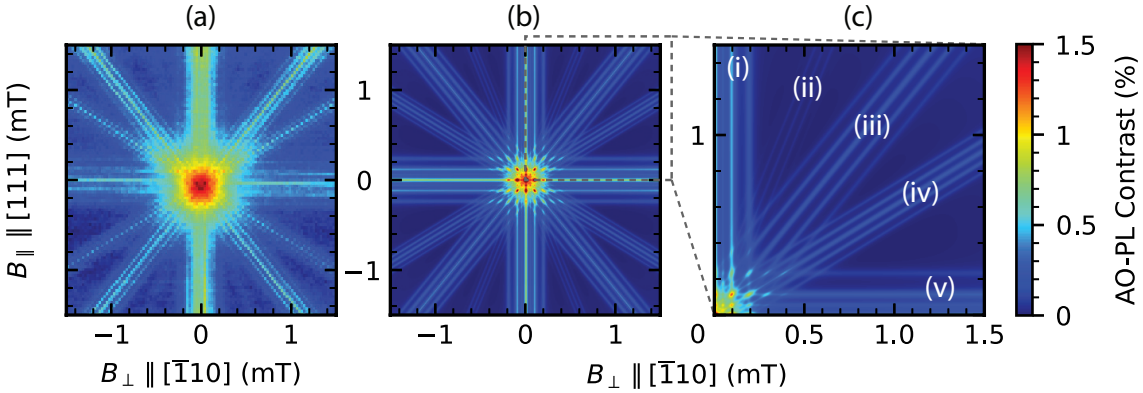


Figure 2.6: (a) Experimentally determined AO-PL contrast as a function of applied magnetic fields using sample S1-14N with $\approx$ 3.8 ppm NV concentration. Large AO-PL contrast around zero applied field, as well as line features at specific θ values are observed. (b) Simulated AO-PL contrast using a fixed dipolar interaction strength. (c) Expanded view of the upper right quadrant in Fig. 2.6(b), with labels at specific line features indicating the cross-relaxation between NVs of orientations along (i) $\hat{n}_\phi$, $\hat{n}_\chi$ and $\hat{n}_\kappa$ at $\theta = 0°$; (ii) $\hat{n}_\kappa$ at $\theta = 22.2°$; (iii) $\hat{n}_\lambda$ and $\hat{n}_\chi$; $\hat{n}_\phi$ and $\hat{n}_\kappa$ at $\theta = 39.3°$; (iv) $\hat{n}_\lambda$ and $\hat{n}_\kappa$ at $\theta = 58.5°$; (v) $\hat{n}_\lambda$ and $\hat{n}_\phi$ at $\theta = 90°$. NV hyperfine interactions contribute to parallel line structures within AO-PL contrast features.

nitudes of AO-PL contrast line features likely arise from the simplicity of the model used. Details of the numerical simulation are included in Sec. 2.4.1. When the ap-

plied magnetic field is near zero ($\lesssim 0.1$ mT), spin transitions for NVs along all four axes are spectrally overlapped, resulting in maximum NV-NV cross-relaxation and AO-PL contrast. The relatively large magnetic field linewidth measured in AO-PL contrast features at near-zero-field may be attributed to the influence of local electric fields [24, 27] and/or magnetic field and strain gradients. The experimental AO-PL contrast maximizes at $B_{\parallel} \approx -0.02$ mT, likely due to a background magnetic field (e.g., from the Earth and other lab instrumentation). Additionally, significant AO-PL contrast is observed in both experiment and simulation at specific polar angles θ from $B_{\parallel}$, consistent with the effect of cross-relaxation among different NV orientations resulting from near-degenerate spin transitions [24, 28, 29]. For example, at $\theta = 0°$ ($B_{\parallel} \neq 0$ and $B_{\perp} = 0$), the magnetic field is aligned with $\hat{n}_{\lambda}$ and the three non-aligned NV orientations (along $\hat{n}_{\chi}$, $\hat{n}_{\phi}$ and $\hat{n}_{\kappa}$) experience equal magnetic field projections. In the experiment, this configuration produces a broad, stripe-like feature with large AO-PL contrast (vertical around $B_{\perp} = 0$ in Fig. 2.6(b)) due to the enhanced cross-relaxation between the three overlapping NV spin resonances. The simulation using the simple two-NV model does not fully capture this broad stripe feature, as seen in Fig. 2.6(c, d). This discrepancy may arise from ensemble averaging in the experiment, including magnetic field and strain gradients, as well as variation in NV spacing.

At $\theta = 39.3°$, two sets of NV orientations (along $\hat{n}_{\lambda}$ and $\hat{n}_{\chi}$; $\hat{n}_{\phi}$ and $\hat{n}_{\kappa}$) experience the same applied field magnitude, with resulting degeneracies in NV spin transitions. Here, cross-relaxation from the two sets of degenerate NV orientations creates a line feature with moderate AO-PL contrast, in both experiment and simulation, compared to the results at $\theta = 0°$ with three degenerate NV orientations. Additional line features

of moderate AO-PL contrast are observed in both experiment and simulation for other specific polar angles that induce degeneracies between pairs of NV orientations, as seen in Fig. 2.6(b, c, d). At $\theta = 22.2°$, where the total applied field is transverse to NVs oriented along $\hat{n}_\kappa$, there is a line feature with very weak AO-PL contrast.

2.3.2 AO-PL Spectra with Different NV Concentrations

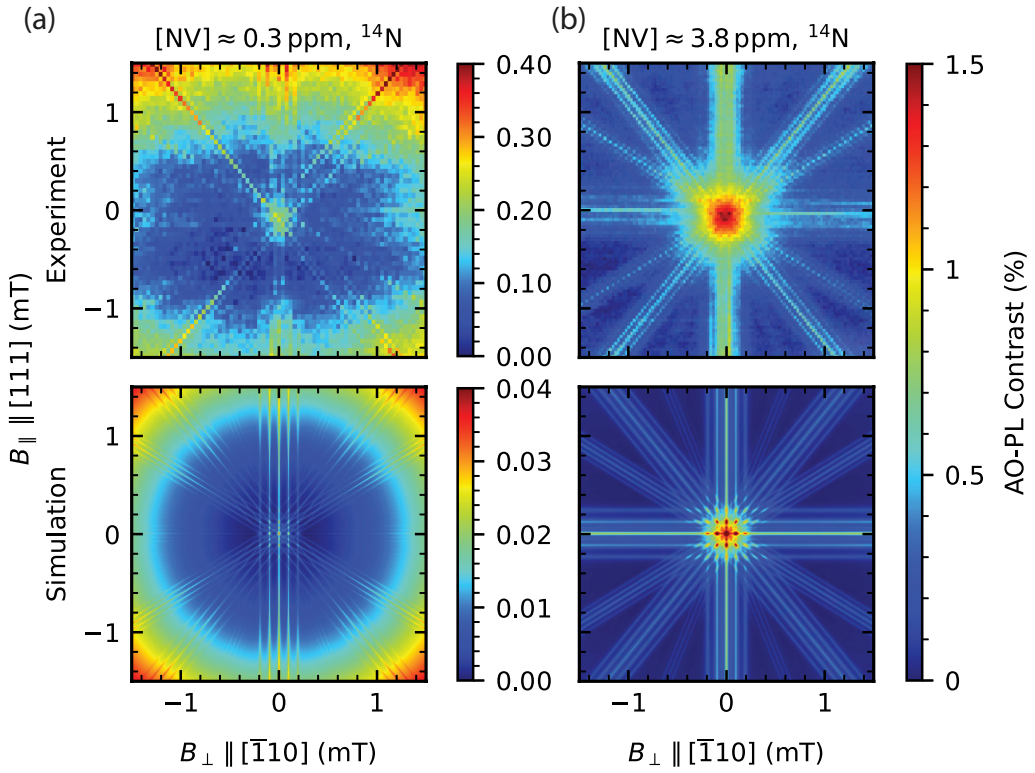


Figure 2.7: (a) (Top) Experimentally measured AO-PL contrast as a function of applied magnetic fields using sample S5-14N with ≈ 0.3 ppm [NV]. Weak NV-NV cross-relaxation features are observed in addition to the background contrast from magnetic-field-dependent spin mixing. (Bottom) Simulated AO-PL contrast using a fixed dipolar interaction strength from 0.3 ppm [NV]. Both spin mixing and NV-NV cross-relaxation AO-PL contrast features are seen. (b) (Top) Experimentally measured AO-PL contrast as a function of applied magnetic fields using sample S1-14N with ≈ 3.8 ppm [NV]. (Bottom) Simulated AO-PL contrast using a fixed dipolar interaction strength from 3.8 ppm [NV].

Figs. 2.7(a) and 2.7(b) show the measured (top) and simulated (bottom) AO-PL

contrast as a function of $B_{\parallel}$ and $B_{\perp}$ from sample S5-14N with ≈ 0.3 ppm NV concentration and sample S1-14N with ≈ 3.8 ppm NV concentration, respectively. Clusters of linear AO-PL contrast features arising from NV-NV cross-relaxation are experimentally observed near zero-field, $\theta = 0$, and $\theta = 39.3°$ for both the low and high NV concentration samples, which have relatively weak and strong NV-NV dipolar interaction strength, respectively. In addition, there is a non-negligible AO-PL contrast background, increasing with bias field magnitude, due to the mixing of NV electronic spin states from magnetic fields that are not aligned with the NV quantization axis [5]. Future work may incorporate field-dependent transition rates between spin sublevels and thereby improve simulations of AO-PL contrast from both spin mixing and NV-NV cross-relaxation.

2.3.3 Hyperfine Interaction and NV-NV Cross-relaxation

The experimental and simulation results in Fig. 2.6 also display multiple parallel structures within each θ-dependent AO-PL contrast feature. To investigate the role of the NV hyperfine interaction in this AO-PL sub-structure, we conduct comparative measurements on ^{14}N and ^{15}N samples with the same NV concentration (samples S1-14N and S2-15N). Fig. 2.8(a) shows AO-PL experimental results for positive-only values of $B_{\parallel}$ and $B_{\perp}$, taken with a smaller magnetic field step size ($\approx$ 0.01 mT) than the results in Fig. 2.6(b). (Similar results are found for the other ($B_{\parallel}$, $B_{\perp}$) quadrants.) In addition, we measure AO-PL contrast at fixed $B_{\parallel}$ = 1.24 mT by scanning $B_{\perp}$ with an even finer step size ($\approx$ 0.002 mT) to resolve the individual cross-relaxation line shapes more clearly (solid lines in Fig. 2.8(b)). As $B_{\perp}$ approaches 0 mT, there are overlap-

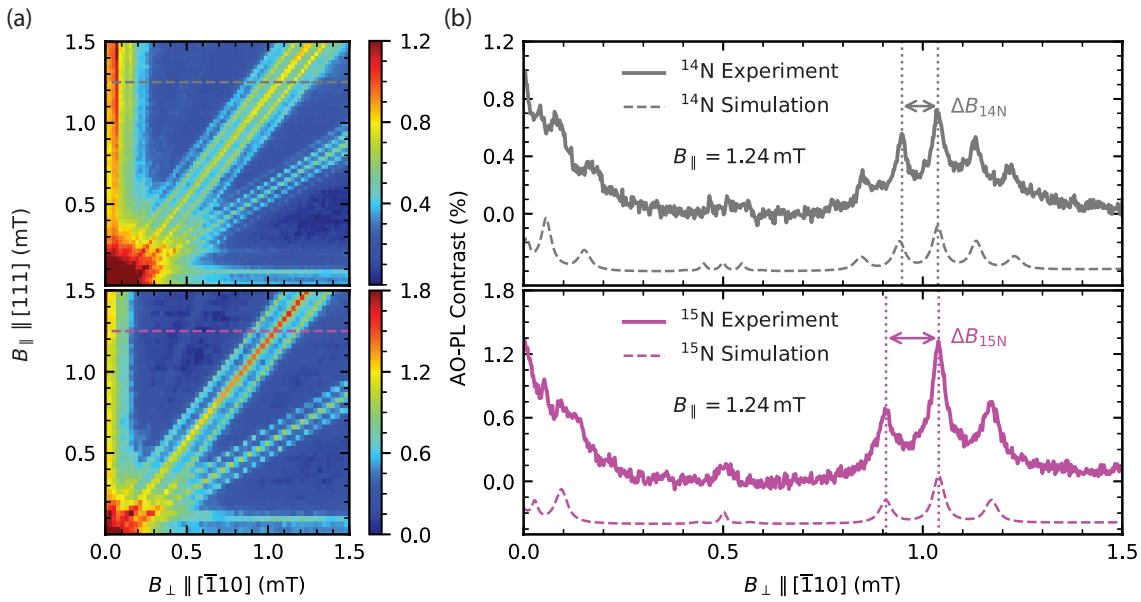


Figure 2.8: (a) Experimentally measured AO-PL contrast as a function of $B_\parallel$ and $B_\perp$ using ^{14}N-enriched sample S1-14N (top) and ^{15}N-enriched sample S2-15N (bottom) with the same NV concentration ($\approx$ 3.8 ppm). Horizontal dashed lines (orange for S1-14N and purple for S2-15N) indicate line-cut of data shown in Fig. 2.8(b) for $B_\parallel$ = 1.24 mT. (b) Experimentally measured AO-PL contrast for samples S1-14N and S2-15N (solid lines) and numerical simulations (dashed lines) at fixed $B_\parallel = 1.24$ mT. Vertical offsets are applied to the simulation results for visual clarity. In each measurement as $B_\perp$ approaches 0 mT, there are overlapping, unresolved AO-PL contrast peaks from the increased number of near-degenerate spin transitions for all NV orientations. At $B_\perp \approx 0.5$ mT, the limited SNR in experimental measurements hinders the identification of cross-relaxation features predicted by numerical simulations. At $B_\perp \approx 1.05$ mT, there are five (three) AO-PL contrast peaks with separation $\Delta B_{14N} \approx 0.09$ mT ($\Delta B_{15N} \approx 0.13$ mT) and amplitude ratio of 1:2:3:2:1 (1:2:1) in the top (bottom) data and simulations, respectively, consistent with the effect of NV hyperfine interactions in the two samples.

ping, unresolved AO-PL contrast peaks due to the increasing number of spin transition degeneracies between different NV orientations. At $B_\perp \approx 1.05$ mT, equivalent to $\theta \approx 40°$ in Fig. 2.8(a), two sets of NV orientations (along $\hat{n}_\lambda$ and $\hat{n}_\chi$; $\hat{n}_\phi$ and $\hat{n}_\kappa$) are near-degenerate. In this parameter regime, the NV hyperfine interaction provides additional depolarization channels and splits the NV-NV cross-relaxation resonances, with associated AO-PL contrast features. In particular, the number of AO-PL contrast peaks varies between the two samples. The ^{14}N spectrum in Fig. 2.8(b, top) shows five peaks with

a separation $\Delta B_{14N} \approx 0.09\,\text{mT}$ between neighboring peaks. The ratio of individual peak amplitudes follows 1:2:3:2:1, as expected for the ^{14}N nuclear spin quantum number $I = 1$. Similarly, the ^{15}N spectrum in Fig. 2.8(b, bottom) displays three peaks with $\Delta B_{15N} \approx 0.13\,\text{mT}$, and a ratio of individual peak amplitude given by 1:2:1, consistent with $I = 1/2$ for ^{15}N. The magnetic field separation between neighboring peaks can be calculated from the nitrogen nuclear hyperfine splitting A_N and the projection angles of the NVs as $\Delta B_N = A_N/[\gamma_e \cos(\alpha)]$, where γ_e is the gyromagnetic ratio of the NV electronic spin and α is the angle between $B_\perp$ and NVs along axis $\hat{n}_\chi$ or $\hat{n}_\kappa$ (see Sec. 2.5.3).

These experimental results are in good agreement with calculations using the same model from Sec. 2.3.1 (dashed lines in Fig. 2.8(b)). However, the limited experimental SNR hinders identification and analysis of AO-PL features with modest contrast (e.g., near $B_\perp \approx 0.5\,\text{mT}$). To address this issue, we perform lock-in measurements of AO-PL from the ^{15}N sample (S2-15N), with its simpler hyperfine structure, by amplitude modulating $B_\perp$. Fig. 2.9(a) shows the normalized in-phase output (X) of the LIA as a function of $B_\perp$, for fixed $B_\parallel = 1.24\,\text{mT}$. This LIA measurement is effectively a higher SNR derivative of the AO-PL signal of Fig. 2.8(b, bottom). We highlight two regions of the LIA results that resolve distinct dispersive AO-PL features from NV-NV cross-relaxation: small "shoulders" for $B_\perp$ near 0.46 mT and 0.6 mT in the wings of a prominent feature at $B_\perp \approx 0.53\,\text{mT}$ [Fig. 2.9(b, left)]; and a triplet feature split by $\Delta B_{15N} \approx 0.13\,\text{mT}$ around $B_\perp \approx 1.05\,\text{mT}$ [Fig. 2.9(b, right)], matching well the results in Fig. 2.8(b).

To further characterize the effects of NV-NV cross-relaxation and the NV hyperfine interaction on PL features, we perform microwave-based CW-ODMR measurements on sample S2-15N as a function of $B_\perp$ and for fixed $B_\parallel = 1.24\,\text{mT}$, with results sum-

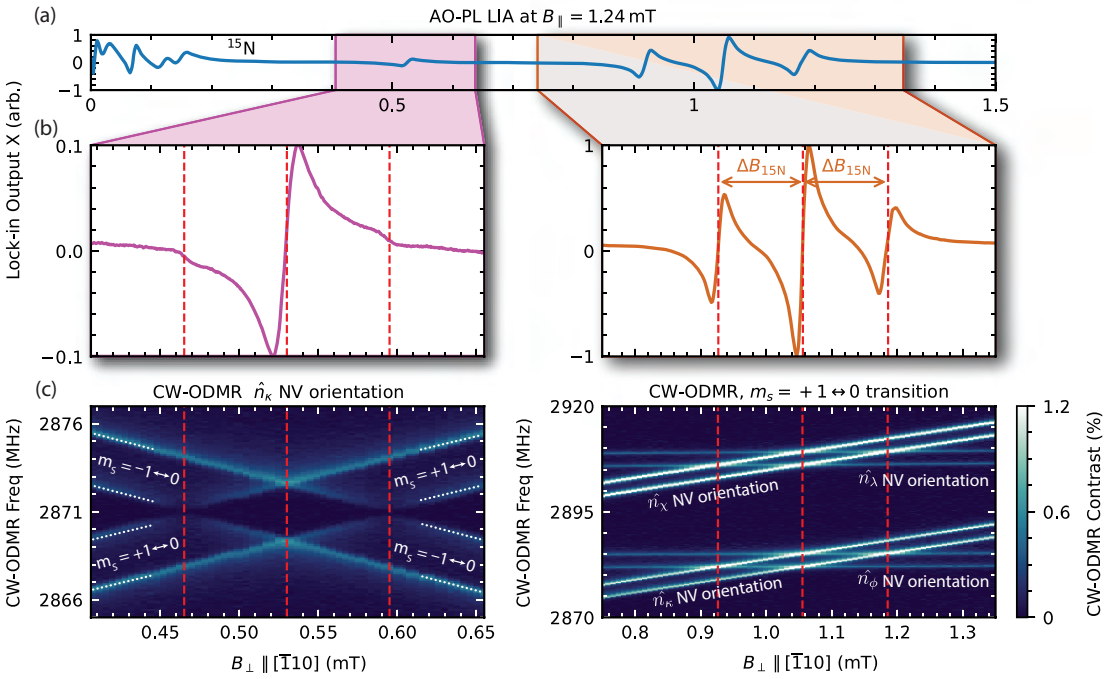


Figure 2.9: (a) Normalized AO-PL LIA measurements as a function of $B_\perp$ from ^{15}N-enriched sample S2-15N at fixed $B_\parallel = 1.24$ mT. Focus is on LIA features around 0.5 mT (purple) and 1 mT (orange). (b) AO-PL LIA signals with a smaller $B_\perp$ step size ($\approx$ 0.002 mT) from shaded areas in (a). Two weak features are observed in the shoulder of the dispersive signal with central zero crossing at about 0.53 mT (left). Near 1 mT, three dispersive features are measured with splitting $\Delta B_{15N} \approx 0.13$ mT (right). For both (left) and (right), vertical dashed lines indicate near-degeneracy of hyperfine transitions. (c) Summary of measurements of microwave-based CW-ODMR NV spin transition frequencies as a function of $B_\perp$, including different NV orientations and hyperfine splitting, for the same sample (S2-15N) and at fixed $B_\parallel = 1.24$ mT. Between $B_\perp \approx 0.4$ mT and 0.65 mT (left), NVs along orientation $\hat{n}_\kappa$ experience near-zero total applied magnetic field, leading to multiple avoided crossings between the hyperfine-split $|m_s = +1 \leftrightarrow 0\rangle$ and $|m_s = -1 \leftrightarrow 0\rangle$ spin transitions. Between $B_\perp \approx 0.8$ mT and 1.3 mT (right), results are shown for all NV orientations, including only hyperfine-split $|m_s = +1 \leftrightarrow 0\rangle$ transitions for better clarity. (Consistent CW-ODMR results are found for $|m_s = -1 \leftrightarrow 0\rangle$ transitions.) Two groups of NV spin resonances are observed, each of which consists of two different NV orientations (along $\hat{n}_\lambda$ and $\hat{n}_\chi$; $\hat{n}_\phi$ and $\hat{n}_\kappa$). Within each spin resonance group, a single hyperfine resonance overlaps at both $B_\perp \approx 0.93$ mT and 1.19 mT; whereas two hyperfine resonances overlap at $B_\perp \approx 1.05$ mT. $B_\perp$ values for near-degenerate spin transition frequencies align well with those of zero crossings in the AO-PL LIA signals in (b), indicated by vertical dashed lines.

marized in Fig. 2.9(c). These microwave-based measurements extract the spin transition frequencies for all NV orientations and determine the values of $B_\perp$ where these spin tran-

sitions become nearly degenerate. In addition, CW-ODMR measurements clearly resolve small (few MHz) splittings from NV hyperfine interactions. In the range of $B_\perp \approx 0.4$ mT to 0.65 mT, NVs of the same orientation (along $\hat{n}_\kappa$) exhibit several nearly degenerate (avoided crossing) spin transitions in the CW-ODMR spectrum [Fig. 2.9(c, left)], which correspond well with observed features in AO-PL LIA measurements [Fig. 2.9(b, left)]. For $B_\perp \approx 1.05$ mT, CW-ODMR measurements show near-degeneracies in both hyperfine resonances from two sets of NV orientations (along $\hat{n}_\lambda$ and $\hat{n}_\chi$, or $\hat{n}_\phi$ and $\hat{n}_\kappa$); whereas for the two nearby shoulder features (at $B_\perp \approx 0.92$ mT and 1.18 mT), only one hyperfine resonance has a near-degeneracy for each set of NV orientations [Fig. 2.9(c, right)]. These CW-ODMR spectroscopic measurements are consistent with the $B_\perp$ values and amplitude ratios for the observed AO-PL LIA features, see dashed vertical lines in Fig. 2.9; and also with the ratio of AO-PL contrast peak amplitudes for sample S2-15N shown in Fig. 2.8(b, lower right). Comparing to the AO-PL LIA measurements for $B_\perp \approx 0.4$ mT and 0.65 mT, the increased number of NVs with near-degenerate spin transitions at $B_\perp \approx$ 0.92 mT, 1.05 mT, and 1.18 mT contributes to the larger AO-PL LIA output amplitudes at the larger $B_\perp$ values [Fig. 2.9(a)].

2.3.4 AO Sensitivity Characterization

In this section, we detail the characterization of DC magnetic field sensitivity from our experimental setup using AO-PL LIA measurements. The PL signal collected by the photodiode is demodulated using a LIA with a sensitivity of 1 mV, a modulation frequency of 100 Hz, and a modulation depth $\approx 10\,\mu$T (see Sec. 2.2.5 for calibration).

The LIA time constant (τ) is set to 300 ms, with a filter order of 24 dB per octave. Fig. 2.10 presents the demodulated AO-PL LIA spectrum around $B_\perp \approx 1.05$ mT with

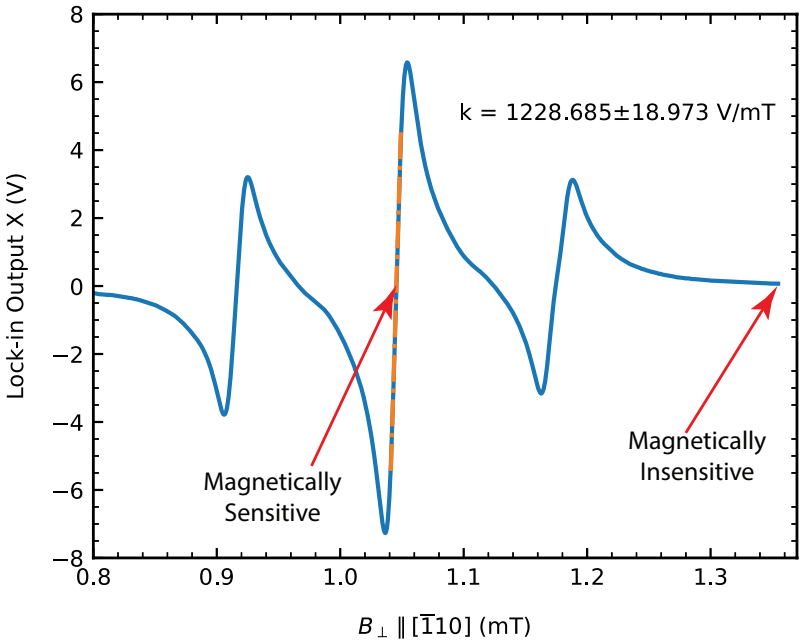


Figure 2.10: Demodulated AO-PL LIA spectrum for sample S2-15N around $B_\perp \approx 1.05$ mT with fixed $B_\parallel$ =1.24 mT. A linear fit is applied around the zero-crossing point to convert the LIA output voltage to the magnetic field strength along the $[\bar{1}10]$ direction. The sensitivity for magnetically sensitive (insensitive) regions of the spectrum is calculated using the standard deviation σ from nine LIA output voltage measurements at $B_\perp \approx 1.05$ mT ($B_\perp \approx 1.35$ mT), respectively.

fixed $B_\parallel$ =1.24 mT using sample S2-15N, averaged over nine measurements. The linear slope $k = 1228.685 \pm 18.973$ V/mT, extracted from the zero-crossing point of the central dispersive feature, relates the LIA output voltage to the magnetic field strength along the $[\bar{1}10]$ direction. The DC magnetic field sensitivity is calculated using the formula $\frac{1}{k}\sigma\sqrt{\tau}$, where σ is the standard deviation of the nine AO-PL LIA voltage measurements at a specific magnetic field region of the spectrum, with results for magnetically sensitive (insensitive) regions (see Fig. 2.10): 37.8 ± 0.6 (5.3 ± 0.1) $\mathrm{nT}/\sqrt{\mathrm{Hz}}$, at $B_\perp \approx 1.05$ mT ($B_\perp \approx 1.35$ mT), respectively.

2.3.5 Dependence of AO-PL Contrast on Laser Power

We next characterize AO-PL contrast as a function of laser power for two ^{14}N samples at fixed $B_{\parallel} = 1.24\,\text{mT}$ and $B_{\perp} = 1.05\,\text{mT}$, i.e., near the maximum contrast from the quintet of hyperfine peaks, as in Fig. 2.8(b, top). The reference AO-PL contrast is measured at $B_{\perp} = 0.73\,\text{mT}$ where all NV orientation classes are spectrally separated. The two samples are from the same growth process, with identical nitrogen concentration ([N] $\approx 16\,\text{ppm}$) but different electron irradiation doses, which allows varying NV concentration while keeping other material properties and experimental conditions (laser spot size, etc.) constant: sample S3-14N ([NV] $\approx 3.8\,\text{ppm}$) and sample S4-14N ([NV] $\approx 2\,\text{ppm}$), see Table 2.1.

Fig. 2.11 shows the measured change of AO-PL contrast for each sample, with laser power varied from 0.1 mW to 50 mW, in reasonable agreement with numerical results from a rate-equation model. In this model, we include relaxation between $|m_s = \pm 1\rangle$ and $|m_s = 0\rangle$ spin sublevels in both the electronic ground and excited states. Details of the rate-equation model, supporting measurements are given in Sec. 2.4.3.

For both samples, the observed AO-PL contrast initially increases with laser power, reaches a maximum value, and then decreases at higher power. We attribute the initial increase of AO-PL contrast to improved spin polarization from optical pumping, consistent with the low-field AO-PL measurements from Ref. [30]. At higher laser power, optical pumping polarizes NV centers to the $|m_s = 0\rangle$ state at a rate faster than relaxation between the bright $|m_s = 0\rangle$ and dark $|m_s = \pm 1\rangle$ states, decreasing AO-PL contrast. Including the decay rates between spin sublevels to be both NV-concentration and spin-

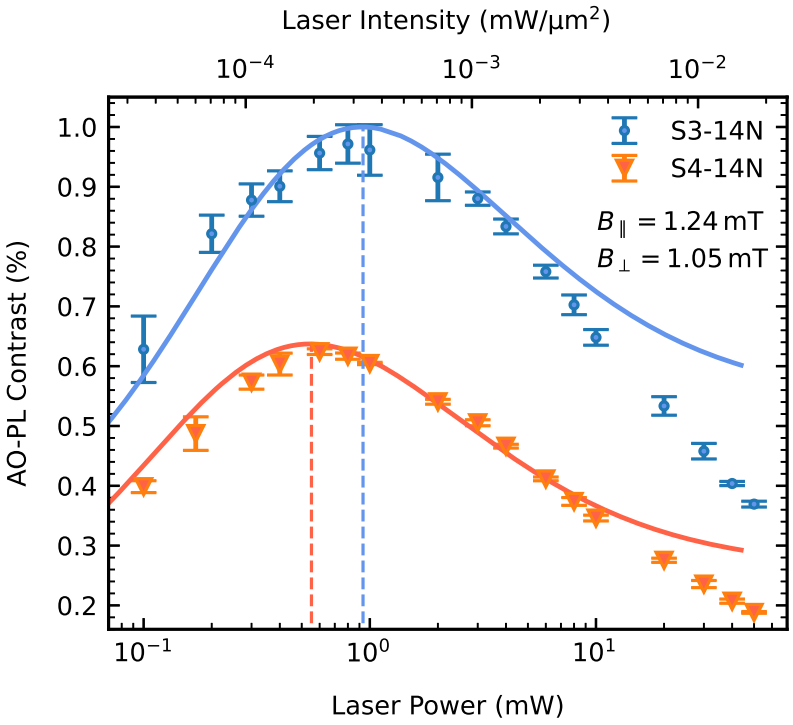


Figure 2.11: AO-PL contrast at $B_{\parallel} = 1.24\,\mathrm{mT}$ and $B_{\perp} = 1.05\,\mathrm{mT}$ as a function of laser power and intensity for samples S3-14N ([NV] $\approx 3.8\,$ppm) and S4-14N ([NV] $\approx 2\,$ppm). The laser intensity is calculated by approximating a Gaussian excitation laser beam profile of radius $\approx 30\,\mu m$. Markers indicate values determined from experimental measurements, with the standard deviation given by error bars; solid lines are from a rate-equation model with NV-concentration and spin-resonance-dependent relaxation rates between spin sublevels. For both samples, the contrast exhibits a maximum determined by the trade-off between optical pumping and spin relaxation. Sample S3-14N has higher overall AO-PL contrast, for all laser powers, because of its larger [NV] and hence stronger NV-NV dipolar interactions and cross-relaxation features.

resonance-dependent [22, 23], our rate-equation model reproduces the experimentally observed shift of maximum AO-PL contrast to higher laser power for sample S3-14N, with its larger [NV] and hence stronger NV-NV dipolar interactions; see solid lines in Fig. 2.11. Note that at high 532 nm laser excitation intensities, NV ionization and charge cycling may occur, decreasing the population of negatively-charged NVs via conversion to the neutral charge state (NV^0), and thereby further reducing AO-PL contrast [31–33].

2.4 Numerical Simulation of AO-PL Response to Magnetic Field and Laser Power

2.4.1 Numerical Simulation Model for AO-PL as a Function of Magnetic Field

To simulate the PL of an ensemble of NV centers with a given NV concentration, we assume that: (1) only spin evolution in the electronic ground state needs to be considered, as the time that the system stays in the electronic excited state is much shorter than the time in the ground state; (2) optical spin polarization defines the initial condition for evolving the ground spin state; (3) evolution of the system is coherent [26]; (4) the total PL is the average of the steady state PL from all possible pairs of interacting NV centers, with each positioned along four possible crystallographic orientations; and (5) the dipolar interaction strength between NVs is fixed by the concentration of the ensemble.

The Hamiltonian that describes the ground state of an isolated NV center H_{gs} is

described by summing Eq. 1.1 and Eq. 1.3:

$$\frac{\hat{H}_{gs}}{\hbar} = \hat{S} \cdot \mathbf{D} \cdot \hat{S} + \hat{S} \cdot \mathbf{A} \cdot \hat{I} + \hat{I} \cdot \mathbf{Q} \cdot \hat{I} + \frac{\mu_B}{h} \vec{B} \cdot \mathbf{g} \cdot \hat{S}. \tag{2.2}$$

Here, **D**, **A**, **Q**, and **g** correspond to the fine structure tensor, hyperfine tensor, nuclear electric quadrupole coupling tensor, and g-factor tensor, respectively. In addition, $\hat{S}$ and $\hat{I}$ correspond to the NV electronic and nuclear spin operators. $\vec{B}$, μ_B, and h are the bias magnetic field applied uniformly to the system, the Bohr magneton constant, and the Planck constant, respectively.

The magnetic dipolar interaction Hamiltonian H_{int} between two NV centers due to the electronic spin operators $\vec{S}_1$ and $\vec{S}_2$ is given by Eq. 2.1. D_{dd} describes the dipolar interaction strength, which depends on the relative separation between two NVs, $\vec{r}$. For an NV ensemble with ∼3.8 ppm [NV], $D_{dd} \sim 35$ kHz and scales as $1/|\vec{r}|^3$. The unit vector between the two NVs is defined as $\hat{n}_{12} = \vec{r}/|\vec{r}|$. For simplicity, we take D_{dd} to be constant for all NV in a given ensemble, as determined by the average NV concentration within the diamond host (assumption (5) above).

Assuming that the bias magnetic field is aligned along the quantization axis of a single NV orientation class, it is then possible to rewrite Eq. 2.2, with all the physical parameters being discussed in Sec. 1.1, as:

$$\begin{aligned} \frac{\hat{H}_{gs}}{\hbar} =& D\left[\hat{S}_z^2 - \hat{S}^2/3\right] \\ &+ \frac{\mu_B g_e}{h}\left(B_x\hat{S}_x + B_y\hat{S}_y + B_z\hat{S}_z\right) \\ &+ A_\parallel \hat{S}_z\hat{I}_z + A_\perp[\hat{S}_x\hat{I}_x + \hat{S}_y\hat{I}_y] + P\left[\hat{I}_z^2 - \hat{I}^2/3\right]. \end{aligned} \tag{2.3}$$

In general, the magnetic dipolar interaction Hamiltonian H_{int} in Eq. 2.1 can be written as,

$$H_{\text{int}} = D_{dd}(A + B + C + D + E + F), \tag{2.4}$$

$$A = S_z^1 S_z^2 \left(1 - 3\cos^2\theta\right), \tag{2.5}$$

$$B = \frac{1}{2}\left(1 - \frac{3}{2}\sin^2\theta\right)\left(S_+^1 S_-^2 + S_-^1 S_+^2\right), \tag{2.6}$$

$$C = -\frac{3}{2}\sin\theta\cos\theta e^{-i\phi}\left(S_z^1 S_+^2 + S_+^1 S_z^2\right), \tag{2.7}$$

$$D = -\frac{3}{2}\sin\theta\cos\theta e^{i\phi}\left(S_z^1 S_-^2 + S_-^1 S_z^2\right), \tag{2.8}$$

$$E = -\frac{3}{4}\sin^2\theta e^{-2i\phi} S_+^1 S_+^2, \tag{2.9}$$

$$F = -\frac{3}{4}\sin^2\theta e^{2i\phi} S_-^1 S_-^2. \tag{2.10}$$

Here, θ and ϕ correspond to the polar and azimuthal angles for $\hat{n}_{12}$, respectively.

In the above expressions, the term A acts as a local static field, while B leads to flip-flop interactions that produce a change of the electronic spin quantum number of each NV to the opposite value, which conserves the overall system electronic spin quantum number. Both of these terms commute with $H_{gs1} + H_{gs2}$, given by Eq. 2.3 for two NVs, since $\Delta m = 0$. For this reason, there terms are known as the secular part of the dipole-dipole interaction. Finally, the full Hamiltonian of two neighboring NV centers in a ensemble is $H = H_{gs1} + H_{gs2} + H_{int}$.

We use the von Neumann equation to simulate the PL emission based on the coherent evolution of ground state spins, which can be described as:

$$\dot{\rho} = -i\left[H, \rho\right]. \tag{2.11}$$

The coupled spin states of the NV electronic spin and nuclear spin for two NVs can be expressed through the following tensor product:

$$\rho_0 = \rho_{s1} \otimes \rho_{s2} \otimes \rho_{I1} \otimes \rho_{I2}. \tag{2.12}$$

Additionally the initial optical spin polarization can be described by:

$$\rho_{s1} = \alpha \begin{bmatrix} 0 & 0 & 0 \\ 0 & 1 & 0 \\ 0 & 0 & 0 \end{bmatrix} + \frac{1}{3}(1-\alpha) \begin{bmatrix} 1 & 0 & 0 \\ 0 & 1 & 0 \\ 0 & 0 & 1 \end{bmatrix}, \tag{2.13}$$

where α corresponds to the degree of polarization of the system to $|m_s = 0\rangle$. We solve this von Neumman equation in the frame of reference of the full Hamiltonian by diagonalizing

the density matrix:

$$\rho_0^{eb} = \hat{V}^{-1}\rho_0\hat{V}. \tag{2.14}$$

Here, $\hat{V}$ is the unitary matrix formed by the normalized eigenvectors of the full ground state spin Hamiltonian.

We calculate the density matrix in the rotating frame via the following equations:

$$[H^{eb}, \rho^{eb}] = 2\pi \left(E_i - E_j\right) \rho_{ij}^{eb}, \tag{2.15}$$

$$\begin{aligned} i\frac{d\rho_{ij}^{eb}}{dt} =& 2\pi \left(E_i - E_j\right) \rho_{ij}^{eb} \rightarrow \rho_{ij}^{eb}(t) \\ =& \rho_{ij}^{eb}(0) \exp\left(-2\pi i \left(E_i - E_j\right) t\right). \end{aligned} \tag{2.16}$$

We then convert the density matrix back into the lab frame of reference as follows:

$$\rho(t) = \hat{V}\rho^{eb}(t)\hat{V}^{-1}. \tag{2.17}$$

Next, we calculate the population in the PL bright $|m_s = 0\rangle$ state by projecting the above density matrix onto the $|m_s = 0\rangle$ spin state as:

$$\rho_{00}(t) = \text{Tr}\left(P_0\rho(t)\right). \tag{2.18}$$

We then calculate the average spin population ρ_{00} in the $|m_s = 0\rangle$ state using the following expressions:

$$\langle \rho_{00} \rangle = \mathrm{Tr}\left(P_0 \frac{1}{\tau} \int_0^\infty \rho(t) \exp\left(-t/\tau\right) dt \right), \tag{2.19}$$

$$\begin{aligned} &\frac{1}{\tau} \int_0^\infty \rho(t) \exp\left(-t/\tau\right) dt \\ =&\frac{1}{\tau} \int_0^\infty \hat{V}^{-1} \rho^{eb}(t) \exp\left(-t/\tau\right) \hat{V} dt, \end{aligned} \tag{2.20}$$

$$\rho_{ij}^{st} = \int_0^\infty \rho^{eb}(t) \exp\left(-t/\tau\right) dt = \frac{\rho_{0,ij}^{eb}}{\left(1 + 2\pi i \left(E_i - E_k\right)\tau\right)}. \tag{2.21}$$

$$\langle \rho_{00} \rangle = \mathrm{Tr}\left(P_0 \hat{V} \rho^{st} \hat{V}^{-1} \right). \tag{2.22}$$

Finally, by using Eqs. (2.21, 2.22) we calculate the AO-PL intensity from two interacting NVs through the full Hamiltonian and a fixed value of the dipolar interaction strength. As each NV can be aligned along four possible crystallographic orientations, we describe the total AO-PL intensity from the NV ensemble by averaging the simulated PL from 16 possible configurations of two interacting NVs. Numerical simulations of low-field AO-PL intensity use fixed values for hyperfine and other relevant parameters taken as equal to the approximate values given earlier in this section, with the exception of the dipolar interaction strength D_{dd}, which is scaled based upon [NV]. The simulated AO-PL contrast is calculated by the normalized difference in simulated intensities $C = 1 - I_{\mathrm{sig}}/I_{\mathrm{ref}}$ between a simulated AO-PL signal I_{sig} and an AO-PL reference I_{ref} determined from the maximal simulated AO-PL intensity for a given scan of $B_{\|}$. This normalization process is similar to the calculation of experimental AO-PL contrast as

described in Sec. 2.2.2.

2.4.2 Hamiltonian Analysis of AO-PL Features

Here we discuss the physical origin of the various AO-PL contrast features at different magnetic fields given by the numerical simulation using the model presented in the previous section.

Taking advantage of the additivity of the von Neumman equation, the model allows us to study the effect of each component of the Hamiltonian by isolating the associated terms. We decompose the simulated AO-PL spectrum to understand the contributions from pairs of NV centers along various crystallographic orientations.

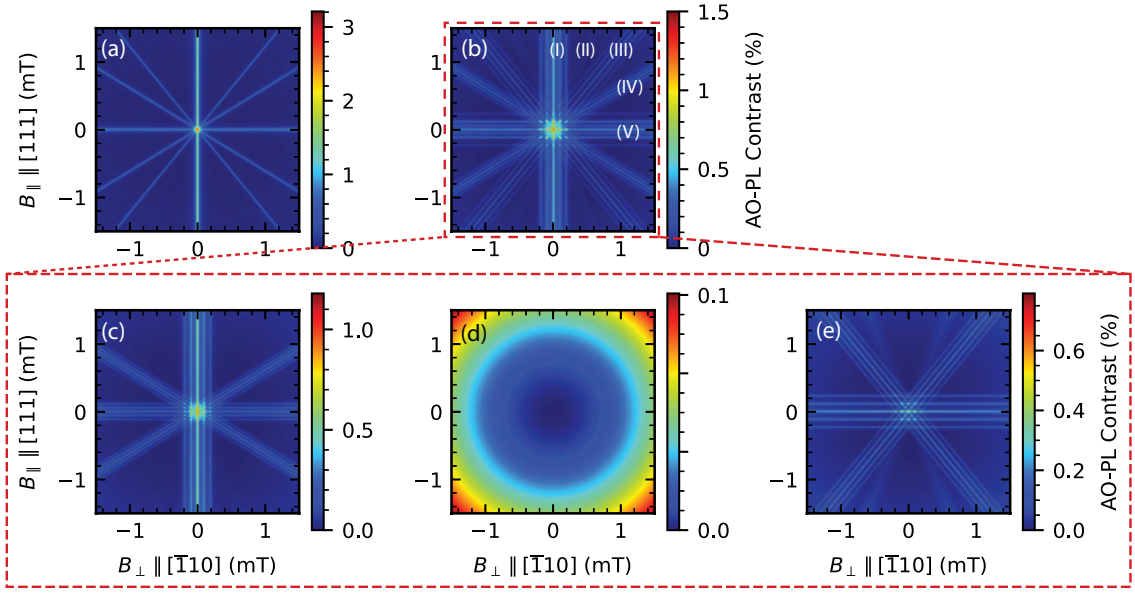


Figure 2.12: Numerical simulation of low-field AO-PL contrast as a function of applied magnetic fields, from: (a) dipole-dipole electronic interactions only (i.e., no hyperfine); (b) full Hamiltonian including hyperfine interactions, with clusters of linear AO-PL contrast features labeled for the first quadrant; (c) only secular terms $H_A + H_B$; (d) only $H_C + H_D$; and (e) only $H_E + H_F$.

Fig. 2.12(b) shows the numerically simulated low-field AO-PL contrast spectrum

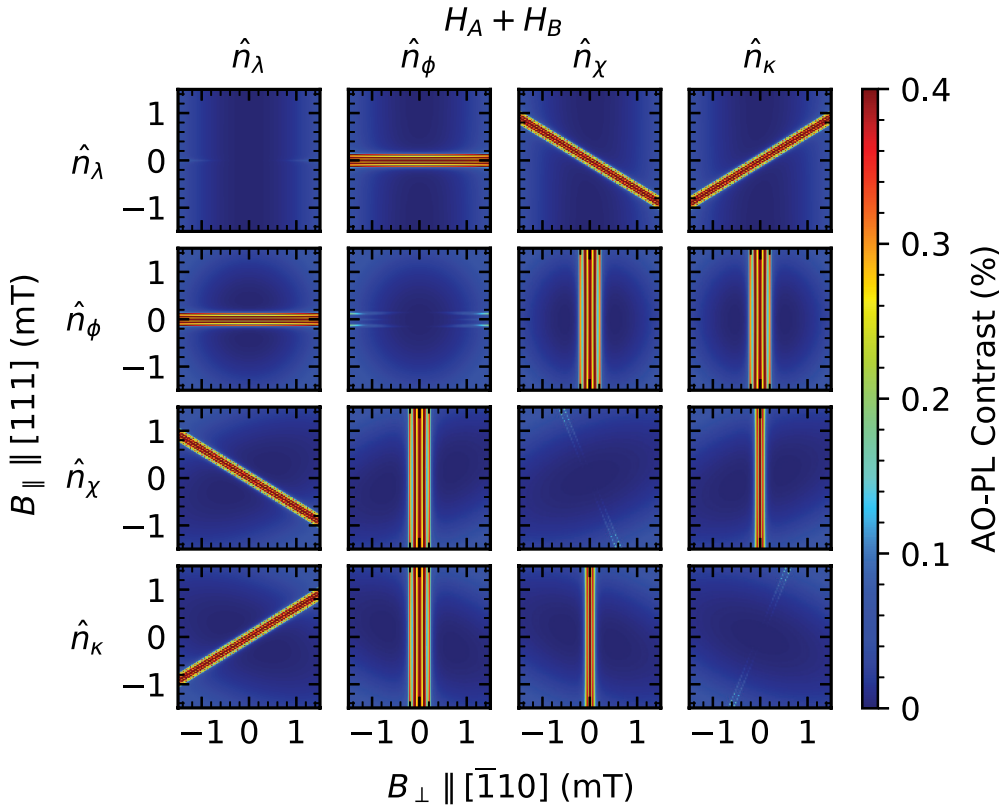


Figure 2.13: Decomposition of simulated AO-PL contrast as a function of applied magnetic fields, for specifically oriented interacting NV center pairs with contributions from the secular terms ($H_A + H_B$). Each panel contains 16 sub-figures, corresponding to decompositions for NV pairs aligned along one of the four possible crystallographic orientations.

for the full Hamiltonian, averaged over all 16 pairs of NV orientations and for values of $B_\parallel$ and $B_\perp$ similar to that used in this study's experiments. The simulation shows different clusters of linear AO-PL contrast features; those in the first quadrant are labeled as (I), (II), (III), (IV) and (V). We start with simulations that remove the hyperfine interaction (i.e., NV electronic interactions only), as shown in Fig. 2.12(a). The number of lines (linear AO-PL contrast features) within each cluster are reduced in this case, while the normalized AO-PL contrast is higher. This result is consistent with the NV hyperfine interaction introducing additional cross-relaxation channels for the NV spin population, including various shoulder AO-PL features as discussed in Sec. 2.3.1.

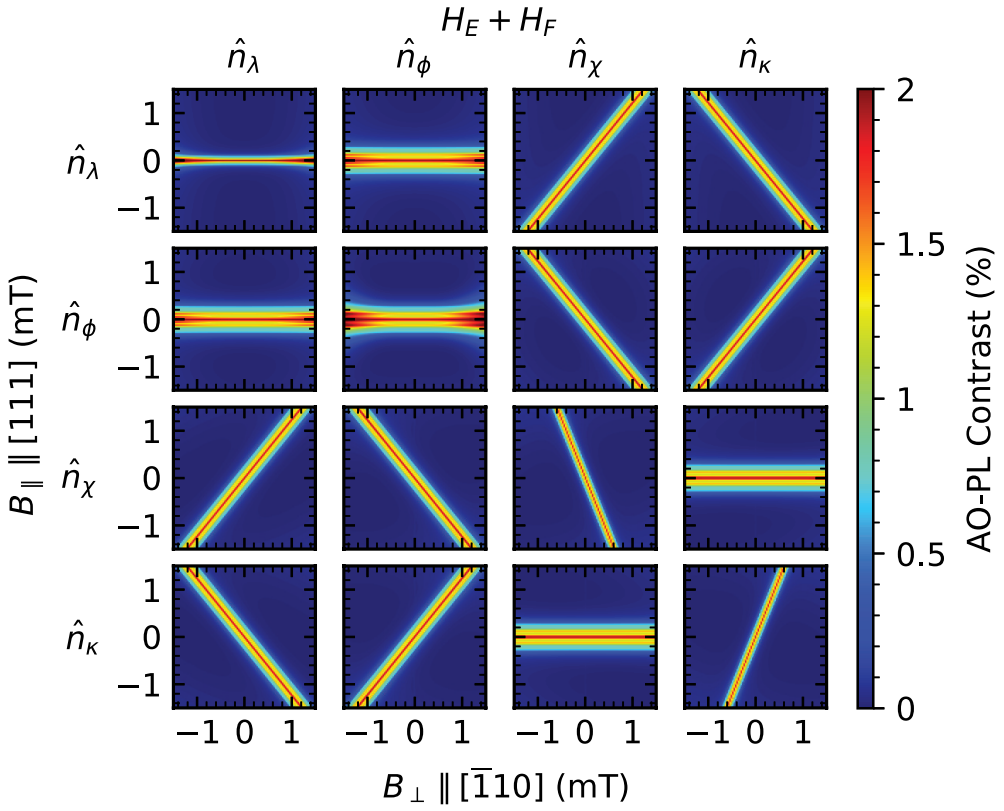


Figure 2.14: Decomposition of simulated AO-PL contrast as a function of applied magnetic fields, for specifically oriented interacting NV center pairs with contributions from non-secular terms ($H_E + H_F$). Each panel contains 16 sub-figures, corresponding to decompositions for NV pairs aligned along one of the four possible crystallographic orientations.

Figs. 2.12(c), (d), and (e) show simulated AO-PL contrast for only $H_A + H_B$, $H_C + H_D$, and $H_E + H_F$ in Eq. 2.4, respectively. When the secular terms $H_A + H_B$ are considered [Fig. 2.12(c)], there are no AO-PL contrast features within cluster (III), and the number of lines in clusters (II) and (V) are reduced. Terms $H_C + H_D$ describe magnetic-field-dependent spin-mixing and associated AO-PL contrast features [Fig. 2.12(d)], with no NV-NV cross-relaxation signals. Terms $H_E + H_F$ describe double spin-flip processes at specific magnetic field angles [Fig. 2.12(e)] that contribute to the remaining AO-PL features.

We next consider the AO-PL contrast features from the perspective of constraints

placed by the interaction Hamiltonian (Eq. 2.4) on m and m', the magnetic moment quantum numbers for the electronic spins of the two interacting NVs in our model system. These quantum numbers are affected by each term of the interaction Hamiltonian (Eqs. 2.5 to 2.10) in the following way:

$$A : \Delta m = 0, \quad \Delta m' = 0, \quad \Delta(m + m') = 0,$$

$$B : \Delta m = \pm 1, \quad \Delta m' = \mp 1, \quad \Delta(m + m') = 0,$$

$$C : \Delta m = \begin{cases} 0, \\ \\ 1, \end{cases} \quad \Delta m' = \begin{cases} 1, \\ \\ 0, \end{cases} \quad \Delta(m + m') = 1,$$

$$D : \Delta m = \begin{cases} 0, \\ \\ -1, \end{cases} \quad \Delta m' = \begin{cases} -1, \\ \\ 0, \end{cases} \quad \Delta(m + m') = -1,$$

$$E : \Delta m = 1, \quad \Delta m' = 1, \quad \Delta(m + m') = 2,$$

$$F : \Delta m = -1, \quad \Delta m' = -1, \quad \Delta(m + m') = -2.$$

Term A has the same form as two classical interacting dipoles and describes the effect of a static local field. Term B allows for a simultaneous flip of two neighboring NV electronic spins in opposite directions while keeping the total electronic spin quantum number of the system (S1 + S2) unchanged; this 'flip-flop' term corresponds to the resonance effect of the local field from the NV-NV dipolar interaction.

The contributions of terms C and D make the energies of the two NVs not degenerate, and hence do not introduce any NV-NV spin cross-relaxation and associated AO-PL contrast.

Finally, terms E and F describe a simultaneous electronic spin flip from both NVs. This 'double spin-flip' process is the origin of cluster (III) in Fig. 2.12(b) and contributes to additional shoulder features in clusters in (V) and (II).

Further decomposition of the contributions from specific interaction terms can be performed by considering pairs of interacting NV classes separately, providing a clearer understanding of the nature of each AO-PL contrast feature, as shown in Fig. 2.13 and Fig. 2.14. For instance, this analysis indicates that vertical cross-relaxation lines (I) in Fig. 2.12(b) arise from flip-flop interactions driven by off-axis ($\hat{n}_\phi, \hat{n}_\kappa, \hat{n}_\chi$) NV pairs belonging to different NV classes. Horizontal lines (V) in Fig. 2.12(b) result from contributions of both flip-flop and double spin-flip interactions, involving same- and different-class NV pairs from $\hat{n}_\lambda$ and $\hat{n}_\phi$. Additionally, a double spin-flip interaction occurs between an NV pair where one center belongs to the $\hat{n}_\chi$ class and the other to the $\hat{n}_\kappa$ class. This suggests that certain peaks along these cross-relaxation lines are specifically linked to flip-flop, double spin-flip, or a combination of both interactions.

On the other hand, examination of Fig. 2.13 and Fig. 2.14 indicates that cross-relaxation lines (II) in Fig. 2.12(b) originate from flip-flop and double spin-flip contributions within the same NV class, specifically from $\hat{n}_\kappa$ and $\hat{n}_\chi$. Lines (IV) in Fig. 2.12(b) appear when on-axis NVs $\hat{n}_\lambda$ interact with off-axis NVs in the n_χ and n_κ directions via flip-flop interactions. Finally, lines (III) in Fig. 2.12(b) are due to the double spin-flip terms, arising from pairs of interacting NV centers oriented along $\hat{n}_\lambda$ and $\hat{n}_\chi$; $\hat{n}_\phi$ and $\hat{n}_\kappa$.

The insight that some AO-PL contrast features are predominantly governed by either flip-flop or double spin-flip transitions opens opportunities to further explore the underlying physics, e.g., the effect of applied electric fields, which have been shown to

enhance double spin-flip transition rates in previous studies [34]. Additionally, the ability to isolate different NV-class contributions in the AO-PL feature map can be further leveraged in combination with techniques such as Fourier imaging [35, 36], enabling targeted analysis of specific NV classes.

2.4.3 Modeling AO-PL Contrast Changes from Optical Pumping and Resonant NV-NV Interaction

Sec. 2.4.1 describes the use of a density matrix approach to calculating the AO-PL contrast from an NV ensemble, with two NV centers at fixed dipolar interaction strength that are then averaged over all possible pairs of crystallographic orientations. This method provides reasonable agreement with low-field AO-PL experimental results [Figs. 2.6(b, c), 2.7]. However, the model only considers the initial spin polarization without accounting for details of the optical pumping process. To understand the dependence on laser power of the maximum AO-PL contrast from the quintet peaks, as discussed in Sec. 2.3.5, we now describe an alternative numerical model using rate equations for a single NV in one of the four orientations in the diamond host. We find results from this rate-equation model are in reasonable agreement with measurements, including AO-PL contrast line features as a function of applied magnetic field and AO-PL contrast as a function of laser power.

For the diamond samples in the present study, the average nearest-neighbor NV-NV dipole interaction $\sim$30 kHz, which is much smaller than the energy separation between NVs of different orientations when their electronic spin transitions (with typical linewidth $\sim$1 MHz) are spectrally separated. Therefore, we first proceed by diagonaliz-

ing the ground state Hamiltonian described in Eq. 2.2 without adding the dipole-dipole interaction terms (Eq. 2.1), and then calculate the steady-state AO-PL by solving the resulting rate equations. The total AO-PL is determined by summing over all possible NV orientations, similar to the procedure described in Sec. 2.4.1. In the presence of near-degenerate transition frequencies, e.g., induced for particular on ($B_{\parallel}$) and off ($B_{\perp}$) axis bias magnetic fields or by hyperfine interactions, the decay rates between various spin states increase. Results to support this reduction in spin polarization lifetime (T_1) are discussed in Sec. 2.5.1.

We simplify a 5-level spin population model [1, 37] of a single NV — which includes ground and excited electronic states, as well as a single metastable state representing the singlet state manifold, as shown in Fig. 1.1(b) — to a 4-level system by integrating out the intersystem crossing singlet state, as diagrammed in Fig. 2.15(a). Given that we perform steady-state operations in the experiment, and the singlet state is a short-lived intermediate state with a lifetime ≈ 300 ns, we model the transitions through this state via an effective radiative decay from electronic excited states to the ground states.

In addition, we introduce relaxation rates between the $|\pm 1\rangle$ and $|0\rangle$ spin sublevels in both the electronic ground (Γ) and excited states (D). Therefore, the model 4-level system can be described with the following rate equations:

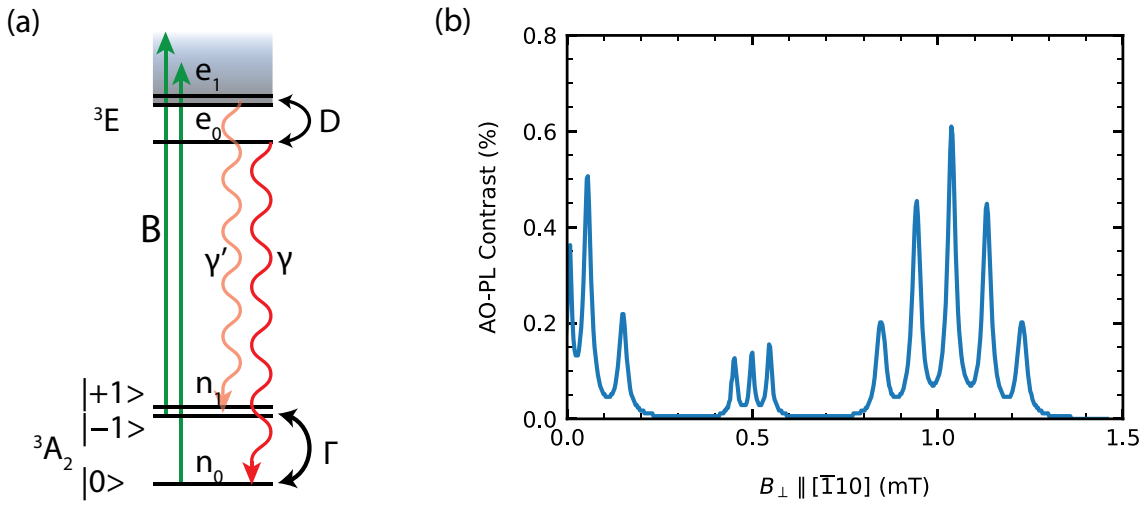


Figure 2.15: (a) Simplified 4-level system used in the rate-equation model by integrating out the intersystem crossing singlet state manifold shown in Fig. 1.1(b). Relaxation rates are included between ground (Γ) and excited (D) spin sublevels. (b) Simulated AO-PL contrast as a function of $B_\perp$ at fixed $B_\parallel = 1.24\,\text{mT}$ using the 4-level population model provides comparable results to the density matrix method described in Sec. 2.4.1.

$$
\begin{aligned}
\partial_t e_0 &= B(n_0 - e_0) - \gamma e_0 + D(\beta' e_1 - (1-\beta')e_0), \\
\partial_t e_1 &= B(n_1 - e_1) - \gamma' e_1 - D(\beta' e_1 - (1-\beta')e_0), \\
\partial_t n_0 &= -B(n_0 - e_0) + \gamma_a e_0 + \gamma_b e_1 \\
&\quad + \Gamma(\beta n_1 - (1-\beta)n_0), \\
\partial_t n_1 &= -B(n_1 - e_1) + \gamma'_a e_1 + \gamma'_b e_0 \\
&\quad - \Gamma(\beta n_1 - (1-\beta)n_0).
\end{aligned}
\tag{2.23}
$$

Here, $n_{0,1}$ ($e_{0,1}$) refer to the population in the electronic $|0\rangle$ and $|\pm1\rangle$ ground states (excited states, respectively). The parameter B is proportional to the optical pumping intensity. $\beta' = \beta = \frac{1}{3}$ sets the equilibrium population distribution across the $|0\rangle$ and $|\pm1\rangle$ states without optical excitation. $\gamma + \gamma' = \gamma_a + \gamma_b + \gamma'_a + \gamma'_b$ are the net excited state decay rates into the ground states that arise from integrating out the singlet state,

where γ (γ') is the effective decay rate from the excited $|0\rangle$ (respectively $|\pm1\rangle$) states; γ_a and γ_b (γ'_a and γ'_b) are the decay rates towards the ground $|0\rangle$ (respectively ground $|\pm1\rangle$) states. We follow the summary of experimental NV results given in Ref. [1] and use the approximate expressions $\gamma = s + s'/7$, $\gamma' = s + s'$, where s is the direct radiative decay rate from the excited state manifold and s' is the decay rate from the excited state to the singlet state, with $s = s'$ = $6.7 \times 10^7 s^{-1}$. Integrating out the singlet intermediate state yields $\gamma_a = s + 2s'/21$, $\gamma_b = 2s'/3$, $\gamma'_a = s + s'/3$ and $\gamma'_b = s'/21$. The AO-PL intensity is finally calculated as being proportional to the excited state populations in each electronic spin state. An example of simulated AO-PL contrast as a function of $B_\perp$ at fixed $B_\parallel = 1.24\,\mathrm{mT}$ is shown in Fig. 2.15(b).

Ref. [22] indicates that the NV spin depolarization rate increases when sub-ensemble spin transitions become degenerate, and samples with larger [NV] have shorter NV ground state spin polarization lifetime T_1. Thus, we associate the ground state spin relaxation rate Γ and the excited state spin relaxation rate D introduced in the 4-level model [Fig. 2.15(a)] to depend on both spin transition degeneracy and NV concentration. Spin transition degeneracy can lead to maximal state mixing between different NV classes, with enhanced NV-NV cross-relaxation and hence reduction in AO-PL. We model Γ to include a term that is proportional to [NV]^2, as expected from Fermi's golden rule and associated squaring of the matrix element for the dipolar interaction strength (see Eq. 2.1 and also [22]). The resulting ground state spin relaxation rate Γ is parameterized as:

$$\Gamma = \Gamma_0 + \kappa[NV]^2(1 + d). \tag{2.24}$$

Here Γ_0 is the single NV ground state spin relaxation rate, κ is a parameter calibrated by comparing simulation with experiment, and d is a scaled dipolar interaction strength characterizing NV-NV cross-relaxation. We use an analogous expression for D, the excited state spin relaxation rate.

Sec. 2.5.1 describes the procedures to experimentally extract the ground state T_1 lifetime at different magnetic field configurations. The coefficient $\Gamma|_{d=0}$ is given by the inverse of this measured T_1 lifetime when there are no spin state degeneracies. κ and d are indirectly determined from the measured ground state T_1 lifetime as a function of magnetic field configuration ($B_\parallel$ and $B_\perp$). For example, for sample S3-14N (≈ 3.8 ppm [NV]) we measure the ground state spin relaxation rate (Γ) $\approx 0.21 \pm 0.005\,\mathrm{ms}^{-1}$ at magnetic field configurations where NV-NV cross-relaxation occurs (i.e., at linear AO-PL contrast features). When all NV ground state spin resonances are spectrally well-separated, we measure the spin relaxation rate ($\Gamma|_{d=0}$) $\approx 0.18 \pm 0.005\,\mathrm{ms}^{-1}$. By incorporating a Gaussian excitation laser beam profile of radius 33 μm, we then determine the associated parameters for D, the excited state spin relaxation rate, by numerical fit of the 4-level model to the measured AO-PL contrast as a function of laser power for this sample, as shown by the blue solid line in Fig. 2.11.

Taking these results and scaling [NV] down by a factor of $1.35\times$, we find the simulated AO-PL contrast as a function of laser power to be in reasonable agreement with the measured results from sample S4-14N (≈ 2 ppm [NV], orange solid line in Fig. 2.11). This scaling factor is roughly consistent with the $\sim 2\times$ [NV] ratio between sample S3-14N and S4-14N inferred from the variations of irradiation dose during electron implantation [31].

Table 2.2 summarizes the measured and inferred relaxation rates between ground state sublevels Γ and excited state sublevels D used to generate the model-based curves for samples S3-14N and S4-14N shown in Fig. 2.11. Γ and D apply to magnetic field configurations where AO-PL contrast features are maximally degenerate; $\Gamma|_{d=0}$ and $D|_{d=0}$ refers to configurations where all electronic spin states are spectrally well-separated.

Table 2.2: Relaxation rates between NV spin sublevels, both with (Γ and D) and without ($\Gamma|_{d=0}$ and $D|_{d=0}$) spin-state degeneracies, as used in the 4-level rate equation simulation model. Values with * are determined experimentally. Other values are inferred from measurements as described in Sec. 2.4.3.

Sample #	Γ **(ms^{-1})**	$\Gamma\|_{d=0}$ **(ms^{-1})**	D **(ms^{-1})**	$D\|_{d=0}$ **(ms^{-1})**
S3-14N	0.21 ± 0.005*	0.18 ± 0.005*	249	7.1
S4-14N	0.13	0.12	119	2.1

We associate the observed initial increase of AO-PL contrast at laser power < 1 mW (Fig. 2.11) to improved NV electronic spin polarization from optical pumping; and attribute the subsequent decrease of contrast at higher laser powers to competition between increased net optical pumping and depolarization from NV-NV cross-relaxation. By taking Γ and D to be both [NV] and spectral degeneracy dependent, our model reproduces the experimentally observed behavior that the maximum AO-PL contrast for sample S3-14N with larger [NV] occurs at a higher laser power (≈ 0.95 mW) than for sample S4-14N (≈ 0.55 mW). Further study will be necessary to fully delineate the physical processes most relevant for the observed AO-PL contrast behavior.

2.5 Characterization of AO-PL Contrast Feature Lineshapes

2.5.1 Polarization Lifetime (T_1) Measurements

Fig. 2.16(a) shows the experimental sequence employed to measure the NV ground state spin polarization lifetime (T_1) of sample S3-14N as a basis for the 4-level population model described in Sec. 2.4.3. NV electronic spins are first optically polarized by an initial laser pulse to (mostly) ground spin state $|0\rangle$; and are then optically read out after a variable dark time τ. In the second half of the sequence, as a reference measurement, a MW π pulse (orange) prepares the NV electronic spin to $|+1\rangle$ or $|-1\rangle$. By dividing the two results, the NV spin polarization $P(t)$ can be expressed as $P(t) = e^{-t/T_1}$.

Fig. 2.16(b) presents an example CW-ODMR measurement where all NV orientation classes are spectrally well-separated (with $B_{\parallel} \approx 2.4\,\text{mT}$ and $B_{\perp} \approx 1.1\,\text{mT}$). Employing the measurement sequence in Fig. 2.16(a), a fit of P(t) to the peak amplitude of the leftmost ODMR resonance feature as a function of τ yields $T_1 = 5.46 \pm 0.05\,\text{ms}$ [Fig. 2.16(c)]. We repeat these measurements and fitting procedure for the peak amplitudes of all ODMR resonances in Fig. 2.16(b); and then average the fit T_1 values for all resonances and obtain $\overline{T_1} = 5.51 \pm 0.15\,\text{ms}$, equivalent to an NV spin relaxation rate with no spin-state degeneracies $\Gamma|_{d=0} = 0.18 \pm 0.005\,\text{ms}^{-1}$.

Next, we change the bias magnetic field so that the pair of NVs along $\hat{n}_\lambda$ and $\hat{n}_\chi$ and the pair of NVs along $\hat{n}_\phi$ and $\hat{n}_\kappa$ have degenerate spin resonances, with $B_{\parallel} = 1.24\,\text{mT}$ and $B_{\perp} \approx 1.05\,\text{mT}$. An example CW-ODMR measurement for this bias field configuration is shown in Fig. 2.16(d). Again employing the measurement sequence in Fig. 2.16(a), we

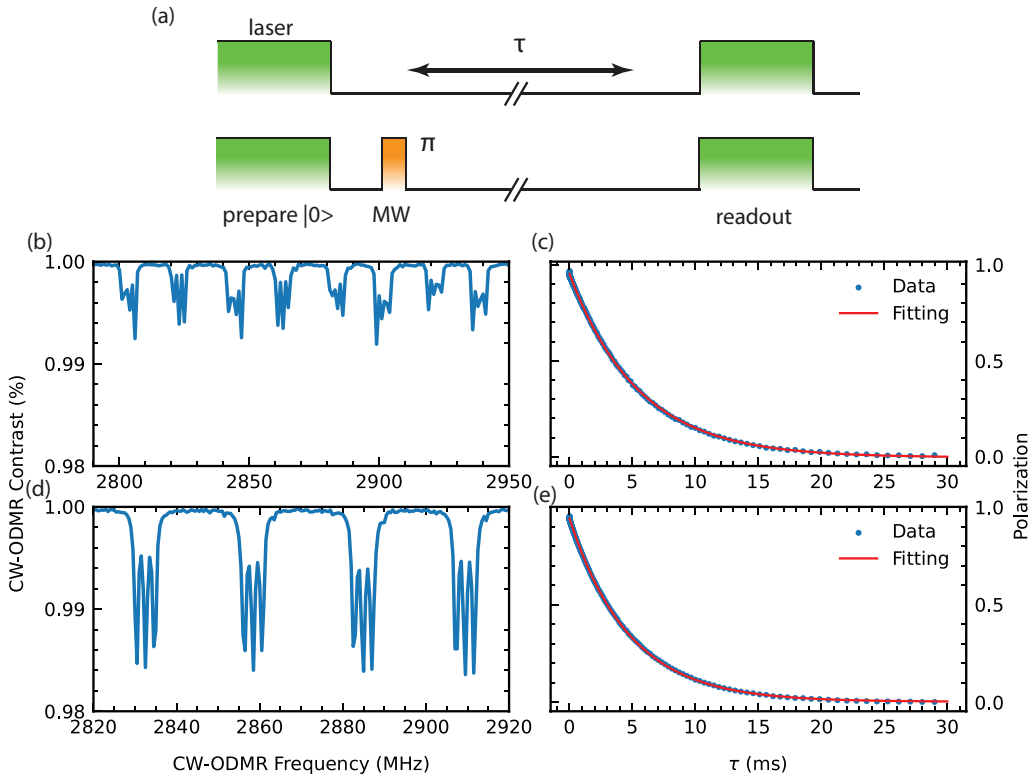


Figure 2.16: Measurement of sample S3-14N polarization lifetime (T_1) under different magnetic field configurations. (a) Experimental sequence used to measure T_1. (b) CW-ODMR measurement with spectrally well-separated spin resonances for all NV orientations ($B_{\parallel} \approx 2.4\,\text{mT}$ and $B_{\perp} \approx 1.1\,\text{mT}$). (c) Measured peak amplitude of leftmost ODMR resonance in (b) as a function of delay time τ shown in experimental sequence in (a). Fit of decay yields $T_1 = 5.46 \pm 0.05\,\text{ms}$. T_1 measurements and fits are repeated for all ODMR resonances in (b), giving averaged $\overline{T_1} = 5.51 \pm 0.15\,\text{ms}$. (d) CW-ODMR measurement with degenerate spin resonance for NV orientations $\hat{n}_\lambda$ and $\hat{n}_\chi$; $\hat{n}_\phi$ and $\hat{n}_\kappa$. (e) Measured peak amplitude of leftmost ODMR resonance in (d) as a function of τ; fit yields $T_1 = 4.72 \pm 0.04\,\text{ms}$. T_1 measurements and fits are repeated for all ODMR resonances (d), giving averaged $\overline{T_1} = 4.74 \pm 0.1\,\text{ms}$.

find $\overline{T_1} = 4.74 \pm 0.1\,\text{ms}$ [Fig. 2.16(e)], equivalent to an NV spin relaxation rate with spin-state degeneracies $\Gamma = 0.21 \pm 0.005\,\text{ms}^{-1}$.

2.5.2 AO-PL Linewidth as a Function of Laser Power

As described in Sec. 2.3.3, the ratio of individual AO-PL contrast peak amplitudes using a ^{14}N-enriched sample can be described as 1:2:3:2:1, at $B_{\parallel} = 1.24\,\text{mT}$ and $B_{\perp} \approx$

1.05 mT [Fig. 2.8(b, top)]. We model the observed quintet of peaks as a function of $B_\perp$ using the following multi-Lorentzian function $L(x)$:

$$\begin{aligned} L(x) =& \frac{A_1}{\left[1+\frac{(B_\perp - B_1)}{(\gamma/2)}^2\right]} + \frac{2A_1}{\left[1+\frac{(B_\perp - (B_1+\Delta B))}{(\gamma/2)}^2\right]} \\ &+ \frac{3A_1}{\left[1+\frac{(B_\perp - (B_1+2\Delta B))}{(\gamma/2)}^2\right]} + \frac{2A_1}{\left[1+\frac{(B_\perp - (B_1+3\Delta B))}{(\gamma/2)}^2\right]} \\ &+ \frac{A_1}{\left[1+\frac{(B_\perp - (B_1+4\Delta B))}{(\gamma/2)}^2\right]} + kB_\perp \end{aligned} \tag{2.25}$$

Here, A_1 and B_1 describe the left-most peak's AO-PL contrast and resonance location, respectively. We restrict the fit model by assuming all peaks have the same linewidth γ and separation ΔB. A change of baseline is seen in the experimental data between $B_\perp \approx$ 0.8 and 1.4 mT due to magnetic-field-dependent spin mixing, which we model as a linear shift $kB_\perp$. The fits are done in MATLAB using the nonlinear curve-fitting toolbox with a Levenberg-Marquardt algorithm.

Fig. 2.17 shows the measured AO-PL contrast and the corresponding model fit as a function of $B_\perp$, at fixed $B_\parallel = 1.24$ mT, for sample S3-14N at (a) 2 mW and (b) 50 mW laser excitation power. At the higher laser power, we observe a decrease of AO-PL contrast; also the shift of contrast baseline from spin-mixing becomes more prominent. Note that the fit to experimental data is used to determine the linewidth, peak separation, and linear baseline shift (i.e., γ, ΔB, and k are free fit parameters) from this quintet AO-PL feature. AO-PL contrast at the central peak is calculated from the ratio of a measurement at $B_\perp = 1.05$ mT and a reference measurement at $B_\perp = 0.73$ mT, both at $B_\parallel = 1.24$ mT as described in Sec. 2.3.5.

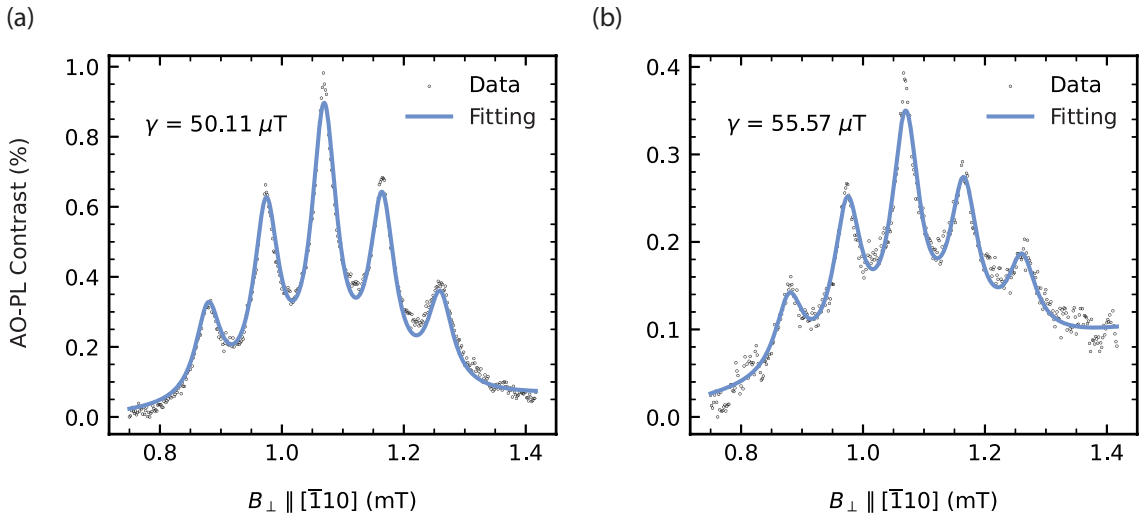


Figure 2.17: Experimentally measured AO-PL contrast as a function of $B_\perp$ and at fixed $B_\parallel = 1.24\,\text{mT}$ (dotted markers) with multi-Lorentzian fits (solid lines) for sample S3-14N at (a) 2 mW and (b) 50 mW laser excitation power. Fit values for the AO-PL contrast peak linewidth γ are shown. A linear shift of baseline due to magnetic-field-dependent spin mixing becomes more prominent at higher laser powers accompanied by a reduction of AO-PL contrast.

Fig. 2.18 shows the AO-PL contrast peak feature linewidth γ, determined from fits of Eq. 2.25 to measurements such as in Fig. 2.17, as a function of laser power using samples S3-14N and S4-14N with varying [NV] (≈ 3.8 ppm and 2 ppm, respectively). Sample S3-14N with higher [NV], and hence stronger NV-NV dipolar interaction, exhibits a roughly 50% greater linewidth than sample S4-14N across all laser powers studied.

Our results of linewidth as a function of laser power deviate from the reported linewidth narrowing with increased laser power using nanodiamonds in Ref. [29].

2.5.3 Contribution of Hyperfine Splitting to Separation of AO-PL Contrast Peaks

To determine the splitting ΔB_{15N} from the measured triple AO-PL contrast peaks using sample S2-15N (see Figs. 2.8 and 2.9), we perform a multi-Lorentzian fit to the

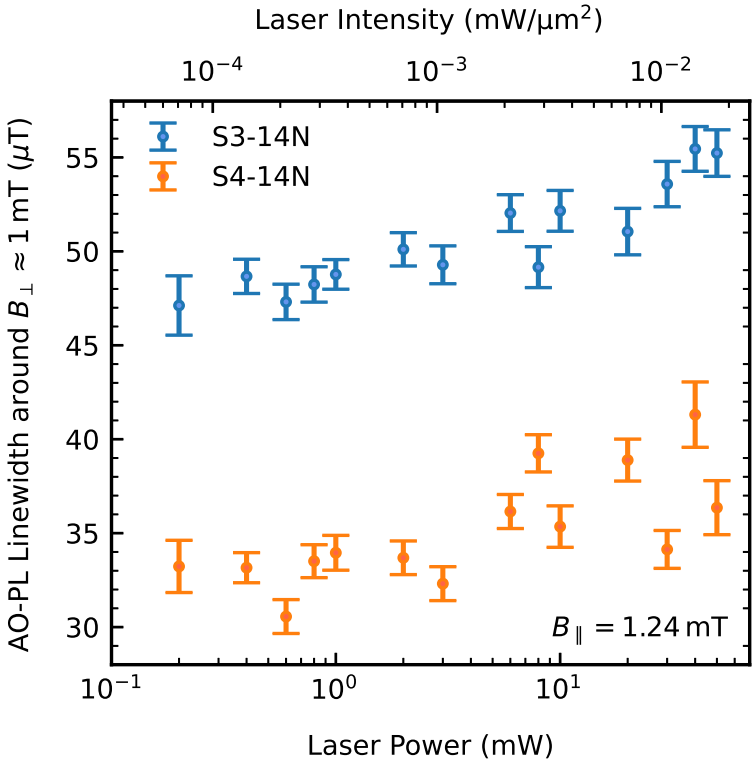


Figure 2.18: Extracted AO-PL contrast feature linewidths γ from fits to measurements around $B_\perp \approx 1\,\text{mT}$ using samples S3-14N (blue) and S4-14N (orange) as a function of laser power and intensity. The laser intensity is calculated by the same procedure described in Fig. 2.11. Each sample exhibits broader linewidth at higher laser power. Sample S3-14N has higher [NV] and significantly larger linewidth than sample S4-14N.

data that is similar to $L(x)$ in Eq. 2.25, except that there are only three peak amplitudes following a 1:2:1 ratio. As shown in Fig. 2.19(a), the fit yields $\Delta B_{15N,\text{AO–PL}} = 0.1289 \pm 0.0002\,\text{mT}$.

Since $B_\perp$ is transverse to both $\hat{n}_\lambda$ and $\hat{n}_\phi$ for these measurements, the spin transition frequencies from the NVs along either orientation should remain the same as $B_\perp$ is varied, separated by the associated nitrogen nuclear spin hyperfine splitting. In contrast, $B_\perp$ has non-zero projection along NV orientations $\hat{n}_\chi$ and $\hat{n}_\kappa$. Thus, the magnetic field separation between neighboring AO-PL peaks and CW-ODMR spin transition fre-

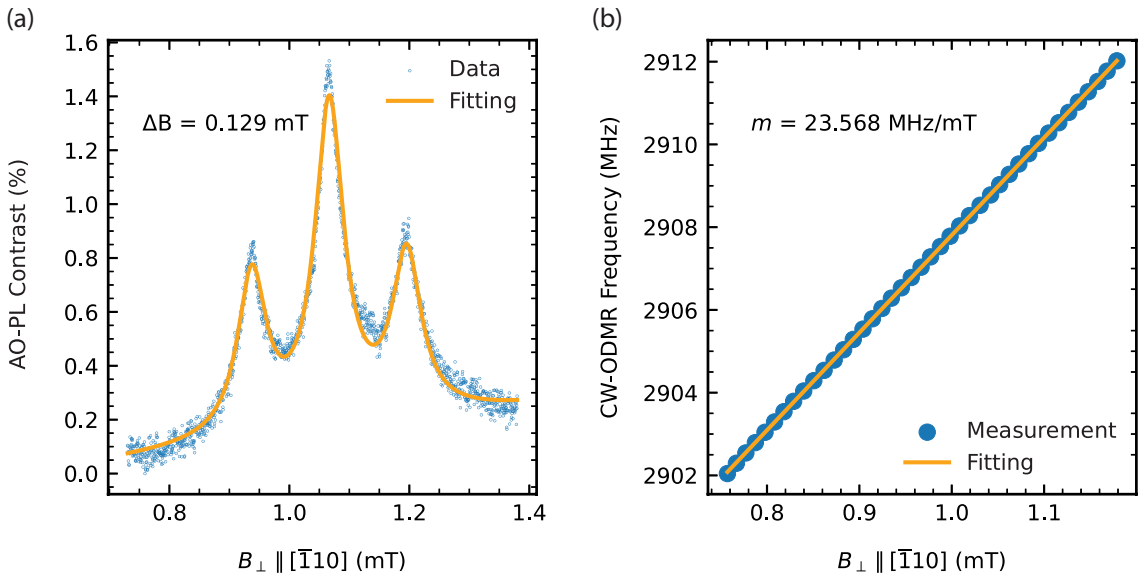


Figure 2.19: (a) Measured AO-PL contrast as a function of $B_\perp$ (dotted markers) with multi-Lorentzian fit (solid line) for sample S2-15N and fixed $B_\parallel$ =1.24 mT. The extracted separation between AO-PL contrast peaks $\Delta B_{15N,\text{AO–PL}}$ = 0.1289 $\pm$ 0.0002 mT. (b) Linear fit applied to CW-ODMR transition frequencies as a function of $B_\perp$ for NV orientations $\hat{n}_\chi$ and $\hat{n}_\kappa$, from measurements shown in Fig. 2.9(c, right) with fixed $B_\parallel$ =1.24 mT. The linear slope $m = 23.568 \pm 0.034$ MHz/mT can be treated as the effective gyromagnetic ratio of the NV electronic spin for $B_\perp$ along $[\bar{1}10]$.

quencies for these orientations can be calculated through consideration of the hyperfine splitting A_N, the NV electronic spin gyromagnetic ratio γ_e, and the angle factor $\cos(\alpha)$ from the projection of $B_\perp$ along each NV orientation, as described in Sec. 2.3.3, yielding $\Delta B_N = A_N/[\gamma_e \cos(\alpha)]$. The linear slope of the measured CW-ODMR transition frequencies from NVs along $\hat{n}_\chi$ and $\hat{n}_\kappa$, shown in Fig. 2.9(c, right), can then be associated to $\gamma_e \cos(\alpha)$. Fig. 2.19(b) shows the fit slope from these CW-ODMR transition frequencies as a function of $B_\perp$, giving $m = 23.568 \pm 0.034$ MHz/mT. For ^{15}N, the hyperfine splitting $A_{15N} \approx 3.03$ MHz. Therefore, we calculate the CW-ODMR triple feature splitting $\Delta B_{15N,\text{CW–ODMR}} = 0.1286 \pm 0.0002$ mT. The good agreement between $\Delta B_{15N,\text{AO–PL}}$ and $\Delta B_{15N,\text{CW–ODMR}}$ confirms that NV hyperfine interactions contribute to the observed

AO-PL signals, including the separation between AO-PL contrast peaks. In addition, we can extract the AO-PL contrast feature linewidth $\gamma = 58.34 \pm 0.66\,\mu T$ through the same fit shown in Fig. 2.19(a). By using the fit slope value m from Fig. 2.19(b), this linewidth in magnetic field units can be converted to $\gamma' = 1.375 \pm 0.016$ MHz in frequency units.

2.5.4 AO-PL Line Shape Comparisons Between Near-Zero-field and Low-Field

Fig. 2.20 depicts the measured AO-PL contrast as a function of $B_\perp$ using samples S3-14N and S4-14N, which differ by [NV] (see Table 2.1). At $B_\parallel = 1.24$ mT and near $B_\perp = 1.05$ mT, Fig. 2.20(b, d), the AO-PL contrast feature linewidth γ is extracted using the same Lorentzian fit function as described in Sec. 2.5.2 by constraining the peak contrast to follow 1:2:3:2:1. For the fit of data near zero-field ($B_\parallel = 0.05$ mT), Fig. 2.20(a, c), due to the increased number of spectral degeneracies, we set the amplitudes of the left three AO-PL contrast peaks as free parameters, while the amplitudes of the remaining two peaks on the right are constrained to mirror those on the left. For these fits, we find that the linewidth γ decreases by $\sim 2.3\times$ (from 119.3 μT to 50.9 μT) and $\sim 2.5\times$ (from 83.5 μT to 33.5 μT) when comparing near-zero-field to low-field, using samples S3-14N and S4-14N, respectively. The increased linewidth near zero-field could be due to NV spin-state mixing induced by local electric fields [24] and/or inhomogeneities in the system. We note that the misalignment of magnetic fields near zero-field can easily broaden the linewidth by enhancing overlap of NV spin spectral features and making hyperfine structures harder to resolve.

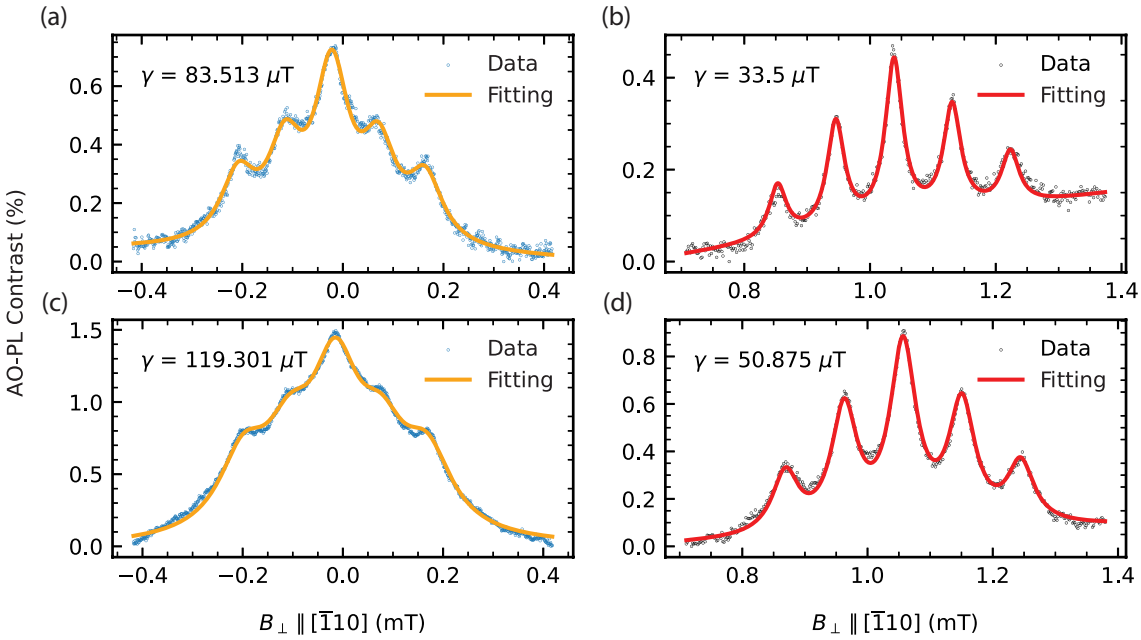


Figure 2.20: Measured AO-PL contrast as a function of $B_\perp$ (dotted markers) with multi-Lorentzian fits (solid lines) using samples (a, b) S4-14N and (c, d) S3-14N. Left: results near zero-field ($B_\parallel = 0.05\,\text{mT}$). Right: results near $B_\parallel = 1.24\,\text{mT}$ and $B_\perp = 1.05\,\text{mT}$. Both samples exhibit AO-PL contrast feature linewidths $\sim 2.5\times$ broader than values at low-field. Sample S4-14N has $\sim 2\times$ lower [NV] and also narrower AO-PL contrast feature linewidths than sample S3-14N. $B_\perp$ values for maximum AO-PL contrast in (a, c) are shifted from 0 due to the presence of a background field.

To compare AO-PL magnetic sensitivity between near-zero-field and low-field, we determine the linear slope extracted from the zero-crossing point of the central dispersive feature acquired with AO-PL lock-in detection for sample S3-14N at a fixed laser excitation power. Fig. 2.21 shows measurements and fits indicating that the slope k at (b) low-field is $\sim 3\times$ larger than that at (a) near-zero-field, despite lower overall AO-PL contrast at low-field.

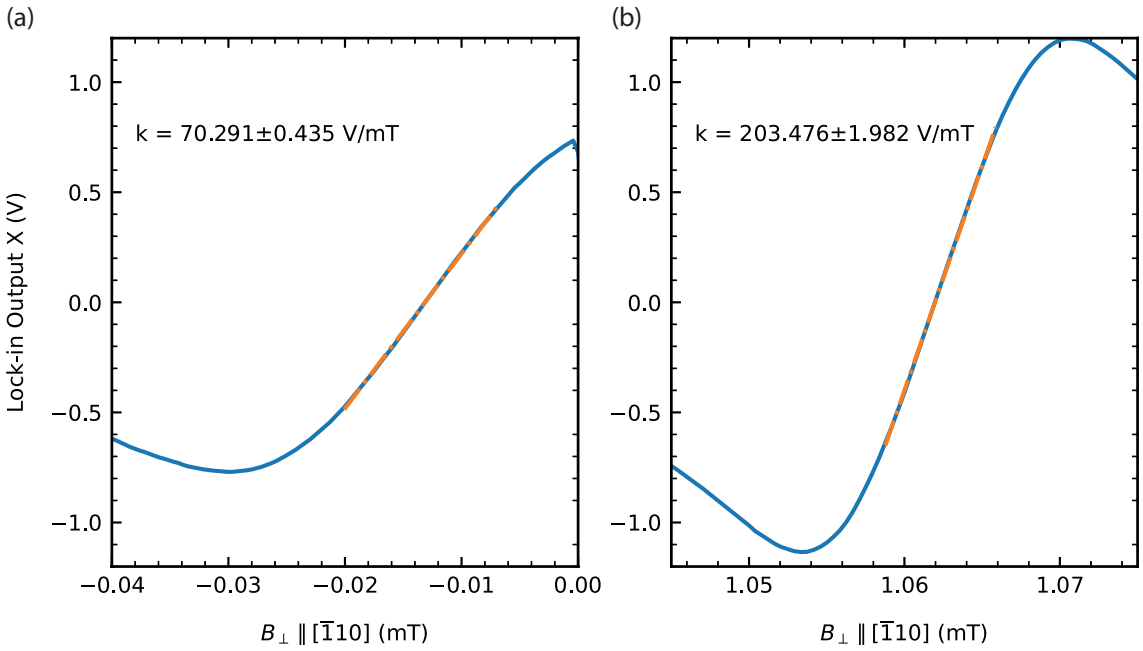


Figure 2.21: Demodulated AO-PL LIA spectra for sample S3-14N around (a) near-zero-field with fixed $B_\parallel = 0.05\,\text{mT}$ and (b) $B_\perp \approx 1.06\,\text{mT}$ with fixed $B_\parallel$ =1.24 mT. Linear fits are applied around the zero-crossing point. The slope k from low-field measurements is larger than the near-zero-field slope by a factor of $\sim 3\times$.

2.6 Outlook

Our results indicate that an NV spin optical pumping rate comparable to the depolarization rate from NV-NV cross-relaxation yields optimal low-field AO-PL contrast. By using a diamond sample with higher NV concentration, which increases dipolar interactions and associated spin relaxation, one may be able to use higher laser excitation power to achieve improvements in both AO-PL contrast and total photon emission, which can be expected to provide improved AO NV magnetic field sensitivity. As shown in Fig. 2.19, the measured AO-PL contrast $C \approx 1.5\%$ and magnetic field linewidth $\Delta\gamma \approx 58\,\mu\text{T}$ (equivalent to 1.37 MHz) are comparable to those obtained with CW-ODMR for the NV-diamond samples and experimental conditions used in this study (see Sec. 2.5.2).

Future work in this direction may include experimental study and modeling of the role of NV ionization and charge-state dynamics at higher laser power. Although AO-PL contrast is largest at near-zero-field, as NVs from all four orientations in the diamond host can resonantly interact, we find the magnetic field linewidth of near-zero-field AO-PL features to be $\approx 2.5\times$ broader than at finite fields ≈ 1 mT (see Sec. 2.5.4). The increased feature linewidth at near-zero-field may arise from NV spin-state mixing induced by local electric fields [24, 27] and/or magnetic field and strain gradients in the system. Therefore, the optimal conditions for near-zero-field AO NV magnetic sensing may rely on both diamond engineering and technical optimization.

The AO, microwave-free approach to ensemble NV magnetometry offers opportunities to reduce device complexity and avoid introducing disturbances to sensing targets [18, 38, 39]. In particular, given the robustness of the diamond host and NV properties [1], low-field AO measurements may be performed in harsh environments (extreme temperature, pressure, radiation, etc.), where efficient microwave delivery and application of a substantial bias magnetic field are challenging or may adversely affect the system under study [40]. With optimal AO-PL contrast occurring at modest optical pumping power (mW-scale), AO operation may allow sensitive NV magnetometry in a device of relatively low size, weight, and power (low-SWaP), enabling diverse applications beyond a controlled laboratory environment. Finally, our studies may prove advantageous when extending AO measurements to other defect ensemble systems with spin-dependent optical properties, such as in silicon carbide (SiC) [41, 42] and hexagonal boron nitride (h-BN) [43, 44].

Chapter 3: Noise Suppression via Pulsed All-Optical Magnetometry with Nitrogen-Vacancy Ensembles

Chapter 2 presents a systematic study of AO-PL contrast features arising from NV-NV cross-relaxation at low fields (< 2mT). As shown in Fig. 2.8(b), the detection of CW AO-PL changes is highly susceptible to laser intensity noise, particularly in the absence of "sig/ref" normalization, which is commonly employed in MW-based protocols using on- and off-resonant MW frequencies [Sec. 1.2.1.1]. To mitigate this issue, lock-in detection with the application of amplitude-modulated magnetic fields can greatly improve the measurement SNR. However, two major challenges remain. First, as detailed in Sec. 2.2.4, the modulation rate was kept low at $f_m = 100\,\text{Hz}$ to produce larger demodulated output amplitude, due to the adiabatic exchange of NV electronic spin population across the avoided crossing. This low f_m leads to a less effective noise suppression as low-frequency noise components, such as from laser intensity fluctuations and environmental vibrations, can overlap with the modulation frequency. Furthermore, the introduction of amplitude modulated magnetic fields can add design complexity, and may perturb sensitive samples such as superconducting materials [45–47].

This chapter is primarily based on the work reported in Ref. [48]. The work in this chapter was initiated and largely performed by me, with useful input on concepts and

technical challenges by several current and past members of the Walsworth group, particularly Jeyson Támara-Isaza, John W. Blanchard, Connor A. Hart, and Johannes Cremer, as well as Prof. Michael Crescimanno. In this work, we demonstrate a pulsed AO sequence to experimentally resolve AO-PL contrast features in NV ensembles at near-zero magnetic field. This sequence, referred to as the single-τ sequence, incorporates a fixed dark time duration τ between optical pulses; and has previously been employed with single NV spin relaxometry to improve the data acquisition speed in nanoscale magnetic noise imaging [49–52]. By implementing two PL readouts – one near the beginning and the other near the end of an optical pulse – we perform normalized AO measurements that suppress common-mode noise more effectively than conventional CW AO techniques. This approach allows us to better characterize the NV-ensemble based AO-PL contrast features with common-mode noise suppression without resorting to amplitude-modulated magnetic fields required for lock-in detection, achieving up to $10\times$ improvement in the low-frequency noise floor compared to conventional CW AO techniques. Furthermore, we measure the dependence of AO-PL contrast on the timing of PL readouts. As a function of the dark time duration τ between optical pulses, we find the optimal τ for maximum of AO-PL contrast is NV-concentration dependent. These findings provide insights into optimizing NV-diamond samples for effective AO operation across diverse applications.

3.1 Experimental Details

3.1.1 Experimental Setup

532 nm CW laser light (Lighthouse Photonics Sprout-H-10W) is modulated with an AOM (G&H 3250-220), after which the first order diffracted beam is transmitted through a single-mode optical fiber (Thorlabs P3-460B-FC-5). The modulated laser beam is then focused through a microscope objective (Olympus 20X/NA 0.45) to create a Gaussian excitation laser beam profile of radius $\approx 30\,\mu m$ to optically excite NV centers in the diamond samples under study. NV-diamond sample properties are summarized in Table 2.1. NV photoluminescence (PL) is collected through the same objective, directed with a dichroic mirror (Semrock FF552-DI02), filtered with a long-pass filter (Semrock BLP01-532R-25), and focused onto a high-bandwidth avalanche photodiode (Thorlabs APD430A) through a 25.4 mm lens (Thorlabs LA1951-B-ML). A schematic overview of the experimental apparatus is shown in Fig. 3.1.

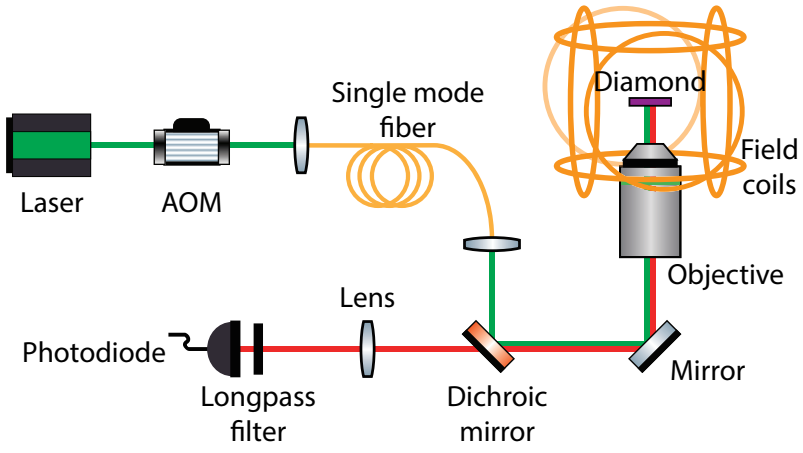


Figure 3.1: Schematic of the experimental setup for near-zero-field pulsed AO magnetometry.

A three-channel power supply (Rohde & Schwarz HMP4030) connected to relay boards (Winford RLY202-5V-DIN) is used to drive a three-axis Helmholtz coil array (Ferronato BH300-3-A) to provide a bias magnetic field of controllable magnitude and direction. Calibration of applied current to bias magnetic fields is in Sec. 2.2.3. The NV-diamond sample is mounted on a piezoelectric rotational stage (Thorlabs ELL14) to independently align the applied magnetic field with respect to the NV crystallographic axes, with $B_0 \parallel [\bar{1}10]$, and $B_1 \parallel [100]$ and $B_2 \parallel [010]$ aligned separately.

The output of the photodiode used to collect NV PL is sent to a high-speed data-acquisition device (Gage RazorMax CSE50216) for time-resolved measurements with a 200 MS/s sampling rate. Measurement pulse sequences are synthesized by a pulse generator (Swabian Instruments Pulse Streamer 8/2): channel 0 provides TTL pulses to a solid state switch (Mini-Circuits ZASW-2-50DRA+) to gate the AOM; and channel 1 synchronizes the data acquisition on Gage RazorMax. A signal generator (Stanford Research Systems SG384) provides the RF signal at 225 MHz that, together with an RF amplifier (Mini-Circuits ZHL-03-5WF+), drives the AOM. The RF amplitude from the signal generator to the AOM is varied to control the laser power delivered to the NV-diamond sample. The same signal generator is used to provide amplitude-modulated RF generation via the noise modulation function to introduce additional optical intensity noise to the experiment.

3.1.2 Experimental Principle and Operation

T_1-based relaxometry is commonly employed for NV magnetic noise sensing [5]. The typical relaxometry pulse sequence, shown in Fig. 3.2(a), consists of an initial optical pulse to initialize the NV ground electronic spin states to $|m_s = 0\rangle$, which subsequently relax towards a mixture of $|m_s = 0, \pm 1\rangle$ after a variable dark time τ. A second optical pulse is applied for PL read out to determine the resulting electronic spin state; and also to optically polarize the NV for the next of N repetitions of the sequence.

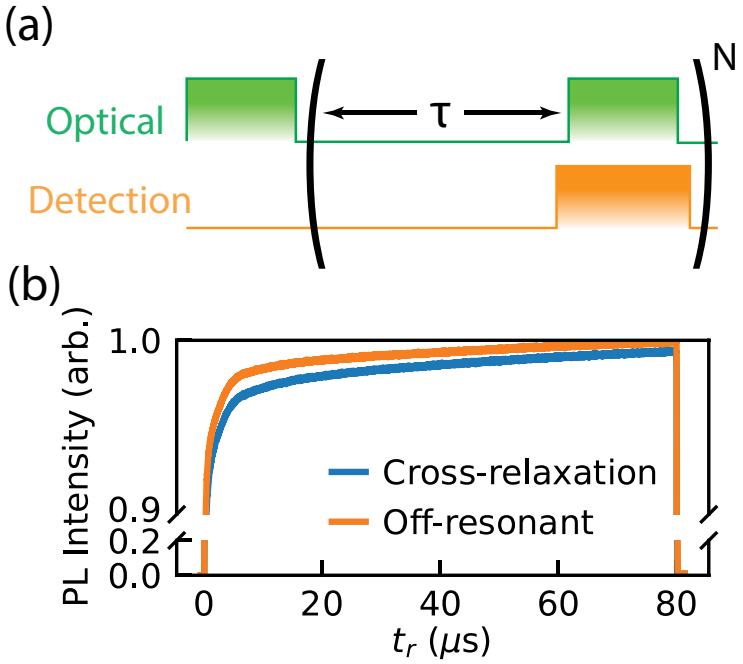


Figure 3.2: (a) Relaxometry pulse sequence for measuring the NV electronic spin lifetime T_1. (b) Example time-resolved PL intensity during optical illumination for resonant NV-NV cross-relaxation at near-zero magnetic field (blue) and for off-resonant conditions with an applied magnetic field (orange), respectively. The intensity of PL signals during NV-NV cross-relaxation is reduced.

At near-zero magnetic field, NV centers aligned along the four crystallographic orientations exhibit degenerate electronic spin transition frequencies due to insignificant Zeeman shifts. Consequently, resonant NV-NV dipolar interactions, known as NV-NV

cross-relaxation, induce spin-state mixing and shorten the NV longitudinal spin relaxation time T_1 [24]. The time-resolved PL intensity from an NV ensemble can be measured over time t_r following optical illumination, as shown in Fig. 3.2(b). NV-NV cross-relaxation at near-zero magnetic field reduces the measured PL intensity compared to the off-resonant case, where the spin transition degeneracy is lifted by an applied magnetic field. By tuning the magnetic field, AO-PL contrast features associated with NV-NV cross-relaxation and the NV hyperfine interaction can be resolved [21].

3.2 Experimental Results

3.2.1 Normalization with Two AO-PL Measurements

We perform normalized measurements of pulsed AO-PL intensity, collected in signal (I_{sig}) and reference (I_{ref}) readout windows, each with a length of 1 μs, within an optical pulse [Fig. 3.3(a)]. I_{sig} is measured at t_r from the beginning of the optical pulse and I_{ref} is measured during the final 1 μs of the pulse. We choose the optical pulse length to be 80 μs, which is sufficient to achieve steady-state NV spin polarization under the applied 275 mW laser power used in this work. This AO-PL normalization allows for suppression of common-mode noise that equally affects both measurements, such as relatively slow variations in optical intensity. The readout window length of 1 μs is selected to apply a moving average filter for transient PL measurements, integrating neighboring time-resolved PL intensities to improve SNR while balancing AO-PL contrast. The normalized AO-PL intensity ($n = \overline{I_{\text{sig}}}/\overline{I_{\text{ref}}}$) at a given (near-zero) magnetic field is further compared to the value at a reference off-resonant magnetic field $B_0 = 0.45\,\text{mT}$ ($n' = \overline{I'_{\text{sig}}}/\overline{I'_{\text{ref}}}$)

where the NV-NV cross-relaxation effect is minimal. The pulsed AO-PL contrast is then calculated as $C = 1 - n/n'$.

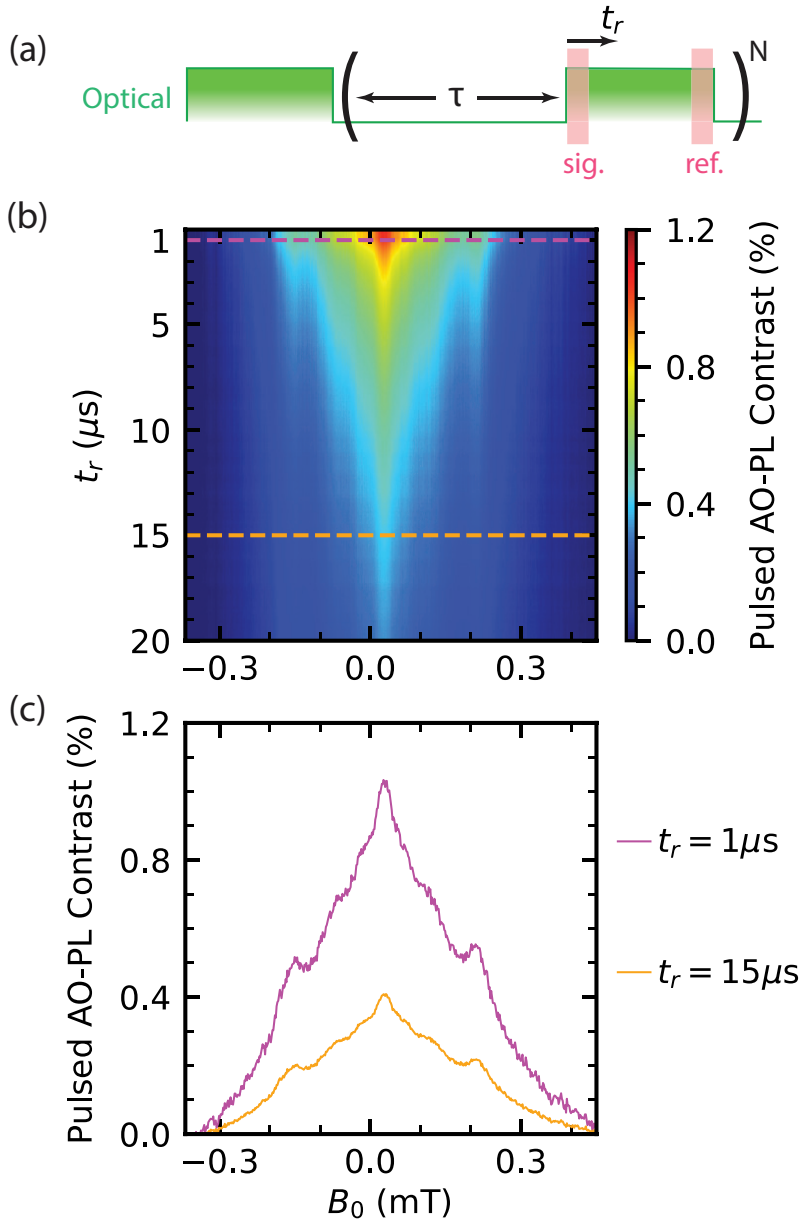


Figure 3.3: (a) Relaxometry pulse sequence for measuring the NV electronic spin lifetime T_1. (b) Example time-resolved PL intensity during optical illumination for resonant NV-NV cross-relaxation at near-zero magnetic field (blue) and for off-resonant conditions with an applied magnetic field (orange), respectively. The intensity of PL signals during NV-NV cross-relaxation is reduced.

3.2.2 Pulsed AO-PL Contrast as a Function of Signal Readout Timing t_r

Using this pulsed measurement protocol, we experimentally determine the pulsed AO-PL contrast for sample S3-14N as a function of B_0 along $[\bar{1}10]$ and t_r, with fixed dark time $\tau = 2\,\text{ms}$ [Fig. 3.3(b)]. The results with t_r between 0 and 0.5 μs are omitted in Fig. 3.3(b) due to low PL intensities shortly after optical excitation, leading to noisier resolved AO-PL features. Fig. 3.4 shows a comparison of measured near-zero-field pulsed AO-PL contrast features for sample S3-14N, with fixed dark time $\tau = 2\,\text{ms}$, and for signal readout pulse values $t_r = 0.4\,\mu\text{s}$ and $t_r = 1\,\mu\text{s}$. The result with $t_r = 0.4\,\mu\text{s}$ exhibits weaker AO-PL contrast and worse SNR. The weaker AO-PL contrast is attributed to poor optical spin polarization shortly after the optical pulse, as a longer τ allows the NV electronic spins to relax toward thermal equilibrium. In addition, the lower PL emission intensity lead to worse SNR. For t_r between $0\,\mu\text{s}$ and $0.4\,\mu\text{s}$, the near-zero-field AO-PL contrast features are no longer identifiable in measurement with our setup.

Fig. 3.3(c) shows examples of the measured near-zero-field AO-PL contrast as a function of B_0, at fixed $t_r = 1\,\mu\text{s}$ and $t_r = 15\,\mu\text{s}$. The observed AO-PL contrast peaks in Fig. 3.3(c) result from the NV hyperfine interaction with the ^{14}N nuclear spin, which provides additional electronic spin depolarization channels and splits the NV-NV cross-relaxation resonance near zero fields [21]. In addition, the measured pulsed AO-PL contrast decreases as t_r increases, for all values of B_0. As a consequence, higher pulsed AO-PL contrast is achieved with the I_{sig} readout occurring shortly after optical excitation and I_{ref} readout towards steady-state. This result is consistent with the difference of measured transient NV-PL in Fig. 3.5 with a moving average filter applied, where larger

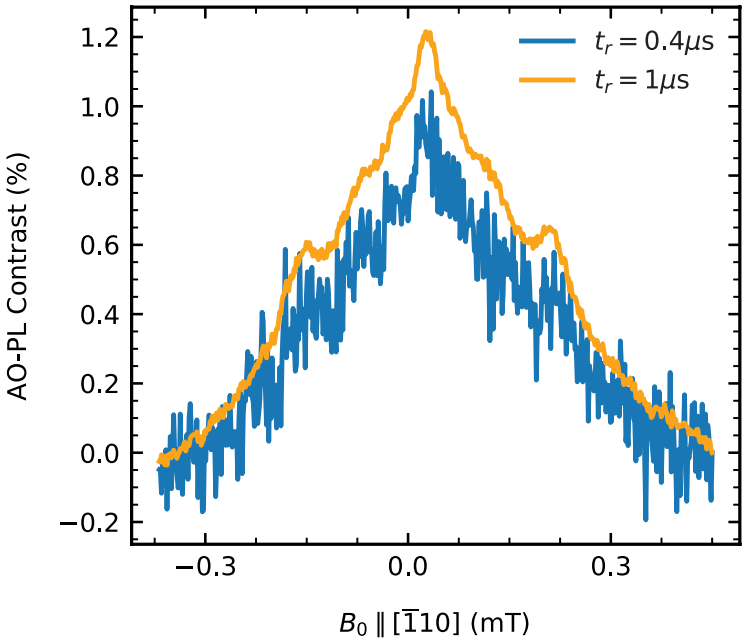


Figure 3.4: Pulsed AO-PL contrast of sample S3-14N measured for signal readout pulse values $t_r = 0.4\,\mu$s and $t_r = 1\,\mu$s, with dark time $\tau = 2$ ms. $t_r < 1\,\mu$s yields weaker AO-PL contrast and worse SNR due to poor optical spin polarization after the optical pulse.

reductions in PL intensity are seen during NV-NV cross-relaxation for times closer to the activation of optical excitation rather than at steady-state.

3.2.3 Pulsed AO-PL Contrast as a Function of Dark Time τ

We next measure the pulsed AO-PL contrast as a function of dark time τ at fixed $t_r = 1\,\mu$s and $B_0 = 0.03$ mT, i.e., near the maximum contrast from the near-zero-field AO-PL feature. The pulsed AO-PL contrast $C(\tau)$, from both sample S3-14N ([NV] $\approx$ 3.8 ppm) and sample S4-14N ([NV] ≈ 2 ppm), initially increase with τ, reach a maximum value, and then decrease at longer τ [Fig. 3.6(a)]. For τ ranging from 0.5 to 20 ms, we fit these experimental results quantitatively using a bi-exponential function:

$$C(\tau) = A_{\text{cr}} e^{-\tau/T_{\text{cr}}} + A_{\text{in}} e^{-\tau/T_{\text{in}}}. \tag{3.1}$$

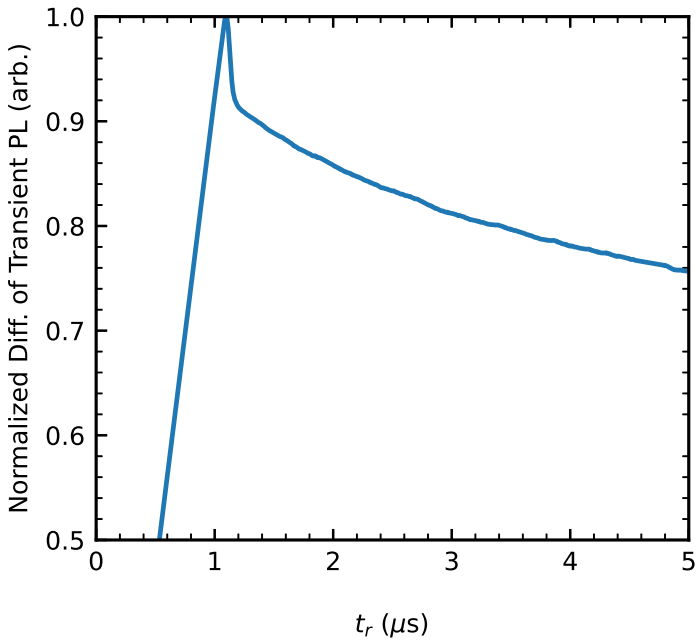


Figure 3.5: Normalized difference of transient PL intensity between from resonant NV-NV cross-relaxation at near-zero magnetic field and from off-resonant conditions with an applied magnetic field. A moving average filter with 1 μs window length is applied to both transient PL measurements before taking the difference. The maximum occurs near $t_r = 1\,\mu$s and is in agreement with the result in Fig. 3.3.

Here, we attribute T_{cr} and T_{in} to the characteristic timescales of NV-NV cross-relaxation and intrinsic depolarization, respectively, with A_{cr} and A_{in} being the corresponding amplitudes. For sample S3-14N, $A_{\text{cr}}^{\text{S3}} = -2.69 \pm 0.38$, $A_{\text{in}}^{\text{S3}} = 2.86 \pm 0.41$, $T_{\text{cr}}^{\text{S3}} = 1.77 \pm 0.18$ ms and $T_{\text{in}}^{\text{S3}} = 4.81 \pm 0.34$ ms; and for sample S4, $A_{\text{cr}}^{\text{S4}} = -1.76 \pm 0.4$, $A_{\text{in}}^{\text{S4}} = 1.83 \pm 0.42$, $T_{\text{cr}}^{\text{S4}} = 2.75 \pm 0.39$ ms and $T_{\text{in}}^{\text{S4}} = 7.36 \pm 0.85$ ms. These results indicate that stronger dipolar interactions from higher [NV] shortens both timescales, creating higher maximum pulsed AO-PL contrast with a shorter dark time τ.

Fig. 3.7(a) presents the experimentally-determined NV ground-state spin-polarization lifetime (T_1) of sample S3-14N as a function of dark time τ from 0 to 30 μs, using the relaxometry pulse sequence shown in Fig. 3.2. The normalized pulsed AO-PL $S(\tau)$ mea-

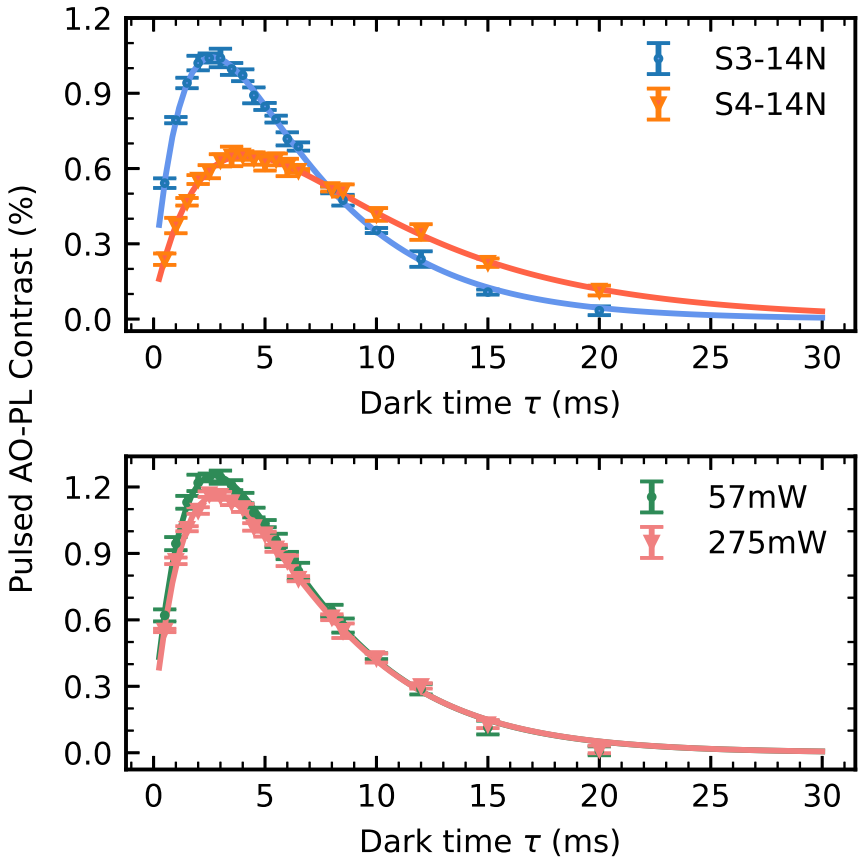


Figure 3.6: (a) Pulsed AO-PL contrast at $B_0 = 0.03\,\text{mT}$, 275 mW laser power, and $t_r = 1\,\mu\text{s}$, as a function of dark time τ for samples S3-14N ([NV] ≈ 3.8 ppm) and S4-14N ([NV] ≈ 2 ppm). Markers are the experimental contrast values $C(\tau)$, with measurement uncertainty indicated. Solid lines are from a bi-exponential fit to experimental $C(\tau)$ values. For both samples, the fit yields two characteristic timescales T_{cr} and T_{in} that can be associated with NV-NV cross-relaxation and intrinsic depolarization, respectively. (b) Pulsed AO-PL contrast at $B_0 = 0.03\,\text{mT}$ and $t_r = 1\,\mu\text{s}$ as a function of dark time τ for sample S3-14N ([NV] ≈ 3.8 ppm) at two laser powers, 57 mW and 275 mW. The two fit timescales are consistent within error bars.

surements are fit with a stretched exponential function (not shown in Fig. 3.7(a)) with a stretched factor β as:

$$S(\tau) = A(1 + \exp(-(\frac{\tau}{T_1})^{\beta})) \tag{3.2}$$

When NV-NV cross-relaxation is strongest at magnetic field $B_0 = 0.03\,\text{mT}$, the fit yields $T_1 = 2.602 \pm 0.008\,\text{ms}$, with $\beta = 0.926 \pm 0.004$. At the off-resonant magnetic field

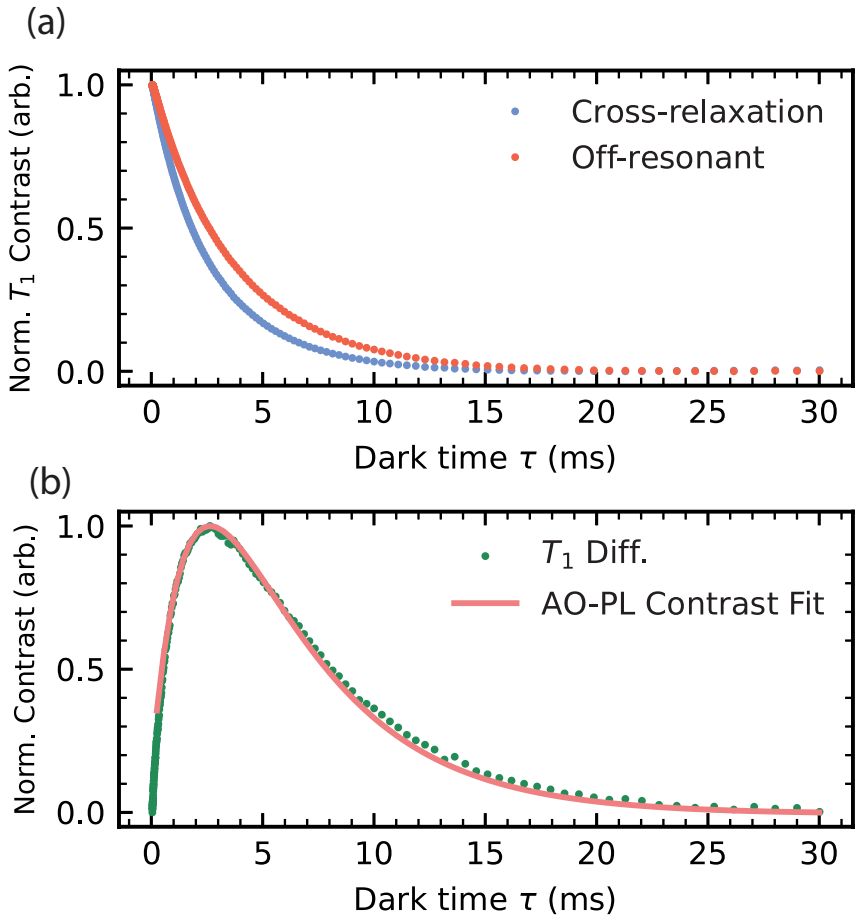


Figure 3.7: (a) Experimentally-determined NV ground-state spin-polarization lifetime (T_1) of sample S3-14N as a function of dark time τ. Fits of pulsed AO-PL decay (not shown) yield $T_1 = 2.602 \pm 0.008$ ms with cross-relaxation magnetic field at $B_0 = 0.03$ mT, and $T_1 = 3.70 \pm 0.012$ ms with off-resonant magnetic field at $B_0 = 0.45$ mT. (b) Differences of T_1 results in Fig. 3.7(a) and a bi-exponential fit to the measured AO-PL contrast of sample S3-14N in Fig. 3.6(a) as a function of dark time τ, with good consistency found between the methods.

$B_0 = 0.45$ mT, $T_1 = 3.7 \pm 0.012$ ms, with $\beta = 0.976 \pm 0.004$. The reduction of stretched factor β near zero field indicates stronger depolarization, and is consistent with results reported in Ref. [22, 24].

Fig. 3.7(b) shows the normalized difference between these two T_1 relaxometry measurements alongside the normalized bi-exponential fit of pulsed AO-PL contrast as a function of τ presented in Fig. 3.6(a, blue). The good agreement between these normalized

results indicate that the optimal τ for achieving maximum AO-PL contrast is linked to the differences of T_1 between cross-relaxation and off-resonant conditions, and is therefore dependent on the NV concentration.

We next repeat the measurements on sample S3-14N for different laser powers, 57 mW and 275 mW [Fig. 3.6(b)]. The optical pulse is extended from the previous value of 80 μs to 300 μs to ensure sufficient optical excitation at the end of the pulse for both laser powers. Fitting the data to the bi-exponential function in Eq. 3.1 yields $A_{\text{cr}} = -3.56 \pm 0.91$ (-3.64 ± 1.19), $A_{\text{in}} = 3.75 \pm 0.96$ (3.8 ± 1.23), $T_{\text{cr}} = 1.88 \pm 0.3$ ms (2.04 ± 0.36 ms) and $T_{\text{in}} = 4.66 \pm 0.52$ ms (4.65 ± 0.6 ms) at 57 mW (275 mW), respectively. For the two laser powers, the fitted T_{cr} and T_{in} values are in agreement within error bars, consistent with these timescales being primarily dependent on sample properties such as [NV]. The modest observed reduction in maximum AO-PL contrast ($\sim$0.1%) at 275 mW may result from NV ionization and charge cycling, which decrease the population of negatively-charged NVs by converting them to the neutral charge state (NV^0) [31–33].

3.2.4 Comparison of Noise Suppression Performance Between Pulsed and CW AO Operation

In this section, we compare the noise suppression performance of pulsed AO to conventional CW AO operation for sample S3-14N without the use of lock-in detection. We start by measuring 30 1-s time traces at $B_0 = 0.05$ mT where the AO magnetometer is magnetically sensitive. For pulsed AO operation, we set the optical pulse duration to $80\ \mu$s for shorter time spacing between I_{sig} and I_{ref} readout timings, and keep the total sequence

duration at 2.5 ms (i.e., sampling rate of 400 S/s and Nyquist frequency of 200 Hz); for CW AO operation, we use a sampling rate of 100 kS/s. Each measured 1-s time trace is converted into a power-spectral-density (PSD) plot using the calibrated slope of the AO-PL contrast feature at $B_0 = 0.05$ mT, before being averaged. A fixed test signal with an amplitude of 1 μT at $f_{\text{test}} = 43$ Hz is applied for both pulsed and CW AO operation. The averaged PSDs are subsequently normalized with respect to the PSD amplitude at f_{test}. This normalization allows us to compare the noise suppression performance in units of decibels (dB), with 0 dB at f_{test} due to the PSD normalization. To ensure both pulsed and CW AO operation are optimally sensitive to the applied test signal, we apply laser power of 275 mW for pulsed and 4 mW for CW AO measurements. Modest CW optical power is needed for AO-PL measurements utilizing NV-NV cross-relaxation, in order to balance the optical pumping and spin relaxation processes [21].

We achieve $\sim$ 10 dB improvement in the near DC frequency range from pulsed relative to CW AO operation, with diminishing noise suppression capability $>$ 10 Hz, as shown in Fig. 3.8(a). Above 10 Hz, the CW AO method exhibits a lower noise floor, primarily due to its much higher sampling rate (100 kS/s). In contrast, pulsed AO operation, with an effective sampling rate of 400 S/s, is susceptible to aliasing, whereby high-frequency noise components fold back into the 0–200 Hz band, elevating the noise floor in the 10–200 Hz region [53, 54].

We introduce additional optical intensity noise via amplitude modulation (AM) to the AOM RF power, with a 0.2% depth and 200 Hz bandwidth from the noise modulation function. It is worth noting that the AM depth is defined relative to the AOM RF power, which varies between CW and pulsed AO operation modes to achieve different average

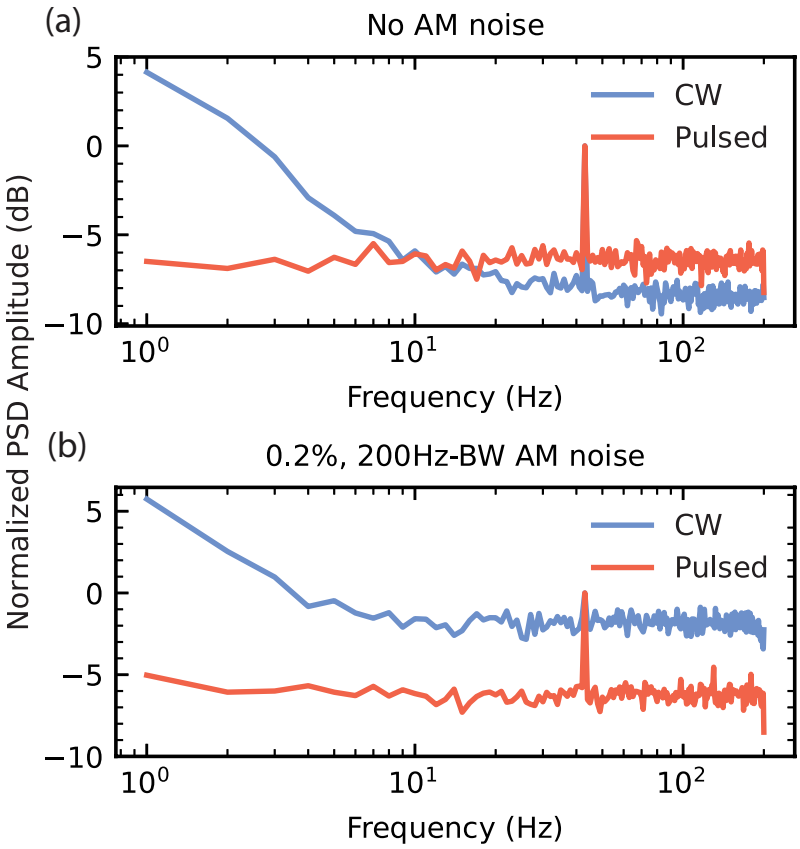


Figure 3.8: Normalized power-spectral-density (PSD) relative to a test signal (1 μT, 43 Hz) for CW and pulsed AO measurements of sample S3-14N. (a) No AM noise added to the AOM RF power. (b) Additional AM noise with 0.2% depth and 200 Hz bandwidth.

laser powers. This approach allows us to characterize the noise suppression performance under realistic conditions, including the effects of relative optical intensity noise. The 0.2% AM modulation depth is chosen in order to obtain a minimally measurable test signal for CW AO operation. In Fig. 3.8(b), the pulsed AO normalization method shows a similar $\sim$ 10 dB improvement near DC similar compared to the case without added optical intensity noise [Fig. 3.8(a)]. Additionally, pulsed AO normalization maintains a consistently 4-5 dB lower noise floor across the higher-frequency (10-200 Hz) range relative to the CW AO method.

To further evaluate the noise suppression performance, we increase the AM depth to

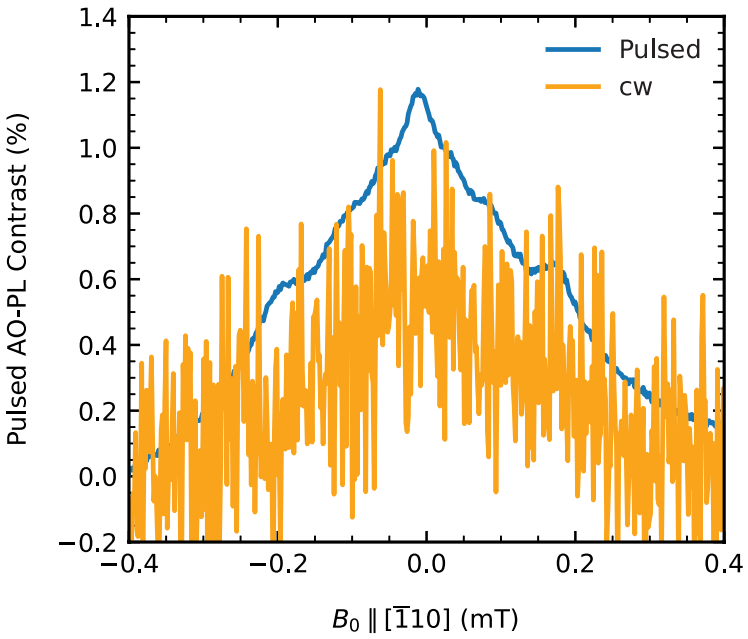


Figure 3.9: Measured near-zero-field AO-PL contrast of sample S3-14N using pulsed (blue) and CW (orange) methods as a function of B_0. Additional optical intensity noise is applied through AM with 1% depth and 200 Hz bandwidth from noise modulation of the AOM RF power. The pulsed method can still resolve clear AO-PL contrast features under substantial optical intensity noise.

1% and compare the measured near-zero-field AO-PL contrast features of sample S3-14N for CW and pulsed operation, as shown in Fig. 3.9. The wall time for both measurements is kept approximately identical to ensure a fair comparison, as CW AO measurements have a higher sampling rate and average more data points at each magnetic field. The results show that while the CW technique fails to resolve AO-PL contrast features with good SNR under strong optical noise, the pulsed technique maintains good robustness.

The results from Figs. 3.8 and 3.9 demonstrate the advantage of the proposed pulsed AO magnetometry protocol in effectively rejecting common-mode noise compared to the conventional CW AO technique, for both measuring an oscillating (AC) magnetic signal at a fixed bias field and resolving AO-PL contrast features during applied magnetic field sweeps, which are typically slower (∼DC).

3.2.5 Pulsed AO-PL Contrast from Spin-State Mixing

Fig. 3.10 shows experimental results for pulsed AO-PL contrast as a function of $B_1 \parallel [100]$ and $B_2 \parallel [010]$, using sample S5-14N with approximately 0.3 ppm NV concentration (top) and sample S3-14N with approximately 3.8 ppm NV concentration (bottom), respectively. We vary both B_1 and B_2 from 0 to 1.5 mT, with step size approximately 0.04 mT. The lower NV concentration in sample S5-14N allows for the measurement of AO-PL contrast from NV electronic spin states mixing under applied magnetic fields that are not aligned with the NV quantization axis, as the AO-PL contrast arising from NV-NV cross-relaxation is much weaker [21]. We plot the pulsed AO-PL contrast from I_{sig} at $t_r = 1\,\mu$s [Fig. 3.10(a)], I_{ref} at $t_r = 79\,\mu$s [Fig. 3.10(b)], and normalized values using the steps described in Sec. 3.2.1 [Fig. 3.10(c)]. Each two-dimensional AO-PL contrast plot is normalized to the maximum intensity from a given scan of (B_1, B_2).

By implementing two PL readout normalization with sample S5-14N, we successfully measure pulsed AO-PL contrast from spin-state mixing as a non-negligible background, along with contributions from weak NV-NV cross-relaxation as stripelike features [Fig. 3.10(c, top)]. A stronger background spin-state mixing pulsed AO-PL contrast is observed in the reference readout measurement [Fig. 3.10(b, top)] compared to the signal readout measurement [Fig. 3.10(a, top)], and is consistent with the CW result reported in Fig. 2.7 from Sec. 2.3.2.

This result differs from that of sample S3-14N, where pulsed AO-PL contrast arising from NV-NV cross-relaxation is primarily observed in the signal readout window [Fig. 3.10(a, bottom)], as described in Sec. 3.2.2. These findings suggest that the pulsed

AO technique can be adapted to measure AO-PL contrast using various measurement protocols under a wide range of applied magnetic fields. Optimizing AO pulse sequences for specific operational conditions will be explored in future studies.

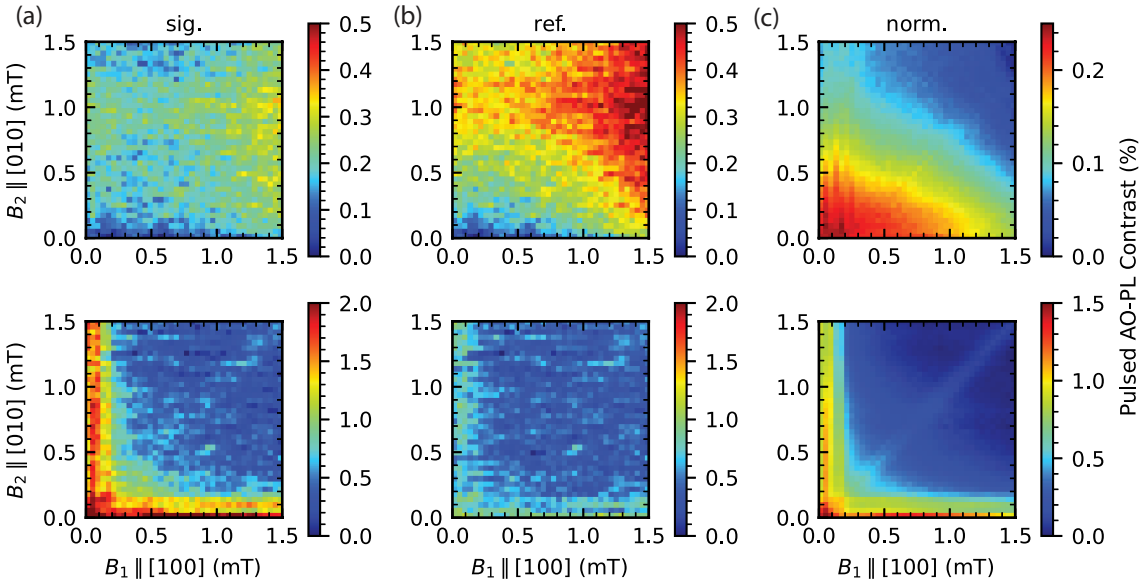


Figure 3.10: Pulsed AO-PL contrast as a function of applied magnetic field magnitude and direction, for: (a) signal readout pulse value $t_r = 1\,\mu$s; (b) reference readout pulse value $t_r = 79\,\mu$s; and (c) after normalization, using sample S5-14N with ≈ 0.3 ppm [NV] (top) and sample S3-14N with ≈ 3.8 ppm [NV] (bottom). Implementing two PL readout normalization with sample S5-14N allows the characterization of pulsed AO-PL contrast from both spin-state mixing as a non-negligible background and weak NV-NV cross-relaxation as stripelike features. Unlike pulsed AO-PL contrast from NV-NV cross-relaxation, which is primarily observed in the signal readout measurement (a, bottom), a significant portion of pulsed AO-PL contrast from spin-state mixing appears in the reference readout measurement (b, top). Future studies will explore optimizing AO pulse sequences for specific operational conditions.

3.2.6 Comparison of Near-Zero-Field AO-PL Contrast Features Between ^{14}N and ^{15}N Samples

Chapter 2 Sec. 2.3.3 provides extensive comparison of CW AO-PL contrast features from ^{14}N and ^{15}N samples (samples S1-14N and S2-15N) under low magnetic fields

($B_{\parallel}$ =1.24 mT, $B_{\perp}$ ≈1 mT. Fig. 3.11 shows the comparison of near-zero-field AO-PL contrast features by using pulsed AO-PL sequence on ^{14}N and ^{15}N samples (samples S3-14N and S2-15N). It is evident that sample S2-15N exhibits a cleaner near-zero-field AO-PL contrast feature with three prominent peaks. This is resulted from the simpler hyperfine structure from ^{15}N. The greater spectral overlap near zero field may also account for the higher pulsed AO-PL contrast compared to the result from sample S3-14N, which suggests that samples with ^{15}N nuclear spin might be more suited for near-zero-field AO magnetometry.

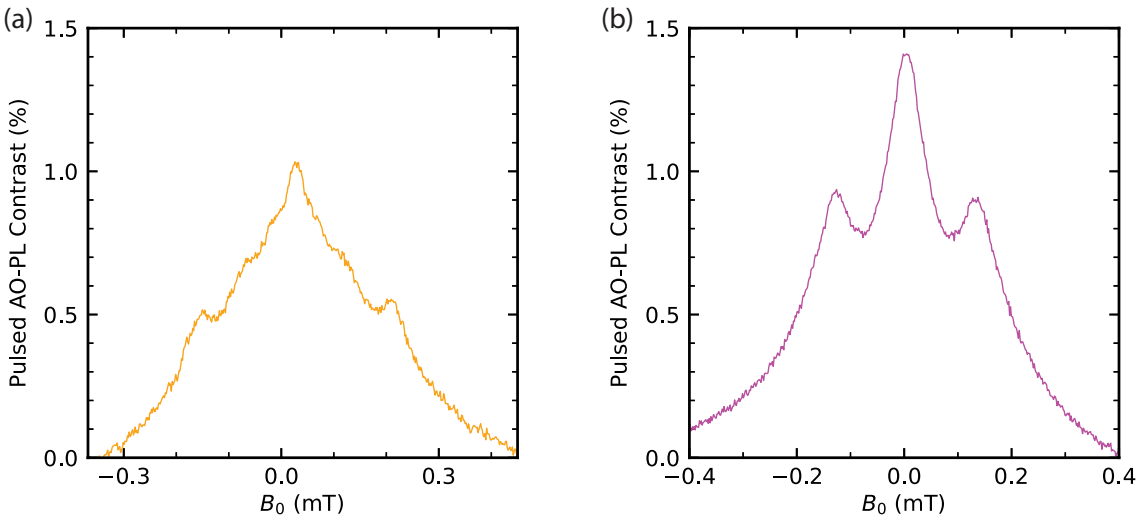


Figure 3.11: Measured near-zero-field AO-PL contrast of sample S3-14N (a) and S2-15N (b) as a function of B_0. The simpler hyperfine structure from ^{15}N leads to a cleaner contrast feature with three prominent peaks. The increased pulsed AO-PL contrast in (b) may result from the better spectral overlap near zero field.

3.2.7 Comparison of AO-PL Contrast Feature Linewidth Between CW and Pulsed Operation

Sec. 1.2.1.1 provides an overview of MW-based CW and pulsed ODMR magnetometry. Pulsed ODMR provides a narrower linewidth and hence a better magnetic sensitivity than CW ODMR if the interrogation time from the MW pulse is properly chosen, as the MW and optical fields are no longer applied simultaneously. In this section, we investigate whether the pulsed AO protocol can be analogous to pulsed ODMR method and achieve the similar benefit of reducing AO-PL contrast feature linewidth than CW technique. We use the following multi-Lorentzian function $L_{15N}(x)$, modified from Eq. 2.25, to fit the near-zero-field AO-PL contrast feature measured from sample S2-15N:

$$\begin{aligned} L_{15N}(x) =& \frac{A_1}{\left[1+\frac{(B_\perp - B_1)}{(\gamma/2)}^2\right]} + \frac{A_2}{\left[1+\frac{(B_\perp - (B_1+\Delta B))}{(\gamma/2)}^2\right]} \\ &+ \frac{A_1}{\left[1+\frac{(B_\perp - (B_1+2\Delta B))}{(\gamma/2)}^2\right]} + kB_\perp \end{aligned} \tag{3.3}$$

Here, we remove the 1:2:1 amplitude ratio used in the low-field AO-PL fit in Sec. 2.3.3 due to the increased number of spectral degeneracies near zero field, while keeping the linewidth γ fixed for all three peaks.

Fig. 3.12 shows the comparison of measured near-zero-field AO-PL contrast using pulsed (blue) and CW (orange) AO protocols, along with their fits. We find that the AO-PL linewidth γ does not vary significantly from $114.25 \pm 1.89\,\mu$T to $112.63 \pm 2.23\,\mu$T when comparing pulsed to CW AO operations. The low AO-PL contrast from CW mea-

surements might be due to the unideal experimental control, e.g. applied laser power, as CW AO-PL contrast can reach $\sim 1.5\%$ using sample S3-14N with nearly identical [NV] [Fig. 2.20(c)].

This result indicates that the pulsed AO-PL protocol might not be regarded as a MW-free equivalent to the pulsed ODMR method. In AO operations based on NV-NV cross-relaxation, spin depolarization in the dark can be viewed as a mechanism analogous to MW irradiation, altering PL intensity by modifying the spin population distribution. As mentioned previously, pulsed ODMR benefits from the separation of optical spin polarization and MW interrogation time. However, the spin depolarization contributed by NV-NV cross-relaxation is still CW, as the bias (on-resonance) magnetic field is kept constant during the sequence. Therefore, the two processes of spin depolarization and optical polarization are still occurring simultaneously in the optical interrogation window during the pulsed AO sequence, and may explain why the corresponding measured linewidth remains consistent.

3.2.8 Pulsed AO-PL Fit Linewidth as a Function of Signal Readout Timing t_r

Here, we study the near-zero-field AO-PL linewidth as a function of signal readout timing t_r from 1 μs to 2.5 μs for sample S2-15N. The fit linewidth values are extracted using the same multi-Lorentzian function $L_{15N}(x)$ described in Sec. 3.2.7. Fig. 3.13(a) shows the fit amplitude A_2 from the central peak decreases as t_r increases. This decrease of AO-PL contrast is consistent with the result from Fig. 3.2.2(b) using sample S3-14N.

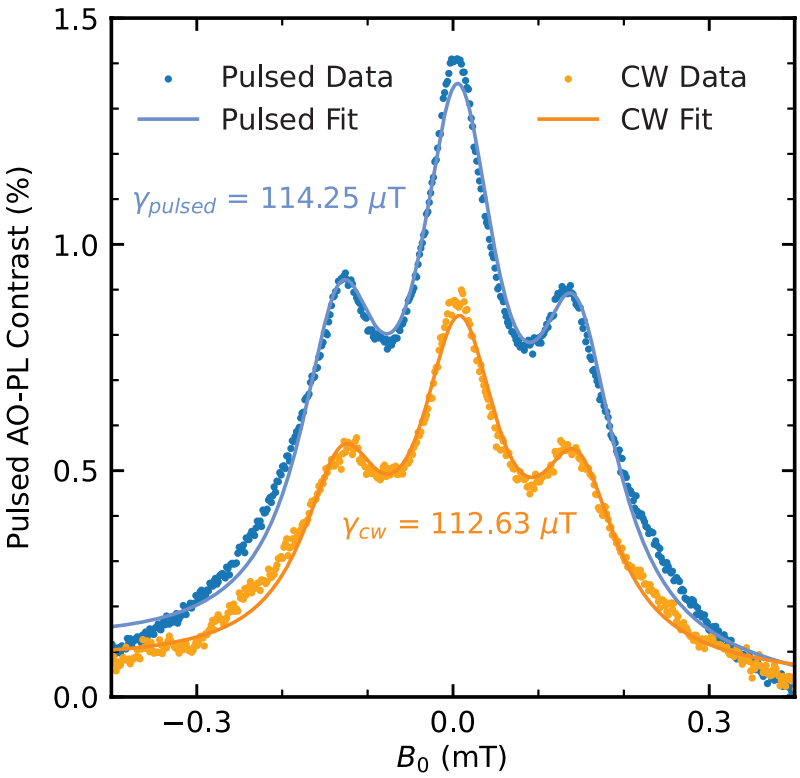


Figure 3.12: Measured near-zero-field AO-PL contrast of sample S2-15N using pulsed (dotted blue) and CW (dotted orange) methods with multi-Lorentzian fits (solid lines) as a function of B_0. The sample exhibits a AO-PL contrast feature linewidth of 114.25 $\pm$ 1.89 μT (112.63 $\pm$ 2.23 μT) using pulsed (CW) protocols, respectively. No significant variation in this linewidth of AO-PL contrast features is observed between the two measurements.

In contrast, the fit linewidth γ is roughly consistent without error bars.

3.3 Discussion

The measured variation in AO-PL contrast as a function of sequence dark time τ reflects the interplay between NV-NV cross-relaxation and intrinsic depolarization processes. These dynamics collectively determine the optimal τ, which varies with NV concentration for the maximum AO-PL contrast. In this study, the NV-diamond sample with higher [NV] (≈ 3.8 ppm) exhibits stronger AO-PL contrast at a shorter τ of about 2.5 ms.

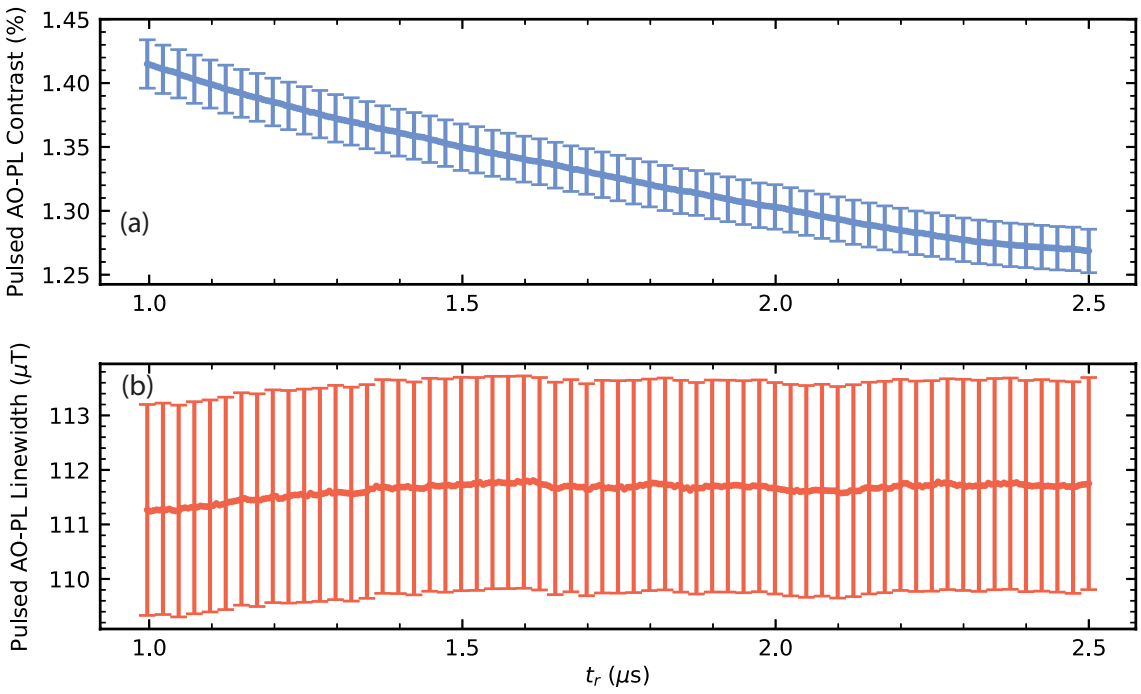


Figure 3.13: Fit amplitude (a) and linewidth (b) from the central near-zero-field AO-PL contrast of sample S2-15N as a function of signal readout timing t_r. Markers are the fit values with uncertainty indicated. While the amplitude reduces as t_r increases (consistent with results from Fig. 3.2.2(b) using sample S3-14N), the fit linewidth values are roughly consistent within error bars.

However, this millisecond-scale τ results in a low duty cycle for the pulsed AO sequence used here, emphasizing the need for further optimization to achieve higher sampling rates and enable sensitive pulsed AO measurements of higher-frequency magnetic signals. Employing NV-diamond samples with high [N] presents a potential solution. In bulk samples, [N] can reach $\sim$ 100 ppm, enabling [NV] $\sim$ 50 ppm and reducing T_1 to $\sim$ 70 μs [22]. While such higher [N] and [NV] may improve AO-PL contrast and pulsed AO sequence duty cycle by shortening both T_{cr} and T_{in} timescales, this approach also introduce trade-offs that require further evaluation for pulsed AO optimization, including: broader AO-PL linewidths and reduced effectiveness of common-mode noise rejection from longer optical spin polarization times due to higher optical absorption.

As discussed in Sec. 3.2.7, the pulsed AO protocol does not temporally separate the spin depolarization and optical polarization processes, and therefore is not analogous to pulsed ODMR to achieve an improvement in AO-PL linewidth. One possible solution is to apply magnetic field pulses to decouple the contribution of NV-NV cross-relaxation during the optical interrogation window. However, this method can further increase experimental complexity and may defeat the purpose of using the pulsed AO protocol for its simplicity.

Our findings provide new insights on NV-diamond sample selection and AO magnetometry protocols relevant to low size, weight, and power (low-SWaP) quantum sensors. Such devices can be particularly well suited for sensitive NV magnetometry in challenging environments, including extreme temperature, pressure, corrosive, and radiation conditions, broadening the diversity of quantum sensing applications [40].

Chapter 4: All-Optical Magnetometry at High Magnetic Fields

The investigations into high-field AO NV magnetometry described in this chapter were first conceptualized in the Walsworth group with Matthew J. Turner, who went on to be the initial lead researcher on this project, with support from the Department of Energy. Matthew's pivotal research on the feasibility of NV quantum sensing for fusion plasmas diagnostics contributed significantly to the motivation presented in Sec. 4.1. This chapter reports my ongoing work on performing AO magnetometry in high magnetic fields $> 100\,\mathrm{mT}$, with useful technical inputs from several current and past members of the Walsworth group, particularly Matthew J. Turner, Connor A. Hart, John W. Blanchard, Kristine V. Ung, and Paul V. Petruzzi. I first present the motivation for AO NV magnetic sensing as a tool for fusion plasmas diagnostics, then discuss the underlying physical principles for high-field AO operation, and finally present results measured at intermediate fields $\sim 10\,\mathrm{mT}$ and at high fields $> 100\,\mathrm{mT}$. The measurements performed at high fields utilize the pulsed AO protocol discussed in Chapter 3, and would not have been possible without the contribution from Corey Hawkins in constructing the optical system and helping me generate the correct pulse sequence using an Arbitrary Waveform Generator (AWG).

4.1 Motivation

4.1.1 Magnetic Diagnostics for Fusion Plasmas

Pursuing clean energy generation has been an active research focus amid the growing concerns of climate change. Fusion offers the potential to generate energy from abundant fuel supplies by using a confined plasma, without producing greenhouse gases or long-lived radioactive waste. The tokamak is a leading device for confining plasma with strong magnetic fields to achieve net energy gain, as shown in Fig. 4.1. As a potential substitute for low temperature superconductors (LTS), which became practical in the 1960s [55] operating around 4 K, the new generation of high-temperature superconductors (HTS) has successfully demonstrated higher-field generation (> 20 T) across a temperature range of 4.5 K to 77 K [56], enabling much smaller tokamaks. Measuring the magnetic fields from both the magnetic coils and the produced plasma is crucial for fusion plasma confinement.

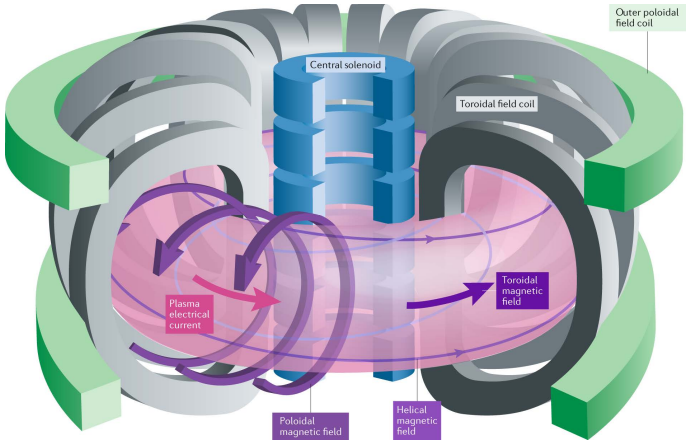


Figure 4.1: Example of toroidal and poloidal magnetic field for tokamak plasma confinement [3]. In high-field tokamaks, the toroidal field is $\sim$20 T and the poloidal field is $\sim$5 T at magnetic sensor locations.

These magnetic field measurements are used as inputs into the plasma control system, where a model for the plasma magnetohydrodynamic (MHD) equilibrium generates control signals for the magnet power supplies. These measurements need to be performed at a rate of $\sim$100 Hz, with an accuracy on order of 1% or less. The plasma shape must be controlled to remain within a margin of the bounds of the plasma-facing components inside the vacuum chamber. This control is particularly important for high-performance, highly-elongated and diverted plasmas, since elongation increases the demand on the system maintaining the vertical position of the plasma. In addition to overall plasma equilibrium control, magnetics measurements also support more detailed assessment of the plasma state. A wide variety of MHD-related fluctuations ($\sim$MHz) can increase losses of particles and energy. Magnetic sensors are used to detect these fluctuations and trigger ameliorative actions. Both equilibrium and turbulence measurements require sensors distributed around the outside of the plasma to capture the spatial variation of the magnetic field, as shown in Fig. 4.2.

4.1.2 Limitations of Current Sensors

Traditional electronic-based magnetic field probes, including inductive pickup coils and Hall probes, have been the main tools for diagnosing magnetic field in tokamaks [57]. The goal is to keep extending the burning plasma duration, from around 8 minutes in the International Thermonuclear Experimental Reactor (ITER) to a target of nearly 2 hours per plasma pulse in Demonstration Power Plant (DEMO) fusion reactor and eventually for much longer periods in future systems. This increase of burning plasma duration can

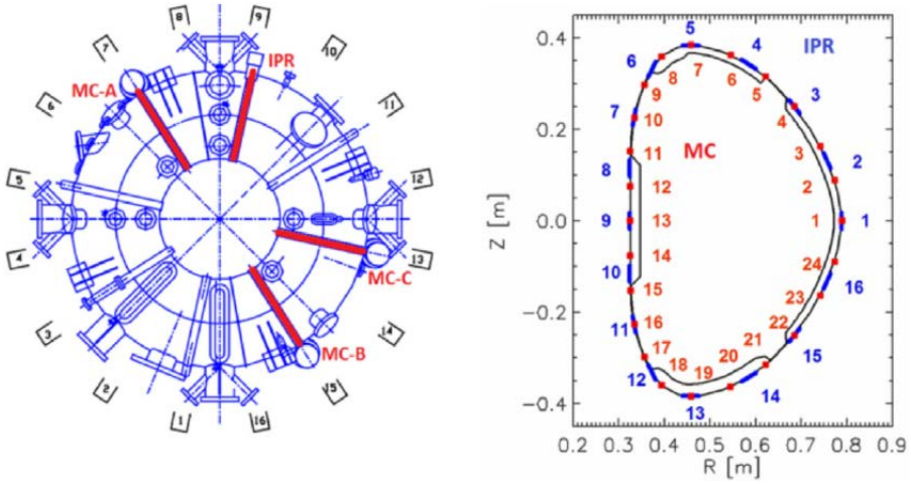


Figure 4.2: Example locations of diagnostic magnetic sensors in a tokamak [4]. The left panel shows top-down view of a tokamak vacuum vessel; red notations indicate four toroidal locations of sensor locations in this example. The right panel shows a side section view of a tokamak vacuum vessel; red and blue notations indicate poloidal sensor locations and the typical spatial sensor density needed for plasma control and turbulence measurements.

lead to greater error accumulation in inductive coils, since their operation relies on signal integration, and the harsh electromagnetic environment of a tokamak can introduce significant noise. In addition, electronic probes are highly susceptible to radiation-induced effects. These effects include increased radiation-induced conductivity as well as radiation damage to the insulation of the coil wire [58]. The increasingly hostile environment inside future reactors, with high neutron fluences and elevated gamma-radiation levels, and longer radiation exposure times, can severely challenge the existing measurement techniques. Furthermore, sensors placed at the vessel wall, directly between the hot plasma chamber and the external superconducting magnets, will need to tolerate operating temperature up to 300°C. The response of traditional Hall probes to external magnetic fields is also temperature-dependent, leading to inaccurate measurements over time without periodic re-calibration.

To summarize, the tokamak fusion environment presents four key challenges: 1) large operating voltages, ranging from a few hundred volts to a few kilovolts; 2) high magnetic field of up to 20 T; 3) elevated temperatures in the vacuum vessel and cryogenic temperatures in the superconducting magnets; and 4) radiation exposure. There is a strong need for developing new magnetometers capable of long-term operation inside the fusion system.

4.1.3 Motivation for AO NV Magnetometry

Diamond-based quantum sensors are a promising alternative to electronic probes for measuring magnetic fields inside a tokamak, owing to their radiation hardness and wide dynamic range. The underlying physical principles of NVs enable vector measurements with high sensitivity, and the direct connection between the magnetic measurements and fundamental physical constants offers the added advantage of reduced sensor calibration. However, constructing a conventional MW-based NV-diamond sensor within a tokamak would face several significant challenges: delivering the ~ 500 GHz MW control fields needed to coherently manipulate the NV electronic spin states under a 15-20 T bias field, mitigating the non-negligible inductive and capacitive coupling between the MW antenna and the tokamak's surrounding structure, and survivability of the MW antenna in the harsh tokamak environment.

Therefore, a more compact NV-diamond sensor with reduced electronic and optical complexity and greater potential ruggedness is desired for magnetic field diagnosis in fusion environments. By exploiting the PL quenching effect induced by spin state mixing

(detailed in Sec. 4.2), an alternative NV magnetometry protocol can be implemented that is both AO and MW-free. Although AO NV magnetometry is generally less sensitive than conventional MW-based techniques, it may still resolve mT-scale fluctuations (much smaller than the typical 1% fluctuations in an operational tokamak, as mentioned above) in the presence of a substantial background fields (∼15-20 T).

4.2 NV Spin-Mixing Physics

Recapping discussions in previous thesis chapters, the ground-state spin Hamiltonian of a single NV, neglecting the hyperfine interactions, can be written as:

$$H_{gs}/\hbar = D_{gs}{S_z}^2 + \gamma B_x S_x + \gamma B_y S_y + \gamma B_z S_z, \tag{4.1}$$

where (B_x, B_y) are the transverse magnetic field perpendicular to the NV symmetry axis, B_z is longitudinal field aligned along the NV symmetry axis, $D_{gs} = 2.87\,\text{GHz}$ is the ground state zero-field splitting, $\gamma = 2.8\,\text{MHz/G}$ is the NV electron gyromagnetic ratio, and (S_x, S_y, S_z) are the dimensionless electronic spin-1 operators. When the bias magnetic field is mostly aligned with one of the four NV orientations, the quantization axis is fixed by the NV defect, and Eq. 4.1 can be reduced to:

$$H_{gs}/\hbar = D_{gs}{S_z}^2 + \gamma B_z S_z. \tag{4.2}$$

The eigenstates from Eq. 4.2 correspond to the spin projections $|m_s = 0, +1, -1\rangle$. Under this bias field configuration (mostly axial field), the optical excitation and emission pro-

cesses can be treated as spin-conserving, preserving the NV optical spin polarization and spin-dependent PL readout, as detailed in Sec. 1.1.1 [Fig. 4.3(b)].

However, in the presence of a non-negligible transverse (off-axis) magnetic field [Fig. 4.3(a)], $\gamma B_x S_x$ and $\gamma B_y S_y$ terms can no longer be neglected in Eq. 4.1 and the quantization axis is no longer fixed by the NV axis. Diagonalization of the Hamiltonian in Eq. 4.1 yields different energy eigenstates, as depicted in Fig. 4.3(c). These eigenstates are the superpositions of the well-defined eigenstates obtained from Eq. 4.2. As a result, the optical excitation and emission processes are no longer spin-conserving (for example, the ground $|m_s = 0\rangle$ state is excited to a mixture of excited $|m_s = 0, +1, -1\rangle$ states), leading to inefficient optical spin polarization and reduced the PL emission.

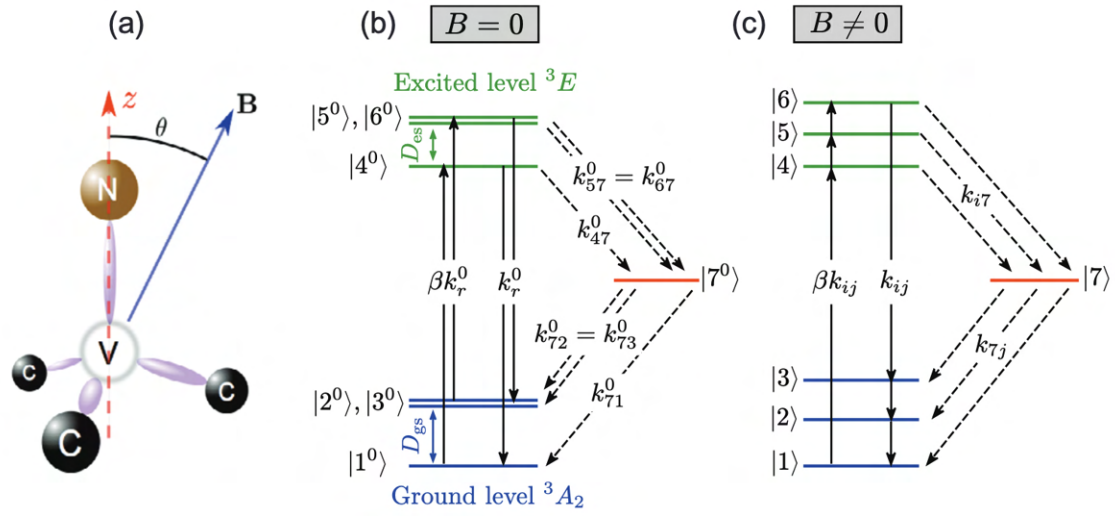


Figure 4.3: Under the presence of a non-negligible transverse field relative to the NV symmetry axis (a), the NV energy levels and associated transition rates between spin levels at zero field (b) are altered due to the spin-mixing effect (c) [5].

4.2.1 Numerical Simulation for Spin-Mixing

Diagonalizing the full Hamiltonian $H_{gs}/\hbar$ (and $H_{es}/\hbar$, treated analogously) in Eq. 4.1 with non-negligible (B_x, B_y) produces new eigenstates that are linear combinations of the eigenstates in zero-field, as described by Eq. 4.3 [5]. The coefficients $\alpha_{ij}(B)$ are computed from the expressions for H_{gs} and H_{es}; $\alpha_{77} = 1$, since $|7\rangle = |7^0\rangle$.

$$|i\rangle = \sum_{j=1}^{7} \alpha_{ij}(B)|j^0\rangle, \tag{4.3}$$

The new transition rates $k_{ij}(B)$ between the seven energy levels can then be calculated from the zero-field transition rates k_{ij}^0 through Eq. 4.4.

$$k_{ij}(\boldsymbol{B}) = \sum_{p=1}^{7}\sum_{q=1}^{7} |\alpha_{ip}|^2|\alpha_{jq}|^2 k_{ij}^0. \tag{4.4}$$

The zero-field transition rates are adapted from Ref. [5], with $k_{41}^0 = k_{52}^0 = k_{63}^0 = 63.7\,\mu s^{-1}$, $k_{14}^0 = \beta k_{41}^0$, $k_{25}^0 = \beta k_{52}^0$, $k_{36}^0 = \beta k_{63}^0$ where β is the optical pumping coefficient, $k_{57}^0 = k_{67}^0 = 53\,\mu s^{-1}$, $k_{72}^0 = k_{73}^0 = 0.5\,\mu s^{-1}$, $k_{47}^0 = 9.6\,\mu s^{-1}$, and $k_{71}^0 = 0.9\,\mu s^{-1}$.

Solving the classical system of rate equations described by Eq. 4.5, using the new transition rates $k_{ij}(B)$, then yields the spin population distributions across all seven levels at a given time. The steady-state PL from a single NV can then be calculated using Eq. 4.6, evaluated at a t sufficiently longer than spin state lifetime. The Hamiltonians for the other three NV classes are obtained by applying rotation matrices to project the bias field onto each orientation, then substituting the resulting components in place of (B_x, B_y, B_z) in

Eq. 4.1. The total PL emission from an NV ensemble is then produced by summing the steady-state PL intensity calculated from the Hamiltonian for each of the four NV classes.

$$\frac{dn_i}{dt} = \sum_{j=1}^{7}(k_{ji}n_j - k_{ij}n_i) \tag{4.5}$$

$$R(B,t) = \eta \sum_{i=4}^{6}\sum_{j=1}^{3} k_{ij}n_i(0)e^{-t/\tau_i}. \tag{4.6}$$

Fig. 4.4 shows the simulated normalized AO-PL intensity as a function of axial field B_z from 0 to 150 mT. The normalized intensity is determined by referencing the PL intensity to the corresponding value at $B_z = 0$. The optical pumping coefficient is set to $\beta = 0.05$ to reproduce the spin-mixing-induced normalized AO-PL changes measured near 10 mT for an NV ensemble in Ref. [59]. Two prominent AO-PL changes are visible near 50 and 100 mT, arising from the ESLAC and GSLAC processes, respectively. Because this simulation model is based on a single-NV Hamiltonian, it cannot capture cross-relaxation-induced AO-PL changes, such as NV-P1 cross-relaxation near 50 mT, and NV-NV cross-relaxation near zero-field and 60 mT.

To investigate the feasibility of AO operation at high fields, we simulated the normalized AO-PL intensity as a function of applied fields (B_z, $B_\perp$), with B_z from 0.15 to 15 T and $B_\perp$ from 0.15 to 5 T, as shown in Fig. 4.5(a). The normalized intensity is determined by referencing the simulated PL intensity to the maximum value within a given (B_z, $B_\perp$) scan. We further compute the slope of the normalized AO-PL intensity with respect to $B_\perp$ (b) and B_z (c). Fig. 4.5(b) shows that, under substantial bias fields ($B_z \sim 10$ T and $B_\perp \sim 1$ T), larger AO-PL changes arise from variations in $B_\perp$ than from variations

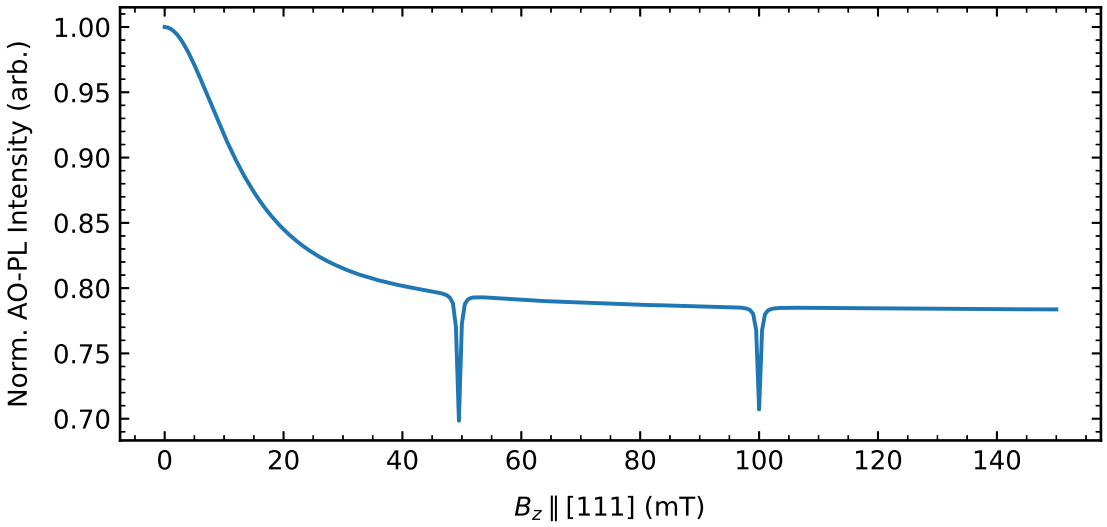


Figure 4.4: Simulated normalized AO-PL intensity as a function of B_z from 0 mT to 150 mT. The spin-mixing effect leads to a prominent AO-PL intensity reduction between 0 and 40 mT. Two sharp AO-PL intensity drops are visible near 50 and 100 mT, due to the ESLAC and GSLAC processes, respectively.

in B_z. The slope with respect to $B_\perp$ is about 3%/T in the presence of a 10 T B_z and 1 T $B_\perp$ field. The target 1% magnetic field change (of 100 mT, described in Sec. 4.1) would therefore yield a 0.3% change in the measured PL intensity for an NV ensemble. Sensing B_z changes is also achievable, but with 10× worse sensitivity than detecting $B_\perp$ variations. These results indicate the feasibility of AO operation at high fields (near 10 T for the proposed tokamak magnetic diagnosis), given the presence of a substantial transverse field $B_\perp \sim 1$ T.

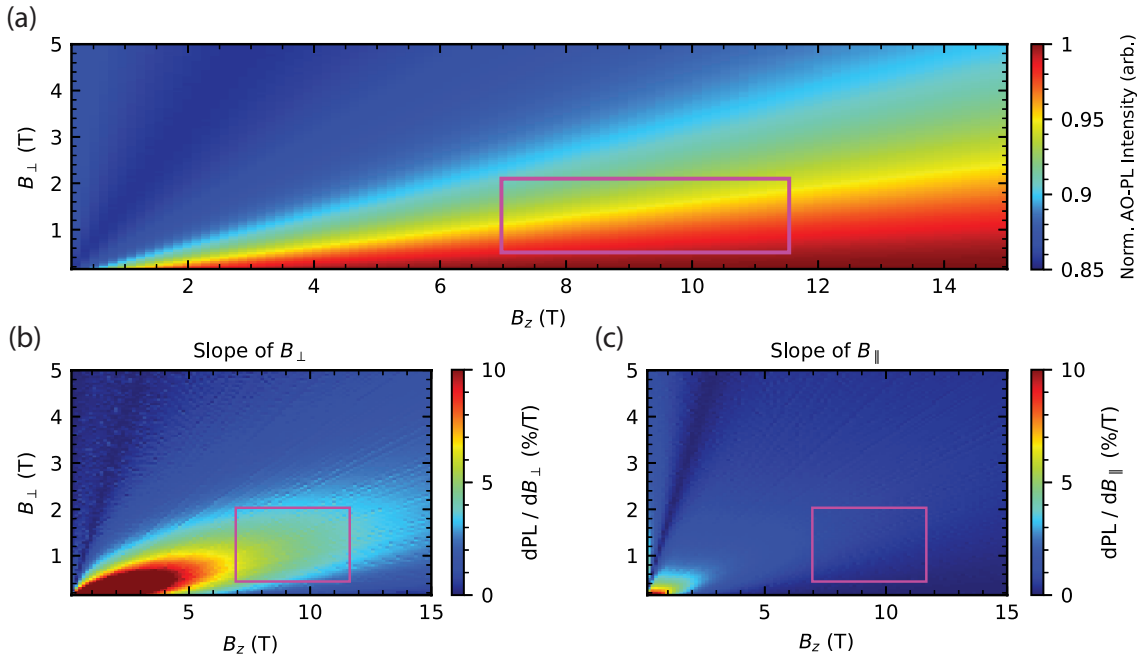


Figure 4.5: (a) Simulated normalized AO-PL intensity from an NV ensemble as a function of axial field B_z from 0.15 to 15 T and transverse field $B_\perp$ from 0.15 to 5 T. (b) Derivative of the normalized AO-PL intensity with respect to $B_\perp$, showing nontrivial sensitivity to $B_\perp$ changes. (c) Derivative of the normalized AO-PL intensity with respect to B_z. In the high field regime, sensitivity to B_z changes is reduced by roughly a factor of 10 relative to $B_\perp$. Boxed purple areas indicate optimal NV alignment in order to be sensitive to $B_\perp$ at high fields inside a tokamak.

4.3 Experimental Results

4.3.1 AO-PL Changes with Intermediate Bias Magnetic Fields

Sec. 2.3.2 of Chapter 2 demonstrated AO-PL contrast from spin mixing at low magnetic fields (< 2 mT) using sample S5-14N with ≈ 0.3 ppm [NV].

As shown in Fig. 1.6, a large AO-PL intensity change from spin mixing is observed between 5 and 20 mT. To further validate the numerical model described in Sec. 4.2.1, we applied a bias field of about 19 mT using a permanent magnet, and applied external B_z and $B_\perp$ fields using two separate coils. Each coil is estimated to produce ~ 0.5 mT

at the location of the NV-diamond, based on its geometry, the applied current, and the number of turns. Fig. 4.6 illustrates the optical setup. The NV PL is first collected by a light pipe attached to the diamond, then transmitted to the photodiode for readout through a multi-mode optical fiber.

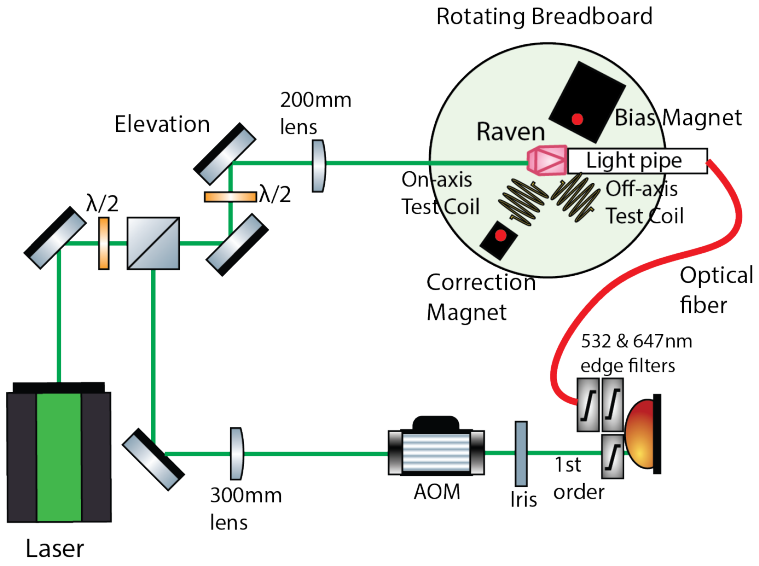


Figure 4.6: Schematic of the optical system to measure spin-mixing-induced AO-PL changes in a bulk NV-ensemble diamond. A permanent magnet provides a bias field of about 19 mT. Two coils placed near the NV-diamond provide B_z and $B_\perp$ modulations separately. An AOM and a balanced photodiode, together with a feedback system, mitigate long-timescale PL intensity drift due to local temperature changes at the NV-diamond.

4.3.1.1 Drift Mitigation

Because the measurements discussed in this section rely on CW AO-PL detection, it is crucial to mitigate PL intensity drift on both short timescales, e.g., during coil modulation, and long timescales, e.g., across repeated experiment runs.

To suppress long-timescale drifts arising from both local temperature changes at the NV-diamond and laser intensity fluctuations, we utilized an AOM and a balanced photo-

diode to keep the measured voltage on the balanced channel consistent across experiment repetitions, as illustrated in Fig. 4.6. This is achieved with a software feedback system that controls the laser power delivered to one input channel of the balanced photodiode by tuning the RF power driving the AOM.

To reduce the effect of short-timescale drifts on the averaging performed within each experiment run, we apply four sets of field modulations for each value of $(B_\perp, B_z)$, as shown in Fig. 4.7. For each $(B_\perp, B_z)$ value, the PL readout with both coils turned off during the final window serves as a baseline PL intensity. By keeping the baseline voltages consistent across the $(B_\perp, B_z)$ scan during data post-processing, we can ensure that data averaging improves measurement SNR without washing out genuine AO-PL changes from residual readout drifts.

4.3.1.2 Spin-Mixing Results

By implementing the aforementioned drift mitigation methods, we measured the AO-PL intensity by sweeping the magnetic field created by the coils from 0 to 0.5 mT with a step size of 0.05 mT. With the permanent magnet providing the bias field, the axial field B_z was taken to vary from 19 to 19.5 mT. The resulting AO-PL changes as a function of $B_\perp$ and B_z are shown in Fig. 4.8(a). This experimental result is in agreement with the numerical result obtained using the method described in Sec. 4.2.1 with the same model parameters [Fig. 4.8(b)]. The change of AO-PL from B_z and $B_\perp$ resembles the near-zero-field result in Fig. 2.7 measured using sample S5-14N with ≈ 0.3 ppm [NV]. The experimental result, however, exhibits an AO-PL change about $10\times$ smaller than

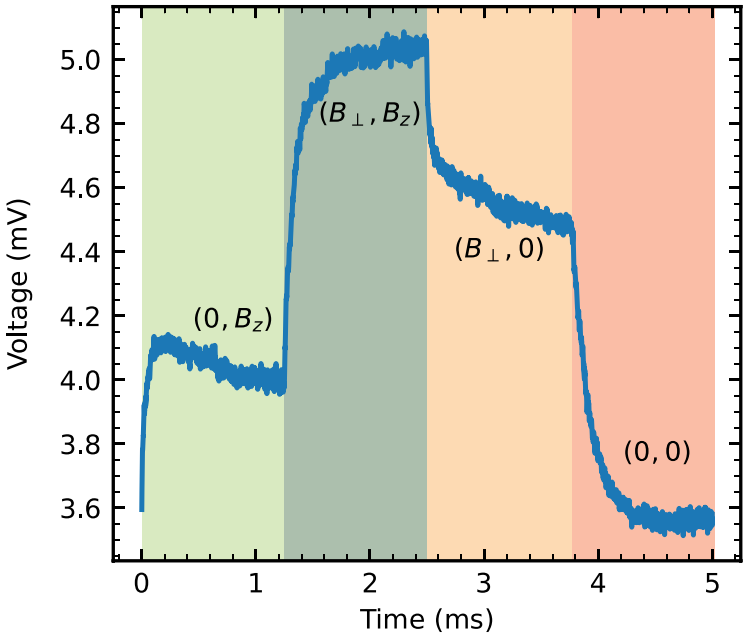


Figure 4.7: An example AO-PL intensity measurement from the photodiode voltage over one modulation period. During this period, the fields produced by both coils are modulated to form four distinct readout windows. The AO-PL intensity with both coils turned off (0, 0) serves as the baseline measurement. Short-timescale drifts is mitigated by keeping the baseline measurements consistent across the $(B_\perp, B_z)$ scan during data post-processing.

that predicted by the numerical model. This discrepancy may stem from our use of an NV ensemble, whereas the numerical model is based on a single NV. Nonetheless, this agreement in the trend of AO-PL changes indicates the feasibility of $B_\perp$ and B_z sensing at this intermediate ($\sim 20\,\text{mT}$) field, and supports the ability to scale AO operation to the proposed high-field regime.

4.3.2 AO-PL Changes in Strong Bias Magnetic Fields

4.3.2.1 Experiment Apparatus

Having shown that AO-PL changes from spin mixing can be resolved at intermediate magnetic fields around 20 mT using a permanent magnet, we next aim to perform

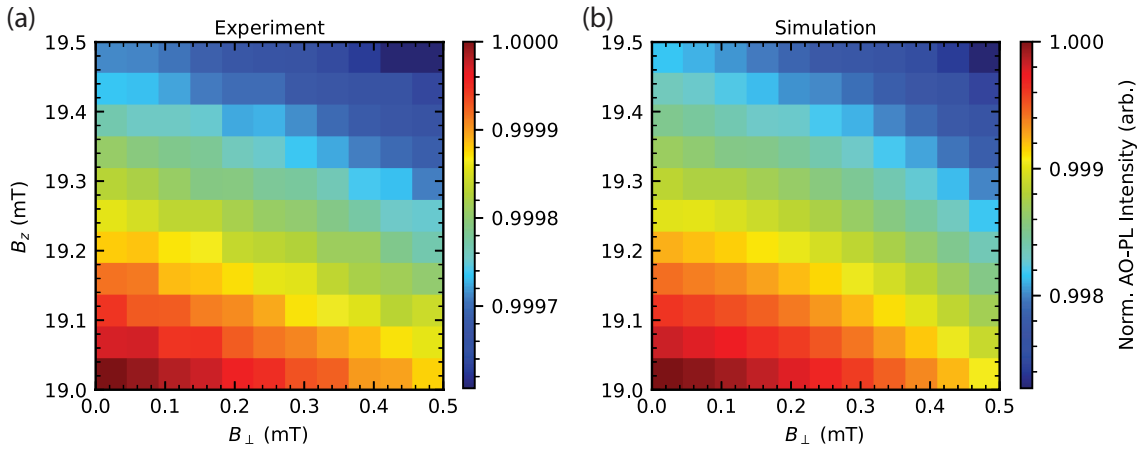


Figure 4.8: (a) Experimentally determined normalized AO-PL intensity as a function of applied magnetic fields. (b) Simulated normalized AO-PL intensity using the model described in Sec. 4.2.1. The experimental AO-PL changes from an NV ensemble are about $10\times$ smaller than the numerically predicted results modeled from a single NV.

measurements at strong fields. To produce a bias field $> 100\,\mathrm{mT}$, we switched to an electromagnet capable of generating up to 300 mT without an additional water-cooling system. This required us to switch to a different optical system than that shown in the previous section [Fig. 4.6], leading to several challenges.

First, the optical system became more sophisticated, particularly since it is also shared with NV-NMR projects. A single-mode fiber transmits a CW or pulsed laser beam to a separate optical system before exciting the NV-diamond. Second, we incorporated two rotational stages to carefully align the NV orientations to the bias field. This required a cantilever-arm design to accommodate both rotational degree of freedom and laser beam propagation, introducing mechanical instability for the NV-diamond positioned at the center of the electromagnet. The combination of both optical and mechanical stability challenges necessitates the use of the pulsed AO protocol, detailed in Chapter 3, to suppress this slow-timescale noise.

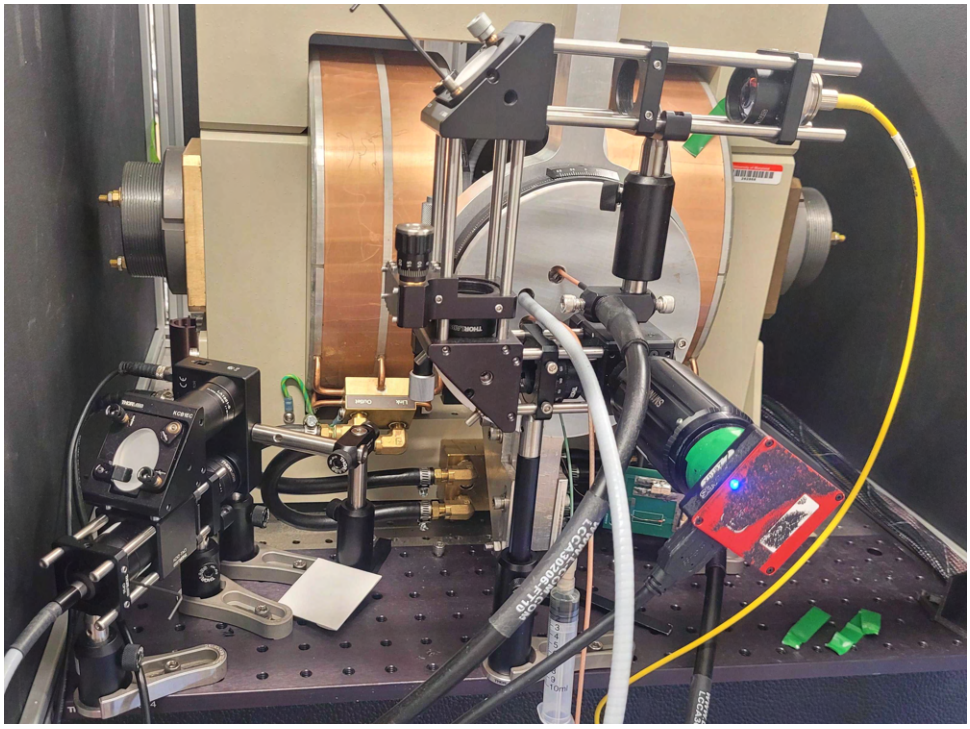


Figure 4.9: The electromagnet provides a bias field up to $\sim$ 300 mT. Two rotational stages allow careful alignment of the NV orientations to the applied field. A single-mode fiber transmits a CW or pulsed laser beam to optically excite the NV-diamond, and a separate liquid light guide collects the NV PL.

4.3.2.2 AO-PL as a Function of B_z

We began by measuring the pulsed AO-PL intensity as a function of axial field B_z from 0 to 240 mT, using a sequence dark time of $\tau = 3$ ms. The normalized AO-PL intensity is determined by referencing the PL intensity to the corresponding value at $B_z = 120$ mT. In Fig. 4.10, in addition to the spin-mixing-induced AO-PL change from 10 to 40 mT, two further AO-PL features are visible: one near 50 mT (NV-P1 cross-relaxation) and one near 100 mT (GSLAC, see inset). These results support the pulsed AO protocol as an effective method for resolving AO-PL changes arising from spin mixing and other mechanisms in the presence of a non-negligible $B_\perp$, as discussed in Sec. 3.2.5.

We repeated the measurements with a shorter dark time $\tau = 1$ ms. Rather than shifting the normalized AO-PL intensity across the entire B_z scan, this change of τ mainly improves the signal from the spin-mixing process for B_z between 0 to 40 mT, as shown in Fig. 4.10. Optimizing τ to resolve spin-mixing-induced pulsed AO-PL intensity changes is left for future work.

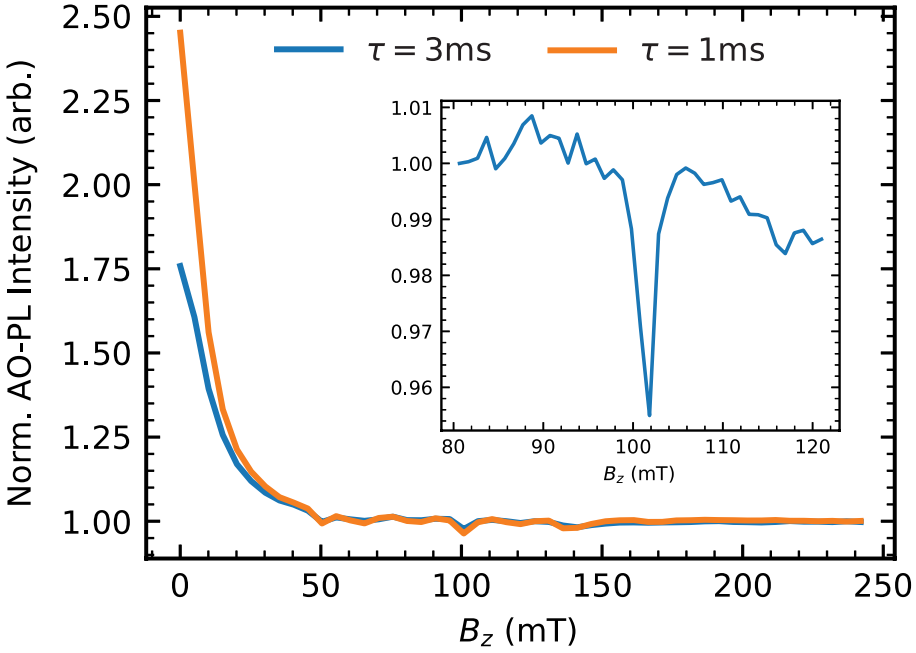


Figure 4.10: Experimentally measured pulsed AO-PL intensity as a function of B_z from 0 to 240 mT, with sequence dark time $\tau = 3$ ms (blue) and $\tau = 1$ ms (orange). Inset shows the resolved AO-PL feature from the GSLAC process around 100 mT, measured with $\tau = 3$ ms.

4.3.2.3 AO-PL Changes From Off-axis Magnetic Fields

A separate perturbation coil is mounted close to the NV-diamond to provide $B_\perp$ for the measurement. Fig. 4.11 illustrates the geometry of the field from the coil relative to the NV-diamond [100] plane (purple) and the bias field from the electromagnet (red arrow). The constrained space near the NV-diamond within the electromagnet restricts

the coil design, resulting in a non-optimal perturbation-field direction of 54.73° relative to B_z, rather than the ideal 90°.

Based on the numerical simulation in Fig. 4.5(b), NV is most sensitive to changes in $B_\perp$ at high field, provided a substantial $B_\perp$ bias is already present. Because the bias field from the electromagnet is fixed along z, we manually misaligned the NV-diamond by rotating it about the x-axis (green arrow in Fig. 4.5(b)) by about 5°. This introduces a significant $B_\perp$ component relative to the NV orientation, via projection of the bias field.

We then measured the pulsed AO-PL intensity as a function of current applied to this perturbation coil, under a bias field $B_z = 20, 120,$ and 300 mT, as shown in Fig. 4.11(b). At $B_z = 20$ mT, there is a visible change in the pulsed AO-PL intensity as the field produced by the coil increases, which is expected given our findings described in the previous section [Fig. 4.8]. However, this trend, particularly between $I_\perp = 2$ A and $I_\perp = 4$ A, becomes inconsistent as B_z gets larger. Given the non-optimal field geometry produced by the perturbation coil, it remains inconclusive whether any observed change in pulsed AO-PL intensity arise from field variations in the axial field B_z or the transverse field $B_\perp$. Fig. 4.12 shows the simulated derivative of the normalized AO-PL intensity with respect to $B_\perp$ under an applied $B_\perp$ from 50 to 100 mT and B_z from 100 to 300 mT. A reduction in normalized AO-PL intensity by a factor of 10 is applied here from the experimentally observed result using an NV ensemble, as discussed in Sec. 4.3.1.2. With misalignment under the maximum applicable bias field of 300 mT, depicted by the purple boxed area, the predicted AO-PL contrast is very modest, around $0.01\%/\text{mT}$. This indicates that a system with low optical intensity noise is needed to measure transverse field $B_\perp$ variations on the order of a few mT.

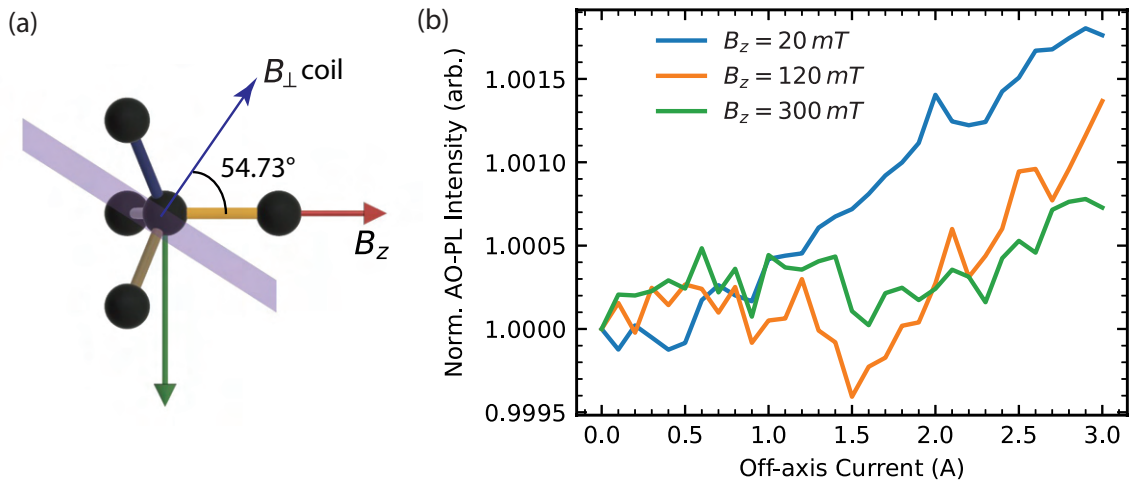


Figure 4.11: (a) Illustration of the perturbation field produced by a coil that is perpendicular to the NV-diamond's [100] face (purple). The perturbation field for the measurement is 54.73° relative to the B_z bias field, instead of 90°. (b) Experimentally measured pulsed AO-PL intensity as a function of applied current to the perturbation coil under a bias field $B_z = 20\,\text{mT}$ (blue), $B_z = 120\,\text{mT}$ (orange), and $B_z = 300\,\text{mT}$ (green). Spin-mixing-induced AO-PL intensity change is visible at $B_z = 20\,\text{mT}$, but is inconsistent at the higher fields $B_z = 120\,\text{mT}$ and $B_z = 300\,\text{mT}$.

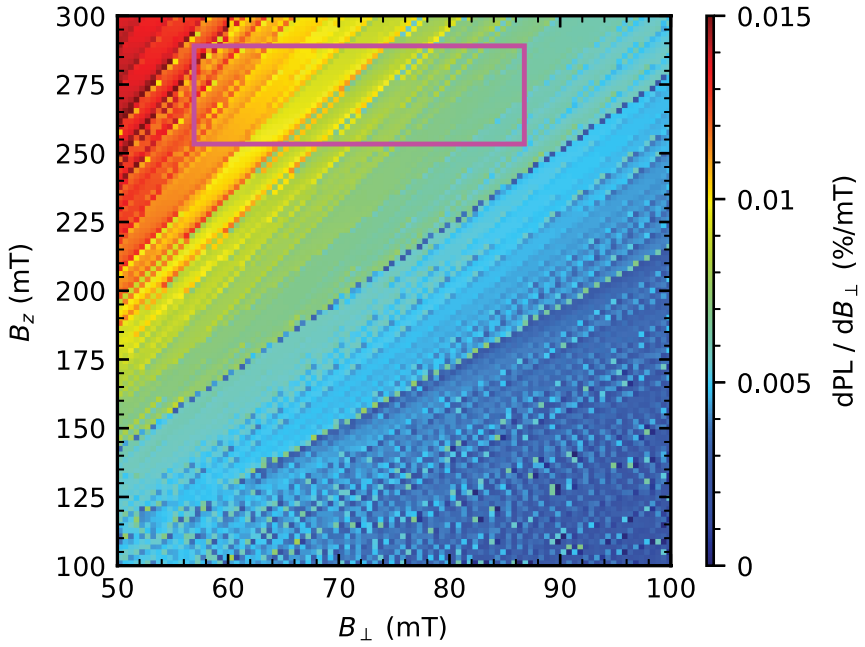


Figure 4.12: Simulated derivative of the normalized AO-PL intensity with respect to $B_\perp$ as a function of transverse field $B_\perp$ from 50 to 100 mT and axial field B_z from 100 to 300 mT. Around 0.01% of AO-PL contrast is predicted for every mT change of $B_\perp$ with a misalignment of the NV system inside the electromagnet producing a maximum bias field of 300 mT, as indicated by the purple box.

4.4 Future Work

This chapter has primarily described the progress in validating the spin-mixing-induced AO-PL intensity changes at intermediate fields ($\sim 20\,\mathrm{mT}$) and the feasibility of using the pulsed AO protocol for measurements at higher fields ($> 100\,\mathrm{mT}$). To demonstrate clear evidence of AO-PL intensity variations arising from changes in $B_\perp$ at high fields, improvements in the mechanical placement of perturbation coils and in the AO magnetometry protocol can be made in future work.

4.4.1 Mechanical Improvements

The current electromagnet configuration limits the placement of perturbation coil(s) for optimal AO operation. Instead of using an electromagnet, a Halbach array could also produce a substantial bias field, with increased positional flexibility for the diamond sensor, particularly since sweeping the bias field is no longer required. This may allow better control over both the NV diamond rotation and the applied $B_\perp$. With proper calibration of the produced $B_\perp$, we may be able to demonstrate AO magnetometry in this high-field regime.

4.4.2 Pulsed AO magnetometry Protocol

As shown in Fig. 4.10, optimizing the sequence dark time τ can lead to an increased spin-mixing-induced AO-PL intensity change. To study this τ-dependence, we can introduce a ground-state depolarization between the NV electronic spin sublevels to the numerical model [Sec. 4.2.1], which alters the initial spin population distribution after

a dark time τ. However, this milliseconds-scale τ leads to a low sequence duty cycle and limits the bandwidth of $B_\perp$ signals measurable with the pulsed AO protocol. For the proposed magnetic-diagnostic application inside a tokamak, measuring MHD-related fluctuations ($\sim$MHz) is of interest in addition to detecting slower magnetic field fluctuations at a rate $\sim$100 Hz. Future work may consider bulk NV-diamond samples instead of the thin-layer NV-ensemble samples used in the present study. The higher [N] and natural abundance of ^{13}C nuclear spins in bulk samples can lead to a shorter T_1, which in turn affects the optimal choice of τ for resolving spin-mixing-induced AO-PL changes, similar to the discussion in Sec. 3.3.

4.4.3 Measurement of Possible Radiation-induced Effects on AO Operation

The radiation hardness of NV-diamond is another topic to be explored. In particular, high neutron fluences anticipated for future tokamaks can lead to more vacancies inside the diamond lattice [60]. More NV may form as a result, aided by the elevated temperature inside a tokamak. Conversely, gamma radiation can decrease the population of NV^- used for magnetometry via conversion to the neutral charge state (NV^0) [31–33, 61]. Future work can investigate these radiation-induced effects on high-field AO magnetometry, including the resulting need to re-calibrate the AO sensitivity as the NV^- concentration changes.

Chapter 5: NV-Diamond CW-ODMR Magnetometry for a Quantum Hardware Teaching Lab

Given the robustness of diamond and the ambient-condition operation of the NV center, NV-diamond systems can serve as a powerful platform to demonstrate quantum sensing outside the laboratory, in settings with limited access to sophisticated electronic equipment. Previous chapters focused on my exploration of AO magnetometry, whose simplified, MW-free system design gives it strong potential for real-world applications. This chapter describes the development of a benchtop NV-diamond education module for CW-ODMR magnetometry and its associated learning goals, designed for the quantum hardware teaching lab (ENEE 493) in the Department of Electrical and Computer Engineering at the University of Maryland. Such an education module is an effective tool for preparing undergraduate students for more demanding quantum measurement tasks, by guiding them to understand the underlying physics while gaining hands-on experience. I developed the initial optical setup and provided technical assistance as Gavishta Liyanage led subsequent modification to the system. Prof. Julius Goldhar supervised the design iteration and first taught the lab course in the Fall 2025 semester. Matthew L. Markham of Element Six provided the HPHT NV-diamonds used in the setup.

5.1 Motivation

CW-ODMR is the most widely used NV magnetometry protocol, owing to its easy experimental implementation. The principles of CW-ODMR operation are detailed in Sec. 1.2.1.1. A typical CW-ODMR experiment contains these crucial components: a green laser, an RF signal generator capable of producing MW signals near 2.87 GHz, a MW antenna, a photodetector, and most importantly, an NV-diamond sample.

Because of this simplicity, a CW-ODMR system can also serve as an effective teaching tool. First, students can get familiar with several core physical principles from working through the CW-ODMR protocol, including optical spin polarization, MW spin manipulation, spin-state-dependent PL, and the Zeeman shift. In addition, carrying out CW-ODMR experiments gives students hands-on experience with optical alignment, MW antenna design and placement, and electronics control, all without the need for cryogenics or vacuum systems.

5.2 Learning Objectives

5.2.1 NV Physics

With the assumption of one lab class per week lasting around 3 hours, a student team is expected to spend one to two weeks completing the NV-diamond educational module. By the end of this module, a student should be able to:

- Understand the four distinct NV crystallographic orientations and why they enable vector magnetometry.

- Explain, in their own words, the spin-state-dependent NV PL emission process and why it enables optical readout.
- Predict how the CW-ODMR resonance frequencies shift with an applied bias magnetic field through the Zeeman interaction, and relate that shift to the NV electronic spin gyromagnetic ratio.

5.2.2 Experiment Control

In addition to understanding the NV physics, a student should gain valuable hands-on experience with:

- Operating a Class IIIa laser and following the laser safety procedures.
- Optical alignment of components such as mirrors, lenses, dichroic beamsplitters, and photodetectors.
- Alignment of the MW antenna and bias coils, and the effect of misalignment on the measured spectrum.
- Connecting laboratory electronics such as RF signal generator and oscilloscope.
- The workflow and use of the instrument control software and measurement protocols.
- Debugging the setup to obtain expected measurement results.

5.3 Experiment Apparatus

Two considerations guided the experiment design: (1) students work only with a Class IIIa laser (maximum CW power 5 mW) to avoid laser safety hazards; and (2) electronics components are reusable across other course modules (e.g., SQUID, outside the scope of this dissertation) to reduce the overall cost.

Fig. 5.1 shows an overview of the NV CW-ODMR education module. The main electronics components include the computer running Python-based experiment control (a), the oscilloscope for data acquisition (b), the RF signal generator providing MW signals near 2.87 GHz (c), the main optical system with the NV-diamond (d), and power supply in (e) that drives currents through the coils in (d) to produce magnetic fields of varying magnitude. Among these components, the computer, oscilloscope, photodetector and camera in (d) are also used in other modules offered in the lab course.

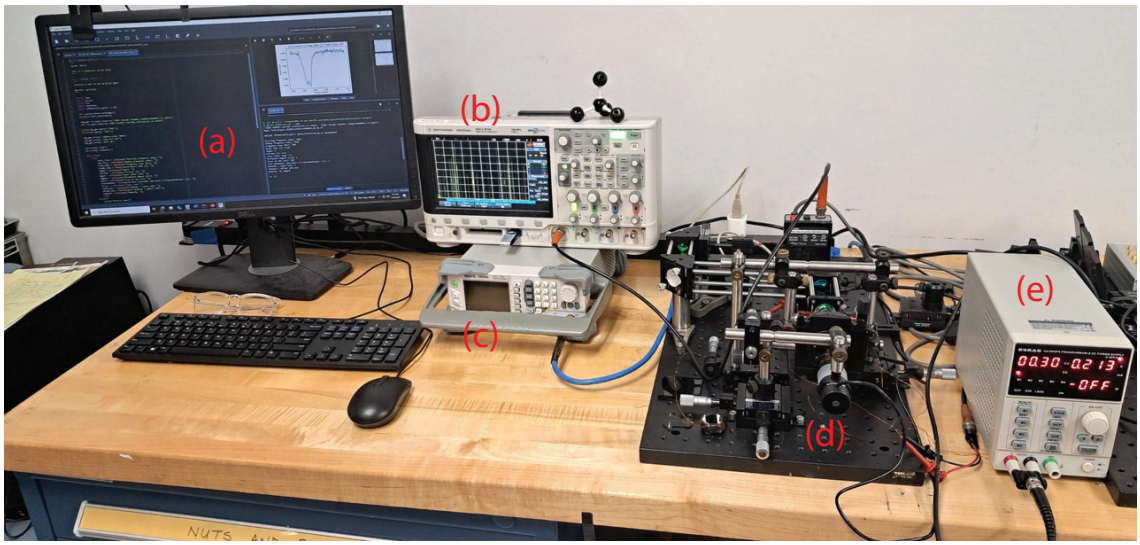


Figure 5.1: An overview of the NV CW-ODMR education module, with (a) computer and display for experiment control and data analysis; (b) oscilloscope for data collection; (c) RF signal generator; (d) optical system on a breadboard; and (e) power supply to drive electrical coils to produce magnetic fields with controllable magnitudes.

The benchtop NV experiment setup on the breadboard [Fig. 5.1(d)] is designed to be minimal, both to keep cost and footprint low and to make every functional block visible. Its relatively simple optical system, incorporating various translation stages, provides flexible adjustability for a student building the setup for the first time. The subsystems are described in more details below.

5.3.1 Optical Excitation and Collection

A low-cost 520 nm laser diode (VLM-520-74 LPT, max power 4 mW) is directed through two optical mirrors and a dichroic beamsplitter, then focued onto the NV-diamond sample by a plano-convex lens (f=25 mm), as illustrated in Fig. 5.2(a). The plano-convex lens focuses the laser beam to achieve higher optical excitation intensity, while simultaneously collimating the red PL emitted from the NV-diamond for collection. The dichroic beamsplitter reflects the incoming green laser beam and transmits the red PL. The red PL is then focused onto a photodetector through a second converging lens and a longpass filter.

5.3.2 NV-diamond Sample

The NV-diamond samples used in the system are provided by Element Six Ltd. Unlike the quantum-grade samples listed in Table 2.1, these are monodie synthetic single crystal diamond intended for wire drawing applications (Monodie MD111). They have an inscribed circle diameter of about 1 mm and a thickness of 1 mm, containing roughly 4.5 ppm [NV]. Fig. 5.3 shows an HPHT NV-diamond (sample S7-14N, see Table E.1)

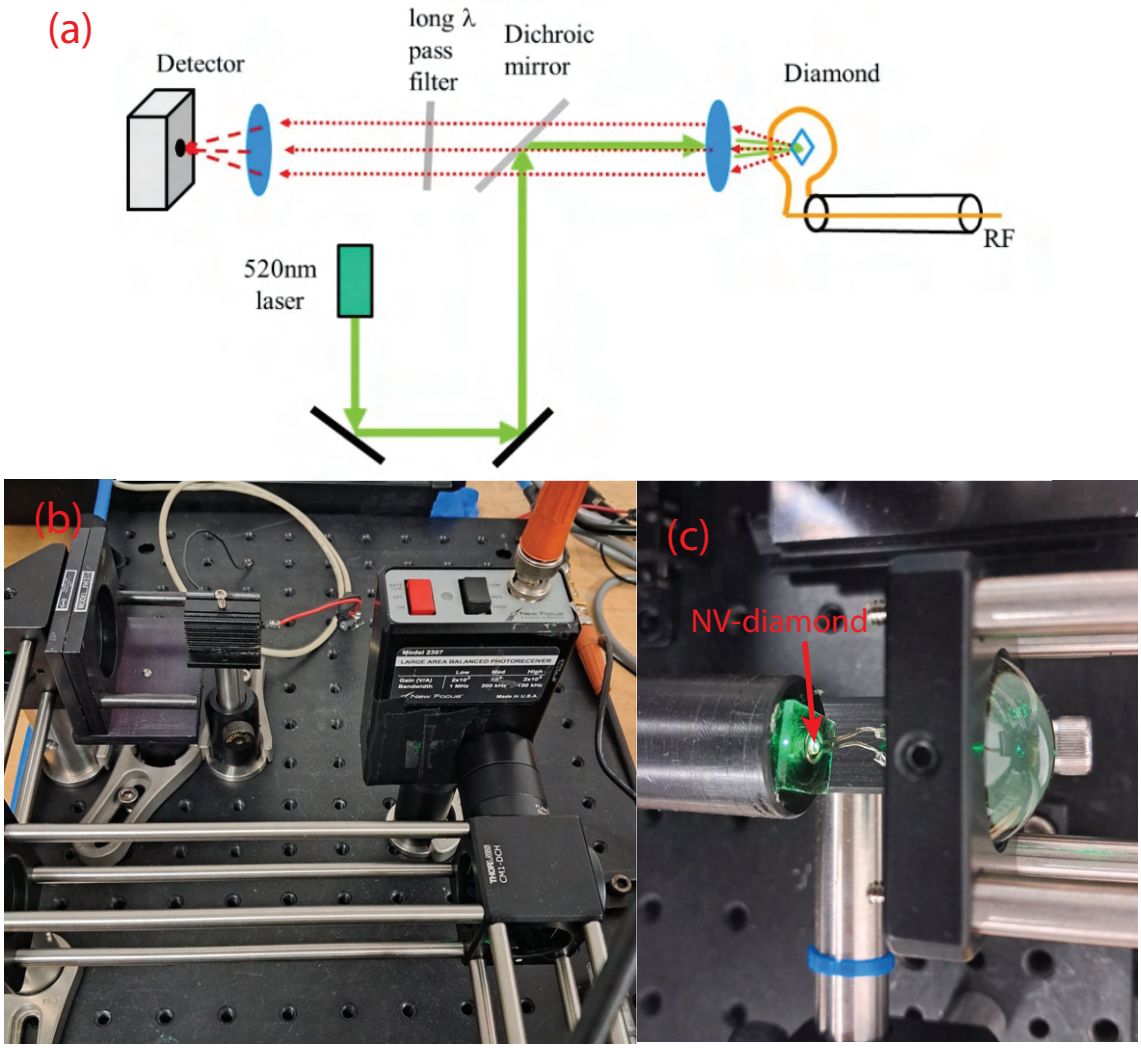


Figure 5.2: (a) Schematic of the experimental setup for the NV CW-ODMR education module. (b) Optical components include a 520 nm laser diode, optical mirrors, a dichroic beamsplitter, and a photodetector. (c) A f=25 mm plano-convex lens focuses the laser beam onto the NV-diamond mounted on a glass substrate. A home-made antenna is placed around the NV-diamond to provide a MW control field.

with red PL emission, captured by the camera in the setup. In addition, these diamond samples are HPHT-grown [111] plates, meaning the optical axis normal to the diamond's [111] face aligns with one of the four NV orientations. This differs from the [100]-plate diamonds used in previous chapters [Fig. 2.3(a)] and requires a different alignment procedure.

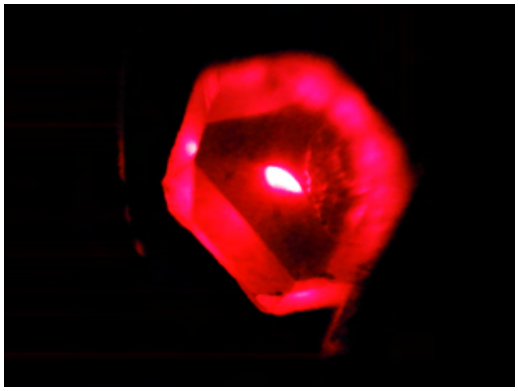


Figure 5.3: An monodie synthetic single crystal HPHT diamond (Element Six Monodie MD111) with red PL emission, imaged by a camera in the optical setup.

5.3.3 Microwave Excitation

An RF signal generator (Rigol DSG830) sweeps in frequency across the region near 2.87 GHz and drives a simple wire loop positioned close to the diamond [Fig. 5.2(c)]. This antenna is mounted on a translation stage, allowing precise adjustment of its position for efficient MW driving.

5.3.4 Bias Magnetic Field Control

Fig. 5.4 shows a pair of transverse coils and one axial coil that provide bias magnetic fields, driven by an external power supply (Korad KA3005ps). As described in Sec. 5.3.2, the [111]-plate geometry places one of the four NV orientations normal to the diamond face, aligning it with the axial field $B_{\parallel}$ produced by the axial coil. The pair of transverse coils, producing a transverse magnetic field $B_{\perp}$, further allows the student to observe the effect of a vector bias field on the resulting ODMR spectrum. This $(B_{\perp}, B_{\parallel})$ field configuration is identical to that illustrated in Fig. 2.2(b).

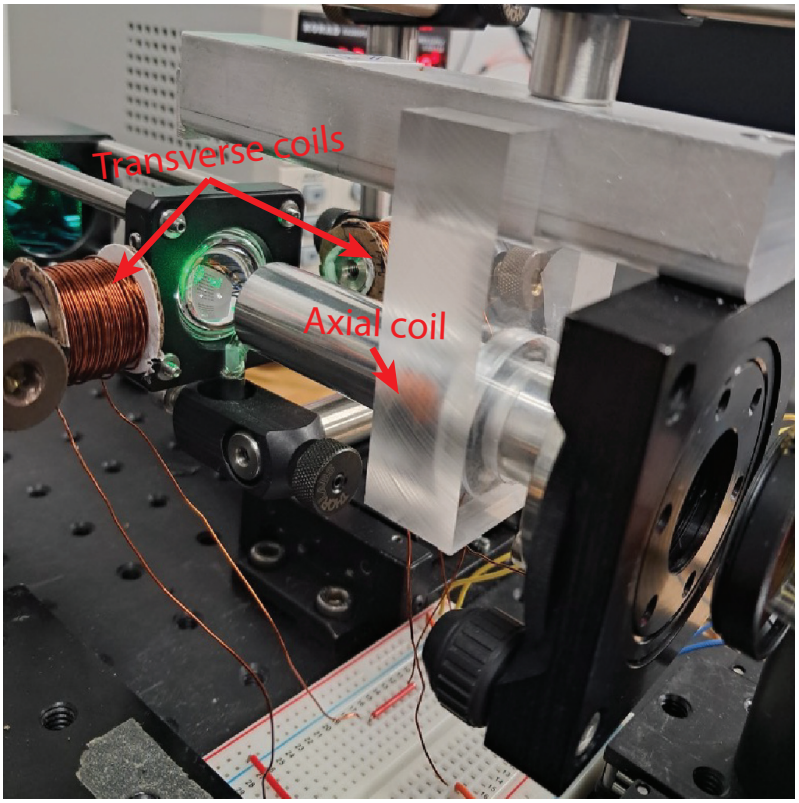


Figure 5.4: A pair of transverse coils and an axial coil provide bias magnetic fields of controllable direction and magnitude for CW-ODMR measurements.

5.3.5 Optomechanical Components

Several manual stages are incorporated into the system to give students finer control over the experiment. Linear translation stages enable positional adjustment of the MW loop antenna and the transverse and axial coils, each of which affects the measured ODMR spectrum. Furthermore, the NV-diamond is mounted on a rotational stage [Fig. 5.4], allowing students to observe how the ODMR resonances change as the sample is rotated under a bias vector field.

5.3.6 Data Acquisition

Rather than using a high-sampling rate data-acquisition device (DAQ), which is commonly used in research labs, an oscilloscope (Agilent DSO-X-2014A) records the analog output voltage from the photodetector. The MW frequency is stepped in 100 kHz increments with a dwell time of 10 ms at each frequency. This dwell time allows the oscilloscope to record, for each MW frequency, a value averaged over the voltages measured during this window. These averaged voltages are then plotted as a function of MW frequencies on the computer through a separate data analyzing process; representative results are shown in the next section.

5.4 Experiment Results

This education module is not intended to provide highly sensitive measurements, but rather a transparent, hands-on demonstration of the essential physics underlying the CW-ODMR protocol. Because a [111]-plate NV-diamond is used, the transverse coils provide a magnetic field ($B_\perp$) perpendicular to the [111] NV orientation class, which is aligned normal to the diamond surface. Therefore, the ground-state Hamiltonian for the [111] NV class, neglecting the hyperfine interactions, can be written as:

$$H_{gs}/\hbar = D_{gs}{S_z}^2 + \gamma B_\perp S_x \cos(\theta) + \gamma B_\perp S_y \sin(\theta) + \gamma B_\parallel S_z, \tag{5.1}$$

where $D_{gs} = 2.87\,\text{GHz}$ is the ground-state zero field splitting, $\gamma = 28.024\,\text{MHz/mT}$ is the NV electron gyromagnetic ratio, θ is the rotational angle of the NV-diamond about the

[111] axis, and $B_{\parallel}$ is the axial magnetic field produced by the axial coil. The Hamiltonian for the other three NV classes are obtained by applying rotation matrices to project the bias field onto each orientation, then substituting the resulting components in place of $(B_{\perp}\cos(\theta), B_{\perp}\sin(\theta), B_{\parallel})$ in Eq. 5.1.

Fig. 5.5 compares the measured CW-ODMR spectra at $\theta = 0°$ (a) and $\theta = 30°$ (b) with the corresponding simulation results. The measured voltage values are normalized to the average voltage of the final five frequencies, producing a contrast value in percent. Each ODMR resonance is approximated by a Lorentzian lineshape $L(f)$ as a function of applied MW frequency f:

$$L(f) = \frac{A}{\left[1 + \frac{(f-f_c)^2}{(\Gamma/2)}\right]}, \tag{5.2}$$

where A is the resonance depth, f_c is the resonance frequency, and Γ is the resonance linewidth. The simulation ODMR spectrum is then produced by summing Lorentzian lineshapes centered at the transition frequencies (both $|\pm 1\rangle$ states) calculated from the Hamiltonian for each of the four NV classes. The simulation spectrum [Fig. 5.5, orange] is in good agreement with the experimental results, for $B_{\perp} = 0.9\,\text{mT}$ and $B_{\parallel} = 0\,\text{mT}$. In addition, hyperfine structures from ^{14}N is visible from the leftmost resonance of the experimental ODMR spectrum at $\theta = 0°$ [Fig. 5.5(a), blue], with a splitting of about 2.2 MHz. This indicates that, with a good magnetic field alignment and decent measurement SNR, hyperfine structures can still be resolved in these HPHT diamonds, even though they were not designed for quantum sensing applications.

The magnetic field produced by a solenoid coil at the NV-diamond's location can

be calculated as:

$$B = \int_{-l}^{l} \frac{\mu_0 * \frac{N}{2l} * I * r^2}{2\left[(d-x)^2 + r^2\right]^{\frac{3}{2}}} dx. \tag{5.3}$$

Here, l is half-length of the solenoid; $\mu_0 = 4\pi \times 10^{-7}$ H/m is the vacuum permeability; N is the number of turns in the coil; I is the applied current; r is the coil radius; and d is the distance from the NV-diamond to the center of the solenoid. In our experiment, a current of $I = 0.6$ A is applied to each coil, with $N = 150$ turns over $l = 0.65$ cm and $r = 0.7$ cm. With each transverse coils placed $d = 1.85$ cm from the NV-diamond, the pair produces a total field $B_\perp \approx 0.86$ mT, consistent with the 0.9 mT value used in the simulation.

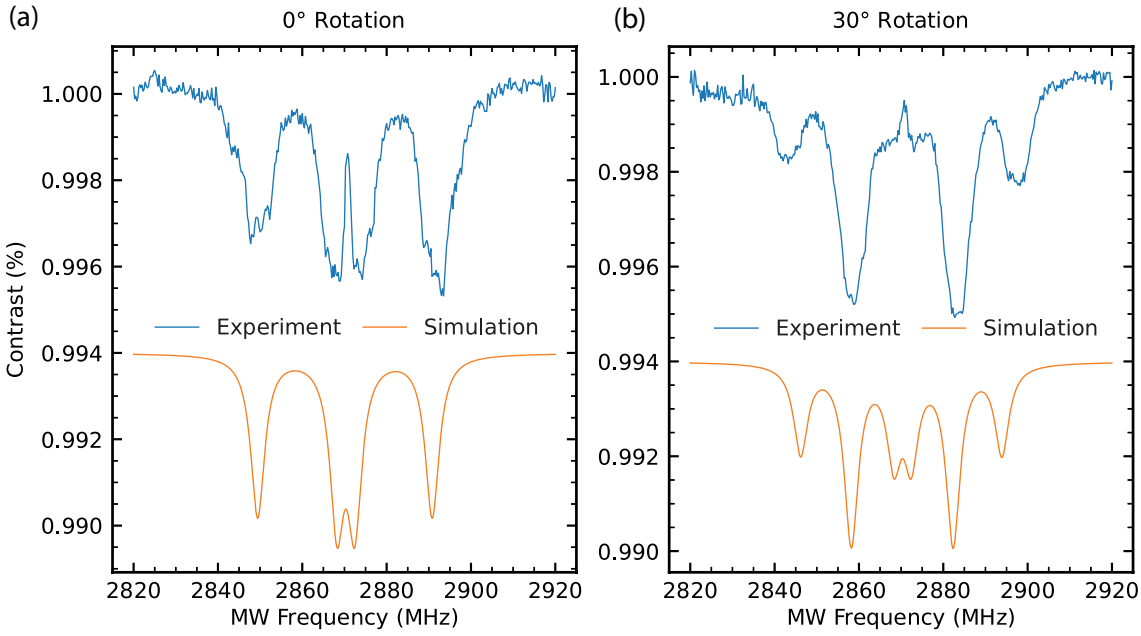


Figure 5.5: Experimentally measured (blue) and simulated (orange) CW-ODMR spectra as a function of MW frequency, for NV-diamond rotation angles of (a) $\theta = 0°$ and (b) $\theta = 30°$ and a bias field produced by the transverse coils. The experimental and simulated results are in good agreement for both cases. Hyperfine structures are visible in the leftmost resonance of (a).

5.5 Outlook

The experimental results in Fig. 5.5 shows relatively poor SNR, for three main reasons: weak ODMR contrast, arising from weak MW irradiation due to high coupling loss at the loop antenna and the absence of a MW amplification stage; a low collected PL photon count, due to limited laser power; and the absence of normalization to suppress the slow, low-frequency noise present during measurement. MW irradiation power can be improved with a more efficient antenna design, avoiding the added cost of an RF amplifier. Although "sig/ref" normalization can suppress slow, common-mode noise in CW-ODMR magnetometry [Sec. 1.2.1.1], the device communication time at each MW frequency (typically ~ 200 ms significantly slows the measurement. In this NV education module, as described in Sec. 5.3.6, the MW frequency is swept with a fixed dwell time synchronized to data acquisition, which shortens the measurement time at the cost of forgoing normalization.

A future iteration could utilize the RF signal generator's *List* function instead of its *Sweep* function, inserting a reference (off-resonant) MW frequency after each frequency step. This approach would enable normalization during data post-processing while also reducing device communication time. Lock-in measurements can also be performed using frequency-modulated (FM) MW signals, if the added cost of a lock-in amplifier and the extra time needed for students to understand this technique are acceptable for this module. Sec. 5.4 shows consistent magnetic field values extracted from the ODMR simulation spectrum and from the analytical solenoid calculation. Additional measurements could record the ODMR resonance frequencies as a function of current applied to the coils. This

would allow students to extract a current-to-field calibration for the coils, using a similar method as discussed in Sec. 2.2.3. To allow consistent measurements across different applied currents, the coil design will need to be improved for better field alignment and homogeneity.

In addition to performing magnetometry, students may also measure the PL spectra emitted from the NV-diamond using an spectrometer, identifying the NV^0 zero-phonon line (ZPL) at 575 nm and NV^- ZPL at 637 nm, as shown in Fig. 5.6 [6].

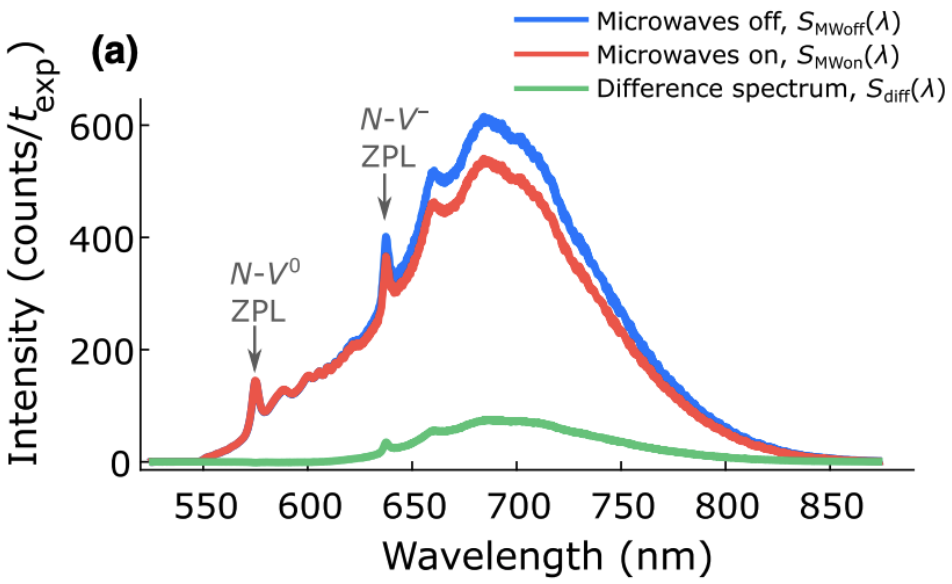


Figure 5.6: Adapt from Ref. [6]. Measured MW-on (red) and MW-off (blue) PL spectra with both the NV^0 and NV^- zero-phonon lines (indicated by gray arrows) visible at 575 nm and 637 nm, respectively.

Finally, given the technical simplicity of AO magnetometry presented in earlier chapters of this dissertation, and the bias field coils already present in this apparatus, AO protocols could also be introduced into a future iteration of the NV education module.

Chapter 6: Outlook

The previous chapters summarized experimental progress in extending NV^- ensemble AO magnetometry across various ranges of bias magnetic fields, as well as techniques to improve AO measurement fidelity. The benefit of AO operation being MW-free offers great potential for applications requiring reduced system complexity and for low-SWaP NV-diamond devices. In this chapter, I outline potential future experiments that build on the near-zero-field NV-NV cross-relaxation effect.

6.1 Near-Zero-Field AO Wide-field Magnetic Imaging

The Quantum Diamond Microscope (QDM) is a magnetic imaging platform that maps magnetic fields with good spatial and temporal resolution. Instead of using a scanning probe with a single NV center at its tip to perform magnetic imaging with nanoscale spatial resolution [50–52, 62, 63], a QDM uses an NV ensemble layer at the surface of a millimeter-scale diamond chip, together with a microwave antenna and a camera, to allow pixel-parallel imaging of local magnetic fields [15, 64, 65]. Fig. 6.1 illustrates a typical QDM setup [7]. Three sets of Helmholtz coils, normally used to apply a fixed bias field for MW-based measurements, can also be driven by a variable current supply for AO operation. This allows AO magnetometry to be integrated more easily with existing QDM

setups.

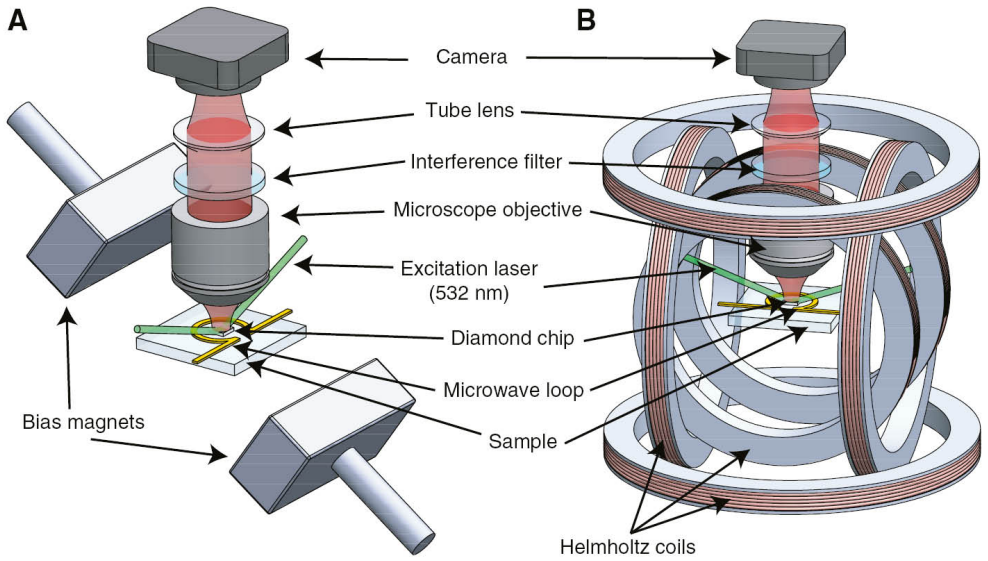


Figure 6.1: Illustrations of a Quantum Diamond Microscope (QDM) [7]. Example QDM setups using (a) a pair of permanent magnets and (b) Helmholtz coils to apply a bias magnetic field. A 532-nm excitation laser enters the NV-diamond at an angle to perform total internal reflection fluorescence (TIRF) microscopy, with the NV PL captured by a camera.

Total Internal Reflection Fluorescence (TIRF) microscopy is a common optical imaging technique for achieving a large Field of View (FOV) ($\sim 500\,\mu$m) with spatially homogeneous illumination. For a QDM, TIRF illumination is achieved by directing the green excitation laser beam onto the NV-diamond at an angle exceeding the critical angle of a diamond ($\sim 24.4^\circ$ in air). A separate objective lens collects the NV-PL and image it onto the camera. Consistent with the design philosophy of a simplified system for AO operations, epi- and Köhler-illumination offer an alternative wide-field microscopy technique that illuminates the NV-diamond while collecting the NV-PL through the same objective lens [66]. A highly collimated, parallel beam is created by focusing the laser to a tight spot exactly at the back focal plane (BFP) of the objective lens [67]. Because the

collimated excitation beam inherits a Gaussian intensity profile, additional beam-shaping optics may be needed to achieve spatially homogeneous illumination across a large FOV.

Near-zero-field AO magnetic imaging has been demonstrated using nanodiamonds [68]. However, the use of nanodiamonds can lead to poor SNR, due to low photon emissions and a broadened linewidth caused by the random orientation of the NV crystallographic axis. In contrast, a diamond sample with a dense layer of near-surface NVs allows magnetic imaging with improved SNR while maintaining a μm-scale spatial resolution typical of QDM operations [69, 70]. As detailed in Chapter 2, the sufficiently narrow linewidth of the AO-PL contrast features allows substructures from the NV hyperfine interaction to be resolved and improves the magnetic sensitivity. Future research may utilize diamond samples with a thin surface layer of dense NV ensembles for sensitive AO wide-field magnetic imaging with millimeter-scale FOV and μm-scale spatial resolution.

Promising applications for AO wide-field magnetic microscopy include eddy-current imaging for studying conductive samples such as aluminum. The MW irradiation used in CW-ODMR protocols, typically around 2-3 GHz, may perturb such samples due to their small skin depth, resulting in localized heating. This same issue arises when studying biological samples [38], much as a household microwave ovens operating at 2.45 GHz can boil water. The amplitude-modulated AC magnetic fields for AO lock-in detection, described in Chapter 2, can also induce eddy currents in conductive samples to identify magnetic-field discontinuities caused by cracks [18]. The modulation frequencies used for these measurements determine the depth of penetration. Identifying near-surface cracks requires high frequencies, in the range of 100 kHz to a few MHz. However, such high modulation frequencies would decrease the AO magnetic sensitivity, due to weaker

adiabatic exchange of NV electronic spin population across the avoided crossings, as discussed in Sec. 2.2.4. To overcome this challenge, NV-diamonds with a higher [NV] and a greater concentration of magnetic defects may be preferred, to produce a broader avoided-crossing linewidth. Low modulation frequencies, in the range of 100 Hz to 10 kHz, allow inspection of deeper layers. While these low frequencies are more desirable for AO lock-in detection, since they enable better magnetic sensitivity, the strength of the target magnetic signal also decays more significantly with increased depth.

The AO pulse sequence introduced in Chapter 3 can also be applied to wide-field magnetic imaging. To perform two AO PL readout measurements within a single optical pulse for effective common-mode noise suppression, camera exposure time and frame rate are the critical factors to consider in the experimental design. A camera with a low frames per second (FPS) fundamentally limits how fast successive acquisitions can be triggered. For example, a camera operating at 100 FPS requires a minimum of 10 ms between consecutive frames. This ms-scale temporal separation is much longer than the $\sim$ 100μs laser pulse used for photodiode-based measurements in Chapter 3. While a longer camera exposure time allows more photon integration, it may also reduce the AO contrast, particularly for near-zero-field AO magnetometry, by including more steady-state photons within the "signal" readout window. Applying the pulsed AO protocol to wide-field magnetic imaging therefore requires careful considerations of both camera choice and camera settings for optimal performance. Fig. 6.2 shows preliminary experimental results resolving AO-PL contrast as a function of applied magnetic fields B_x and B_y from -1 to 1 mT, using the Köhler illumination technique and a camera (Basler aca1920-155um). Limited to 164 FPS, the laser pulse duration was increased to 6 ms for these normalized

measurements. Although averaging over the entire region of interest (ROI) and applying the pulsed AO protocol together provide a good SNR for resolving the near-zero-field AO-PL contrast features [Fig. 6.2(a)], the single pixel result is much noisier due to reduced photon counts [Fig. 6.2(b)]. Future experimental procedures may require pixel binning, combining adjacent pixels into a single larger pixel, to gather more photons per binned unit with a minor cost to spatial resolution.

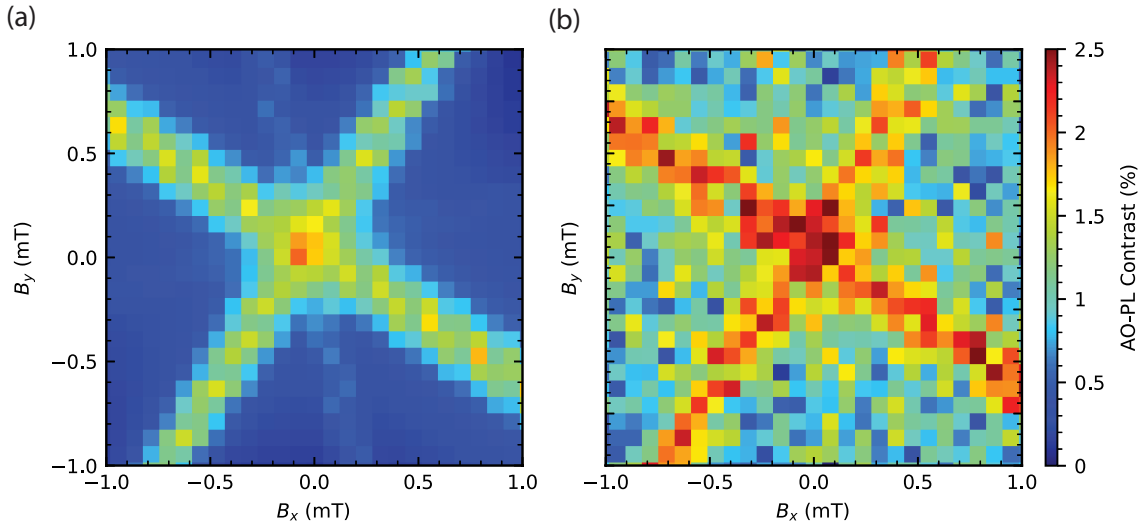


Figure 6.2: Experimentally determined near-zero-field AO-PL contrast as a function of applied magnetic fields B_x and B_y, measured using the Köhler illumination technique and a camera. (a) Averaged over the entire region of interest (ROI). (b) From a single pixel, showing worse SNR than (a) due to fewer collected photons.

The discussion so far has focused the technical implementation and potential applications of a benchtop AO QDM. Alternatively, a portable AO microscope may be realized by coupling a diamond sample with dense NV ensembles to a coherent optical fiber bundle. Within such a fiber bundle, the start and the end of every fiber line up, and each fiber constitutes a pixel. The spatial resolution is therefore determined by the diameter of a single optical fiber. Such an endoscope-like design, with the added benefit of being low-SWaP, could be particularly useful for biomedical applications, for example detecting

magnetic signals from nanoparticles [51, 71]. If diamond samples with a thin NV layer are used for this design, the NV layer would need to sit closer to the optical fiber facet to improve the NV-PL collection efficiency, which in turn increases the standoff distance to the target magnetic sample. Thin-film diamonds, which have been used in quantum networks at thickness of $\sim 200\,\mathrm{nm}$ [72], are a potential candidate for the AO endoscope design.

6.2 Near-Zero-Field Vector AO Magnetometry

The AO magnetometry demonstrated in Sec. 2.3.4 and Sec. 3.2.4 are scalar measurements along the direction of the swept magnetic field. One possible way to achieve sequential vector AO measurements is to track the near-zero-field resonance, similar to the frequency-locking scheme used to track Zeeman-split resonances [73]. Assume the largest AO-PL contrast occurs at zero magnetic field, a small perturbation in any direction will shift the resonance correspondingly. Vector magnetic field information can then be extracted by sequentially sweeping the field along all three directions to keep the AO-PL contrast at its maximum. This approach is similar to a three-dimensional gradient descent (or ascent) problem. Another approach to sequential vector magnetometry uses Bayesian inference, as discussed in Ref. [74].

In MW-based CW-ODMR NV magnetometry, simultaneous vector measurements can also be performed by applying a bias field to separate the resonances of all four NV crystallographic orientations, then driving four concurrent MW tones [16]. This method, which typically requires a bias field $\gtrsim 1\,\mathrm{mT}$, may not translate easily to AO magnetom-

etry, for two reasons. First, NV-NV cross-relaxation relies on spin degeneracy among the various NV classes, and no AO-PL contrast from this effect can be observed once all NV orientations are spectrally separated. Second, the bias magnetic field cannot be manipulated in the same independent, per-orientation way as the four concurrent MW tones. Alternatively, Fourier optical processing has been demonstrated by modulating the NV-PL at the microscope's Fourier plane and decomposing the NV ensemble magnetic resonance spectrum into its constituent orientations [75]. This technique, with the advantage of being applicable at arbitrarily low bias fields, may also be applied to achieve simultaneous vector AO magnetometry through an analogous decomposition of the measured NV-NV cross-relaxation AO-PL features.

6.3 Open Questions

Local strain, and/or electric fields $\vec{E} = (E_x, E_y, E_z)$ couple to the NV ground state Hamiltonian, as shown in Eq. 1.4 and Eq. 1.5. Ref. [34] reports that transverse electric fields enable NV spin-mixing and double-flip processes near zero magnetic field. This electric-field-induced splitting can be associated with the linewidth of the observed zero-field AO-PL feature. Given the sufficiently narrow linewidth of near-zero-field AO-PL contrast features demonstrated in this dissertation using CVD-grown NV-diamond samples, it remains an open question how local strain and electric fields affect these features. In particular, the AO QDM concept introduced above could allow local strain and electric fields to be spatially resolved through analysis of AO-PL contrast features. While strain microscopy within NV-diamond has previously been performed using MW-based

techniques [76], a MW-free approach could eliminate the technical challenge of applying a strong, homogeneous MW drive across a large FOV, while achieving the applied bias field homogeneity may prove comparatively easier.

The temperature dependence of the near-zero-field AO-PL feature is another variable worth exploring. Ref. [29] reports that the AO-PL contrast increases with temperature up to around 100 K, then starts to decrease above $\approx$ 250 K, while the linewidth remains roughly consistent across the temperature range. At both temperature extremes, the photo-ionization process is suppressed, which reduces the number of spin fluctuators available as depolarization channels, which in turn decreases the AO-PL contrast. To assess the feasibility of AO magnetometry in elevated-temperature environments, future work could investigate how both AO-PL contrast and linewidth behave at higher temperatures (> 300 K). If the number of spin fluctuators decreases with the increased temperature, the linewidth may narrow, due to the weaker resonant dipolar interaction among the remaining fluctuators.

In Chapter 3, time-resolved AO PL measurements are used to study the optimal readout timing for the "signal" window. However, most of the PL information between the "signal" and "reference" readout windows is discarded once the readout timing is fixed. A possible future research direction is to use the full time-resolved NV-PL response following optical excitation to perform AO magnetometry. For example, an algorithm, similar to the linear regression concept outlined in Appendix D for MW-based readouts, could infer the NV electronic spin population distribution from the transient AO PL response, given a known dark time τ for spin depolarization.

Other questions, related to the optimal choice of NV-diamond sample for near-

zero-field AO magnetometry, are outlined in Sec. 3.3; optimization of the pulsed AO protocol for spin-mixing effects and possible radiation-induced effects on AO operation are discussed in Sec. 4.4.

Appendix A: Principles of Lock-in Detection

A lock-in amplifier (LIA) is a powerful instrument to extract small signal buried in a noisy environment by performing homodyne detection. This lock-in detection isolates the signal at the desired frequency from all other frequency components through a series of operations. Most of the reported CW-ODMR magnetic sensitivities in the existing literature are acquired through lock-in detection with frequency-modulated MW. This dissertation has also applied lock-in detection to resolve magnetic-field-dependent AO-PL features using amplitude-modulated magnetic fields. This appendix develops the mathematical and hardware principles of lock-in detection in general.

A.1 Basic Working Principle

A.1.1 Phase-Sensitive Detection

A LIA accepts two inputs: a noisy signal of interest with frequency ω_s and a phase θ_{sig} and a clean reference signal with frequency ω_r and a phase θ_{ref} of the form:

$$\begin{aligned} V_{\text{sig}}(t) &= V_{\text{sig}} \sin(\omega_s t + \theta_{\text{sig}}), \\ V_{\text{ref}}(t) &= V_{\text{ref}} \sin(\omega_r t + \theta_{\text{ref}}). \end{aligned} \tag{A.1}$$

The LIA multiplies the two signals together and gives:

$$\begin{aligned} V_{\text{sig}}(t)\, V_{\text{ref}}(t) &= V_{\text{sig}} V_{\text{ref}} \sin(\omega_s t + \theta_{\text{sig}}) \sin(\omega_r t + \theta_{\text{ref}}) \\ &= \frac{1}{2} V_{\text{sig}} V_{\text{ref}} \cos\big[(\omega_s - \omega_r)t + (\theta_{\text{sig}} - \theta_{\text{ref}})\big] \\ &- \frac{1}{2} V_{\text{sig}} V_{\text{ref}} \cos\big[(\omega_s + \omega_r)t + (\theta_{\text{sig}} + \theta_{\text{ref}})\big]. \end{aligned} \tag{A.2}$$

An adjustable low-pass filter is then applied to the multiplication output, discarding the component with higher (summed) frequency $\omega_s + \omega_r$. Thus, the output $V_{LP}(t)$ after the low-pass filter becomes:

$$V_{LP}(t) = \frac{1}{2} V_{\text{sig}} V_{\text{ref}} \cos\big[(\omega_s - \omega_r)t + (\theta_{\text{sig}} - \theta_{\text{ref}})\big]. \tag{A.3}$$

If the reference frequency ω_r matches the signal frequency $\omega_s = \omega_r$, Eq. A.3 can be reduced to a time-independent expression as a DC output with half of the signal input amplitude:

$$V_1 \approx \frac{1}{2} V_{\text{sig}} V_{\text{ref}} \cos\theta, \qquad \theta \equiv \theta_{\text{sig}} - \theta_{\text{ref}}. \tag{A.4}$$

The time constant τ setting on the LIA decides the low-pass filter bandwidth. Any component of the input at a different frequency, $\omega_s \neq \omega_r$, instead produces an oscillating term that the low-pass filter attenuates, with the degree of attenuation set by how far that frequency lies outside the filter bandwidth. This is the mathematical description of the technique's noise rejection: broadband noise is suppressed except within the narrow filter bandwidth centered on the reference frequency ω_r. This reference frequency ω_r should be chosen well above the $1/f$ noise range and within the hardware limit (e.g., photodiode

bandwidth, coil response etc.), so that the signal of interest is displaced away from the residual $1/f$ low-frequency noise. The fact that the term $\cos\theta = \cos(\theta_{\text{sig}} - \theta_{\text{ref}})$ remains in Eq. A.4 is why this method is termed phase-sensitive detection.

A.1.2 Dual-Phase Detection: Amplitude and Phase

Eq. A.4 depends on the unknown relative phase θ between the signal and the reference, and a single demodulation channel alone cannot separate the signal amplitude V_{sig} from this phase offset unless θ happens to be known and zero. Most LIAs resolve this by demodulating the input against two reference channels in quadrature: the original reference signal, and a second reference signal phase shifted by $90°$,

$$V_{\text{ref},2}(t) = V_{\text{ref}} \sin(\omega_r t + \theta_{\text{ref}} + \pi/2) = V_{\text{ref}} \cos(\omega_r t + \theta_{\text{ref}}). \tag{A.5}$$

Repeating the multiplication and filtering step with this second reference gives a second DC output:

$$V_2 \approx \frac{1}{2} V_{\text{sig}} V_{\text{ref}} \sin\theta. \tag{A.6}$$

Normalizing both channels by the known reference amplitude defines the in-phase and quadrature outputs:

$$X \equiv \frac{V_1}{V_{\text{ref}}} \approx \frac{1}{2} V_{\text{sig}} \cos\theta, \qquad Y \equiv \frac{V_2}{V_{\text{ref}}} \approx \frac{1}{2} V_{\text{sig}} \sin\theta, \tag{A.7}$$

from which the signal amplitude and phase are recovered independently of θ:

$$R = \sqrt{X^2 + Y^2} \approx \frac{1}{2} V_{\text{sig}}, \qquad \theta = \tan^{-1}\left(\frac{Y}{X}\right). \tag{A.8}$$

This dual-phase (two-channel) architecture allows a measurement to proceed without first having to manually tune the reference phase to match the signal.

A.2 Bandwidth and Settling Time

The low-pass filter sets the trade-off between measurement bandwidth and noise rejection: a shorter time constant τ increases the bandwidth (faster response to a changing signal, but more residual noise), while a longer τ narrows the effective bandwidth at the cost of a slower response. Commercial LIAs, for example from Zurich Instruments or Stanford Research Systems, offer variable filter orders n by cascading multiple filters. The higher the filter order, the steeper filter roll-off towards higher frequencies, at the cost of a longer settling time. The exact settling time for a given time constant τ and filter order n can be found in the instrument's manual. As an example, with a LIA from Zurich Instruments, an eighth-order filter takes roughly 8.6τ to settle to 63.2% of its final value, compared to 1.0τ for a first-order filter.

A.3 Application to Lock-in CW-ODMR and AO Magnetometry

This section details the application of the lock-in detection principle to two NV magnetometry protocols: CW-ODMR with frequency-modulated MW, and AO measure-

ment with amplitude-modulated magnetic field, used in Chapter 2. Both cases reduce to the same underlying mathematics: the lock-in output approximates a derivative of the measured PL with respect to the modulated variable (MW frequency or magnetic field amplitude), evaluated at the carrier value of that variable.

A.3.1 Small-Signal Derivation for Lock-in CW-ODMR

Starting with a lock-in CW-ODMR measurement, let $V(\omega)$ denote the NV-PL collected on a photodiode as a function of the applied MW frequency ω. Suppose the MW frequency is sinusoidally modulated about a carrier frequency ω_c with modulation depth ω_{dev} and modulation frequency ω_{mod}. The frequency-modulated photodiode output voltage can be described as $V_{fm} = V(\omega_c + \omega_{\text{dev}} \sin(\omega_{\text{mod}} t))$. A first-order Taylor expansion of V_{fm} about ω_c gives

$$V\left(\omega_c + \omega_{\text{dev}} \sin(\omega_{\text{mod}} t)\right) \approx V(\omega_c) + \omega_{\text{dev}} \sin(\omega_{\text{mod}} t) \left.\frac{dV}{d\omega}\right|_{\omega_c}. \tag{A.9}$$

Multiplying this photodiode signal with an in-phase reference $\sin(\omega_r t)$ from the LIA, where $\omega_r = \omega_{\text{mod}}$, the output becomes:

$$\begin{aligned} V\left(\omega_c + \omega_{\text{dev}} \sin(\omega_{\text{mod}} t)\right) * \sin(\omega_{\text{mod}} t) \approx V(\omega_c) \sin(\omega_{\text{mod}} t) \\ + \frac{\omega_{\text{dev}}}{2} \left.\frac{dV}{d\omega}\right|_{\omega_c} - \frac{\omega_{\text{dev}}}{2} \cos(2\omega_{\text{mod}} t) \left.\frac{dV}{d\omega}\right|_{\omega_c}. \end{aligned} \tag{A.10}$$

The low-pass filter removes both the ω_{mod} and the $2\omega_{\text{mod}}$ terms, leaving the lock-in output

$$S(\omega_c) \approx \frac{\omega_{\text{dev}}}{2} \frac{dV}{d\omega}\bigg|_{\omega_c} \approx \frac{V(\omega_c + \omega_{\text{dev}}) - V(\omega_c - \omega_{\text{dev}})}{2}. \tag{A.11}$$

As a result, the lock-in ODMR output can be interpreted directly as a numerical derivative of the PL lineshape with respect to MW frequency, taken across the carrier frequency with a step size set by the modulation depth. This is the origin of the characteristic dispersive (zero-crossing) lineshape of a lock-in ODMR spectrum: it is proportional to the slope of the underlying (absorptive) ODMR resonance; and it crosses zero exactly at the resonance center, where that underlying resonance itself has zero slope (i.e., at its dip minimum).

A.3.2 Lock-in AO Measurements

This same picture applies equally to an amplitude-modulated (rather than frequency-modulated) measurement as a function of magnetic field, which is the configuration used for the AO lock-in protocols in Chapter 2. Instead of modulating the MW frequency around a fixed carrier, the total magnetic field itself is modulated about a fixed DC bias field,

$$B(t) = B_{\text{bias}} + A\sin(\omega_M t), \tag{A.12}$$

while the AO-PL is measured as a function of applied DC magnetic field. Writing the photodiode signal as $V(B(t))$ and Taylor expanding about the bias point, exactly as in

Sec. A.3.1 but with B in place of ω:

$$V(B(t))\big|_{B_{\text{bias}}} \approx V(B_{\text{bias}}) + \left.\frac{dV}{dB}\right|_{B_{\text{bias}}} A\sin(\omega_M t). \tag{A.13}$$

After the demodulation and low-pass filtering, an in-phase lock-in output X can be expressed as

$$X \approx \frac{A}{2}\left.\frac{dV}{dB}\right|_{B_{\text{bias}}}, \tag{A.14}$$

directly proportional to the local slope of the AO-PL with respect to the magnetic field at the chosen bias point, B_{bias}. To resolve AO-PL contrast features using lock-in detection, the modulation field $A\sin(\omega_M t)$ must be applied along the same direction as the bias field B_{bias}; a modulation field with a significant transverse component would instead couple through other field-dependent mechanisms, such as the spin-mixing process discussed in Sec. 4.2, or a shift in the spectral degeneracy between NV orientations, rather than through the intended axial derivative response modeled here.

For both CW-ODMR and AO measurements, integrating the measured in-phase lock-in output X with respect to the swept variable (frequency or magnetic field) can reconstruct the lineshape acquired without the lock-in detection, providing a useful consistency check. However, the modulation depth needs to be carefully chosen with respect to the resonance linewidth, in order to not distort the lineshape.

A.3.3 Hardware for Lock-in Detection

Fig. A.1 shows the hardware wiring diagram for both lock-in CW-ODMR and AO operations. The LIA outputs a reference signal, via its internal oscillator, at the desired modulation frequency. For a typical lock-in CW-ODMR experiment, a MW synthesizer receives this reference signal, commonly through its reference input channel, and outputs a frequency-modulated MW signal through an RF antenna to drive the NV electronic spin transitions. Similarly, for a lock-in AO experiment, a current driver receives the reference signal and uses it to drive, for example, a pair of Helmholtz coils, producing an amplitude-modulated magnetic field at the same modulation frequency to manipulate the NV spin state. In both cases, a photodiode measures the resulting NV PL under this external modulation. The LIA then measures the photodiode's output voltage through its analog input channel and returns a demodulated output signal X (or Y, R, θ), as a function of MW frequency or applied magnetic field.

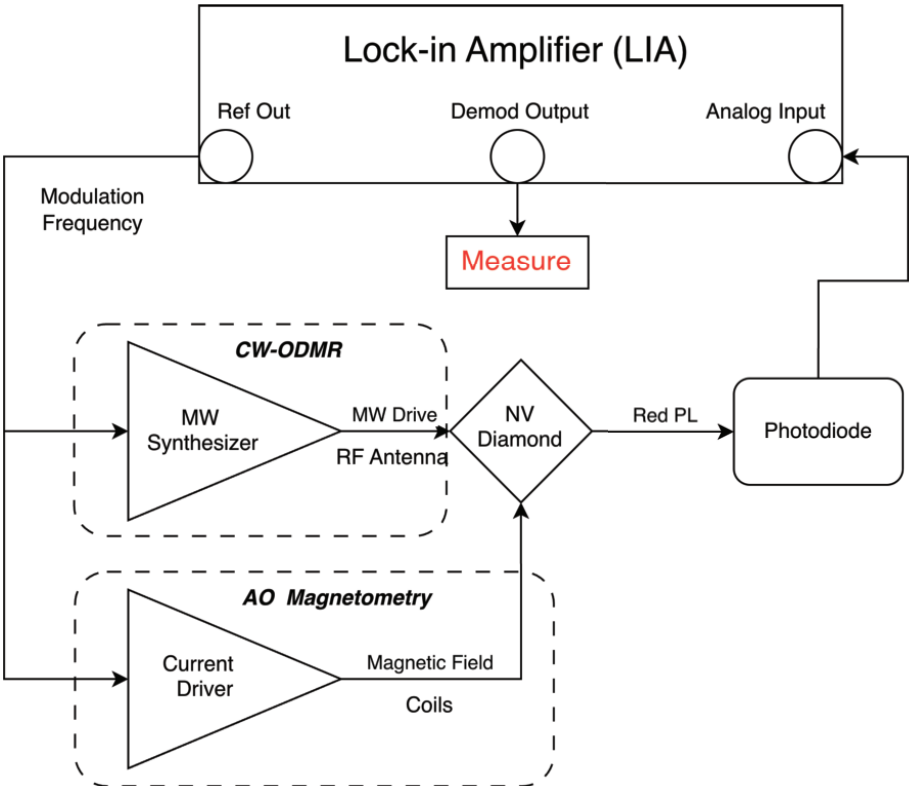


Figure A.1: Hardware wiring diagram to perform lock-in CW-ODMR and AO operations.

Appendix B: Towards a Fiberized NV Magnetometer with Lock-in CW-ODMR

The AO protocols developed throughout this dissertation have the potential to enable low-SWaP magnetometry and be suited to a compact, field-deployable sensor. Such a magnetometer can be more compact by using an optical fiber in replace of bulky free-space collection optics. This appendix documents an effort to characterize the NV-PL photon collection efficiency from various fiber-coupled system design with a consistent input laser excitation power $\sim 200\,\mathrm{mW}$. A proof-of-principle fiberized, MW-based NV magnetic sensitivity is demonstrated at the end of this chapter, by utilizing lock-in detection as discussed in Appendix A.

B.1 Optical System Design

B.1.1 Large-Diameter Multimode Fiber with Discrete Lens Systems

We start by evaluating the optical collection performance using a 400 μm core, 0.5 numerical aperture (NA) multimode fiber. Using an optical fiber with a large core and NA allows simultaneous optical excitation and NV-PL collection with good coupling efficiency. With the idea of keeping the NV sensor area simple, we place a dichroic

beamsplitter before the fiber input so that the NV-PL can be measured through the back-propagation beam path through the fiber.

We use a two-lens system with two aspheric lenses: a $f = 6.24$ mm aspheric (Thorlabs, C110TMD-A) with 0.4 NA roughly collimates the output laser beam from the fiber, and a $f = 3.1$ mm aspheric (Thorlabs, C330TMD-A) with 0.7 NA subsequentally focuses the beam to optically excite the NV with higher optical intensity. The optical components are placed in the following manner: 1) 4.1 mm from the first aspheric lens to the fiber connector; 2) 11 mm between the two aspheric lenses; and 3) 3.1 mm from the second aspheric lens to the diamond.

A Zemax ray-tracing simulation of the C110TMD-A/C330TMD-A pair, shown in Fig. B.1 with inter-component distances optimized, confirms that the majority of green rays converge onto the diamond and, by the reversibility of the optical path, that red PL rays converge onto the fiber. The simulation predicts a green spot size of approximately 20 μm at the diamond and a red spot size of approximately 200 μm at the fiber facet, consistent with the good collection efficiency observed experimentally, though the NV numerical aperture used in the simulation (NA = 0.6) is likely an underestimate of the true value.

To further improve the NV-PL collection efficiency through the multimode fiber, the NV-diamond is mounted on a dielectric mirror which can redirect otherwise-lost red PL back toward the collection optics. With ~ 180 mW laser power after the fiber output, about 600 μW NV-PL is measured after the dichroic beamsplitter near the fiber input using a CVD-grown sample S7-14N with ~ 3.5 ppm [NV] (sample property listed in Table E.1).

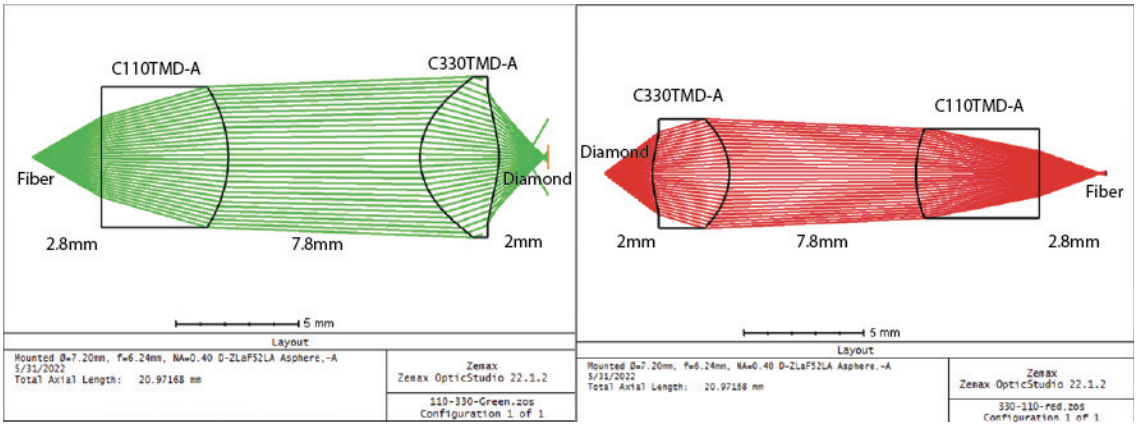


Figure B.1: Zemax ray tracing simulation of C110TMD-A and C330TMD-A aspheric lens system. Left: Green light propagates from a multimode optical fiber to the diamond. Right: Red PL propagates from the diamond to the fiber. Green propagation forms about a 20 μm spot size and red propagation forms about a 200 μm spot size.

A gradient-index (GRIN) lens is also evaluated as a route to further miniaturization, since GRIN lenses are commonly used as 1:1 imaging relays in applications, such as endoscopic neural imaging, where a conventional microscope objective cannot physically access the region of interest. Here, the GRIN lens is intended to focus the green excitation beam onto the diamond while simultaneously imaging the red PL back into the fiber, the same principle for the aforementioned two-aspheric lenses system, and has been demonstrated in an integrated NV magnetometer [8]. Fig. B.2 shows an in-lab photo attaching the fiber to the NV-diamond through the GRIN lens. While $\sim$ 750 μW NV-PL is measured with sample S7-14N, the proper alignment of the GRIN lens introduces a significant challenge and requires a more delicate mounting system for optical components.

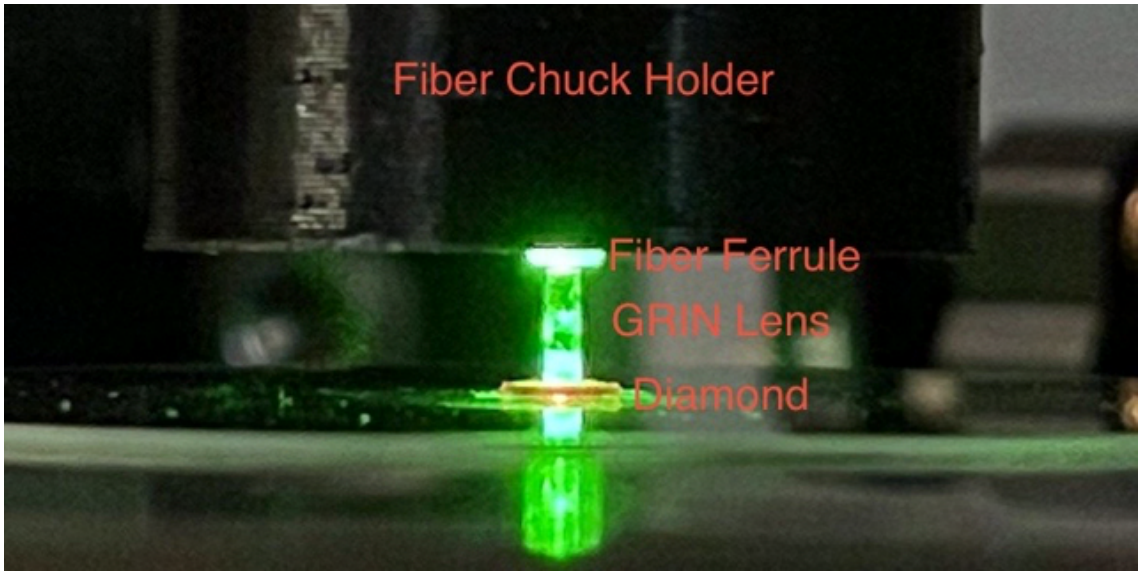


Figure B.2: In-lab photo of an NV optical system using a GRIN lens.

B.1.2 Large-Diameter Multimode Fiber with Direct Fiber-to-Diamond Contact

Attaching the NV-diamond directly to the fiber head can be another approach to eliminate discrete optics entirely for the sensor head. Because diamond has a refractive index $n \approx 2.4$, red PL emitted from the diamond into air with $n \approx 1$ undergoes substantial refraction. We therefore apply an index-matching fluid with $n > 1$ to allow higher NV-PL propagated into the fiber. With sample S7-14N, the measured PL power is further increased to around 950 μW.

This direct contact between the multimode fiber and the NV-diamond provides the highest measured PL power among all optical approaches discussed so far. However, for magnetometry purposes, the PL power is not the only metric to evaluate the optical performance. Fig. B.3 shows a Zemax simulation of the laser beam profile entering the NV-diamond through direct fiber-to-diamond contact and through a GRIN lens in be-

tween [8]. The approach of direct fiber-to-diamond contact creates an inhomogeneous illumination intensity across the NV-diamond. The impact of these optical excitation intensity differences on NV magnetometry can be investigated in future studies.

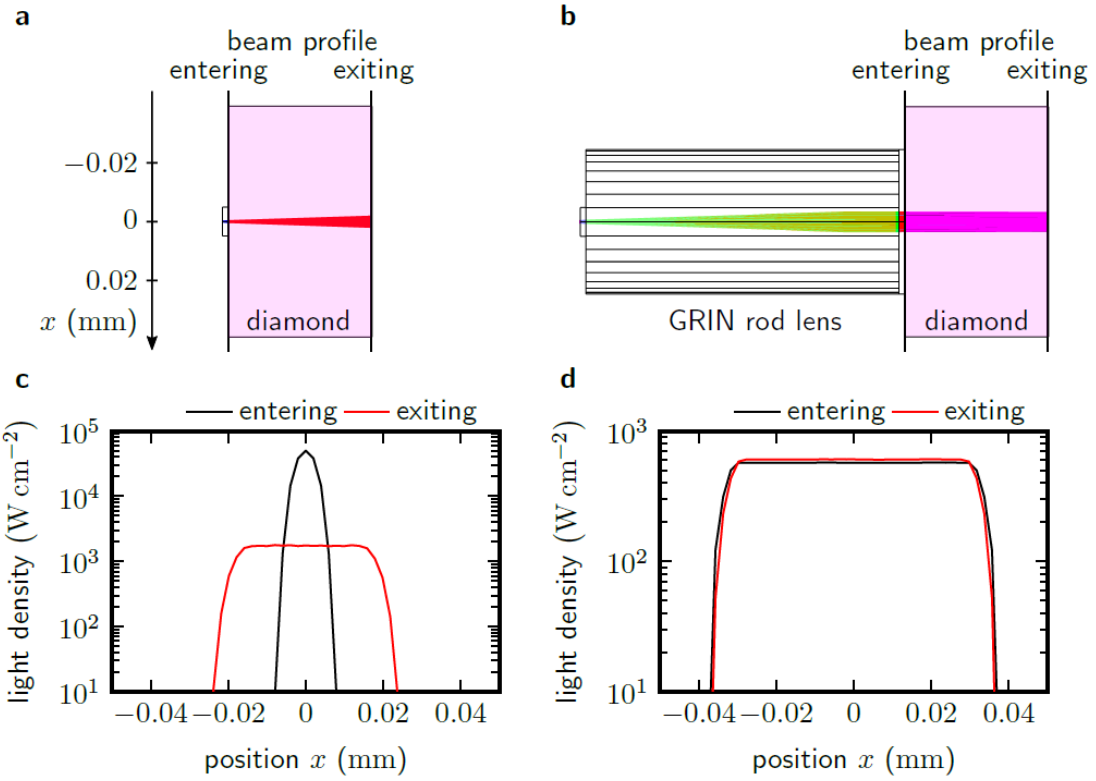


Figure B.3: Zemax simulation of the beam profile propagating through diamond [8]. Left: direct fiber and diamond contact. Right: through GRINTECH GT-LFRL-050-025-50-NC (670) lens to form a well-collimated beam entering/exiting diamond.

B.1.3 Small-Diameter Fiber

We start by evaluating two small-core fiber options, with one being a tapered, lensed multimode fiber (oz Optics TPMJ-3A-1550-8/125-0.4-10-2.5-14-1-AR), with an 8 μm core and a lensed tip producing an approximately 2.5 μm spot size, and the other one being a single-mode fiber (Thorlabs P1-460Y-FC-1, $\sim$ 4 μm mode field diameter). This

approach is motivated by the possibility that a small fiber core could still achieve decent collection efficiency, while avoiding the detrimental mode-mixing effects associated with large-core multimode fibers, which can increase optical intensity noise.

With index-matching fluid applied to the diamond surface and the lensed fiber tip pressed directly against it, the collected red PL is faint and difficult to measure reliably: approximately 0.9 μW using the lensed fiber and approximately 0.4 μW using the single-mode fiber, both orders of magnitude below the collection levels achieved with large-diameter fiber designs discussed prior, presumably due to the combined effect of significant coupling loss of laser beam into the fiber. The best collection efficiency for the lensed fiber occurred just before the lensed tip began to physically bend under contact pressure. Given the combined green-coupling loss and poor PL-collection performance, small-diameter fiber designs were not pursued further with millimeter-scale bulk NV-diamond in this dissertation.

B.2 Demonstration of Fiberized NV Magnetometer Sensitivity

Here we demonstrate a proof-of-principle fiberized NV magnetometer using the lock-in CW-ODMR protocol. We use a 400 μm core, 0.5 NA multimode fiber with a C110TMD-A/C330TMD-A aspheric lens pair, discussed in Sec. B.1.1, to optically excite the NV-diamond and collect its PL simultaneously. A photodiode (Thorlabs PDA36A2) is placed after the dichroic beamsplitter to measures the NV-PL coming out of the optical fiber. Sample S7-14N, used here, is a bulk sample with a 500 μm thickness, ^{14}N isotope, $[\mathrm{N}] = 14$ ppm, $[\mathrm{NV}] \approx 3.5$ ppm, and natural abundance of ^{13}C. A home-made thin coil,

connected to an RF signal generator (SRS SG384), is used to coherently drive the NV electronic spin states for CW-ODMR measurements.

Fig. B.4(a) shows a CW-ODMR spectrum with a bias field of $\approx 3.8\,\mathrm{mT}$. As a result, the resonances from all four NV orientations are spectrally separated. The ODMR contrast is calculated as "sig/ref", where "sig" represents the PL measured at each swept frequency, and "ref" represents the PL measured with no MW applied. For lock-in measurements, the RF signal generator outputs a frequency-modulated MW signal with an 800 kHz modulation deviation, modulated at a frequency of 12 kHz set by the LIA (Zurich Instruments MFLI). The LIA time constant is set to $100\,\mu\mathrm{s}$, with a filter slope of 48 dB per octave, and the LIA output scaling is set to 100. The resulting LIA output X, as a function of MW frequency, is shown in Fig. B.4(b), which resembles a derivative of the spectrum in (a).

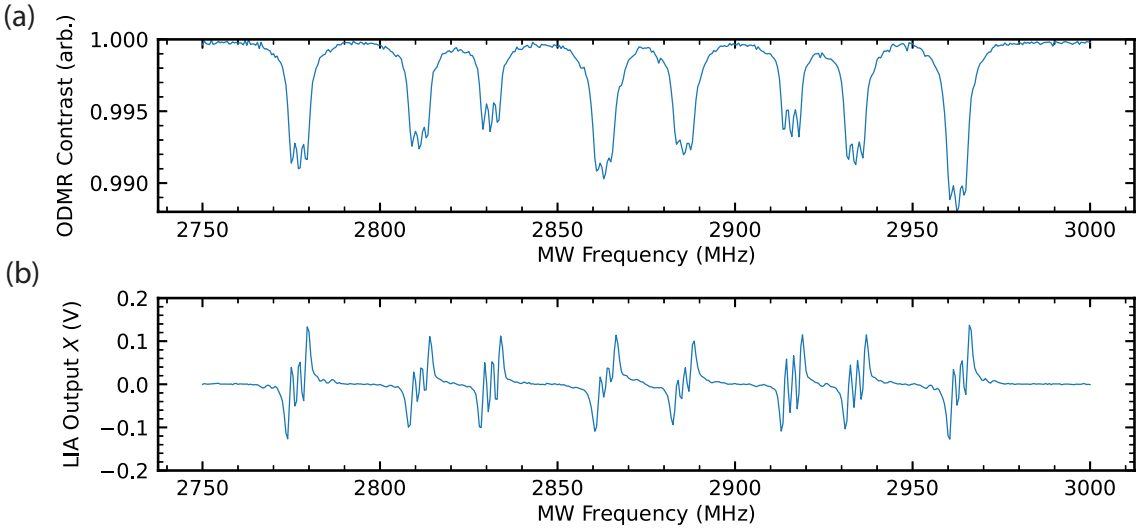


Figure B.4: (a) CW-ODMR and (b) demodulated (lock-in) CW-ODMR spectra, both measured with a bias field of $\approx 3.8\,\mathrm{mT}$.

As an example, we use the resonance centered near 2830 MHz to characterize the single-axis magnetic sensitivity. From the LIA output spectrum, we extract a linear slope

of 0.178 V/MHz, with the zero-crossing occurring at 2832.3 MHz. We measure 30 1-s time traces, at a sampling rate of 10 kHz, with the MW frequency fixed at this zero-crossing frequency, where the fiberized magnetometer is magnetically sensitive. This step is then repeated with the MW frequency set off resonance (at 2000 MHz), rendering the magnetometer magnetically insensitive. The calibration constant is obtained by multiplying the linear slope (V/MHz) by the NV gyromagnetic ratio (2.8×10^{-5} MHz/nT), giving a conversion factor in V/nT. The time traces are converted to PSD estimates using Welch's method, with a sampling rate of 10 kHz and 50 % overlap. Fig. B.5 shows the resulting sensitivity as a function of frequency. Peaks at 60 Hz and its harmonics, likely associated with ambient magnetic noise, for example from the power line, appear only in the magnetically sensitive case. The mean sensitivity over the 1-200 Hz range, excluding these line-frequency peaks, is $\sim 30\,\mathrm{nT}/\sqrt{\mathrm{Hz}}$. To achieve better magnetic sensitivity, improved MW delivery, optimization of MW power and its associated modulation deviation, enhanced PL collection efficiency, and incorporation of hyperfine driving should all be considered [14, 77].

B.2.1 Possible Effect of MW and Photodiode Cross-Talk

The sensitivity results presented above are measured with NV-PL collected through the multimode fiber, using what we refer to below as the fiber-coupled photodiode configuration. This approach allows the sensor head (NV-diamond, MW antenna, and optical components) to be physically isolated from the remaining electronics, such as the RF generator and photodiode. However, because the ensemble NV-PL exits the diamond

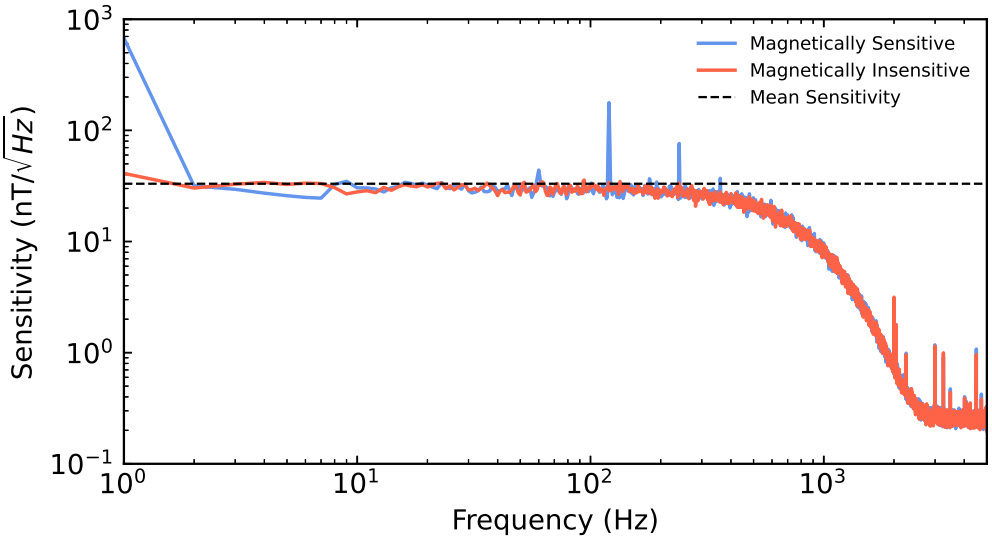


Figure B.5: Demonstrated fiberized NV sensitivity spectra, with a mean sensitivity $\approx 30\,\mathrm{nT}/\sqrt{\mathrm{Hz}}$ from 1 to 200 Hz. The peaks at 60 Hz and its harmonics can be associated with ambient magnetic noise, for example from the power line, and are not observed in the magnetically insensitive case. The noise floor for the magnetically insensitive case is obtained with the MW frequency tuned off resonance (2000 MHz).

over a full range of angles, collecting it through a lens limits the achievable collection efficiency, given the lens's finite NA. An alternative design that addresses this limitation places the photodiode directly adjacent to the NV-diamond, with optical filters positioned in between, which we refer to below as the near-diamond photodiode configuration; this allows a more integrated system design [78].

After testing the improvement of PL collection through the near-diamond photodiode in our fiberized NV system, we found a possible cross-talk effect between the MW antenna and the photodiode. Fig. B.6 shows CW-ODMR measurements without lock-in detection, acquired using the fiber-coupled photodiode (blue) and the near-diamond photodiode (orange). In the MW frequency range from 2800 to 2950 MHz, the ODMR spectrum measured with the near-diamond photodiode exhibits non-unity contrast between neighboring resonances.

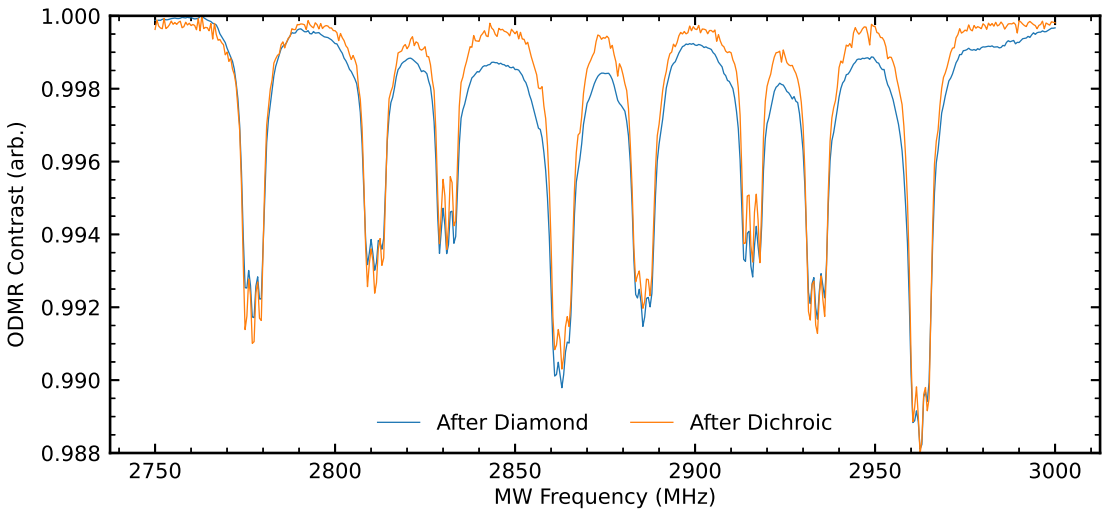


Figure B.6: CW-ODMR spectra measured with the fiber-coupled photodiode (blue) and the near-diamond photodiode (orange). The latter shows non-unity contrast between neighboring resonances across the 2800–2950 MHz range.

We repeat the sensitivity characterization detailed in the previous section using the near-diamond photodiode, as shown in Fig. B.7. Although the near-diamond configuration collects more PL, the mean sensitivity remains $\sim 30\,\mathrm{nT}/\sqrt{\mathrm{Hz}}$, consistent with the prior result; peaks at 120 Hz and 240 Hz are observed in both magnetically sensitive and insensitive cases. In addition, we observe increased measurement fluctuations between neighboring frequency points in the band centered near 1 kHz, despite this range lying within the LIA low-pass filter's roll-off region. This effect may arise because our home-made MW coil is not properly impedance-matched. As a result, a substantial fraction of the MW power may be lost at the connector, and this lost power may couple as cross-talk noise onto the nearby photodiode. Therefore, careful design of the MW antenna, together with careful positioning of the photodiode, should be considered for any integrated NV system design.

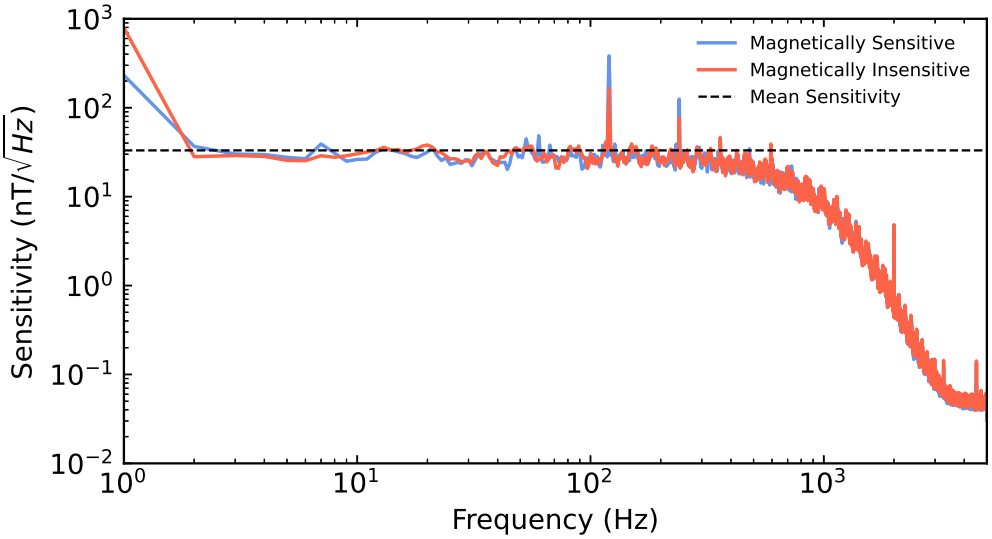


Figure B.7: Fiberized NV sensitivity spectra measured with the near-diamond photodiode, with a mean sensitivity $\approx 30\,\mathrm{nT}/\sqrt{\mathrm{Hz}}$ from 1 to 200 Hz. Peaks at 120 Hz and 240 Hz appear in both the magnetically sensitive and insensitive cases, and may result from crosstalk between the MW drive and the photodiode.

Appendix C: Modeling Readout Optimization in a Pulsed AO Sequence

The pulsed AO sequence introduced in Chapter 3 shows experimentally that early NV AO-PL readout in an optical pulse, rather than waiting for the PL to reach steady state, yields larger AO-PL contrast. This appendix develops a single-NV rate-equation model to qualitatively explain this phenomenon, and to explore how the optimal readout timing and duration depend on the applied laser power. The modeling approach follows the seven-level NV rate-equation framework used in Chapter 4, adapted here to represent the two conditions relevant to near-zero-field AO magnetometry: NV electronic spins in cross-relaxation and spectrally separated.

C.1 Seven-Level Rate-Equation Model

Rather than modeling the time-resolved AO-PL variations through an explicit two-NV dipolar interaction (discussed in Sec. 2.4.1), this appendix instead modifies the standard seven-level single-NV rate-equation model directly. We add a spin-sublevel relaxation rate within the ground electronic manifolds k_g, set to different values depending on whether the modeled condition is on- or off-resonance. Fig. C.1 shows the resulting energy level diagram with this ground-state spin-sublevel relaxation rate k_g.

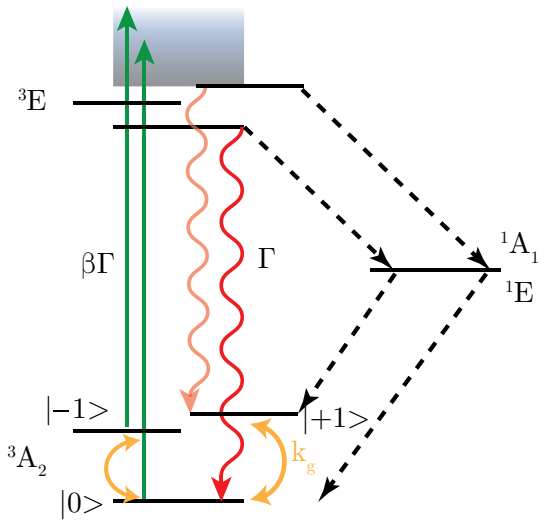


Figure C.1: Modified seven-level rate-equation model, with spin-sublevel relaxation added within the ground state (rate k_g) manifolds. Solid arrows: optical excitation (green, rate $\beta\Gamma$) and spin-conserving radiative decay (red, rate Γ). β is the optical saturation parameter. Dashed arrows: spin-selective intersystem crossing into the singlet manifold and singlet decay back to the ground state.

C.2 Implementation

For a closed three-level ground-state system with two-way sublevel relaxation rate k_g, the spin population distribution after a dark time τ, with a longitudinal relaxation time $T_1 = \left[3k_g\right]^{-1}$ and initial population distribution $n_i(0)$, is given by

$$n_0(\tau) = \frac{1}{3} + \left[n_0(0) - \frac{1}{3}\right] e^{-\tau/T_1}, \tag{C.1}$$

$$n_{\pm1}(\tau) = \frac{1}{3} \pm \left[\frac{n_{+1}(0) - n_{-1}(0)}{2}\right] e^{-\tau/(3T_1)} - \frac{1}{2}\left[n_0(0) - \frac{1}{3}\right] e^{-\tau/T_1}, \tag{C.2}$$

where $|m_s = \pm1\rangle$ are treated as spectrally degenerate [49]. Notably, the exponential decay rate associated with $n_{\pm1}(0)$ in Eq. (C.2) differs from that associated with $n_0(0)$.

Consider this system with all initial population placed in $|m_s = 0\rangle$. Solving the corresponding rate equations gives

$$P_0(\tau) = \frac{1}{3} + \frac{2}{3}e^{-\tau/T_1}, \qquad P_{+1}(\tau) = \frac{1}{3}\left(1 - e^{-\tau/T_1}\right), \qquad P_{-1}(\tau) = \frac{1}{3}\left(1 - e^{-\tau/T_1}\right). \tag{C.3}$$

By the definition of a longitudinal relaxation time (T_1), the remaining population in $|m_s = 0\rangle$ after dark time $\tau = T_1$ should decay to $1/e$ of its initial population above the equilibrium value of $1/3$, giving

$$P_0(T_1) = \frac{1}{3} + \frac{2}{3} \cdot \frac{1}{e} \approx 57.9\%. \tag{C.4}$$

Population in $|m_s = 0\rangle$ should be lost at twice the rate at which population is gained from either $|m_s = -1\rangle$ or $|m_s = +1\rangle$ individually, since $|m_s = 0\rangle$ has two available decay channels (to $|m_s = -1\rangle$ and $|m_s = +1\rangle$) while each of $|m_s = \pm 1\rangle$ has only one channel back to $|m_s = 0\rangle$ in a closed three-level system.

By continuing with the notation $T_1 = 1/(3k_g)$, the population-rate matrix for the electronic spin states becomes

$$\begin{bmatrix} -\Gamma_p - k_g & k_g & 0 \\ k_g & -\Gamma_p - 2k_g & k_g \\ 0 & k_g & -\Gamma_p - k_g \end{bmatrix}, \tag{C.5}$$

where Γ_p is the optical pumping rate (set to zero during a field-free dark interval) and k_g is the spin sub-level relaxation rate.

This matrix is then incorporated into the full seven-level rate equation system, as discussed in Sec. 4.2.1, to calculate the time-resolved PL intensity. The ground-state population immediately following the polarization pulse is set to $[0.7, 0.15, 0.15]$ (population in $|m_s = 0, +1, -1\rangle$, respectively), representative of realistic experimental optical polarization contrast; and the system is then allowed to evolve for a dark time of $\tau \approx 5.5$ ms. The spin-sublevel relaxation rates used to represent the spectrally-separated and cross-relaxation conditions are taken directly from experimentally measured T_1 values reported in Chapter 2: $T_1 = 5.5$ ms for the spectrally-separated condition and $T_1 = 4.7$ ms for the cross-relaxation condition.

With a bias field applied along a single NV axis, an optical pumping parameter $\beta = 1$ (excitation at saturation intensity), and given that two-point readout is performed at each applied field, the pulsed AO-PL contrast is defined as

$$C(t) = \frac{I_{sp}(t)/I_{sp}(t=\infty)}{I_{cr}(t)/I_{cr}(t=\infty)}, \tag{C.6}$$

where $I_{sp}(t)$ and $I_{cr}(t)$ are the simulated PL intensity as a function of time since the readout pulse for the spectrally-separated and cross-relaxation conditions, respectively; and $I_{sp/cr}(t=\infty)$ denotes the corresponding steady-state PL.

C.3 Simulation Results

Fig. C.2 shows the simulated PL intensity and corresponding AO-PL contrast, defined by Eq. (C.6), as a function of laser pulse duration, up to 2 μs. Two qualitative features are apparent. First, the PL intensity under the cross-relaxation condition (shorter

T_1) is measurably reduced relative to the spectrally-separated condition, consistent with faster depolarization of the optically pumped ground-state population. Second, and more directly relevant to sequence design, AO-PL contrast is maximized when the first ("signal") readout window is placed shortly after onset of the optical pulse.

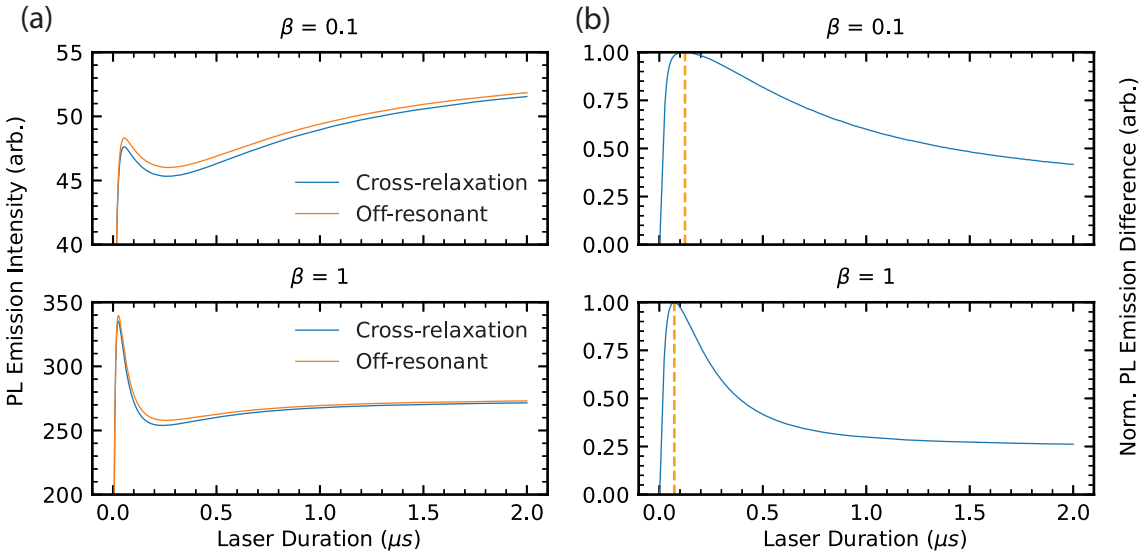


Figure C.2: (a) Simulated time-resolved PL as a function of laser duration between cross-relaxation ($T_1 = 4.7$ ms, blue) and spectrally-separated ($T_1 = 5.5$ ms, orange) conditions, for $\beta = 0.1$ (top) and $\beta = 1$ (bottom). (b) Normalized difference of time-resolved PL between cross-relaxation and spectrally-separated conditions in (a). The yellow dashed line indicates the corresponding laser duration for the maximum PL difference. Stronger optical pumping leads to a larger PL difference, occuring at a shorter timescale.

This qualitative result is reproduced at a lower optical pumping parameter, $\beta = 0.1$, representing operation well below optical saturation. At this lower pumping rate, the maximum simulated AO-PL contrast is reduced, and shifts to a longer optimal readout delay, but decays more gradually, compared to the results from $\beta = 1$. These results

at the lower pumping power are consistent with a slower rate of optical re-polarization competing more directly with spin-sublevel depolarization at a reduced optical excitation intensity.

Experimentally, achieving high AO-PL contrast requires balancing the readout window duration against the applied laser excitation power: higher laser power re-polarizes (re-initializes) the NV ensemble more quickly, so that a longer "signal" readout window can reduce the AO-PL contrast. This power-dependent readout-duration trade-off does not appear to have been documented systematically within the single-NV relaxometry literature, which has generally used a fixed, conventional readout gate duration of approximately 300 ns regardless of excitation power. In Fig. C.2(b), the simulated PL difference for the two conditions decays more gradually at a lower pumping rate, indicating that higher laser power would require a shorter readout window duration to avoid sacrificing AO-PL contrast; this matches the experimental behavior described above.

It is worth noting that the exact shape of the simulated single-NV based time-resolved PL trace does not match experimentally measured traces from an NV ensemble in Fig. 3.2; hence improvement of the simulation model is needed for quantitative matching with experimental results.

Appendix D: Time-resolved NV-PL Decomposition Technique

The rate-equation modeling in the readout-optimization results of Chapter 3 and Appendix C both indicate that the time-resolved NV AO-PL response following an optical pulse carries more information than is used by a single, fixed-timing readout window. This appendix explores that possibility of whether the full time-resolved photodiode trace can be decomposed to recover the underlying NV spin-population distribution at a given time, rather than only a two-point signal/reference contrast. This approach is motivated by an analogous spectral-decomposition technique developed for microwave-assisted charge-state spectroscopy of NV ensembles [6], and is a direct instance of the "full time-resolved AO-PL response" research direction identified as an open question in Chapter 6.

D.1 Decomposition Formalism

Consider a two-level system with basis states $|0\rangle$ and $|1\rangle$ (for example, the NV ground-state sublevels $|m_s = 0\rangle$ and $|m_s = \pm 1\rangle$). A general pure state of this system can be written, using the standard Bloch-sphere parameterization, as

$$|\psi\rangle = \alpha\,|0\rangle + \beta\,|1\rangle = \cos\left(\frac{\theta}{2}\right)|0\rangle + (\cos\varphi + i\sin\varphi)\sin\left(\frac{\theta}{2}\right)|1\rangle\,, \tag{D.1}$$

with polar angle θ and azimuthal angle φ. The probability of measuring the system in $|0\rangle$ is $A \equiv |\alpha|^2$, and the probability of measuring $|1\rangle$ is $B \equiv |\beta|^2$, with $A + B = 1$.

If $X_0(t)$ and $X_1(t)$ denote the time-resolved fluorescence or PL traces measured when the system is prepared purely in $|0\rangle$ or purely in $|1\rangle$, respectively (the two "basis traces"), then the fluorescence or PL trace $Y(t)$ measured from an arbitrary superposition state is modeled as the corresponding linear combination,

$$Y(t) = A\,X_0(t) + B\,X_1(t), \tag{D.2}$$

subject to the constraint $A+B = 1$. Given a measured trace $Y(t)$ and the two basis traces $X_0(t)$, $X_1(t)$, recovering the coefficient A from Eq. (D.2) (for example, via linear regression) determines the polar angle θ of the corresponding Bloch-sphere state, independent of the azimuthal angle φ, through

$$A = \cos^2\!\left(\frac{\theta}{2}\right) = \frac{1}{2}\,(\cos\theta + 1) \quad \Longrightarrow \quad \theta = \cos^{-1}(2A - 1)\,. \tag{D.3}$$

A resonant MW $\pi/2$ pulse produces $\theta = 90°$, $|\psi\rangle = \frac{1}{\sqrt{2}}(|0\rangle + |1\rangle)$, and correspondingly $A = B = 1/2$; a resonant π pulse produces $\theta = 180°$, $|\psi\rangle = |1\rangle$, and correspondingly $A = 0$, $B = 1$, as expected.

D.2 Decomposition on Simulated Data

The decomposition approach of Sec. D.1 is first validated on simulated data, using time-resolved PL traces generated from the five-level rate-equation model of Sec. 1.1.2.

Basis traces are defined for an initial population of 70% in $|m_s = 0\rangle$ (the $|0\rangle$ basis) and 70% in $|m_s = 1\rangle$ (the $|1\rangle$ basis) without additional noise. To produce realistic time-resolved PL traces, laser-intensity-dependent optical noise and background white noise are added to the simulation [Fig. D.1]. The initial $|m_s = 0\rangle$ population is then swept continuously (corresponding to sweeping θ around the Bloch sphere), and for each resulting simulated time-resolved PL trace, MATLAB's `regress()` function is used to fit the linear coefficients of Eq. (D.2) against the two basis traces.

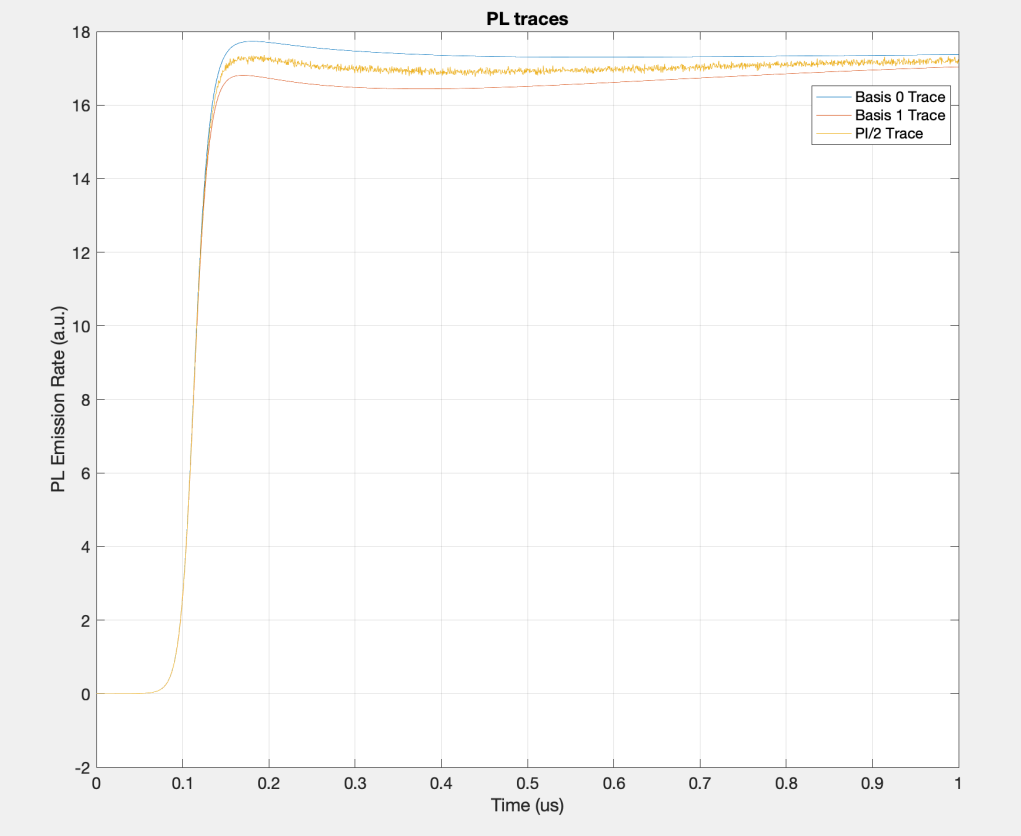


Figure D.1: Simulated time-resolved PL basis traces (for initial population of 70% in $|0\rangle$ and $|1\rangle$) and an example $\pi/2$ trace (equal initial populations) used for decomposition validation.

As Fig. D.2 illustrates, the regression coefficient traced out as a function of MW pulse duration reproduces the expected Rabi-oscillation shape over the swept pulse duration range. In addition, the recovered regression coefficients align closely with the $y = x$ line when plotted against their known theoretical values. This indicates that the simulated PL traces can indeed be decomposed into the two selected basis traces via linear regression, and that the regression recovers the correct population coefficient for each of the two spin states, supporting the validity of the overall approach before applying it to experimental data.

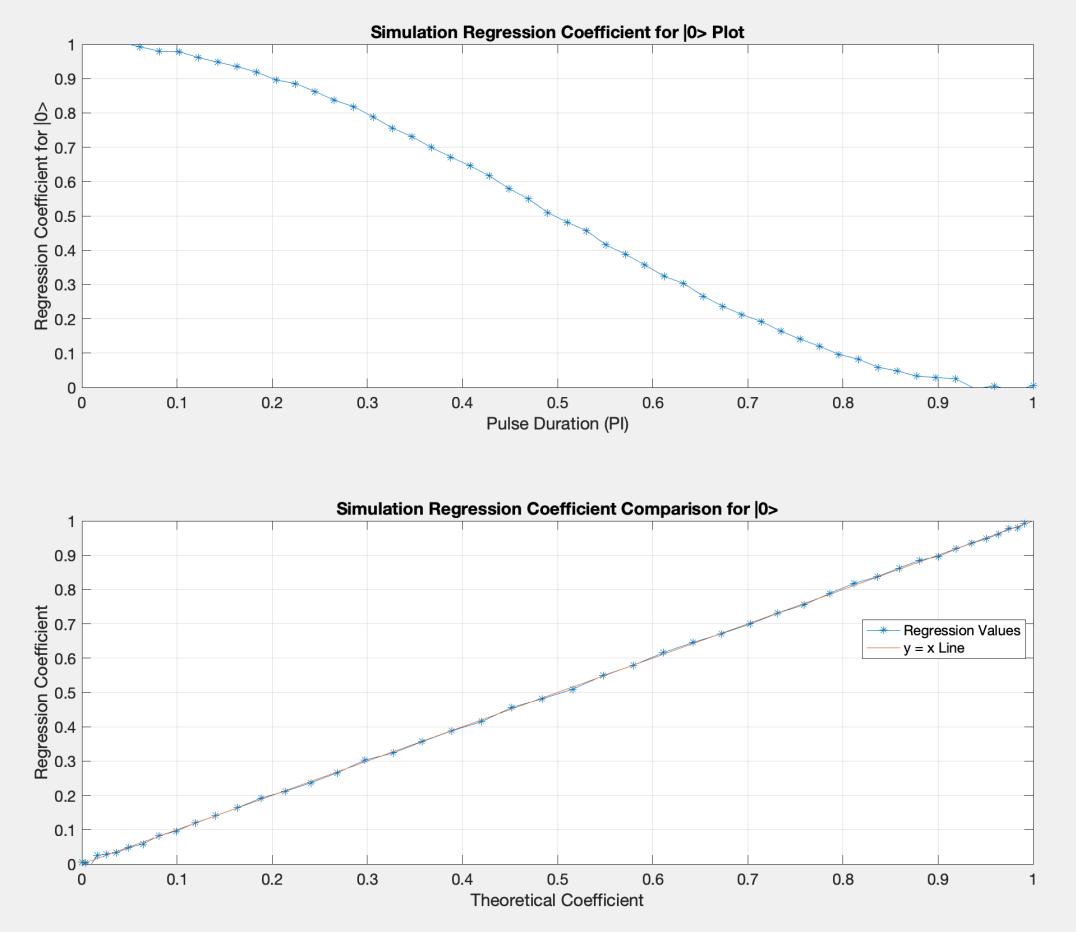


Figure D.2: (Top) Regression coefficient A for $|m_s = 0\rangle$ as a function of MW π-pulse duration. (Bottom) Regression coefficient A as a function of theoretical coefficient of spin distribution follows a linear response.

D.3 Decomposition on Experimental Data

To apply this decomposition technique experimentally, a π-pulse duration of approximately 48 ns is first determined from a conventional "sig/ref" Rabi measurement on NV-diamond sample S8-15N (see Table E.1 for sample details). Time-resolved PL traces are then collected for MW pulse durations from 1 ns to 151 ns (spanning roughly 0 to

3π pulse duration), with the readout pulse timing adjusted to capture the full rising PL dynamics following each MW pulse. Although complete traces are recorded out to 10 μs, the first 1 μs of each trace is expected to carry the most useful information for decomposition, since low-intensity light dominates the PL signal at longer timescales after the initial rise.

The trace corresponding to a 0 ns MW pulse (no MW output) is used directly as the $|0\rangle$ basis trace, and the trace at the independently determined 48 ns π-pulse duration is used as the $|1\rangle$ basis trace, as shown in Fig. D.3.

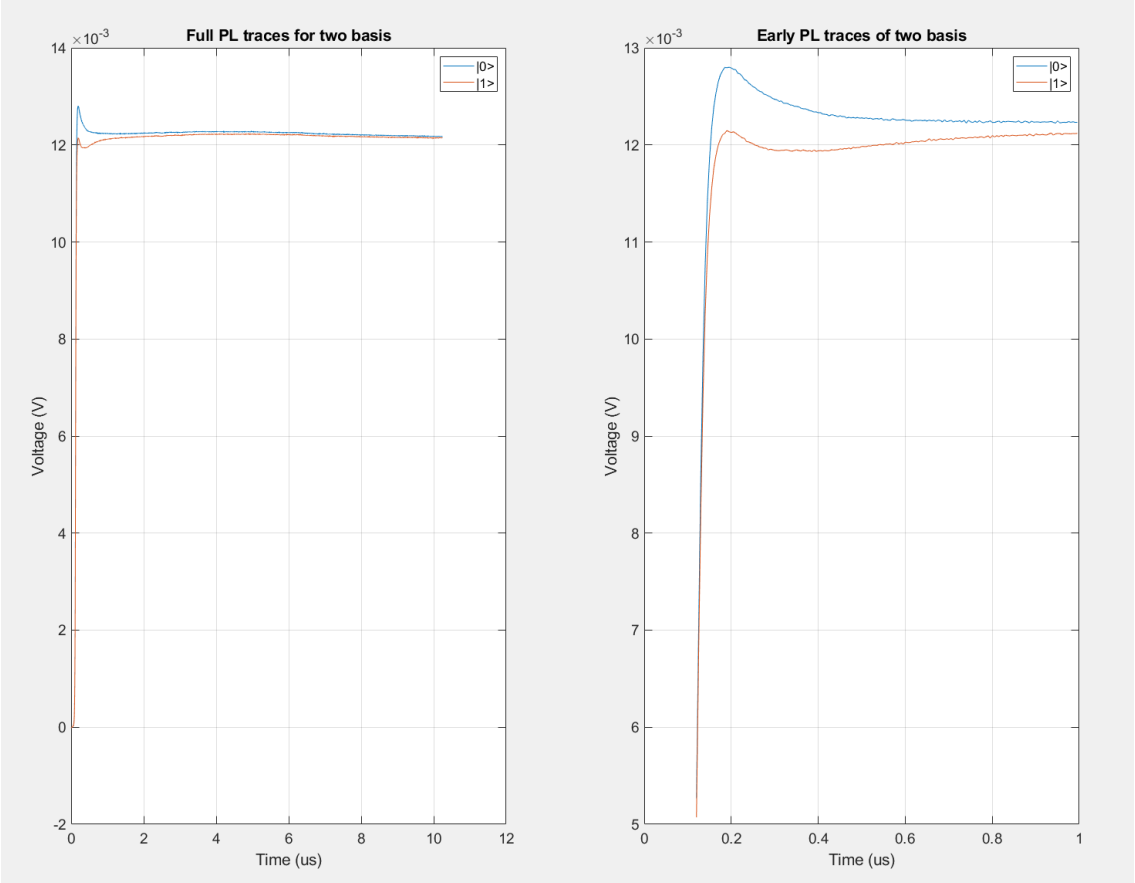


Figure D.3: Experimental basis traces ($|0\rangle$ and $|1\rangle$). The early transient dynamics contains more information for decomposition.

The Rabi curve obtained from the "sig/ref" measurement used throughout this dissertation using a NI-DAQ (500 kS/s sampling rate) is compared directly to the decomposition-based regression coefficients obtained from time-series data acquired with a higher-rate DAQ (200 MS/s sampling rate), though the amount of signal averaging differed between the two acquisition methods. The two curves agree closely, with only small, currently unexplained differences between the coefficient values obtained by each method. Further work is needed to characterize whether the regression-based method can yield better magnetic sensitivity.

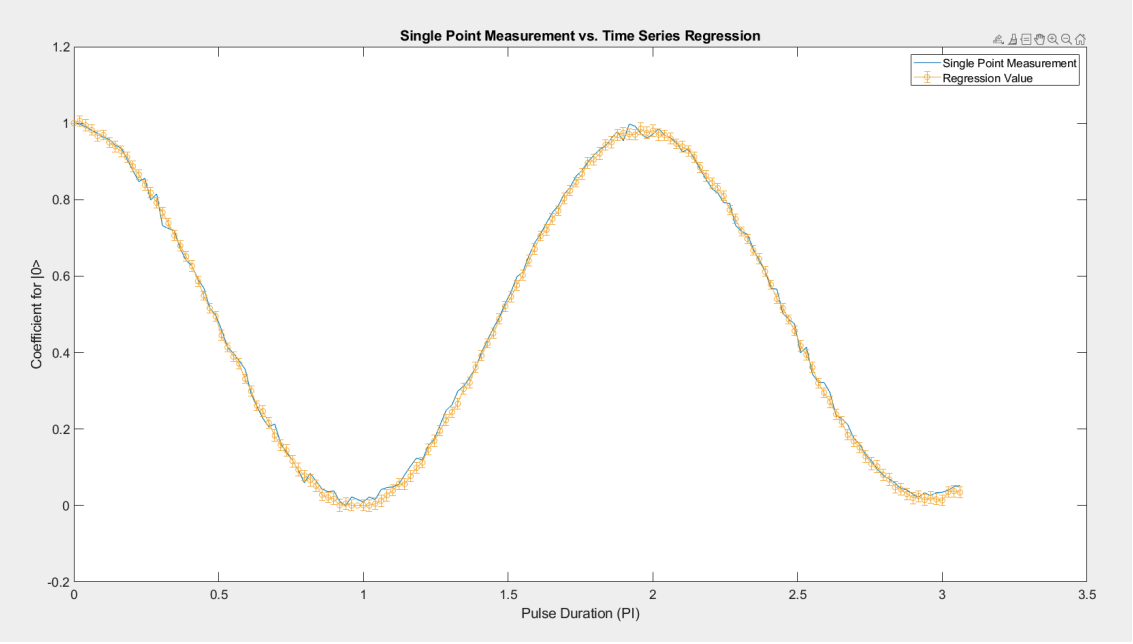


Figure D.4: Rabi curve obtained from "sig/ref" measurement (blue), compared against the regression coefficient (yellow) for $|0\rangle$ obtained from time-resolved PL data via the decomposition technique of Sec. D.1.

D.4 Future Steps

Several extensions of this technique can be considered for future work. First, collecting Rabi-experiment PL traces with progressively less averaging would establish how robust the decomposition approach is to reduced signal-to-noise ratio, and identify the minimum averaging needed for a reliable population estimate. Second, extending the time-resolved measurement window beyond the current 1 μs analysis range would clarify over what timescale the regression approach remains robust, similar to the readout-duration trade-offs characterized in Appendix C.

Third, depending on the robustness of the decomposition approach to noisy, lightly averaged transient PL data, a deep-learning-based denoising pipeline can be applied as a further extension, following a three-phase approach: (1) train a PL-trace denoising model on simulated training and validation data, producing a prototype denoiser; (2) iteratively refine the underlying optical-dynamics simulation until it matches new experimental PL data, producing a working, finalized denoiser; and (3) use the resulting denoised experimental traces, together with a population-labeled simulated training set, to train a regression-based deep-learning model that maps a single PL trace directly to an NV spin-population estimate, validating the result against both a held-out simulated test set and independently obtained experimental data.

This decomposition technique, and the machine-learning extension outlined above, together constitute a direct realization of the time-resolved AO-sensing direction proposed as an open question in Chapter 6: using the full time-resolved NV-PL response, rather than a fixed two-point readout, to infer the underlying spin-population distribution and,

ultimately, to perform AO magnetometry with improved information efficiency per optical pulse.

Appendix E: Summary of Samples

Table E.1: Summary of diamond samples used in this dissertation. The indicated properties are listed as reported by the manufacturer, Element Six Ltd. The dominant nitrogen isotope is listed along with the reported total nitrogen concentration, when available, with relevant additional information provided in the main text.

Sample #	**NV Layer (μm)**	**[N]**	**N Isotope**	**[NV] (ppm)**	**^{13}C (%)**
S1-14N	10	16	^{14}N	≈ 3.8	$<$0.005
S2-15N	10	16	^{15}N	≈ 3.8	$<$0.005
S3-14N	10	16	^{14}N	≈ 3.8	$<$0.005
S4-14N	10	16	^{14}N	≈ 2	$<$0.005
S5-14N	10	16	^{14}N	≈ 0.3	$<$0.005
S6-14N†	1000*	N/A	^{14}N	≈ 4.5	1.10
S7-14N	500*	14	^{14}N	≈ 3.5	1.10
S8-15N	10	17	^{15}N	≈ 2.7	$<$0.01

* Full sample thickness, rather than a doped surface layer.

† HPHT-grown; all other samples are CVD-grown.

Bibliography

[1] John F. Barry, Jennifer M. Schloss, Erik Bauch, Matthew J. Turner, Connor A. Hart, Linh M. Pham, and Ronald L. Walsworth. Sensitivity optimization for NV-diamond magnetometry. *Reviews of Modern Physics*, 92(1):015004, March 2020.

[2] Arne Wickenbrock, Huijie Zheng, Lykourgos Bougas, Nathan Leefer, Samer Afach, Andrey Jarmola, Victor M. Acosta, and Dmitry Budker. Microwave-free magnetometry with nitrogen-vacancy centers in diamond. *Applied Physics Letters*, 109(5):053505, August 2016.

[3] Christopher Ham, Andrew Kirk, Stanislas Pamela, and Howard Wilson. Filamentary plasma eruptions and their control on the route to fusion energy. *Nature Reviews Physics*, 2(3):159–167, March 2020.

[4] R Pánek, J Adámek, M Aftanas, P Bílková, P Böhm, F Brochard, P Cahyna, J Cavalier, R Dejarnac, M Dimitrova, O Grover, J Harrison, P Háček, J Havlíček, A Havránek, J Horáček, M Hron, M Imríšek, F Janky, A Kirk, M Komm, K Kovařík, J Krbec, L Kripner, T Markovič, K Mitošinková, J Mlynář, D Naydenkova, M Peterka, J Seidl, J Stöckel, E Štefániková, M Tomeš, J Urban, P Vondráček, M Varavin, J Varju, V Weinzettl, J Zajac, and the COMPASS team. Status of the COMPASS tokamak and characterization of the first H-mode. *Plasma Physics and Controlled Fusion*, 58(1):014015, January 2016.

[5] J-P Tetienne, L Rondin, P Spinicelli, M Chipaux, T Debuisschert, J-F Roch, and V Jacques. Magnetic-field-dependent photodynamics of single NV defects in diamond: An application to qualitative all-optical magnetic imaging. *New Journal of Physics*, 14(10):103033, October 2012.

[6] D.P.L. Aude Craik, P. Kehayias, A.S. Greenspon, X. Zhang, M.J. Turner, J.M. Schloss, E. Bauch, C.A. Hart, E.L. Hu, and R.L. Walsworth. Microwave-Assisted Spectroscopy Technique for Studying Charge State in Nitrogen-Vacancy Ensembles in Diamond. *Physical Review Applied*, 14(1):014009, July 2020.

[7] Edlyn V. Levine, Matthew J. Turner, Pauli Kehayias, Connor A. Hart, Nicholas Langellier, Raisa Trubko, David R. Glenn, Roger R. Fu, and Ronald L. Walsworth. Principles and techniques of the quantum diamond microscope. *Nanophotonics*, 8(11):1945–1973, November 2019.

[8] Felix M. Stürner, Andreas Brenneis, Thomas Buck, Julian Kassel, Robert Rölver, Tino Fuchs, Anton Savitsky, Dieter Suter, Jens Grimmel, Stefan Hengesbach, Michael Förtsch, Kazuo Nakamura, Hitoshi Sumiya, Shinobu Onoda, Junichi Isoya, and Fedor Jelezko. Integrated and Portable Magnetometer Based on Nitrogen-Vacancy Ensembles in Diamond. *Advanced Quantum Technologies*, 4(4):2000111, 2021.

[9] J. M. Taylor, P. Cappellaro, L. Childress, L. Jiang, D. Budker, P. R. Hemmer, A. Yacoby, R. Walsworth, and M. D. Lukin. High-sensitivity diamond magnetometer with nanoscale resolution. *Nature Physics*, 4(10):810–816, October 2008.

[10] Marcus W. Doherty, Neil B. Manson, Paul Delaney, Fedor Jelezko, Jörg Wrachtrup, and Lloyd C. L. Hollenberg. The nitrogen-vacancy colour centre in diamond. *Physics Reports*, 528(1):1–45, July 2013.

[11] Gergő Thiering and Adam Gali. Theory of the optical spin-polarization loop of the nitrogen-vacancy center in diamond. *Physical Review B*, 98(8):085207, August 2018.

[12] Tse-Luen Wee, Yan-Kai Tzeng, Chau-Chung Han, Huan-Cheng Chang, Wunshain Fann, Jui-Hung Hsu, Kuan-Ming Chen, and Yueh-Chung Yu. Two-photon Excited Fluorescence of Nitrogen-Vacancy Centers in Proton-Irradiated Type Ib Diamond. *The Journal of Physical Chemistry A*, 111(38):9379–9386, September 2007.

[13] D. R. Glenn, R. R. Fu, P. Kehayias, D. Le Sage, E. A. Lima, B. P. Weiss, and R. L. Walsworth. Micrometer-scale magnetic imaging of geological samples using a quantum diamond microscope. *Geochemistry, Geophysics, Geosystems*, 18(8):3254–3267, 2017.

[14] John F. Barry, Matthew J. Turner, Jennifer M. Schloss, David R. Glenn, Yuyu Song, Mikhail D. Lukin, Hongkun Park, and Ronald L. Walsworth. Optical magnetic detection of single-neuron action potentials using quantum defects in diamond. *Proceedings of the National Academy of Sciences*, 113(49):14133–14138, December 2016.

[15] Matthew J. Turner, Nicholas Langellier, Rachel Bainbridge, Dan Walters, Srujan Meesala, Thomas M. Babinec, Pauli Kehayias, Amir Yacoby, Evelyn Hu, Marko Lončar, Ronald L. Walsworth, and Edlyn V. Levine. Magnetic Field Fingerprinting of Integrated-Circuit Activity with a Quantum Diamond Microscope. *Physical Review Applied*, 14(1):014097, July 2020.

[16] Jennifer M. Schloss, John F. Barry, Matthew J. Turner, and Ronald L. Walsworth. Simultaneous Broadband Vector Magnetometry Using Solid-State Spins. *Physical Review Applied*, 10(3):034044, September 2018.

[17] Viktor Stepanov, Franklin H. Cho, Chathuranga Abeywardana, and Susumu Takahashi. High-frequency and high-field optically detected magnetic resonance of nitrogen-vacancy centers in diamond. *Applied Physics Letters*, 106(6):063111, February 2015.

[18] Xue Zhang, Georgios Chatzidrosos, Yinan Hu, Huijie Zheng, Arne Wickenbrock, Alexej Jerschow, and Dmitry Budker. Battery Characterization via Eddy-Current Imaging with Nitrogen-Vacancy Centers in Diamond. *Applied Sciences*, 11(7):3069, January 2021.

[19] Joseph Shaji Rebeirro, Muhib Omar, Till Lenz, Omkar Dhungel, Peter Blümler, Dmitry Budker, and Arne Wickenbrock. Microwave-free wide-field magnetometry using nitrogen-vacancy centers. *Physical Review Applied*, 21(4):044039, April 2024.

[20] David A. Simpson, Jean-Philippe Tetienne, Julia M. McCoey, Kumaravelu Ganesan, Liam T. Hall, Steven Petrou, Robert E. Scholten, and Lloyd C. L. Hollenberg. Magneto-optical imaging of thin magnetic films using spins in diamond. *Scientific Reports*, 6:22797, March 2016.

[21] Xiechen Zheng, Jeyson Támara-Isaza, Zechuan Yin, Johannes Cremer, John W. Blanchard, Connor A. Hart, Michael Crescimanno, Paul V. Petruzzi, Matthew J. Turner, and Ronald L. Walsworth. All-optical photoluminescence response of nitrogen-vacancy ensembles in diamond at low magnetic fields. *Physical Review Applied*, 24(6):064049, December 2025.

[22] Joonhee Choi, Soonwon Choi, Georg Kucsko, Peter C. Maurer, Brendan J. Shields, Hitoshi Sumiya, Shinobu Onoda, Junichi Isoya, Eugene Demler, Fedor Jelezko, Norman Y. Yao, and Mikhail D. Lukin. Depolarization Dynamics in a Strongly Interacting Solid-State Spin Ensemble. *Physical Review Letters*, 118(9):093601, March 2017.

[23] G. Kucsko, S. Choi, J. Choi, P. C. Maurer, H. Zhou, R. Landig, H. Sumiya, S. Onoda, J. Isoya, F. Jelezko, E. Demler, N. Y. Yao, and M. D. Lukin. Critical Thermalization of a Disordered Dipolar Spin System in Diamond. *Physical Review Letters*, 121(2):023601, July 2018.

[24] C. Pellet-Mary, M. Perdriat, P. Huillery, and G. Hétet. Relaxation Processes in Dipole-Coupled Nitrogen-Vacancy Centers in Zero Field: Application in Magnetometry. *Physical Review Applied*, 20(3):034050, September 2023.

[25] S. V. Anishchik and K. L. Ivanov. Sensitive detection of level anticrossing spectra of nitrogen vacancy centers in diamond. *Physical Review B*, 96(11):115142, September 2017.

[26] S. V. Anishchik and K. L. Ivanov. A method for simulating level anti-crossing spectra of diamond crystals containing NV- color centers. *Journal of Magnetic Resonance*, 305:67–76, August 2019.

[27] T. Mittiga, S. Hsieh, C. Zu, B. Kobrin, F. Machado, P. Bhattacharyya, N. Z. Rui, A. Jarmola, S. Choi, D. Budker, and N. Y. Yao. Imaging the Local Charge Environment of Nitrogen-Vacancy Centers in Diamond. *Physical Review Letters*, 121(24):246402, December 2018.

[28] D. S. Filimonenko, V. M. Yasinskii, A. P. Nizovtsev, S. Ya. Kilin, and F. Jelezko. Weak Magnetic Field Effects on the Photoluminescence of an Ensemble of NV Centers in Diamond: Experiment and Modelling. *Semiconductors*, 54(12):1730–1733, December 2020.

[29] Omkar Dhungel, Till Lenz, Muhib Omar, Joseph Shaji Rebeirro, Minh-Tuan Luu, Ali Tayefeh Younesi, Ronald Ulbricht, Viktor Ivády, Adam Gali, Arne Wickenbrock, and Dmitry Budker. Near zero-field microwave-free magnetometry with ensembles of nitrogen-vacancy centers in diamond. *Physical Review B*, 109(22):224107, June 2024.

[30] Omkar Dhungel, Mariusz Mrózek, Till Lenz, Viktor Ivády, Adam Gali, Arne Wickenbrock, Dmitry Budker, Wojciech Gawlik, and Adam M. Wojciechowski. Near-zero-field microwave-free magnetometry with nitrogen-vacancy centers in nanodiamonds. *Optics Express*, 32(12):21936–21945, June 2024.

[31] Andrew M Edmonds, Connor A Hart, Matthew J Turner, Pierre-Olivier Colard, Jennifer M Schloss, Kevin S Olsson, Raisa Trubko, Matthew L Markham, Adam Rathmill, Ben Horne-Smith, Wilbur Lew, Arul Manickam, Scott Bruce, Peter G Kaup, Jon C Russo, Michael J DiMario, Joseph T South, Jay T Hansen, Daniel J Twitchen, and Ronald L Walsworth. Characterisation of CVD diamond with high concentrations of nitrogen for magnetic-field sensing applications. *Materials for Quantum Technology*, 1(2):025001, June 2021.

[32] R. Giri, C. Dorigoni, S. Tambalo, F. Gorrini, and A. Bifone. Selective measurement of charge dynamics in an ensemble of nitrogen-vacancy centers in nanodiamond and bulk diamond. *Physical Review B*, 99(15):155426, April 2019.

[33] Isabel Cardoso Barbosa, Jonas Gutsche, and Artur Widera. Impact of charge conversion on NV-center relaxometry. *Physical Review B*, 108(7):075411, August 2023.

[34] Clément Pellet-Mary. *Cross-Relaxation in Dense Ensembles of NV Centers and Application to Magnetometry*. PhD thesis, Université Paris sciences et lettres, December 2022.

[35] K. Arai, C. Belthangady, H. Zhang, N. Bar-Gill, S. J. DeVience, P. Cappellaro, A. Yacoby, and R. L. Walsworth. Fourier magnetic imaging with nanoscale resolution and compressed sensing speed-up using electronic spins in diamond. *Nature Nanotechnology*, 10(10):859–864, October 2015.

[36] Mikael P. Backlund, Pauli Kehayias, and Ronald L. Walsworth. Fourier optical processing enables new capabilities in diamond magnetic imaging. May 2017.

[37] Lucio Robledo, Hannes Bernien, Toeno van der Sar, and Ronald Hanson. Spin dynamics in the optical cycle of single nitrogen-vacancy centres in diamond. *New Journal of Physics*, 13(2):025013, February 2011.

[38] André Vander Vorst, Arye Rosen, and Youji Kotsuka. *RF / Microwave Interaction with Biological Tissues*. John Wiley & Sons, Hoboken, NJ, February 2006.

[39] Yechezkel Schlussel, Till Lenz, Dominik Rohner, Yaniv Bar-Haim, Lykourgos Bougas, David Groswasser, Michael Kieschnick, Evgeny Rozenberg, Lucas Thiel, Amir Waxman, Jan Meijer, Patrick Maletinsky, Dmitry Budker, and Ron Folman. Wide-Field Imaging of Superconductor Vortices with Electron Spins in Diamond. *Physical Review Applied*, 10(3):034032, September 2018.

[40] Kai-Mei C. Fu, Geoffrey Z. Iwata, Arne Wickenbrock, and Dmitry Budker. Sensitive magnetometry in challenging environments. *AVS Quantum Science*, 2(4):044702, December 2020.

[41] Matthias Widmann, Sang-Yun Lee, Torsten Rendler, Nguyen Tien Son, Helmut Fedder, Seoyoung Paik, Li-Ping Yang, Nan Zhao, Sen Yang, Ian Booker, Andrej Denisenko, Mohammad Jamali, S. Ali Momenzadeh, Ilja Gerhardt, Takeshi Ohshima, Adam Gali, Erik Janzén, and Jörg Wrachtrup. Coherent control of single spins in silicon carbide at room temperature. *Nature Materials*, 14(2):164–168, February 2015.

[42] D. Simin, V. A. Soltamov, A. V. Poshakinskiy, A. N. Anisimov, R. A. Babunts, D. O. Tolmachev, E. N. Mokhov, M. Trupke, S. A. Tarasenko, A. Sperlich, P. G. Baranov, V. Dyakonov, and G. V. Astakhov. All-Optical dc Nanotesla Magnetometry Using Silicon Vacancy Fine Structure in Isotopically Purified Silicon Carbide. *Physical Review X*, 6(3):031014, July 2016.

[43] Andreas Gottscholl, Mehran Kianinia, Victor Soltamov, Sergei Orlinskii, Georgy Mamin, Carlo Bradac, Christian Kasper, Klaus Krambrock, Andreas Sperlich, Milos Toth, Igor Aharonovich, and Vladimir Dyakonov. Initialization and read-out of intrinsic spin defects in a van der Waals crystal at room temperature. *Nature Materials*, 19(5):540–545, May 2020.

[44] Andreas Gottscholl, Matthias Diez, Victor Soltamov, Christian Kasper, Andreas Sperlich, Mehran Kianinia, Carlo Bradac, Igor Aharonovich, and Vladimir Dyakonov. Room temperature coherent control of spin defects in hexagonal boron nitride. *Science Advances*, 7(14):eabf3630, April 2021.

[45] A.L. Kasatkin, V.M. Pan, V.V. Vysotskii, and H.C. Freyhardt. Flux relaxation phenomena in the presence of weak AC magnetic fields. *Physica C: Superconductivity*, 310(1-4):296–301, December 1998.

[46] Vladimir Sokolovsky, Victor Meerovich, Valery Dikovsky, and Eugene Paperno. Penetration of ac magnetic field into bulk high-temperature superconductors: Experiment and simulation. *Journal of Applied Physics*, 95(11):6693–6695, June 2004.

[47] Omkar Dhungel, Saravanan Sengottuvel, Mariusz Mrózek, Till Lenz, Nir Bar-Gill, Adam M. Wojciechowski, Arne Wickenbrock, and Dmitry Budker. All-optical low-field magnetometry of superconductors using NV nanodiamonds. *Measurement*, 283:122080, August 2026.

[48] Xiechen Zheng, Jeyson Támara-Isaza, John W. Blanchard, and Ronald L. Walsworth. Noise Suppression via Pulsed All-Optical Magnetometry with Nitrogen-Vacancy Ensembles, July 2026.

[49] J.-P. Tetienne, T. Hingant, L. Rondin, A. Cavaillès, L. Mayer, G. Dantelle, T. Gacoin, J. Wrachtrup, J.-F. Roch, and V. Jacques. Spin relaxometry of single nitrogen-vacancy defects in diamond nanocrystals for magnetic noise sensing. *Physical Review B*, 87(23):235436, June 2013.

[50] M. Pelliccione, B. A. Myers, L. M. A. Pascal, A. Das, and A. C. Bleszynski Jayich. Two-Dimensional Nanoscale Imaging of Gadolinium Spins via Scanning Probe Relaxometry with a Single Spin in Diamond. *Physical Review Applied*, 2(5):054014, November 2014.

[51] Dominik Schmid-Lorch, Thomas Häberle, Friedemann Reinhard, Andrea Zappe, Michael Slota, Lapo Bogani, Amit Finkler, and Jörg Wrachtrup. Relaxometry and Dephasing Imaging of Superparamagnetic Magnetite Nanoparticles Using a Single Qubit. *Nano Letters*, 15(8):4942–4947, August 2015.

[52] Aurore Finco, Angela Haykal, Rana Tanos, Florentin Fabre, Saddem Chouaieb, Waseem Akhtar, Isabelle Robert-Philip, William Legrand, Fernando Ajejas, Karim Bouzehouane, Nicolas Reyren, Thibaut Devolder, Jean-Paul Adam, Joo-Von Kim, Vincent Cros, and Vincent Jacques. Imaging non-collinear antiferromagnetic textures via single spin relaxometry. *Nature Communications*, 12(1):767, February 2021.

[53] G Heinzel, A Rudiger, and R Schilling. Spectrum and spectral density estimation by the Discrete Fourier transform (DFT), including a comprehensive list of window functions and some new flat-top windows. *Spectrum and spectral density estimation by the discrete Fourier transform (DFT), including a comprehensive list of window functions and some new flat-top windows*, 2002.

[54] James W. Kirchner. Aliasing in $1/{f}^{\ensuremath{\alpha}}$ noise spectra: Origins, consequences, and remedies. *Physical Review E*, 71(6):066110, June 2005.

[55] J. E. Kunzler, E. Buehler, F. S. L. Hsu, and J. H. Wernick. Superconductivity in Nb 3 Sn at High Current Density in a Magnetic Field of 88 kgauss. *Physical Review Letters*, 6(3):89–91, February 1961.

[56] Zachary S. Hartwig, Rui F. Vieira, Brandon N. Sorbom, Rodney A. Badcock, Marta Bajko, William K. Beck, Bernardo Castaldo, Christopher L. Craighill, Michael Davies, Jose Estrada, Vincent Fry, Theodore Golfinopoulos, Amanda E. Hubbard, James H. Irby, Sergey Kuznetsov, Christopher J. Lammi, Philip C. Michael, Theodore Mouratidis, Richard A. Murray, Andrew T. Pfeiffer, Samuel Z. Pierson, Alexi Radovinsky, Michael D. Rowell, Erica E. Salazar, Michael Segal, Peter W. Stahle, Makoto Takayasu, Thomas L. Toland, and Lihua Zhou. VIPER: An industrially scalable high-current high-temperature superconductor cable. *Superconductor Science and Technology*, 33(11):11LT01, October 2020.

[57] I. H. Hutchinson. Principles of Plasma Diagnostics: Second Edition. *Plasma Physics and Controlled Fusion*, 44(12):2603–2603, November 2002.

[58] H.-J. Hartfuss, R. König, and A. Werner. Diagnostics for steady state plasmas. *Plasma Physics and Controlled Fusion*, 48(10):R83–R150, September 2006.

[59] D. Paone, D. Pinto, G. Kim, L. Feng, M.-J. Kim, R. Stöhr, A. Singha, S. Kaiser, G. Logvenov, B. Keimer, J. Wrachtrup, and K. Kern. All-optical and microwave-free detection of Meissner screening using nitrogen-vacancy centers in diamond. *Journal of Applied Physics*, 129(2):024306, January 2021.

[60] Daniel G. Ang, Jiashen Tang, Maximilian Shen, Michael Titze, Gavishta Liyanage, Jordan Chapman, Chinmay Bharathulwar, Andrew T. Gilpin, Tanguy Terlier, Edward S. Bielejec, Vsevolod Ivanov, and Ronald L. Walsworth. Multi-scale reconstruction of single-ion damage tracks in diamond via nitrogen-vacancy centers, June 2026.

[61] Lukas Razinkovas, Marek Maciaszek, Friedemann Reinhard, Marcus W. Doherty, and Audrius Alkauskas. Photoionization of negatively charged NV centers in diamond: Theory and *ab initio* calculations. *Physical Review B*, 104(23):235301, December 2021.

[62] Jean-Philippe Tetienne, Alain Lombard, David A. Simpson, Cameron Ritchie, Jiaming Lu, Paul Mulvaney, and Lloyd C. L. Hollenberg. Scanning Nanospin Ensemble Microscope for Nanoscale Magnetic and Thermal Imaging. *Nano Letters*, 16(1):326–333, January 2016.

[63] Bindu, Amandeep Singh, Amir Hen, Lukas Drago Ćavar, Sebastian Maria Ulrich Schultheis, Shira Yochelis, Yossi Paltiel, Andrew F. May, Angela Wittmann, Mathias Kläui, Dmitry Budker, Hadar Steinberg, and Nir Bar-Gill. Quantum Imaging of Ferromagnetic van der Waals Magnetic Domain Structures at Ambient Conditions. *ACS Applied Materials & Interfaces*, 17(46):63956–63967, November 2025.

[64] David R. Glenn, Dominik B. Bucher, Junghyun Lee, Mikhail D. Lukin, Hongkun Park, and Ronald L. Walsworth. High-resolution magnetic resonance spectroscopy using a solid-state spin sensor. *Nature*, 555(7696):351–354, March 2018.

[65] Connor A. Hart, Jennifer M. Schloss, Matthew J. Turner, Patrick J. Scheidegger, Erik Bauch, and Ronald L. Walsworth. N - V –Diamond Magnetic Microscopy Using a Double Quantum 4-Ramsey Protocol. *Physical Review Applied*, 15(4):044020, April 2021.

[66] S. C. Scholten, A. J. Healey, I. O. Robertson, G. J. Abrahams, D. A. Broadway, and J.-P. Tetienne. Widefield quantum microscopy with nitrogen-vacancy centers in diamond: Strengths, limitations, and prospects. *Journal of Applied Physics*, 130(15):150902, October 2021.

[67] Kosuke Mizuno, Hitoshi Ishiwata, Yuta Masuyama, Takayuki Iwasaki, and Mutsuko Hatano. Simultaneous wide-field imaging of phase and magnitude of AC magnetic signal using diamond quantum magnetometry. *Scientific Reports*, 10(1):11611, July 2020.

[68] Saravanan Sengottuvel, Omkar Dhungel, Mariusz Mrózek, Arne Wickenbrock, Dmitry Budker, Wojciech Gawlik, and Adam M. Wojciechowski. Microwave-free imaging magnetometry with nitrogen-vacancy centers in nanodiamonds at near-zero field. *Physical Review Applied*, 23(3):034001, March 2025.

[69] Jiashen Tang, Zechuan Yin, Connor A. Hart, John W. Blanchard, Jner Tzern Oon, Smriti Bhalerao, Jennifer M. Schloss, Matthew J. Turner, and Ronald L. Walsworth. Quantum diamond microscope for dynamic imaging of magnetic fields. *AVS Quantum Science*, 5(4):044403, December 2023.

[70] Zechuan Yin, Jiashen Tang, Connor A. Hart, John W. Blanchard, Xinyan Xiang, Saipriya Satyajit, Smriti Bhalerao, Tao Tao, Stephen J. DeVience, and Ronald L. Walsworth. Quantum diamond microscope for narrowband magnetic imaging with high spatial and spectral resolution. *Physical Review Applied*, 22(5):054050, November 2024.

[71] Akihiro Kuwahata, Takahiro Kitaizumi, Kota Saichi, Takumi Sato, Ryuji Igarashi, Takeshi Ohshima, Yuta Masuyama, Takayuki Iwasaki, Mutsuko Hatano, Fedor Jelezko, Moriaki Kusakabe, Takashi Yatsui, and Masaki Sekino. Magnetometer with nitrogen-vacancy center in a bulk diamond for detecting magnetic nanoparticles in biomedical applications. *Scientific Reports*, 10(1):2483, February 2020.

[72] Daniel Riedel, Teodoro Graziosi, Zhuoxian Wang, Chawina De-Eknamkul, Alex Abulnaga, Jonathan Dietz, Andrea Mucchietto, Michael Haas, Madison Sutula, Pierre Barral, Matteo Pompili, Mouktik Raha, Carsten Robens, Jeonghoon Ha, Denis Sukachev, David Levonian, Mihir Bhaskar, Matthew Markham, and Bartholomeus Machielse. Scalable Photonic Quantum Interconnect Platform. *Physical Review X*, 16(1):011063, March 2026.

[73] Hannah Clevenson, Linh M. Pham, Carson Teale, Kerry Johnson, Dirk Englund, and Danielle Braje. Robust high-dynamic-range vector magnetometry with nitrogen-vacancy centers in diamond. *Applied Physics Letters*, 112(25):252406, June 2018.

[74] H. Espinós, O. Dhungel, A. Wickenbrock, D. Budker, R. Puebla, and E. Torrontegui. Microwave-free vector magnetometry and crystal orientation determination with nitrogen-vacancy centers using Bayesian inference. *Communications Physics*, July 2026.

[75] Mikael P. Backlund, Pauli Kehayias, and Ronald L. Walsworth. Diamond-Based Magnetic Imaging with Fourier Optical Processing. *Physical Review Applied*, 8(5):054003, November 2017.

[76] Mason C Marshall, Matthew J Turner, Mark J H Ku, David F Phillips, and Ronald L Walsworth. Directional detection of dark matter with diamond. *Quantum Science and Technology*, 6(2):024011, April 2021.

[77] S.M. Graham, A.T.M.A. Rahman, L. Munn, R.L. Patel, A.J. Newman, C.J. Stephen, G. Colston, A. Nikitin, A.M. Edmonds, D.J. Twitchen, M.L. Markham, and G.W. Morley. Fiber-Coupled Diamond Magnetometry with an Unshielded Sensitivity of \$30\phantom{\rule{0.1em}{0ex}}\mathrm{pT}/\sqrt{\mathrm{Hz}}\$. *Physical Review Applied*, 19(4):044042, April 2023.

[78] Felix M. Stürner, Andreas Brenneis, Julian Kassel, Uwe Wostradowski, Robert Rölver, Tino Fuchs, Kazuo Nakamura, Hitoshi Sumiya, Shinobu Onoda, Junichi Isoya, and Fedor Jelezko. Compact integrated magnetometer based on nitrogen-vacancy centres in diamond. *Diamond and Related Materials*, 93:59–65, March 2019.